AFRL-RY-HS-TR-2011-0001 Volume I

PROCEEDINGS OF THE 2010 ANTENNA APPLICATIONS SYMPOSIUM
Volume I of II

Daniel Schaubert et al.

University of Massachusetts at Amherst
Electrical and Computer Engineering
100 Natural Resources Road
Amherst MA 01003

Final Report

December 2010

AIR FORCE RESEARCH LABORATORY
Sensors Directorate
Electromagnetics Technology Division
80 Scott Drive
Hanscom AFB MA 01731-2909

NOTICE AND SIGNATURE PAGE

Using Government drawings, specifications, or other data included in this document for any purpose other than Government procurement does not in any way obligate the U.S. Government. The fact that the Government formulated or supplied the drawings, specifications, or other data does not license the holder or any other person or corporation; or convey any rights or permission to manufacture, use, or sell any patented invention that may relate to them.

This report was cleared for public release by the Electronic Systems Center Public Affairs Office for the Air Force Research Laboratory Electromagnetic Technology Division and is available to the general public, including foreign nationals. Copies may be obtained from the Defense Technical Information Center (DTIC) (http://www.dtic.mil).

AFRL-RY-HS-TR-2011-0001 HAS BEEN REVIEWED AND IS APPROVED FOR PUBLICATION IN ACCORDANCE WITH ASSIGNED DISTRIBUTION STATEMENT.

DAVID D. CURTIS
Chief, Antenna Technology Branch

Robert V. McGahan

ROBERT V. McGAHAN
Technical Communications Advisor
Electromagnetic Technology Division

This report is published in the interest of scientific and technical information exchange, and its publication does not constitute the Government's approval or disapproval of its ideas or findings.

REPORT DOCUMENTATION PAGE

Form Approved
OMB No. 0704-0188

1. REPORT DATE *(DD-MM-YYYY)*	**2. REPORT TYPE**	**3. DATES COVERED** *(From - To)*
December 2010	FINAL REPORT	21 Sep 2010 – 23 Sep 2010

4. TITLE AND SUBTITLE

Proceedings of the 2010 Antenna Applications Symposium, Volume I

5a. CONTRACT NUMBER

5b. GRANT NUMBER

5c. PROGRAM ELEMENT NUMBER

6. AUTHOR(S)

Daniel Schaubert, et al.

5d. PROJECT NUMBER
4916

5e. TASK NUMBER
HA

5f. WORK UNIT NUMBER
01

7. PERFORMING ORGANIZATION NAME(S) AND ADDRESS(ES)
University of Massachusetts Amherst
Electrical and Computer Engineering
100 Natural Resources Road
Amherst, MA 01003

8. PERFORMING ORGANIZATION REPORT

9. SPONSORING / MONITORING AGENCY NAME(S) AND ADDRESS(ES)
Electromagnetics Technology Division
Sensors Directorate
Air Force Research Laboratory
80 Scott Drive
Hanscom AFB MA 01731-2909

10. SPONSOR/MONITOR'S ACRONYM(S)
AFRL-RY-HS

11. SPONSOR/MONITOR'S REPORT NUMBER(S)
AFRL-RY-HS-TR-2011-0001

12. DISTRIBUTION / AVAILABILITY STATEMENT
APPROVED FOR PUBLIC RELEASE; DISTRIBUTION UNLIMITED

13. SUPPLEMENTARY NOTES
Volume I contains pages 1- 255 Public Affairs release Number 66 ABW-2011-0024
Volume II contains pages 256-513

14. ABSTRACT

The Proceedings of the 2010 Antenna Applications Symposium is a collection of state-of-the art papers relating to antenna arrays and elements, millimeter wave antennas, simulation and measurement of antennas, integrated antennas, and antenna bandwidth and radiation improvements.

15. SUBJECT TERMS
Antennas, phased arrays, digital beam forming, millimeter waves, metamaterials, antenna measurements, airborne antenna applications, Vivaldi antennas, waveguide antenna arrays, broadband arrays, electrically small antennas

16. SECURITY CLASSIFICATION OF:			**17.LIMITATION OF ABSTRACT**	**18.NUMBER OF PAGES**	**19a. NAME OF RESPONSIBLE PERSON**
a. REPORT	**b. ABSTRACT**	**c. THIS PAGE**			David D. Curtis
Unclassified	Unclassified	Unclassified	UU	266	**19b. TELEPHONE NUMBER** *(include area code)* N/A

Standard Form 298 (Rev. 8-98)
Prescribed by ANSI Std. Z39.18

2010 ANTENNA APPLICATIONS SYMPOSIUM

21 - 23 September 2010
Monticello, Illinois

Identifiers for Proceedings of Symposia

The USAF Antenna Research and Development Program

Year	Symp. No.	Identifier
1951	First	_____
1952	Second	ADB870006
1953	Third	ADB283180
1954	Fourth	AD63139
1955	Fifth	AD90397
1956	Sixth	AD114702
1957	Seventh	AD138500
1958	Eighth	AD301151
1959	Ninth	AD314721
1960	Tenth	AD244388 (Vol. 1) AD319613 (Vol. 2)
1961	Eleventh	AD669109 (Vol. 1) AD326549 (Vol. 2)
1962	Twelfth	AD287185 (Vol. 1) AD334484 (Vol. 2)
1963	Thirteenth	AD421483
1964	Fourteenth	AD609104
1965	Fifteenth	AD474238L
1966	Sixteenth	AD800524L
1967	Seventeenth	AD822894L
1968	Eighteenth	AD846427L
1969	Nineteenth	AD860812L
1970	Twentieth	AD875973L
1971	Twenty-First	AD888641L
1972	Twenty-Second	AD904360L
1973	Twenty-Third	AD914238L

Antenna Applications Symposium

Year	Symposium	Technical Report #	Identifier
1977	First	None	ADA 955413
1978	Second	None	ADA 955416
1979	Third	_____	ADA 077167
1980	Fourth	_____	ADA 205907
1981	Fifth	_____	ADA 205816
1982	Sixth	_____	ADA 129356
1983	Seventh	_____	ADA 142003; 142754
1984	Eighth	85-14	ADA 153257; 153258
1985	Ninth	85-242	ADA 166754; 165535
1986	Tenth	87-10	ADA 181537; 181536
1987	Eleventh	88-160	ADA 206705; 206704
1988	Twelfth	89-121	ADA 213815; 211396
1989	Thirteenth	90-42	ADA 26022; 226021
1990	Fourteenth	91-156	ADA 37056; 237057
1991	Fifteenth	92-42	ADA 253681; 253682
1992	Sixteenth	93-119	ADA 268167; 266916
1993	Seventeenth	94-20	ADA 277202; 277203
1994	Eighteenth	95-47	ADA 293258; 293259
1995	Nineteenth	96-100	ADA 309715; 309723
1996	Twentieth	97-189	ADA 341737
1997	Twenty First	1998-143	ADA 355120
1998	Twenty Second	1999-86	ADA 364798
1999	Twenty Third	2000-008 (I) (II)	ADA 386476; 386477
2000	Twenty Fourth	2002-001 Vol I & II	ADA 405537; 405538
2001	Twenty Fifth	2002-002 Vol I & II	ADA 405328; 405327
2002	Twenty Sixth	2005-001 Vol I & II	ADA 427799; 427800
2003	Twenty Seventh	2005-005 Vol I & II	ADA 429122
2004	Twenty Eighth	2005-016 Vol I & II	ADA431338; 431339
2005	Twenty Ninth	2005-039 Vol I & II	ADM001873
2006	Thirtieth	2006-0047 Vol I & II	ADA464059
2007	Thirty First	2007-0037 Vol I & II	ADA475327, 475333
2008	Thirty Second	2008-0026 Vol I & II	ADA494632, 494633
2009	Thirty Third	2010-0001 Vol I & II	ADA520099, 520100

2010 Author Index

The Long Road to Affordable Phased Arrays

Louis Coryell, Rich Hoffmann, Raymond Lau and Joseph Shields

US Army CERDEC S&TCD, Fort Monmouth, NJ and Aberdeen Proving Ground, MD

Abstract

Army doctrine has evolved to include an increased reliance on Beyond Line of Sight (BLOS) communications due to a non-contiguous battlefield. Additionally, communications on-the-move (OTM) is required to support delivery of information critical to operation planning as well as during operation execution. The Warfighter requires mobility and network connectivity to provide the needed level of near real-time, tactically-relevant information. Space based communications form a critical layer in supporting these essential networking capabilities.

Efforts to date in On-The-Move SATCOM systems have focused on mechanically steered dish antennas. These systems are affordable, but at the price of a high visual profile on the battlefield. Users want low profile antenna systems to minimize antenna system vulnerability. The ultimate in low profile antennas is the phased array. Affordability and scan loss have been the problems precluding the use of phased arrays. The Space and Terrestrial Communications Directorate (S&TCD) Space Systems Division has been working on phased arrays and related technologies for over 20 years. This paper details the problems associated with phased array affordability and scan loss. Key enabling technologies are identified and solutions discussed in detail. Finally, we present what we believe are the remaining technological hurdles that must be overcome before phased array antenna systems become commonplace on the battlefield.

1. Phased Array Antenna Systems

We have previously described many of the phased array antenna systems that CERDEC has developed for communications on-the-move [1]. We will describe several that have not been discussed previously in detail and briefly review those presented earlier.

1.1. Boeing 64-Element X-Band Phased Arrays

The Boeing phased arrays started life as dual beam optically controlled transmit and receive arrays (Figure 1) [2]. Given the then current high cost of phased arrays, we were looking for something more affordable. Optical control offered the promise of a single control system which was independent of the phased array frequency. Previous work was completed by Boeing on a 16 channel Integrated Optical Phase and Amplitude Controller

(IP-PAC) which was demonstrated to control arrays at 7 GHz and 60 GHz. We found out within a year that affordability was eluding us. The main problem was not optical signal generation or detection, but obtaining sufficient optical power at each antenna element. Three efforts that had been ongoing to develop an amplified optical splitter were unsuccessful, each for different reasons. The only alternative was to employ Erbium doped optical fiber amplifiers. This alternative, however, would add almost $500,000 to the cost of the phased arrays. The decision was made to discontinue the optical control system and to fall back to fabricating conventional electrically controlled phased arrays. The plus side to this was that the development would cost approximately $1,000,000 less than had been planned.

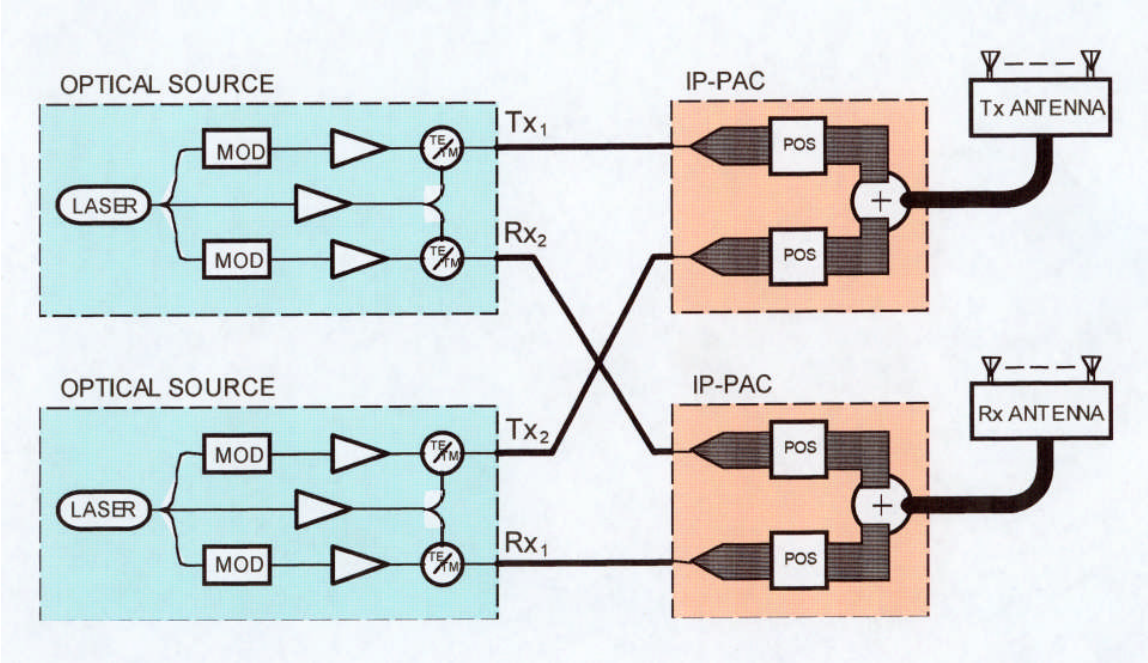

Figure 1. Boeing Optically Controlled Phased Array.

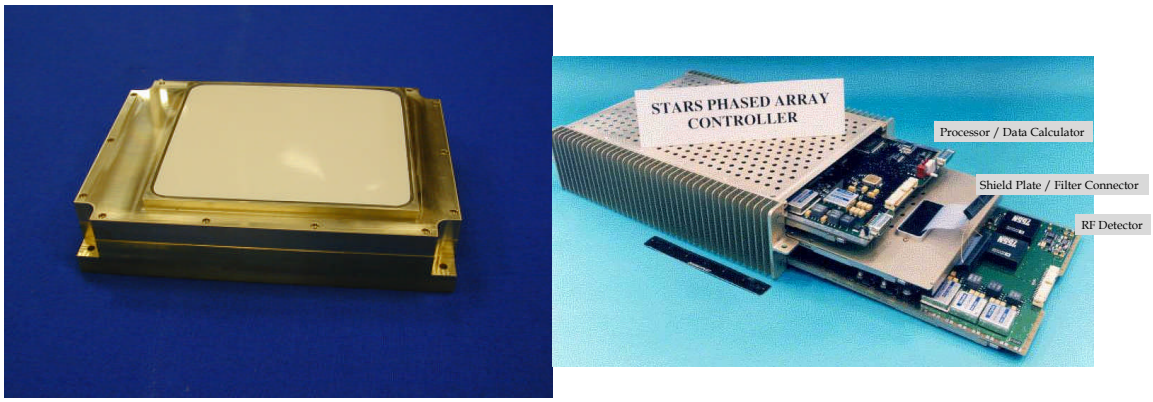

Figure 2. Final Boeing Electrically Controlled Phased Array

The final arrays (Figure 2) included dual transmit and receive beams, each capable of amplitude tapering to reduce sidelobes. Scan loss of the arrays was only 4.9 dB at a 70 degree scan angle. This was achieved with a loaded cavity radiator with orthogonal probe feeds. The dual transmit MMIC, for feeding the two probes, had a PAE of 30% at a P1dB of 21.5 dBm to each probe. The effective noise figure of 2.7 to 3.4 dB was the result of insufficient gain between the filter at the output of the LNA and subsequent combiner and filter stages. Complete specifications of the arrays are given in Table 1.

Transmit Array	
Frequency	7.25 - 7.75 GHz
No. of Elements	64 (with built-in amplitude taper control)
Polarization	RH/LH CP switchable
No. of Beams	2 beams at different frequencies and with same polarization
Max. Scan Angle	±70 deg
EIRP (Boresight)	30 dBW (1 tone); 28.4 dBw (each of 2 tones)
(70 deg)	23.4 dBW (6.6 dB scan loss) (4.9 dB achieved)
Power Dissipation	+5 V with 18 A; -5V with < 0.3 A
Size	"Textbook"
Receive Array	
Frequency	7.90 - 8.40 GHz
No. of Elements	64 (with built-in filter and amplitude taper control)
Polarization	RH/LH CP switchable
No. of Beams	2 beams at different frequencies and with same polarization
Max. Scan Angle	±70 deg
G/T (Boresight) -	-4.0 dB/K
(70 deg)	-10.66 dB/K (6.6 dB scan loss) (4.8 dB achieved)
Power Dissipation	+6 V with 4 A; -5V with < 0.3 A
Size	"Textbook"

Table 1. Boeing X-Band Phased Array Specifications

1.2. Millitech Active Quasioptic Array

The Millitech phased array is designed to utilize line arrays at Ku, K and Ka bands to feed a single quasioptic lens [3]. Azimuth and elevation beam steering are mechanical with an electronic cross elevation scan to eliminate the keyhole effect (Figure 3). One of the main technical contribution is the aperture stacked patch radiator (Figure 4) after Targonski, et.al. [4]. This extremely wide bandwidth radiator has 20 to 25 dB cross polarization isolation (Figure 5). This allows the same radiator to efficiently operate at both K (19.7 to 21.2 GHz) and Ka Bands (29.5-31 GHz). Highly innovative filtering techniques were utilized at Ku band to separate the transmit (13.75 to 14.5 GHz) and receive frequencies (10.95 to 12.75 GHz) in a very constrained space. Due to cost constraints, this antenna is currently being completed as a K/Ka band antenna. The

overall concept of an active quasioptic array remains a strong candidate for future consideration due to its constant G/T and EIRP with scan angle and low profile.

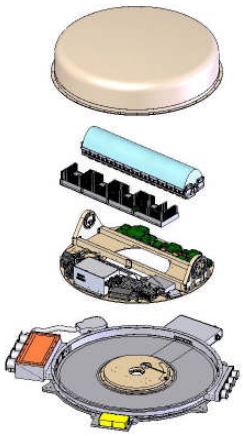

Figure 3. Millitech Quasi-Optic Phased Array

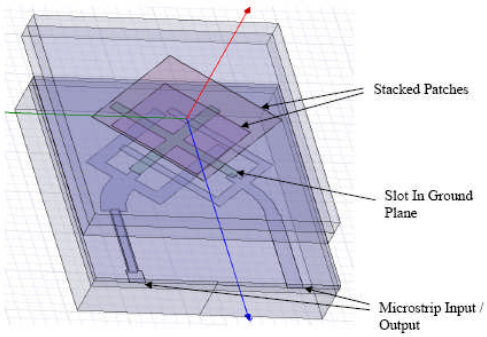

Figure 4. Aperture-Stacked Patch

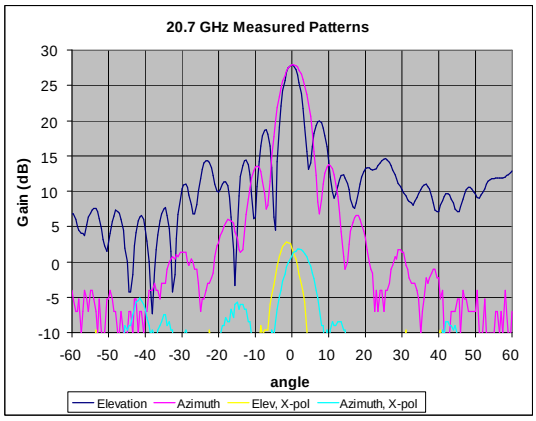

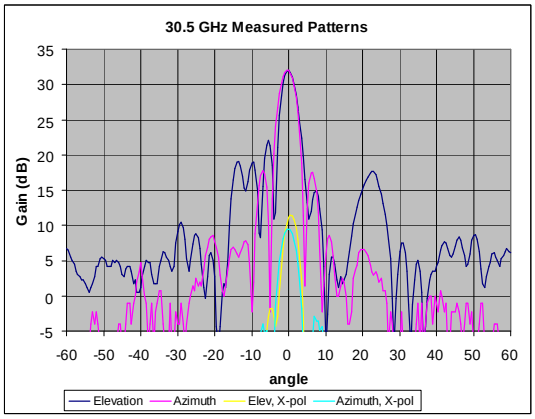

Figure 5. Gain and Cross Polarization of 16 element quasi-optic phased array

1.3. Dual Use Antenna Program (DUAP).

The DUAP X-Band antenna was an effort to reduce costs by utilizing planar apertures and an automatic insertion production line [5]. The transmit and receive circuitry were all discrete components to avoid the high cost of MMIC amplifiers. This reduced the cost from over $3K to just $20 for the power amplifier and $5 for the low noise amplifier. Previously used hand wound helical elements were replaced by stacked patches for receive and a helical transmit element utilizing a foam core and printed spiral attached with adhesive (Figure 6). The other major advance was moving from a $50,000 VME based antenna controller to a ~$5,000 PV-104 based controller (Figure 7). The DUAP antenna design to unit production cost was <$40,000 (100 each) for a transmit/receive pair. This compared to >$500,000 for the previous X-Band design.

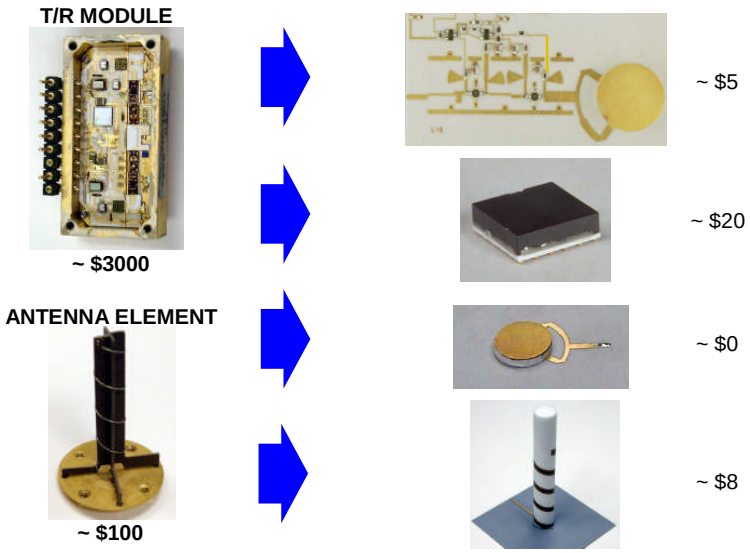

Figure 6. DUAP Low Cost T/R Components

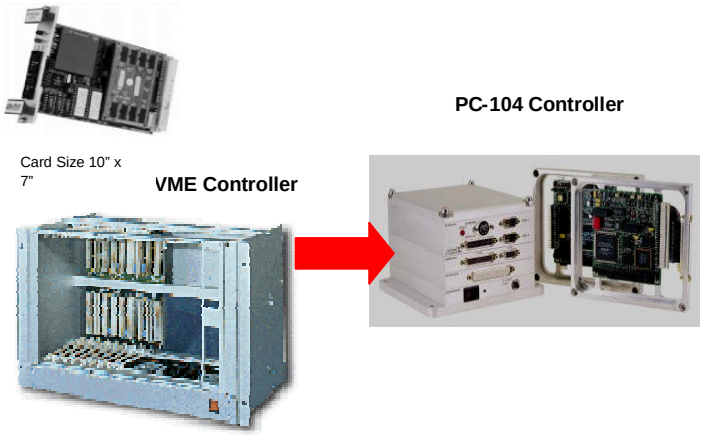

Figure 7. DUAP Controller Evolution

1.4. Dual Use Science & Technology Program (DUST).

These K/Ka antennas were designed to work with the new Wideband Global Satellite [6]. One of the issues we were concerned with was obtaining a sufficiently low axial ratio to allow certification of the antenna. The ability of stacked patch elements to meet the stringent 1.5 dB axial ratio requirements was questionable (Figure 8). This caused us to spend over a year investigating alternative antenna elements.

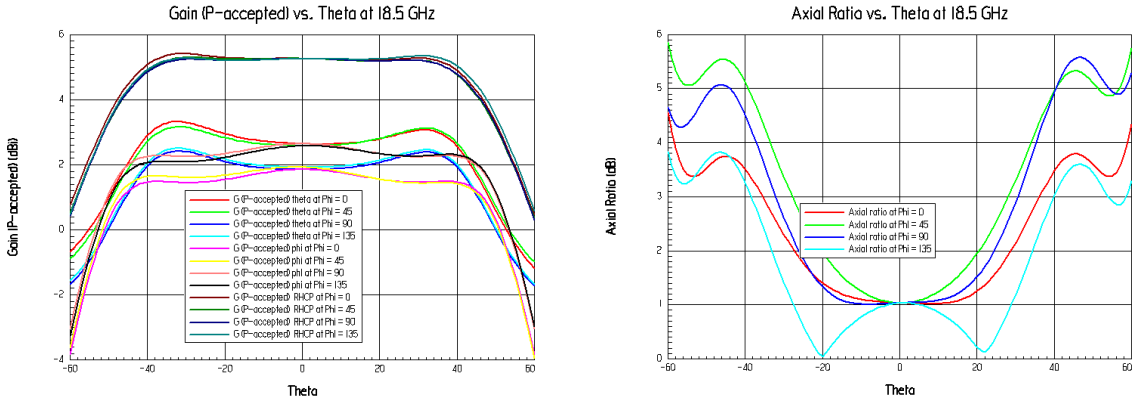

Figure 8. Initial DUST Patch Element

The thought was that we needed an element with height to increase its scan efficiency and achieve an acceptable axial ratio. The first such element considered was a crossed dipole. Simulations showed it could give us the performance we needed (Figure 9). Initial fabrication techniques included printed elements that could be soldered to the printed wiring board. This proved to be time consuming and expensive. We then investigated a cube version of the element. This promising element was also eliminated due to cost considerations.

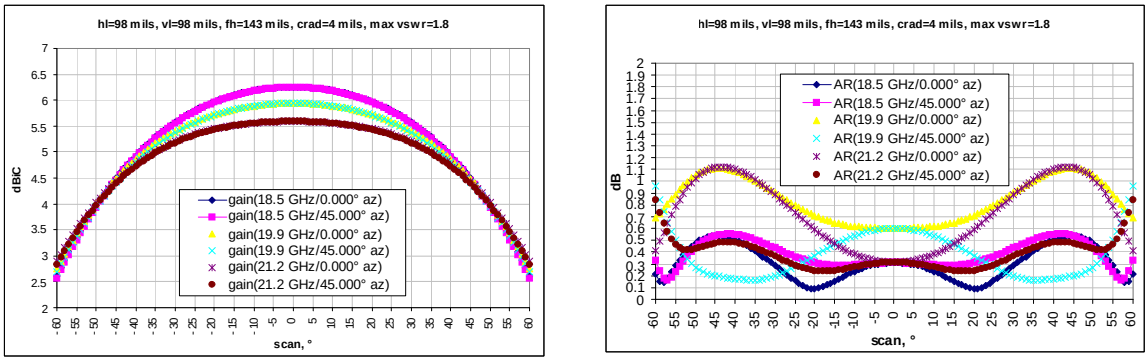

Figure 9. Crossed Dipole Simulated Performance.

The next element we considered was s quadrifilar helix. Computer modeling showed excellent performance (Figure 10). The thought was that we had been able to fabricate an X-Band helix at low cost, so we investigated using the same fabrication techniques for the quadrifilar helix. Unfortunately, the vendor found that the elements would be too expensive to fabricate due to the required counter wound helices required.

There was a bright spot in the effort on the helix. An analysis was conducted to see what the axial ratio would be for an array given relatively poor axial ratio of the individual elements. The results (Table 2) showed that elements with axial ratios as poor as 5 dB to 6 dB resulted in adequate array performance.

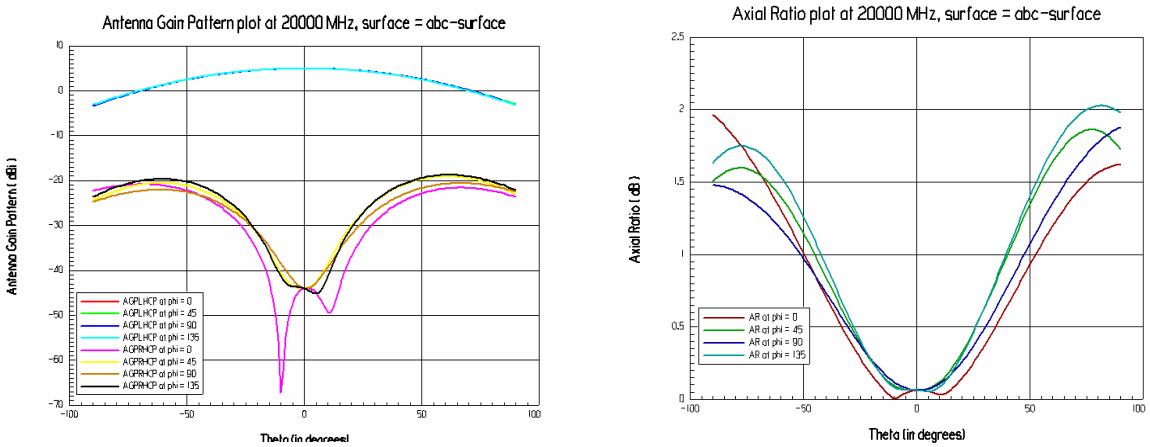

Figure 10. Simulated Performance of Quadrifilar Helix Element.

	Single Element	16 Elements	64 Elements	100 elements
Max Axial Ratio (60)	6.902	2.499	2.367	2.433
Min Axial Ratio (60)	0.359	1.910	1.848	1.916
Max Axial Ratio (45)	6.583	1.673	1.519	1.471
Min Axial Ratio (45)	2.834	0.949	1.236	1.154
Max Axial Ratio (30)	5.950	1.089	0.808	0.774
Min Axial Ratio (30)	2.137	0.049	0.526	0.515

Table 2. Axial Ratio Study Results.

Armed with this information, we fell back to a redesigned patch element. This new patch showed good gain and less than 5 dB axial ratio over scan. Given this performance an 8 element subarray was fabricated. Test results of the subarray (Figure 11) validated that the patch elements would provide adequate performance.

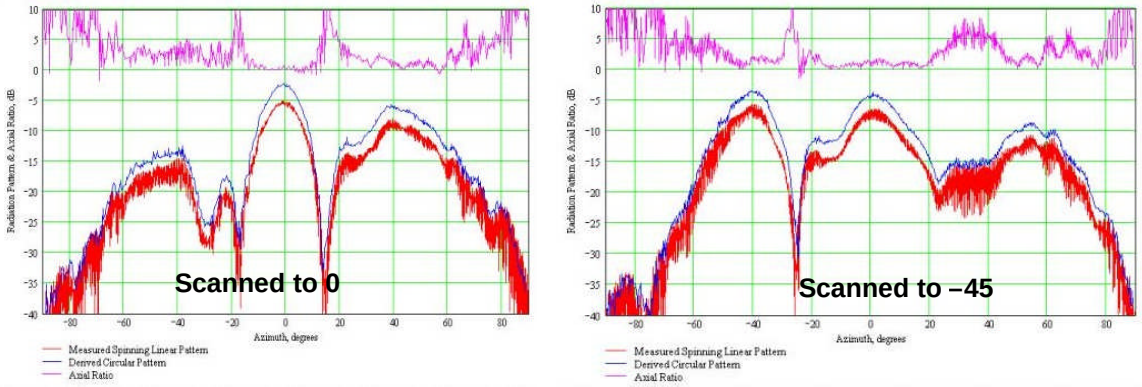

Figure 11. Eight Element Subarray Performance.

The lesson learned for this expensive (in time and dollars) one year phased array element investigation is that simpler is better. The crossed dipole and helix elements showed better axial ratio performance, but in the end the inexpensive patch element was the element of choice.

2. Technology Efforts

The development of phased arrays was put on hold after the DUST program to allow technology to catch up to the point where phased arrays for the Wideband Global Satellite at 20 GHz/30 GHz would be affordable. At $400,000 the DUST arrays were way too expensive for a user that balked at even $200,000 for an on-the-move communications antenna. Work was needed in many different areas: Low Noise Amplifiers, Power Amplifiers, Phase Shifters, Cooling Systems and Antenna Pointing Systems. The solution was a series of Small Business Innovative Research programs to address each component issue.

2.1. Low Noise Amplifiers

Low noise amplifiers (LNA) were too noisy and consumed too much power. A prime example of what was then available is the CHA 4069. This LNA had a noise figure of 2.3 dB and consumed 217 mW to 302 mW, depending on the bias. To attack these problems, an SBIR program was initiated with Custom MMIC Design Services [7]. The initial effort was for LNAs for Ku and Ka bands, both of which were of interest to our users. The TriQuint mHEMT process was found to be optimal. First run success led to a second run to optimize the amplifiers. The performance of a 3 stage Ka Band LNA is given in Table 3. Noise figure was lowered to 1.2 dB and power consumption lowered to 30 mW. Production cost is estimated to be $12 to $15 for these LNAs.

A problem arose, however. TriQuint announced that they were going to discontinue this process due to am insufficient wafer quantity being processed (Subsequent discussions with TriQuint indicates that they may leave the process open if sufficient wafer business evolves). TriQuint suggested an alternative pHEMT process may yield similar results. A third set of masks were designed and devices fabricated (a direct port of the mHEMT designs, not optimized for the pHEMT process). The results of the alternative devices are shown in Table 4. For the same power dissipation a 1.35dB noise figure was attained with a modest 2.5 dB drop in gain. The advantage of this process was that production costs as low as $5 could be attained!

This program has continued and devices successfully fabricated from X-Band to V-Band.

Parameter	Specification	Measured	Compliance	Units
Frequency	20.2-21.2	20.2-21.2	Yes	GHz
Gain	>20	29.4	Yes	dB
Input Return Loss	-10	-14.3	Yes	dB
Output Return Loss	-10	-11.4	Yes	dB
Noise Figure	1.3	1.2	Yes	dB
Voltage	TBD	1.2	Yes	V
P1dB	> +3	+3.5	Yes	dBm
Power Dissipation	25-50	30	Yes	mW

Table 3. mHEMT Second Pass Performance.

Parameter	Specification	Measured	Compliance	Units
Frequency	20.2-21.2	20.2-21.2	Yes	GHz
Gain	>20	26.9	Yes	dB
Input Return Loss	-10	-12	Yes	dB
Output Return Loss	-10	-4.5*	No	dB
Noise Figure	1.3	1.35*	No	dB
Voltage	TBD	2.0	Yes	V
P1dB	> +3	+1.5*	No	dBm
Power Dissipation	25-50	30	Yes	mW

Table 4. pHEMT First Pass Performance.

2.2.Phase Shifters

Phase shifters have been a perennial problem. When they were investigated for the DUST program, TriQuint had the TGP-1439-EPU for 18GHz to 21 GHz. It had a low insertion loss of 5 dB and a cost of $29 in 2500 quantity. The problem was at 30 GHz to 31 GHz. The only available phase shifter was the developmental TriQuint TGP-2100-

EPU. It had an insertion loss of 6 dB, but it cost $150! We looked to a new Army Manufacturing Technology program to provide the answer. The objective of this program was to lower the cost of ferroelectric and MEMS phase shifters from $25 to $50 to less than $10. The Agile RF ferroelectric phase shifters (Figure 12) had fast switching times and losses comparable to MMIC phase shifters [8]. Due to their analog nature, they required only a single control line. While these phase shifters were usable in the DUST arrays, there were problems that have since been addressed. Cost is now comparable to MMIC phase shifters.

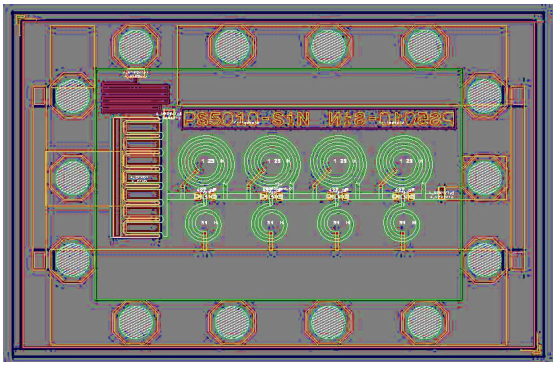

Figure 12. 20 GHz Ferroelectric Phase Shifter

A second type of promising phase shifter is based on micro electromechanical switches (MEMS). These have the advantage of being true time delay devices. This is important for array designers because it eliminates the beam squint with frequency that occurs with conventional phase shifters. This squint causes complications in both the acquisition and control systems of the arrays. The Army manufacturing technology program addressed these phase shifters in a companion program to Raytheon [9]. MEMS devices were fabricated at frequencies up to 35 GHz. Losses as low as 2 dB were achieved (Figure 13). These devises are currently packaged for chip and wire assembly. A new packaging initiative to allow surface mounting will allow these phase shifter to move into the mainstream.

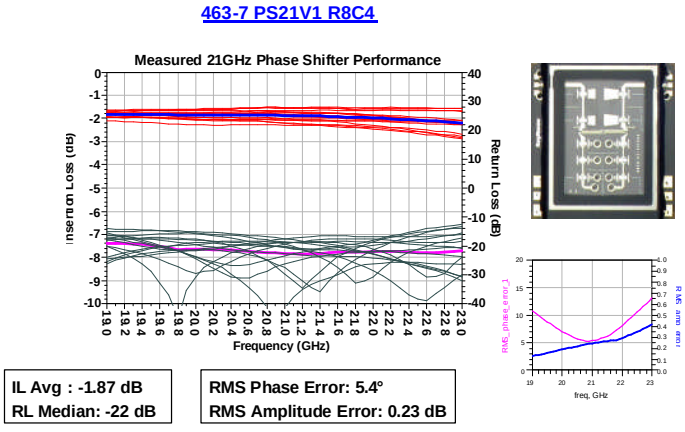

Figure 13. 20GHz MEMS Phase Shifter

2.2. Power Amplifiers

Efficient power amplifiers have been the most elusive component for communications phased arrays. Power added efficiencies (PAE) of 30% are desired at P1dB for Ka band amplifiers. Additionally, the spectral regrowth needs to be no more than -30dBc at 1X the symbol rate removed from the carrier [10]. This contrasts with available power amplifiers with PAEs below 20%. This is true for power amplifiers with output powers as low as 100 mW and as high as 4 W. Spectral regrowth is not stated in data sheets, forcing one to obtain and test samples to see if an amplifier is promising. As an example, the TGA 4513 amplifiers used in the DUST array had a PAE of 20% at a P1dB of 1.5 watts. The problem was , they had to be backed off an additional 3 dB to meet the spectral regrowth requirements. The actual operating PAE was closer to 10%.

The Army Research Laboratory and Defense Advanced Research Projects Agency had some early success with mHEMT amplifiers at the two watt level [11]. The Air Force Research Laboratory had success at the 200 milliwatt level. An SBIR program was started to try to take advantage of these efforts, but it was ultimately not successful with mHEMTs. The program was, however, able to deliver 100 nm and 70 nm pHEMT amplifiers with almost 30% PAE at a Psat of 1.2 watts or greater. pHEMT amplifiers show the most promise for phased arrays that require a P1dB 100-200 milliwatts in the 30 GHz or 44 GHz bands.

Most of today's efforts in high efficiency power amplifiers at higher power levels are in Gallium Nitride. One such effort is an SBIR with Hittite Microwave [13]. Hittite, using the Northrop Grumman foundry, has produced a die with 8 watts power output at 30-31 GHz with a PAE of 25%. The packaged amplifier (Figure 14) has an output power of 6 watts due to the effects of the QFN package. This four stage chip has a power gain of 18 dB. The design assumed a Vcc of 24 volts, but due to safe operating area data supplied by Northrop Grumman, the chip is operated at 18 volts, thereby limiting its performance.

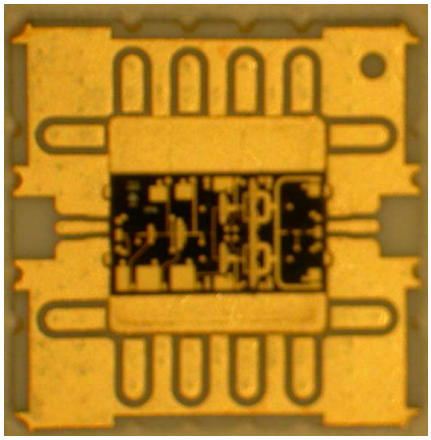

Figure 14. Hittite 30 GHz GaN Power Amplifier

ARL and DARPA are also working on developing GaN at multiple foundries. Foundries include Northrop Grumman, TriQuint and Raytheon. Foundries are focusing on different frequency bands to try to speed up the process of foundries establishing released processes. TriQuint, for example, has released a 0.25 micron GaN process for devices up to 20 GHz in frequency. Northrop Grumman is focusing on 30 GHz, 44 GHz and beyond. CERDEC has partnered with ARL in the design and fabrication of devices using advanced, unreleased processes. The first spin includes multiple 30 GHz designs for CERDEC and 35 GHz designs for AMRDEC. GaN offers smaller die size for a given power level and the promise of reliable operation at increased temperatures with power added efficiencies of 30% and higher.

However, one aspect of power amplifiers has been overlooked. How do we design these MMIC power amplifiers for linear, high power added efficiency operation? Two new SBIR efforts are looking at this power amplifier area. Auriga Microwave and Custom MMIC Design Services are both investigating the linearity/efficiency issue. Each has a different approach, thereby reducing the risk of finding a solution. Due to the reported nonlinearity problems with GaN devices, design alone may not cure the problem. Linearizers, Doherty amplifiers or other solutions may be needed as well. This effort is just starting. It will be interesting to find if we can develop a low cost solution for efficient linear amplifiers.

We note that these GaN amplifiers are not limited to phased arrays, but can have application to other types of antenna systems. One can envision combining multiple GaN amplifiers to obtain higher powers of 50 Watts or more.

2.3. **Cooling Systems**

Cooling was not a problem for our X-Band systems. They could readily be cooled by conduction and convection due to the modest EIRP, G/T and high efficiency of the LNAs and power amplifiers. The situation radically changed with our K/Ka band arrays. Cooling was a major issue due to the large increase in EIRP and G/T needed to close links with the WGS satellite. The 128 power amplifiers drew over a kilowatt of power, with a total transmit power consumption of over 1700 watts. The 1350+ receive LNAs each drew almost 400 watts. This resulted in major cooling problems. A 1000 watt commercial air to air heat exchanger was needed for the receiver and a custom heat exchanger for the transmitter. Instead of being 4 inches in height, the arrays ballooned to over 11 inches due to the heat exchangers (Figure 15).

Three SBIR programs were started to try to address the cooling system problem. Two involved vapor compression cooling using a miniaturized compressor and one was based on extremely high efficiency blowers and vapor chambers. In Phase I, Aspen Systems concentrated on the vapor compression system, while Technology Applications

concentrated on reducing the thermal impedances with partner Ball Aerospace. Creare developed a very high efficiency cross flow blower.

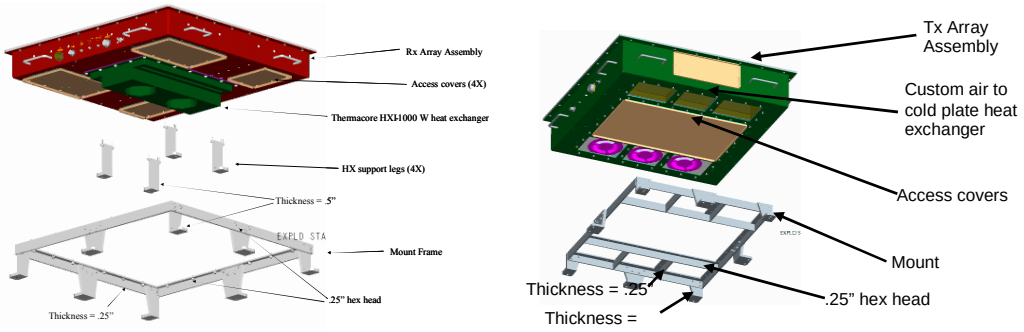

Figure 15. K and Ka Band Phased Arrays

A study [13] indicated that the Creare cross flow blower system would consumed less than 100 watts to liquid cool arrays with a total power dissipation of 900 watts. The Aspen system would consume over 700 watts due to the low coefficient of performance of the vapor compression system. The ultimate conclusion was that two phase pumped liquid cooling consumed the least power and occupied the least volume. This type of system was proposed by Parker-Hannifin (Figure 16). Interestingly, this system was initially brought to our attention by another SBIR contractor, EMAG Technologies. This system was closely followed by pumped single phase liquid cooling systems.

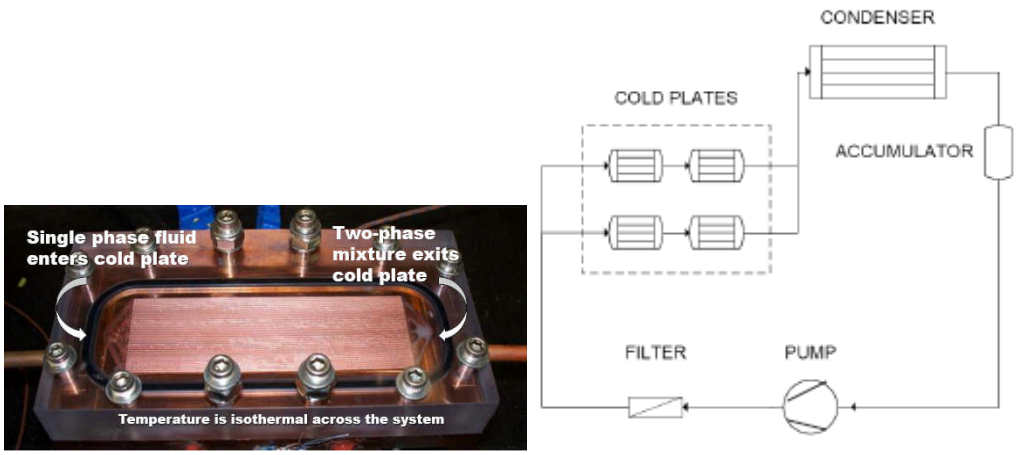

Figure 16. Parker-Hannifin Two Phase Pumped Liquid Cooling System.

2.4. Inertial Navigation/Low Cost Antenna Pointing Systems

All of our early antenna systems utilized the Honeywell Tactical Advanced Land Navigator (TALIN) as the inertial navigation system. The problem with the TALIN was

that it was initially designed for much more stringent applications than antenna pointing. The cost of a single TALIN was (and still is) over $50,000. To combat this problem an SBIR contract was let to Enpoint LLC to develop a low cost antenna pointing system specifically designed for use with on-the-move antenna systems (Figure 17).

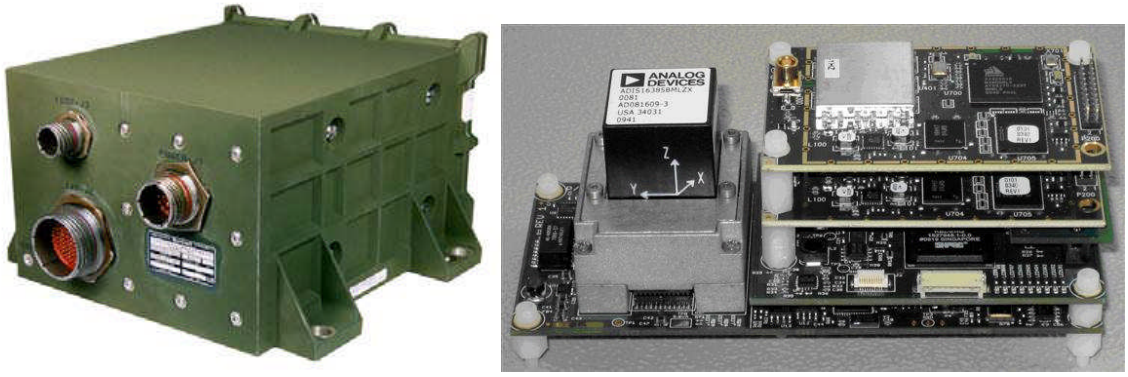

Figure 17. Honeywell TALIN and Enpoint Low Cost Antenna Pointing System

The Enpoint system has taken almost 8 years of development. First as a SBIR Phase I and Phase II Program, it was chosen for a Phase II+ award to continue the development. The initial developmental system was used on dish and phased array antennas. Pointing was found to be indistinguishable from the TALIN in motion table testing. It also had several distinct advantages: It started up faster and it could provide accurate heading information at the halt. This was due to the use of dual phase coherent GPS receivers and low cost MEMS sensors. The development has continued [14] with a developmental contract awarded to Enpoint to port the design to newer and lower cost processors as well as newer GPS receivers. The final Enpoint system uses MEMS gyros with a drift rate of less that 6 degrees per hour. This allows accurate pointing even when GPS is blocked for several minutes or longer. The ultimate cost of the delivered system packaged in a MIL package is estimated to be 1/10 that of a TALIN.

3. Summary

The road to affordable phased array antennas has been a long and difficult journey. We have presented early phased array systems and detailed the successes and failures of each. Problem areas have been Low Noise Amplifiers, Power Amplifiers, Phase Shifters, Cooling Systems, Controllers and Antenna pointing Systems. We believe the LNA problem has been solved, having obtained both low noise figure and extremely low cost. Power amplifiers are an ongoing problem area, with additional efforts needed in both pHEMT and GaN technologies, depending on the power level required. Both have shown promise to deliver power added efficiencies of 30% or more. Power amplifier linearity, however, needs much more attention. Despite efforts in Ferroelectric and MEMS phase shifters, MMIC phase shifters remain the phase shifter of choice. New low cost MMIC processes have made this possible. Pumped two phase liquid cooling systems will eventually prevail due to their low power consumption, volume and cost. In

the interim, pumped single phase liquid cooling systems will continue to proliferate. Low cost PC-104 based controllers have supplanted expensive VME controllers for on-the-move antenna systems. Finally we will have a militarized low cost antenna pointing system within the next year.

Are we there yet? Unfortunately, the answer is no. The ultimate low cost phased array will need to be planar and use low cost automated pick and place machinery for fabrication. Harris showed us this with the early aperiodic X-Band arrays. This type of fabrication is needed with low cost MMICs to make low cost arrays a reality. Several manufacturers are currently exploring this avenue of approach. We hope that at least one of them is successful.

REFERENCES

[1] Herald Beljour, Louis Coryell, Tat Fung, Jim Gallagher, Rich Hoffmann, Gerald Michael and Joseph Shields, "Army SATCOM On-The-Move Initiatives", Proceedings of the Thirty Third Annual Antenna Applications Symposium, September 2009.

[2] The Boeing Company, "Final Report for an Electrically Controlled Phased Array Antenna", June 2001.

[3] Millitech, Inc., Monthly Reports, "SATCOM on-the-move Active Quasioptical Array", June 2007 to pres.

[4] S.D. Targonski, et.al., "Design of Wide-Band Aperture-Stacked Patch Microstrip Antennas", IEEE Transactions on Antennas & Propagation, Vol 46, No. 9, September 1998 page(s) 1245-1251.

[5] Harris Corporation, Government Communication Systems Division, "Final Report for the Low Cost Phased Array Dual Use Application Program", 7 October 2002

[6] Harris Corporation, Government Communications Systems Division, "Final Report for the Low Cost Dual Use Science and Technologies Program", 17 June 2005.

[7] Custom MMIC Design Services, "Quarterly Review for High Efficiency, Low Power, Low Noise Amplifiers for SATCOM", May 6, 2010.

[8] Agile RF, "Final Report for Low Cost Ferroelectric Phase Shifters for Phased Array Antennas", March 31, 2008.

[9] Raytheon Spand and Airborne Systems, "Final Report for Affordable RF Microelectromechanical Switch (RF MEMS) Phase Shifters for Phased Arrays Manufacturing Technology Objective (APSPA MEMS) Program", March 30, 2009.

[10] MIL-STD-188-164A, Change 3, “Interoperability of SHF Satellite Communications Terminals”, 25 August 2009, Page 7, Para 3.9.a.

[11] Private communication with Dr. Alfred Hung of the Army Research Laboratory.

[12] Hittite Microwave, “Monthly Report for Distributed & Flex based Spatially Combined MHEMT Power Amplifiers for Satellite Communications”, May 2010.

[13] Raytheon Space and Airborne Systems, “Ground-Based SATCOM Thermal Control System Trade Study”, 22 December 2009.

[14] Enpoint, LLC, “Monthly Reports for Low Cost Antenna Pointing System Evolution”, Oct 2009 to pres.

A KU BAND PARASITIC ARRAY FOR DATA LINK SYSTEMS

J.P. Doane, L.M. Paulsen

Advanced Technology Center
Rockwell Collins, Inc. Cedar Rapids, IA 52402 USA
jpdoane@gmail.com, lmpaulse@rockwellcollins.com

Abstract: A Circular Switched Parasitic Array (CSPA) is presented for a Ku band data link application. Traditional methods of implementing a parasitic array become impractical at high frequencies because the impedance load of each parasitic element must be precisely controlled. Here, a new circuit topology is presented which overcomes these limitations by using multiple diodes to significantly improve the isolation of the parasitic element from the bias circuitry and provide a stable impedance load across frequency. Practical design considerations for parasitic arrays at Ku band such as minimizing interconnect reactance are discussed. Simulation and measured results are provided, showing 5dBi directional beams. A method to increase the directional gain to >12dBi by adding multiple rings of parasitic elements is described. The Parasitic Array design provides the advantages of a small electronically scanned array (ESA) without the cost and complexity. It is therefore a particularly attractive choice for data link systems on small SWAP challenged UAVs where directionality is needed but gimbaled antennas or full fledged ESAs are not practical.

1. Overview

A Circular Switched Parasitic Array (CSPA) provides a low cost manner of beamforming without the complexities required by a traditional phased array. A CSPA uses a single driven element surrounded by parasitic elements that are excited only by mutual coupling. The magnitude and phase of the currents induced on the parasitic elements can be influenced by carefully controlling the impedance load of the parasitic elements. By appropriately loading each parasitic element, a directional beam can be collimated across the array [1]. Because there is no need for phase shifters or an RF feed network, the CSPA is more efficient and drastically less expensive than a phased array. Additionally, the CSPA can also produce an omnidirectional beam when broadcast functionality is required.

Because the CSPA excites an endfire array mode, the aperture can be mounted flush to the topside or underside of a vehicle and achieve 360 degree field of view. Because the height of the CSPA is on the order of a quarter of a wavelength, it is very low profile at high frequencies (0.2 inches at 15GHz). Additionally, because each switched load handles only a fraction of the incident power, the antenna has very high power handling.

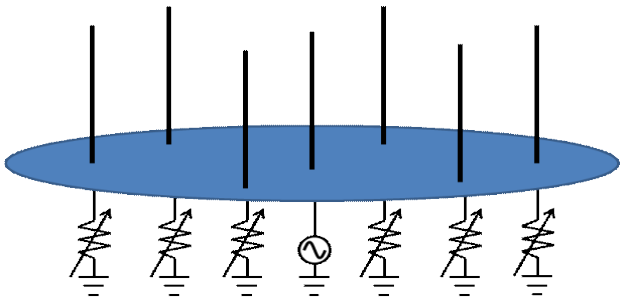

Fig 1. Circular Switched Parasitic Array Concept

Most previous work on parasitic arrays has focused on applications where directivity is emphasized over realized antenna gain, such as Direction of Arrival (DOA) systems [2], diversity systems [3] and spectral re-use [4]. As a result, practical issues for datalink systems such as impedance bandwidth, efficiency, and realized gain have often not been emphasized. Additionally, most implementations rely on circuits and techniques that are impractical for higher frequencies, such as Ku Band.

In this paper, a process is described for determining the optimal reactive load for array gain and impedance match, as well as a circuit topology appropriate for Ku Band operation. Relative to previous work, it is shown that antenna gain can be further increased by adding rings of parasitic elements. With these design improvements, the CSPA architecture becomes a very attractive antenna for datalink systems. The CSPA is especially advantageous on Size, Weight, and Power (SWAP)-challenged platforms, where mechanically steered antennas or phased arrays are prohibitively large, heavy and expensive.

2. Design

Two common parasitic array topologies exist in the open literature and can be classified relative to their respective loading techniques for the passive elements in the array. Antennas which use continuously variable loads are commonly referred to as Electronically Steerable Parasitic Array Radiators (ESPAR), whereas binary switched load arrays are referred to as Circular Switched Parasitic Arrays (CSPA). In order to tune each element's excitation in an ESPAR, they are terminated with an analog variable reactance such as a varactor diode [5]. Unfortunately, beamsteering can require up to a 20:1 reactance tuning range [4] which becomes impractical for higher frequency varactors. While this may be able to be overcome with a more complex tuning circuit, it has been found that using a switched load to toggle between two reactance states is sufficient for beamforming [6]. As a result, the CSPA has the benefit of simplifying control circuitry from analog control to binary digital control. A secondary benefit of this binary control topology is that RF switches such as PIN diodes are less susceptible to nonlinear effects introduced by varactors that are undesirable for many applications.

2.1 Determining Optimal Parasitic Load Impedance

When envisioning a binary switched parasitic array, one's intuition would indicate that the best impedance load conditions would be either a short circuit or an open circuit. The "off" state parasitic elements would require a high impedance, open circuit load, while the "on" state parasitic elements would require a low impedance, short circuit load. With some analysis, however, it can be shown that those two states do not necessarily produce the optimal balance of array gain and impedance bandwidth.

The optimal impedance terminations for can be determined by analyzing the mutual impedance network of the array. The array geometry is chosen to be a 7 element array with a central driven monopole surrounded by 6 parasitic monopoles distributed equally on a λ/4 radius. The corresponding mutual impedance network can then either be determined theoretically or through simulation:

$$\begin{bmatrix} V_0 \\ V_1 \\ V_2 \\ V_3 \\ V_4 \\ V_5 \\ V_6 \end{bmatrix} = \begin{bmatrix} Z_{00} & Z_{01} & Z_{02} & Z_{03} & Z_{04} & Z_{05} & Z_{06} \\ Z_{10} & Z_{11} & Z_{12} & Z_{13} & Z_{14} & Z_{15} & Z_{16} \\ Z_{20} & Z_{21} & Z_{22} & Z_{23} & Z_{24} & Z_{25} & Z_{26} \\ Z_{30} & Z_{31} & Z_{32} & Z_{33} & Z_{34} & Z_{35} & Z_{36} \\ Z_{40} & Z_{41} & Z_{42} & Z_{43} & Z_{44} & Z_{45} & Z_{46} \\ Z_{50} & Z_{51} & Z_{52} & Z_{53} & Z_{54} & Z_{55} & Z_{56} \\ Z_{60} & Z_{61} & Z_{62} & Z_{63} & Z_{64} & Z_{65} & Z_{66} \end{bmatrix} \begin{bmatrix} I_0 \\ I_1 \\ I_2 \\ I_3 \\ I_4 \\ I_5 \\ I_6 \end{bmatrix} \quad (1)$$

Each parasitic element is terminated with an impedance load. Note that current into the load has the opposite sense to the current into the antenna element. The voltage and current in the parasitic elements are related by:

$$V_n = Z_{loadn}(-I_n), \quad n > 0 \quad (2)$$

The mutual impedance matrix can then be rewritten as:

$$\begin{bmatrix} V_0 \\ 0 \\ 0 \\ 0 \\ 0 \\ 0 \\ 0 \end{bmatrix} = \begin{bmatrix} Z_{00} & Z_{01} & Z_{02} & Z_{03} & Z_{04} & Z_{05} & Z_{06} \\ Z_{10} & Z_{11}+Z_{load\,1} & Z_{12} & Z_{13} & Z_{14} & Z_{15} & Z_{16} \\ Z_{20} & Z_{21} & Z_{22}+Z_{load\,2} & Z_{23} & Z_{24} & Z_{25} & Z_{26} \\ Z_{30} & Z_{31} & Z_{32} & Z_{33}+Z_{load\,3} & Z_{34} & Z_{35} & Z_{36} \\ Z_{40} & Z_{41} & Z_{42} & Z_{43} & Z_{44}+Z_{load\,4} & Z_{45} & Z_{46} \\ Z_{50} & Z_{51} & Z_{52} & Z_{53} & Z_{54} & Z_{55}+Z_{load\,5} & Z_{56} \\ Z_{60} & Z_{61} & Z_{62} & Z_{63} & Z_{64} & Z_{65} & Z_{66}+Z_{load\,6} \end{bmatrix} \begin{bmatrix} I_0 \\ I_1 \\ I_2 \\ I_3 \\ I_4 \\ I_5 \\ I_6 \end{bmatrix} \quad (3)$$

Each Z_{load} is switched between two states corresponding to forward and reverse bias states of the PIN diode. Since any resistance in the load would add loss, the optimal impedance loads are assumed to be purely reactive, and are denoted as:

$$Z_{loadn} = \begin{cases} jX_{on} \\ jX_{off} \end{cases} \text{ switched} \quad (4)$$

These reactances are assumed to correspond to a low impedance (on state) and high impedance (off state), with the low impedance state inducing a high current and being

relatively reflective to an incident wave, and the high impedance state inducing minimal current and being relatively transmissive to an incident wave. The high impedance loads are therefore placed in the direction of the desired beam and the low impedance states placed away from the desired beam, as seen in Figure 2.

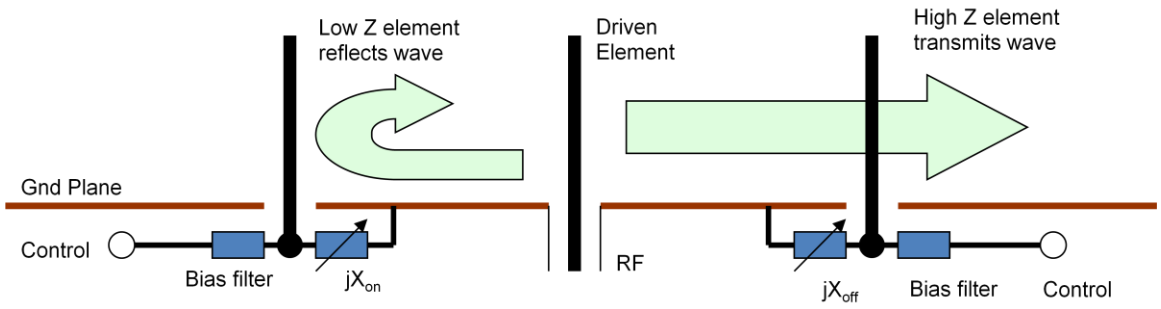

Fig 2. Side view of Parasitic Array

The number of X_{on} and X_{off} elements can be optimized by repeating the following process for each case, and is set to three each, as shown in Figure 3. Note that an even number of X_{on} could be used for additional beam directions.

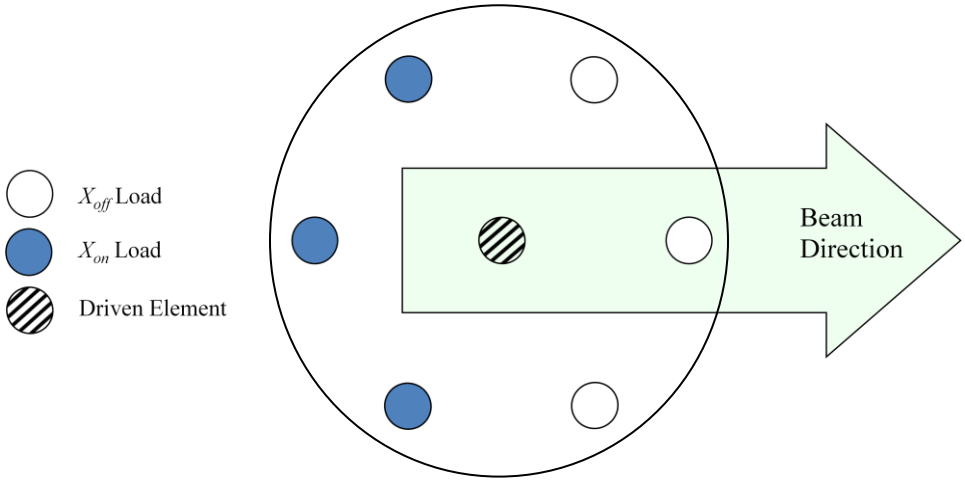

Fig 3. Top view of Parasitic Array

For each value of X_{on} and X_{off}, the matrix equation can be solved for the vector of complex currents, which can then be used to calculate the Array Factor in the forward direction. By sweeping both X_{on} and X_{off}, the optimal reactances which maximize array gain can be determined. Figure 4 shows directivity in the forward direction swept over X_{on} and X_{off}, as well as single cuts for constant X_{on} and X_{off} through the maximum gain point. Note that the element pattern is not considered, so the calculated directivity and gain is a relative rather than an absolute prediction of array performance.

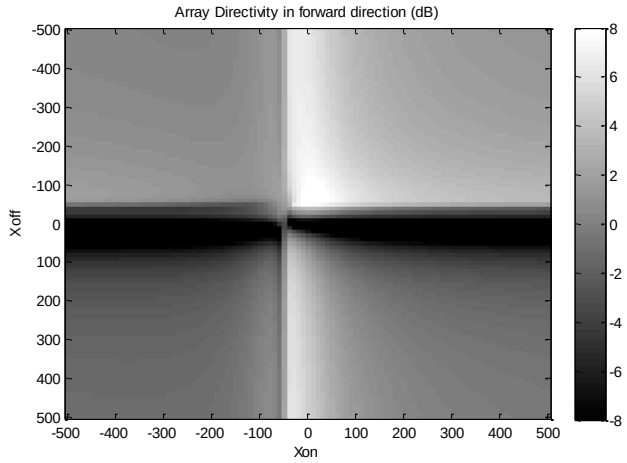

(a)

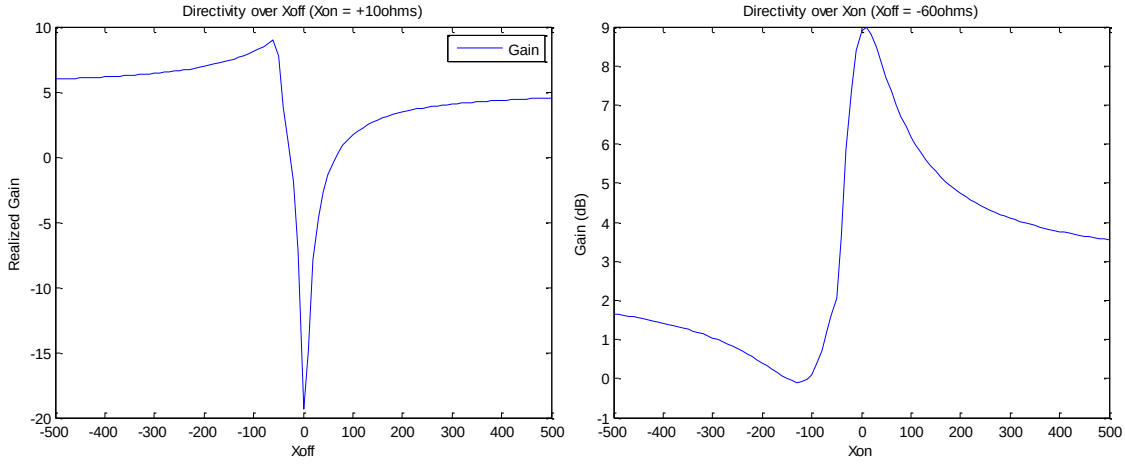

(b) **(c)**

Fig 4. Antenna Directivity in the Forward Direction over X_{off} and X_{on}

The maximum directivity of the array occurs at X_{on} = +10ohms and X_{off} = -60ohms. This corresponds to induced currents that are relatively large (small X yields large I) and in phase with the desired beam direction. Unfortunately, because all of the induced currents are large at this point, much of the energy is reflected back to the driven element and the input impedance is poorly matched relative to 50ohms.

$$Z_{CSPA} = \frac{V_0}{I_0} \tag{5}$$

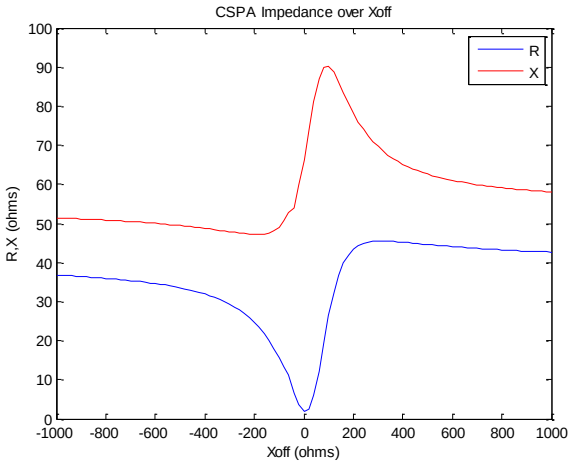

Fig 5. Impedance of CSPA over X_{off}

Although a matching circuit could be used, the reduction in efficiency and bandwidth are undesirable for highly mismatched impedances. Additionally, if the omnidirectional mode is excited (all elements set to X_{off}) the impedance of both modes must be similar enough for a common match. If mismatch is included into the gain calculation (realized gain), a more optimal operating point can be determined.

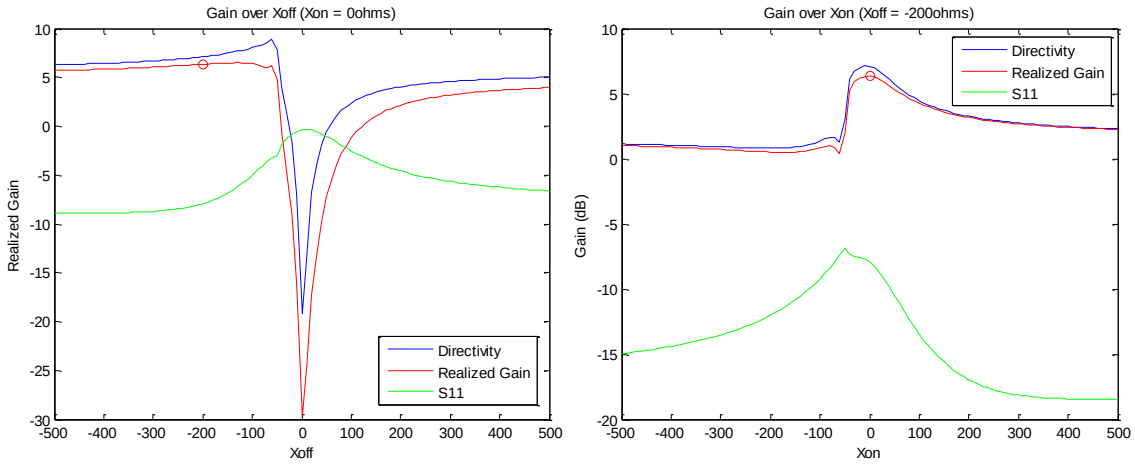

Fig 6. Realized Gain and Return Loss over X_{on} and X_{off}

The optimal design point for the reactive loads is therefore somewhere near X_{off} = -200ohms and X_{on} = +20 ohms, shown as a small circle on the plots of realized gain in Figure 6. This predicts approximately 5.5dB gain with -8dB Return Loss. Choosing this point requires balancing gain vs. VSWR requirements and may vary per the application requirements. The entire antenna design can then be fine tuned using full wave computational simulations by varying additional parameters such as element height, array spacing, capacitive matching on the center element, etc.

2.2 Circuit Design

Designing a circuit to yield precise impedances at the appropriate reference plane across a broad band at high microwave frequencies is non-trivial. At Ku band, the packaging and interconnect of each part adds significant reactance to the circuit. For instance, a typical wirebond has an inductance of 0.5nH, which adds +j50 ohms at 15GHz! Likewise, short traces, pads and vias have significant impedances and must be carefully included in the design of the circuit. Lumped components have package parasitics that overwhelm nominal values, and often are quite lossy at Ku Band.

The straightforward manner of designing an appropriate switched impedance circuit is to use a PIN diode biased through a low pass filter consisting of an RF choke and capacitor, shown in Figure 7a. This approach is avoided at Ku band because of the poor performance of lumped inductors at such high frequencies.

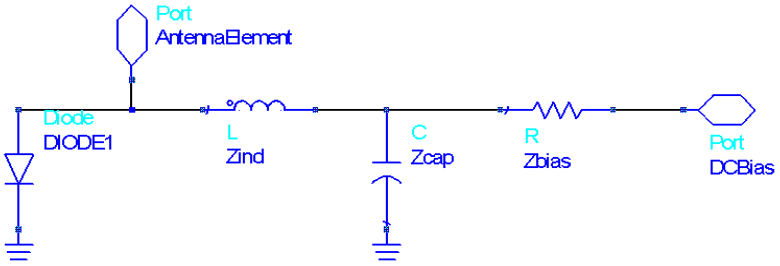

Fig 7a. Traditional CSPA load circuit with RF Choke

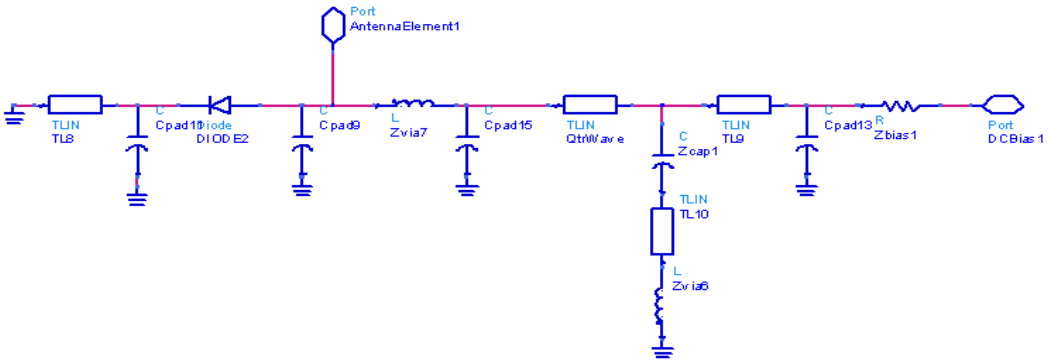

Fig 7b. CSPA load circuit with Quarter-Wave Matching and Associated Parasitics

Initially, a quarter wave transmission line was used in place of the choke to transform the low impedance at the shunt capacitor to a high impedance at the antenna element. A high impedance microstrip trace on 20mil Rogers 4350 was used. The circuit is shown in Figure 7b, including undesired parasitics from interconnect such as vias, pads, and circuit traces. The circuit was tested and significant losses were measured (see Figure 8). It believed that despite attempting to compensate for them in the design, the parasitic inductance, capacitance, and electrical length of the interconnect was sufficient to spoil the high impedance transformation and add unacceptable loss to the circuit.

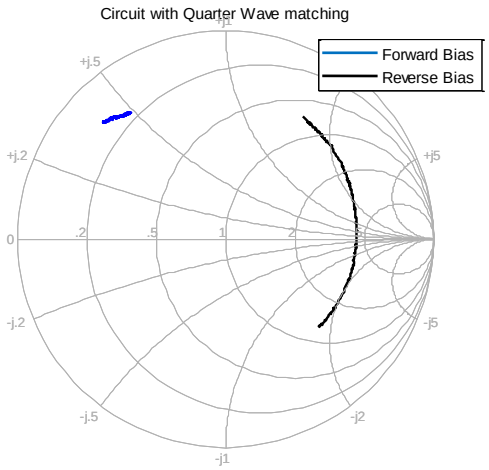

Fig 8. Loss Seen in Load Circuit with a Quarter-Wave Microstrip Transformer

To mitigate these issues, an alternative bias circuit is proposed which replaces the RF choke/quarter-wave matching with a second diode, shown in Figure 9.

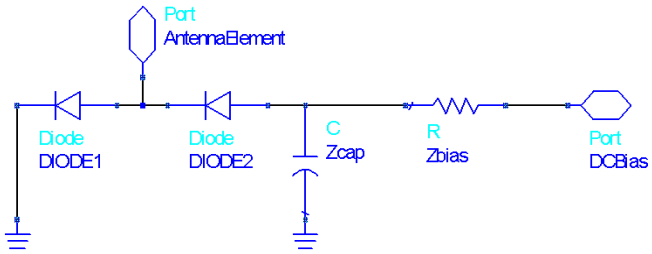

Fig 9. CSPA Load Circuit with Two Diodes (Parasitics not Shown)

The impedance seen at the antenna element can be written as:

$$Z_{load} = \left\{ Z_{diode}{}^{-1} + \left(Z_{diode} + \frac{1}{\left({}^{1}/_{Z_{cap}} + {}^{1}/_{Z_{bias}} \right)} \right)^{-1} \right\}^{-1} \qquad (6)$$

If the shunt capacitor is near resonance at the design frequency so that Z_{cap} is small and a current limiting resistor is used such that $Z_{bias} >> Z_{cap}$, the approximate load impedance can be found by taking the first order terms of the Taylor expansion:

$$Z_{load} \approx \frac{Z_{diode}}{2} + \frac{Z_{cap}}{4} \quad \text{near } Z_{cap} \to 0 \qquad (7)$$

Provided the capacitor has a small impedance in the band of interest, the impedance seen at the antenna element is directly established by the diode, and is a low impedance (small inductance) when the diodes are forward biased, and a high impedance (small

capacitance) when reverse biased, which corresponds to the optimal X_{on} and X_{off} as determined above. Because the diode impedance is halved, the circuit can provide a smaller X_{on} than other configurations, even with significant diode inductance, which improve antenna gain. Note that along with reactance, the resistance of the diode and capacitor must be minimized for efficient performance.

Note that the undesired parasitics of this circuit have not yet been mentioned, but must be dealt with. Typical packaging techniques using vias, pads, and transmission lines will significantly detune the circuit. The circuit can be simulated with a small electrical length inserted between each component (similar to Figure 7b). The overall impedance seen at the element is plotted in Figure 10 with interconnect electrical length ranging from 0 to 1mm (0 to 40mil). The performance of the circuit which is near optimal with zero interconnect length, quickly becomes unusable with even small separation between components.

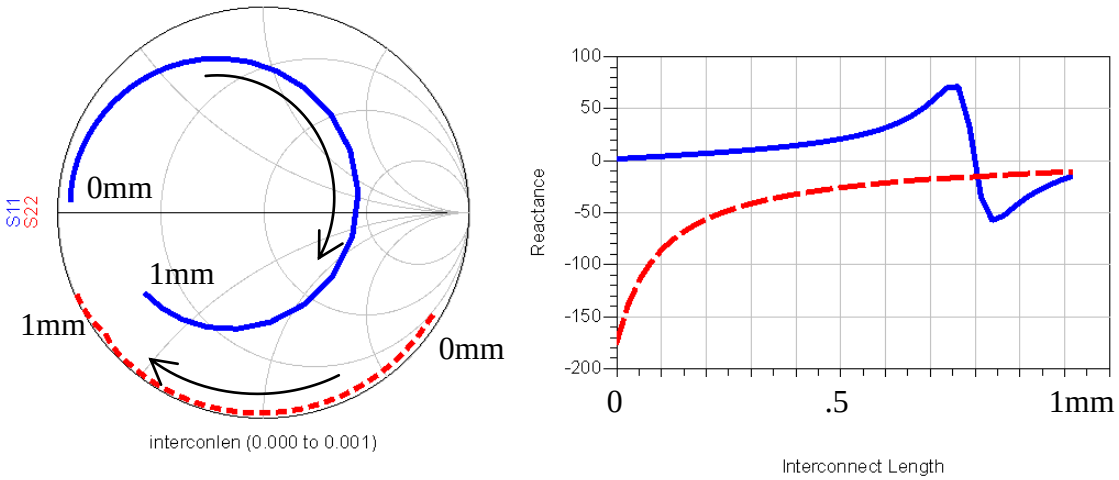

Fig 10. Simulated Impedance of Forward and Reverse Biased circuit with interconnect electrical length swept from 0mm to 1mm

To overcome this issue, components are not bonded to PCB pads and connected with traces, but rather are directly attached to one another with conductive epoxy in order to minimize series reactance. The construction of the circuit is shown in Figure 11, and the measured impedance at the parasitic element plotted in Figure 12. It can be seen that the resistive losses in the circuit are small and the X_{off} and X_{on} closely match the optimal for the CSPA as determined above.

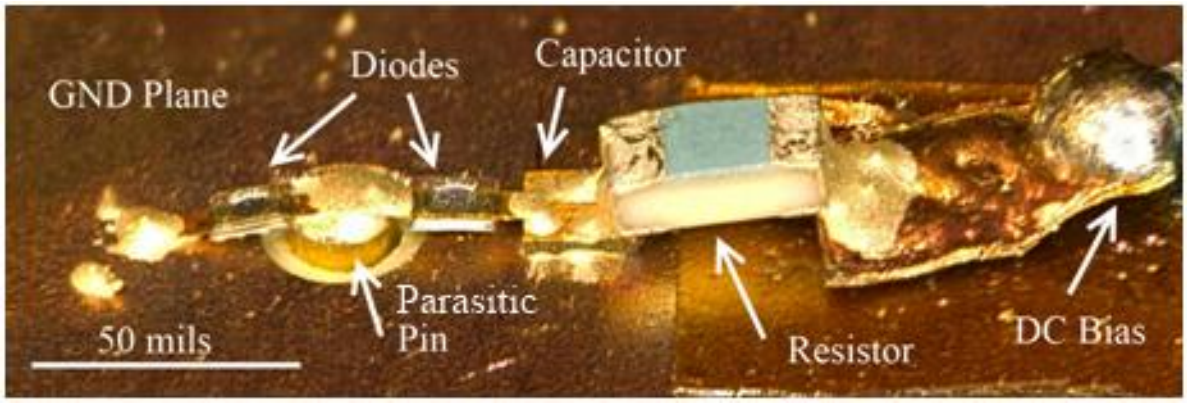

Fig 11. Construction of Parasitic Load circuit

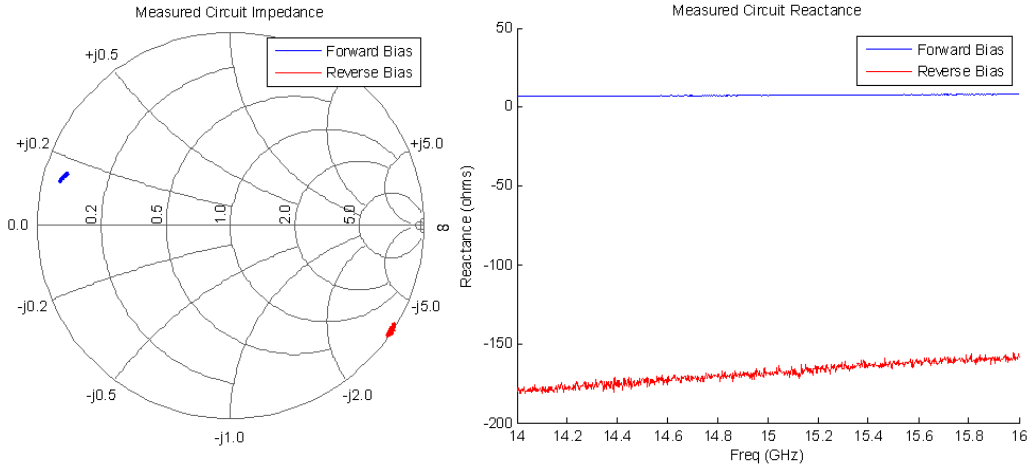

Fig 12. Measured Impedance of Parasitic Load circuit

2.3 Antenna Design and Measurements

2.3.1 Single Ring CSPA

A Ku Band CSPA is constructed from 6 such circuits and a driven monopole element. The antenna is built on a 20 mil Rogers 4350 substrate, with foam supporting the parasitic pins. The length and location of the reactive elements as well as the monopole is optimized using HFSS to achieve 5dBi gain beams with a 2:1 VSWR bandwidth of >10% at Ku Band. The final antenna construction is shown in Figure 13. Simulated and measured gain of both directional and omnidirectional beams is shown in Figure 14.

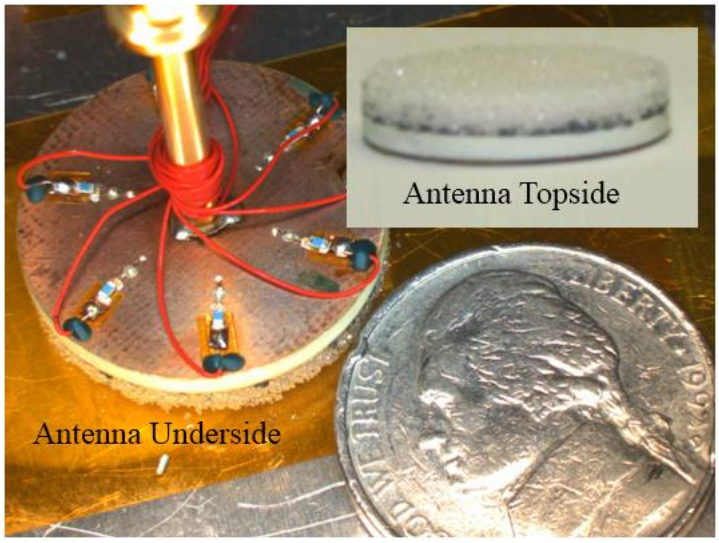

Fig 13. Ku Band CSPA construction

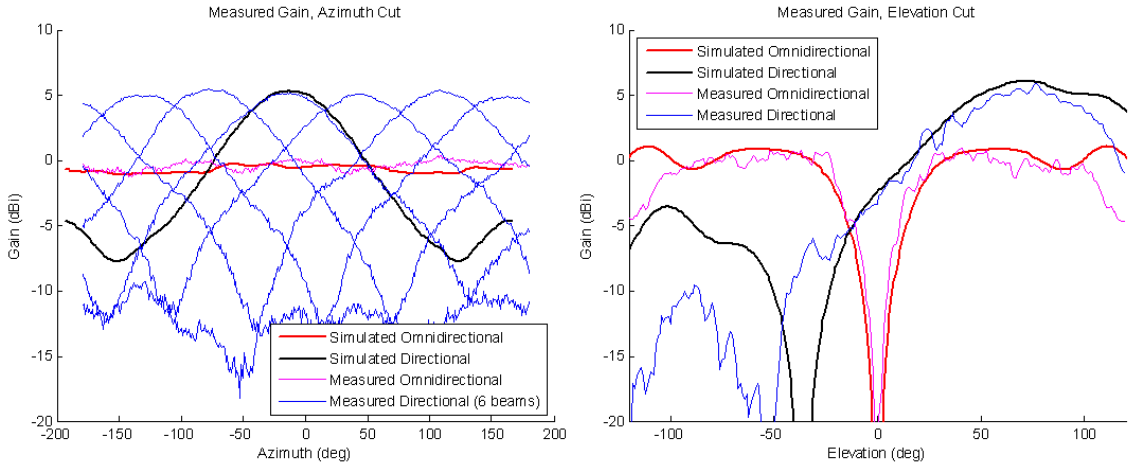

Fig 14. Simulated and Measured Gain of a Ku band CSPA

2.3.2 Multi-Ring CSPA

Improving the basic CSPA design to support narrower beams with increased gain can be accomplished by adding multiple rings of parasitic elements. A similar technique with two concentric rings has been used for a Switched Beam Disc Antenna [7]. It is shown here that the same technique can be used for a CSPA, with each added ring increasing the gain and narrowing the beam. The performance of a multi-ring CSPA ranging from 1 to 5 rings was simulated in HFSS. For each ring, the maximum gain of the antenna (usually ~30 degrees above horizon) as well as the gain at the horizon is plotted in Figure 15.

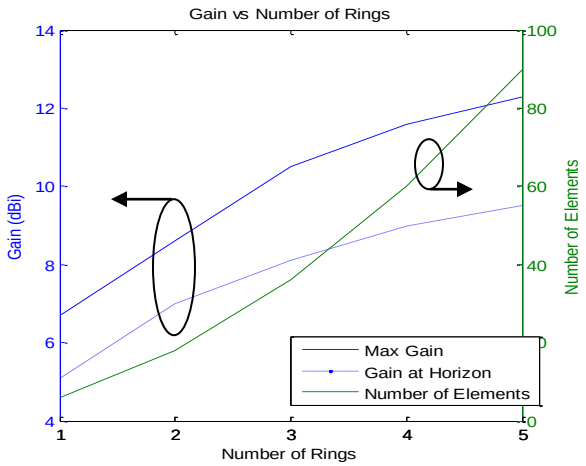

Fig 15. Antenna Gain of Multi-Ring CSPA

It can be seen that the gain of the multi-ring CSPA scales with the diameter, e.g. doubling the diameter adds ~3dB gain. This is to be expected as the effective aperture area of the endfire array is proportional to the height times the diameter (rather than the footprint of the array, as for a broadside array). This suggests that in theory, the gain of the CSPA can be designed to be arbitrarily large. However, because the number of elements (and therefore cost) scales with the square of the diameter, while gain only scales with the diameter (unlike planar broadside staring arrays, whose gain scales directly with number of elements), the practicality of CSPAs is limited for higher gain designs.

A three ring CSPA was built and tested. Due to programmatic needs, this design was done at another frequency other than Ku Band. However, a multi-ring CSPA at Ku band (using the same circuit as the single ring Ku Band CSPA) is expected to be straightforward. Like the single ring CSPA, the elements are approximately $\lambda/4$ tall and the radii of the rings are roughly $\lambda/4$, $\lambda/2$, and $3\lambda/4$. The arrangement of elements and fine tuning of the array geometry is determined through optimization. The construction of three ring CSPA is shown in Figure 16, and its simulated and measured performance is plotted in Figure 17. The 2:1 VSWR bandwidth of the array is >10% and is similar to the single ring CSPA. Note that the peak gain of >12dBi in the elevation cut is higher than the analysis shown in Figure 15 due to the electrically large ground plane on which it was measured.

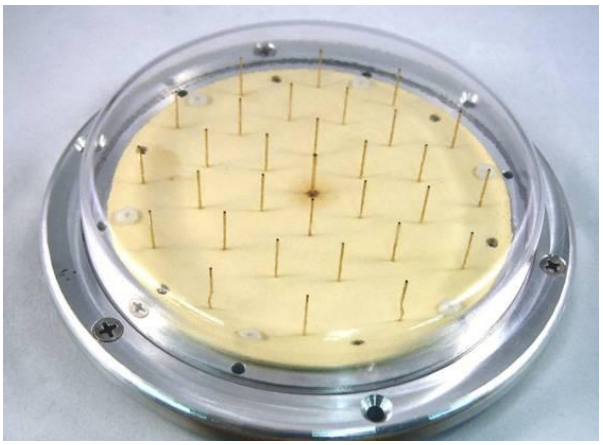

Fig 16. Triple Ring CSPA construction

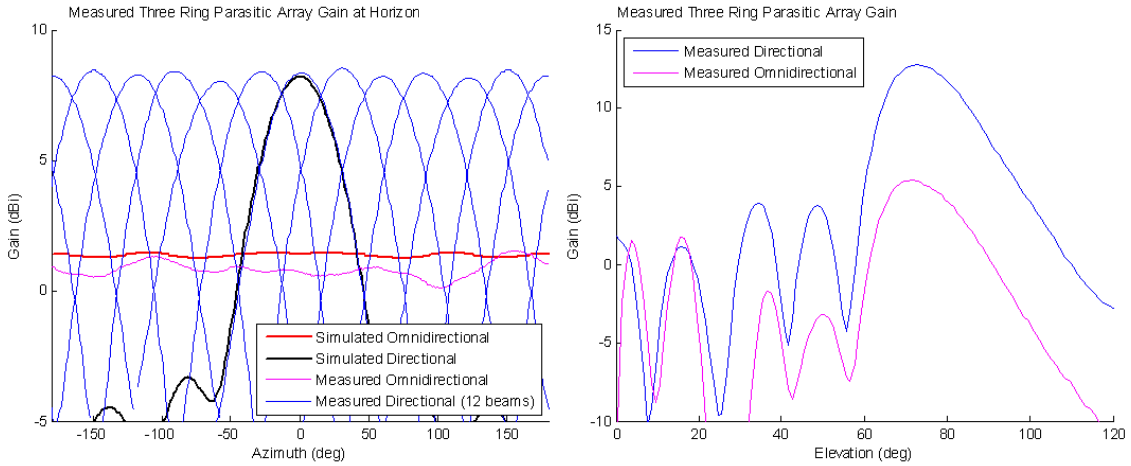

Fig 17. Simulated and Measured Gain of Triple Ring CSPA

3. Conclusion

In this paper, we propose several techniques to determine optimal loading of the parasitic elements to maximize gain and bandwidth, as well as circuit design and construction techniques that function well at Ku Band. A single ring CSPA at Ku Band with 5dBi gain and >10% bandwidth was built and tested, with good agreement between measurement and simulation.

A method of further increasing antenna gain by adding multiple rings of parasitic elements is described. A three ring CSPA with >12dBi gain (8dBi at horizon) and >10% bandwidth was built and tested, also with good agreement between measurement and simulation.

The CSPA is an ideal antenna for many datalink systems on SWAP-challenged platforms that require more link margin than an omnidirectional antenna can provide. A three ring CSPA antenna on both ends of a link can provide 18dB composite gain improvement and will increase the link range by a factor of eight versus two 0dBi omnidirectional antennas. In addition to being much less costly to implement, the CSPA can support

functionality that a mechanically steered antenna cannot, such as omnidirectional broadcast and fast beam switching for TDMA.

4. References

[1] R. Harrington, "Reactively Controlled Directive Arrays*" IEEE Trans. Antennas Prop*, vol. 26, no. 3, May 1978, pp. 390-395

[2] C. Plapous, J. Cheng, E. Taillefer, A. Hirata, T. Ohira, "Reactance Domain MUSIC Algorithm for ESPAR Antennas", *33rd Eur. Microwave Conf.* 2003, pp. 793-796

[3] R. Vaughan, "Switched Parasitic Antennas for Antenna Diversity" *IEEE Trans. Antennas Prop*, vol. 47, no. 2, Feb 1999, pp. 399-405

[4] B. Schaer, K. Rambabu, J. Bornemann, "Design of Reactive Parasitic Elements in Electronic Beam Steering Arrays" *IEEE Trans. Antennas Prop*, vol. 53, no. 6, June 2005, pp. 1998-2003

[5] J. Cheng, M. Hashiguchi, K. Iigusa and T. Ohira, "Electronically steerable parasitic array radiator antenna for omni- and sector pattern forming applications to wireless ad hoc networks" *IEE Proc-Microw. Antennas Prop*, vol. 150, no. 4, Aug. 2003, pp. 203-208

[6] T Bertuch, "A Circular Switched Parasitic Array Antenna for High Power Data Link Applications," 3rd Eur. Conf. on Antennas and Propagation, pp. 2483 – 2487, 2009

[7] G. Cerri, R. De Leo, V. M. Primiana, C. Monteverde, P. Russo, "Design and Prototyping of a Switching Beam Disc Antenna for Wideband Communications" *IEEE Trans. Antennas Prop*, vol. 54, no. 12, Dec. 2006, pp. 3721-3726

EVOLUTION OF A COMMERCIAL PHASED ARRAY

Joseph M. Carey
Fidelity Comtech, Inc.

Abstract: This paper documents the evolution in a commercial phased array antenna. Both the array itself and the way it is used have adapted to meet emerging applications. Commercial phased arrays have different constraints than their counterparts which are intended for military applications. These constraints affect the design trade-offs of the antenna.

1. Introduction

This paper describes the architecture of Fidelity Comtech's Phocus Array System, a commercial phased array. It also describes some of the applications of the phased array and how the array has been adapted to meet the needs of different applications. Development of the Phocus Array was initially funded in part by a grant from the National Science Foundation in 2003 and a SBIR contract from the United States Air Force (AFRL/IF), in 2004.

Historically, phased arrays have been applied almost exclusively to military applications which tend to be much more tolerant of cost but much more demanding in terms of reliability and overall performance. By contrast, commercial devices tend to make low cost a priority and compromise on performance. Furthermore, military phased arrays have historically found use primarily in radar systems, which require relatively high transmit power and very directive antennas; commercial wireless systems tend to be used for relatively low-power communications.

By far the most popular frequency band for commercial operation is the 2.4 GHz ISM band, so it is natural that a commercial antenna should start its product offering there. This band hosts a number of different applications: cordless phones, video cameras, Bluetooth, ZigBee and of course wireless data networks (IEEE 802.11b/g, with a trade name of Wi-Fi).

As with any commercial product, success involves offering the product at a price that provides more value than it costs – and more value than competing choices. This is especially difficult with a phased array, because the electronics involved in creating a beamforming network tend to be fairly expensive and the passive antennas with which phased arrays compete tend to be relatively inexpensive.

The Phocus Array has lowered the cost of building a phased array by taking advantage of low-cost commercial grade components used for cellular and WiFi devices. This is especially important in the beamforming network, where the traditional approach was to use expensive

precision components for the phase and amplitude control. One of the major lessons Fidelity Comtech learned from the cellular industry was not to attempt to control the performance of the RF components too tightly, but rather to accept wide variations and "tune" them to consistent performance using embedded software.

When development of the Phocus Array began, Fidelity Comtech had a small but growing business providing amplifiers to Wireless Internet Service Providers (WISPs). The company believed that the WISP market would continue to grow, and that the Phocus Array could be successfully marketed there. This turned out not to be the case. Fidelity Comtech further believed that municipal mesh networks, based on Wi-Fi, would emerge as a common public utility. For a number of reasons, more political than technical, this hasn't happened.

Nonetheless, some large outdoor enterprises are using the ISM band for mission-critical broadband wireless applications. Of course, Wi-Fi was initially intended as a relatively short range protocol, primarily for indoor applications. So using it in large-scale outdoor applications carries some risk, because the users do not control the spectrum and under FCC regulations they must accept interference. Beamforming antennas, such as the Phocus Array can help increase range and reduce inevitable interference.

2. Architectural Approach

The Phocus Array System has gone through three generations since its development began in 2003. The concept of a "generation" of the Phocus Array refers to the complexity of the beamforming technology, especially the T/R Module. While the Phocus Array has evolved through three generations, it has always had some common architectural features.

The Phocus Array is a phased array with its radiating elements arranged in a circle. Typically, there are eight elements in the phased array, but Fidelity Comtech has also made a version with 32 elements. Eight elements were selected initially because it represented the "knee" of the price-performance curve. That is, Fidelity Comtech believed eight elements provided an optimum realization of price/performance.

A conceptual overall diagram of the Phocus Array is shown in Figure 1. The Phocus array can be portioned into two major sub-assemblies: the IEEE 802.11 access point and the phased array antenna, which Fidelity Comtech markets under the trade-name "Flex-VMT."

A central splitter divides the signal from the COTS WiFi card to each of the Transmit/Receive (T/R) modules. The splitter uses Wilkinson dividers and the signal arrives at each of the T/R modules with very nearly the same phase.

The T/R modules provide precisely controlled phase shift and amplification to control the antenna beam.

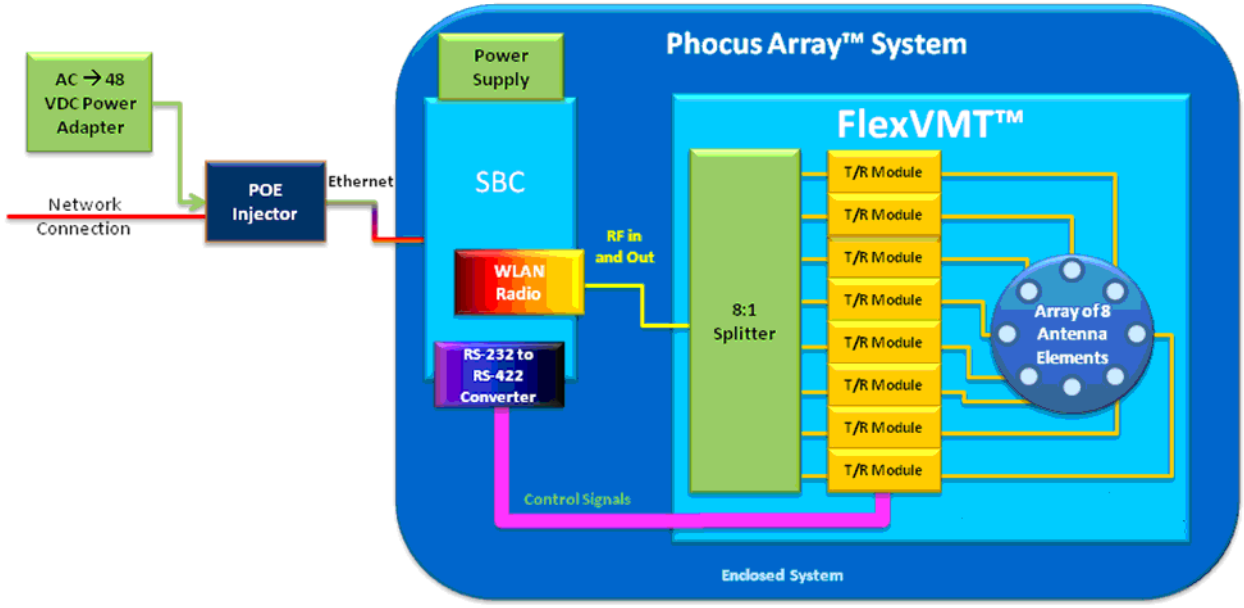

Figure 1. Block Diagram of Phocus Array System

As with most phased arrays, the T/R modules -- the circuit cards which provide the phase and amplitude control -- are the most critical subassembly. Because each antenna element requires a T/R module, the cost of the T/R module drives the cost of the overall system. A block diagram of the T/R module is shown in Figure 2.

Each T/R module includes a power amplifier and low-noise amplifier; performance of these set the overall system parameters, such as output power and noise figure. This distributed gain approach is appealing for commercial applications because it allows relatively low-cost amplifiers to be used. That is, since the FCC-imposed conducted power limit on an 8 element phased array is 500mW overall, each power amplifier is only transmitting 62 mW (approximately 18 dBm).

Each of the T/R modules includes a dedicated microcontroller. The role of the microcontroller has changed as the Phocus Array evolved, as will be described later. However, one role of the microcontroller has always been to interpret high level commands from the access point and implement low-level configuration of the T/R module, especially the vector modulator.

In the first and second generation Phocus Arrays, the control interface to T/R modules was RS-485. RS-485 is a multi-drop differential interface. The single-board computer acts as a bus master and sends commands to the T/Rs. Commands can either be query-response to an individual card, or they can be broadcast to all T/R modules in parallel. The single-board computer in the first generation systems didn't include a native RS-485 interface, so an RS-232 to RS-485 converter was required.

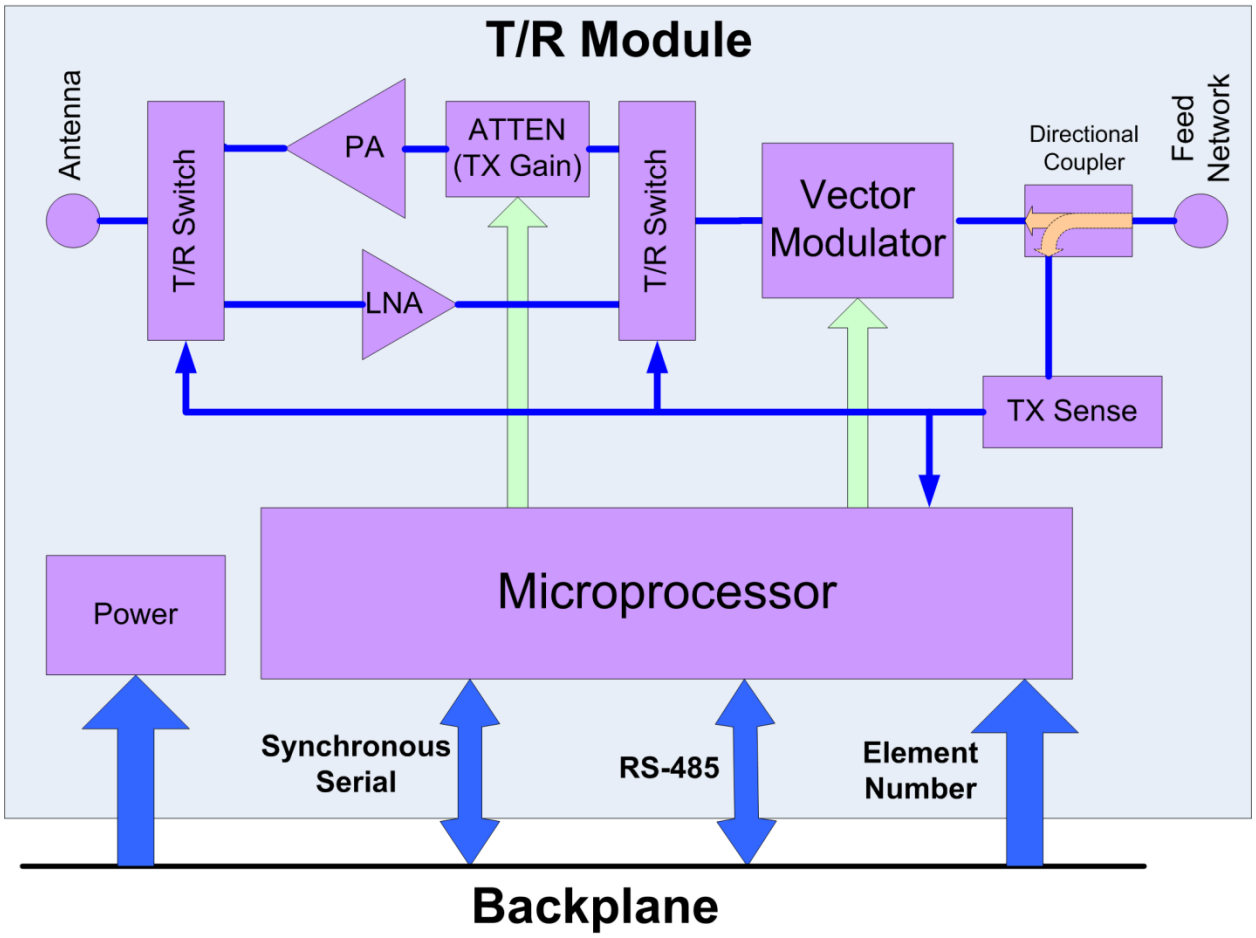

Figure 2. Block Diagram of T/R Module

2.1 An Innovative Vector Modulator

The innovation that enables the Phocus Array is the vector modulator. The vector modulator provides the phase and amplitude control that enable the phased array signal to be adjusted. One vector modulator is required for each antenna element in the phased array.

The vector modulator operates directly on the modulated RF carrier signal, without converting to baseband I/Q signals. It is also reciprocal, providing the same phase shift in both the transmit and receive direction.

The vector modulator used in the Phocus Array system uses a combination of signal delay and amplitude control to achieve precise phase and magnitude control. A concept diagram of the vector modulator is shown in Figure 3.

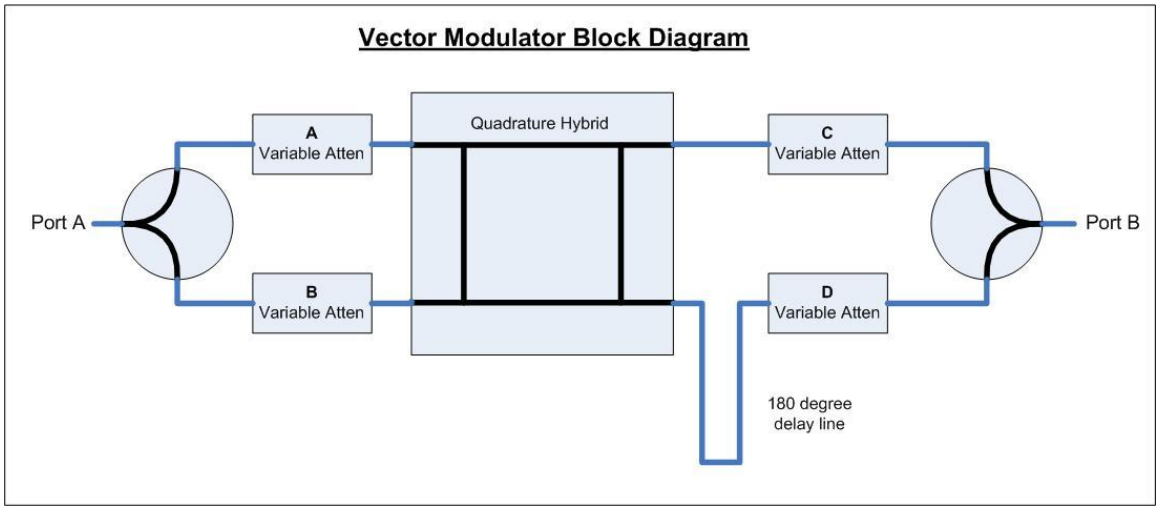

Figure 3. Block Diagram of Vector Modulator

Conceptually, the vector modulator divides the signal into four orthogonal components using delay lines and then combines the signal components needed to provide the desired phase shift. In practice only one dedicated delay line is used; the other delays are incorporated in the branch line coupler. The signal levels from each of the quadrature components are adjusted using PIN diode variable attenuators, which are controlled by the microprocessor on the T/R Module.

The 2.4 GHz ISM band, for which the Phocus Array was designed, covers 2.400 GHz to 2.483 GHz (2.500 GHz internationally), which is only a four percent fractional bandwidth. The vector modulator is easily adjusted over such a small bandwidth.

The vector modulator is covered by US Patent # 6894657 and several international patents.

The appeal of this approach is that while it is difficult to directly control phase, it is relatively easy to precisely control amplitude. The vector modulator takes advantage of precision amplitude control to *indirectly* adjust phase by adding two signals in phase quadrature. Using inexpensive 8-bit DACs to control the PIN diode attenuators, it has been possible to achieve phase resolution of finer than one degree. Correcting for all the non-linear factors has been challenging, especially imperfections in the phase quadrature and non-linear gain curves.

However, once these factors have been addressed, this approach is quite stable with temperature, a requirement for its application and a benefit missing from many alternate approaches.

Finally, and probably most important for a commercial product, the cost of the vector modulator is driven by the cost of PIN diode attenuators, which are quite inexpensive.

This approach does have one significant disadvantage: it introduces a considerable insertion loss, typically about 15 dB. However, because the signal amplitude is relatively small at this point, introducing gain to overcome this loss is relatively inexpensive.

Calibrating the vector modulator is a process that has taken some time to develop. Fidelity Comtech is now on the third iteration of an automated calibration station.

2.2 First Generation Phocus Array

Only a handful of first generation systems were ever manufactured. Their principal purpose was to demonstrate the performance of the vector modulator and circular array. Figure 4 is a photograph of one of the first generation systems.

Figure 4. Photograph of First Generation Phocus Array System

The first generation Phocus Array used PIC microcontrollers on the T/R module. The only task of the PIC microcontroller was to interpret commands from the central processor that set the DAC values on the vector modulator. These ASCII commands were sent over the RS-485 bus. The limited functionality of the microcontroller in the T/R Module required the 802.11 access point to compute the desired phase/amplitude on

each antenna element and then converting this to the required DAC settings. As a result, it could take several hundred milli-seconds to configure the eight elements of the antenna.

2.3 Second Generation Phocus Array

The second generation Phocus Array was the first version to receive FCC approval and sold commercially. A photograph of the second generation system is shown in Figure 5.

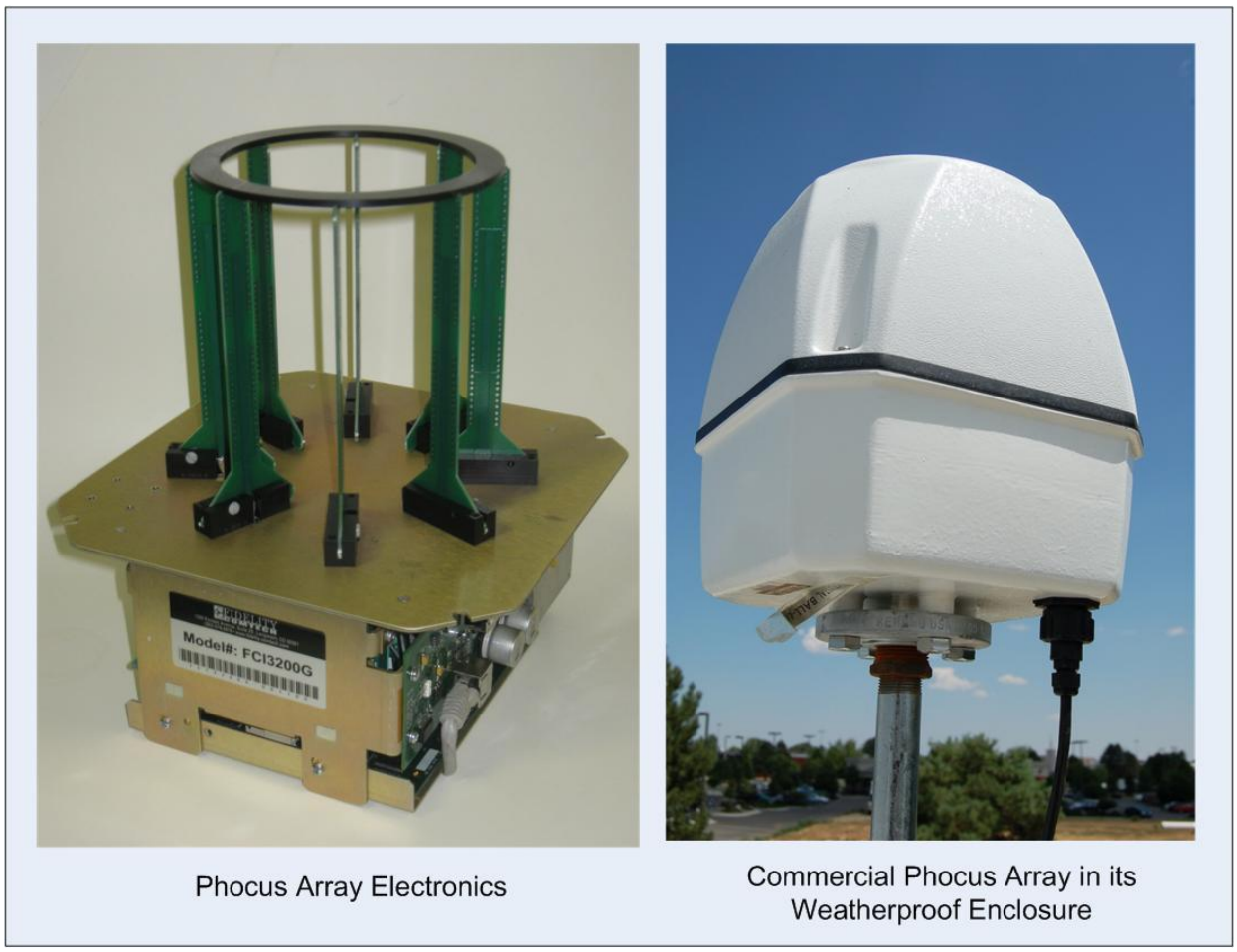

Figure 5. Photograph of Second Generation Phocus Array System

The second generation implemented some significant changes from the initial version:

1. The system was packaged in a weatherproof enclosure.
2. The PIC microcontroller in the T/R Module was replaced with an MSP430, which is more capable and performs more functions. Included in these new functions is managing the calibration factors and computing the DAC values for the vector modulator – a task that had previously been performed in the central CPU.

3. The monopole antenna elements were replaced with a stacked dipole, which was fabricated on a printed circuit. These elements nominally produce about 5.5 dBi of gain.
4. The notion of a "pattern library" was introduced and implemented. Pattern Libraries are described later in this paper.
5. The off-the-shelf single-board computer that served as an AP was replaced with a custom design that includes dedicated ports such as RS-485 for driving the array.

3. Anticipated Applications

When development of the second generation Phocus Array began, Fidelity Comtech expected that the municipal Wi-Fi market would take off. However, for a variety of reasons, that market never materialized. Instead, beginning with the second generation, the Phocus Array has found application in a number of other markets, both commercial and government, which are discussed below.

Early market feedback indicated that it was important for the Phocus Array to provide packet-by-packet beamsteering. This would be especially important in mesh networking systems, which can realize tremendous increases in performance through spatial re-use with beamforming antennas. However, the first generation T/R modules would not support packet-by-packet beamforming because it took too long to send all the information regarding individual DAC values from the central CPU to the T/R modules. Pattern libraries address this issue.

3.1 Pattern Libraries

Because the second generation T/R Modules include calibration factors, it is possible to send them phase magnitude pairs directly. Phase is sent in decimal degrees and magnitude in linear percent of full scale, with units of Volts/volts. So, for example, the command 0x70:90 is interpreted as "Element Zero, set phase to 70 degrees and magnitude to 90% of full scale." The microcontroller in the TR module takes this command, applies whatever calibration factors are necessary, and computes the DAC values necessary to realize the desired phase / magnitude setting.

The second generation of the Phocus Array introduced the concept of "Antenna Pattern Libraries." Because the vector modulator in the Phocus Array is capable of such a tremendous flexibility, a huge number of patterns can be realized. However, in any given situation, only a few such patterns make sense.

In practice, most applications make repeated use of a relatively few patterns. Also, a limiting factor in the array is the speed with which the central CPU can communicate with the T/R Modules -- it is very time consuming to send the complete antenna weight vector, which is typically eight phase and magnitude pairs. Describing the pattern can

take between 40 and 60 bytes. Pattern libraries are a way for the user to define a collection of antenna patterns and recall individual patterns from the collection using an index. The pattern library is loaded into the T/R module at boot time, or whenever it makes sense to redefine the patterns.

A typical pattern library consists of between 17 and 45 antenna patterns, each enumerated with an index. Once a pattern has been loaded once, which involves sending 8 phases and 8 amplitudes, an index is assigned to it. After that, recalling the pattern is a simple matter of calling for that index, which is much faster than sending the entire antenna weight vector. This improves utilization of the bandwidth constrained bus between the central CPU and the T/R Modules.

Developing a library of antenna patterns involves synthesizing each of patterns and is done off-line on a relatively powerful PC. Fidelity Comtech has developed libraries that include the following types of antenna patterns:

1. Omnidirectional patterns
2. High efficiency patterns. These patterns achieve the highest possible gain, but exhibit relatively high sidelobes (-8 dB).
3. Low Sidelobe Patterns. These patterns achieve relatively good sidelobe levels (-20 dB), through amplitude tapering, but sacrifice some antenna gain.
4. Sector Patterns (90˚, 180˚)
5. Figure-Eight Patterns

Figure 6 is a comparison of two patterns that might be in the same library. The pattern on the left is a high efficiency pattern, which exhibits high sidelobes. The figure on the right has much lower sidelobes, both in absolute terms and relative to the main beam, but also has less overall gain and a broader half-power-beamwidth.

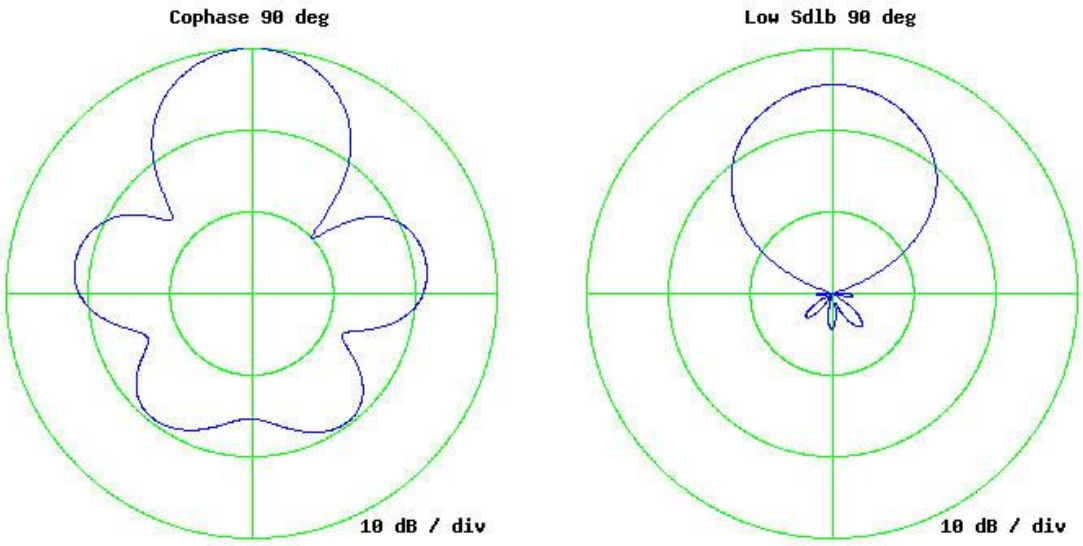

Figure 6. Comparison of two patterns in a library

3.2 Application: Direction Finding

The principal use of the Phocus Array in government applications is direction finding, and by extension, Geolocation of WiFi emitters.

There is a great body of literature on Angle-of-Arrival estimation and direction finding using techniques such as MUSIC and ESPRIT. These techniques cannot be used with this hardware architecture because the WiFi card only reports power measurements, not phase. Furthermore, the WiFi card only provides one power measurement per packet.

Therefore, in order to make an estimate of AoA with the Phocus Array, several packets must be received on different antenna beams. Fidelity Comtech has a version of firmware that it makes available to the US Government that correlates the RSSI of packets on beams "aimed" in different directions with the direction from which the signal came.

Because there are only 11 WiFi channels available in the United States, it is common that several dozen stations will be in view simultaneously. Therefore, an important part of implementing direction finding of WiFi stations is to do some rudimentary packet demodulation and inspection to determine the MAC address of the station that transmitted the packet. Not all packets include a MAC address for the transmitting station, but many do.

Details of the Phocus Array's direction finding performance are considered sensitive but unclassified, so they will not be discussed here. Interested readers should feel free to contact the author directly.

3.3 Application: Replace Gimbal & Dish

Figure 7. Photograph of 32 element array

Another application of the second generation Flex-VMT technology in the Phocus Array was to replace the traditional Gimbaled Dish antenna. In this particular application, a dish antenna was being used to track an unmanned aerial vehicle (UAV). The customer wanted to control the UAV from a small boat and felt that the dish and gimbal wasn't suited to tracking the UAV as the boat maneuvered.

This application required considerably more antenna gain than is provided by the standard eight element array, so a 32 element array was fabricated. Fortunately, the Flex-VMT architecture is extensible; extending from 8 to 32 elements was a relatively simple matter of connecting four sets of 8 T/R modules, each in a daisy chain and adding additional splitters. The same electronics (T/R Modules, SBCs and Splitters) were used.

The 32 element array exhibited an 11 degree half-power beamwidth. With equal-amplitude antenna patterns, which produce maximum gain, the sidelobe level was the same -8 dB as for the eight element array. This was expected and not considered a problem for this application. Based on the 11 degree beamwidth, the pattern library used with the 32 element array was comprised of 72 high gain beams on 5 degree increments, plus an omnidirectional pattern.

Fidelity Comtech also added a compass and GPS as well as some control software to the 32 element array. The Phocus Array antenna then received a data feed from the ground station that included the GPS coordinates of the UAV. Based on this information, the CPU in the antenna used was able to automatically compute the direction to the UAV.

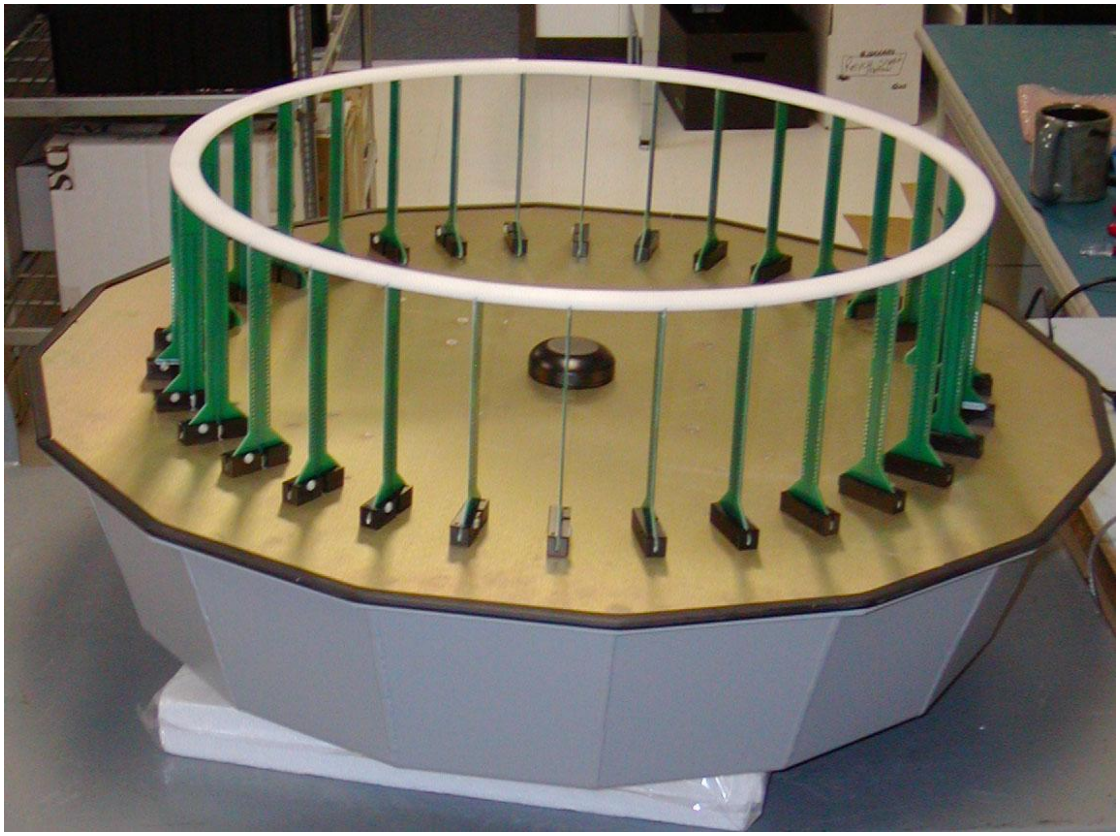

Figure 8. Photograph of 32 element array interior (second generation technology)

3.4 Application: Maritime Ports / Outdoor Networks

This is the principle commercial market for Phocus Array Systems.

Maritime Ports and container yards tend to be quite large – typically several miles across and as much as a mile or so inland. Furthermore, the metal shipping containers can be stacked a high as 70 feet, making them similar to urban environments, at least in terms of wireless propagation.

Data networks, especially wireless networks, play a vital role in the maritime port. The location of every container on the port is stored in a central database. These containers are constantly being rearranged, if only because containers on top must be moved to gain access to the containers on the bottom. Each time a container is moved, the database must be updated and this is best done via a wireless network (anything else would be infeasible).

The Phocus Array has found application in this environment because the phased array provides considerable reach compared with traditional antennas. The increased reach is

a result of two factors: antenna gain and a diversity effect from the eight antenna elements. Furthermore, these customers value the fact that the antenna can be adjusted from the Network Operation Center (NOC). This is important because it is often necessary to adjust the antennas to compensate for the changing conditions in the container stacks.

Today adjusting the antenna pattern in a maritime port is a manual process. In 2010, Fidelity Comtech received a Phase I SBIR grant from the National Science Foundation to investigate automatic pattern adaptation. Unlike most prior work in adaptive antennas, which optimizes a communications channel between a single transmitter and a single receiver, this work optimized the coverage in a region.

Figure 9. Sensor Nodes measuring performance in a container yard.

To achieve adaptive patterns, we implemented a feedback system where Fidelity Comtech staff drove around the port sampling the signal-to-noise ratio at various locations. Special sensors were created for this system, which would act as a reference beacon and transmit its location.

The value of feedback, of course, is that the propagation in a container yard is non-uniform. Some areas will experience deep shadows and others will have clear line-of-

sight. Practically speaking, it is impossible to predict the propagation over a large area, but it is possible to measure it and apply some statistical analysis.

Once enough data had been sampled, we were able to determine which areas could be improved and how that would affect the other areas in the region of interest. This is an iterative process: measure coverage by drive testing, adjust the patterns in the Phocus Array, and retest. Adjusting the patterns in this way is an automated process, implemented in a computer algorithm. The particular approach used was a variation on a steepest descent algorithm.

In principle, each pass through the process should improve coverage slightly, until the process finally converges and improvement is no longer possible. In practice, not every iteration improved coverage, but overall it was possible to increase average SNR in the region of interest by up to 10 dB.

This research yielded promising results, but is not mature enough to be deployed commercially yet.

3.5 Third Generation Phocus Array

The Third Generation of the Phocus Array is currently in development. Prototypes are now being tested.

Unlike the second generation phased array, which began as a piece of network equipment, the emphasis has been on developing a smaller, rugged phased array for mobile and vehicular applications.

The principal architectural changes have been:

- Replacement of the individual microprocessors on each T/R Module with a more powerful ARM microcontroller and FPGA.
- Addition of embedded GPS and inertial sensors.

The stacked dipole elements remain, but their feed structure was changed to improve performance in the circular array. It also served to broaden the bandwidth of the overall system.

The addition of the FPGA has enabled much faster beam switching. Whereas the second generation phased array could switch patterns in less than 100 microseconds, in principle the third generation phased array will be capable of switching in only a few microseconds.

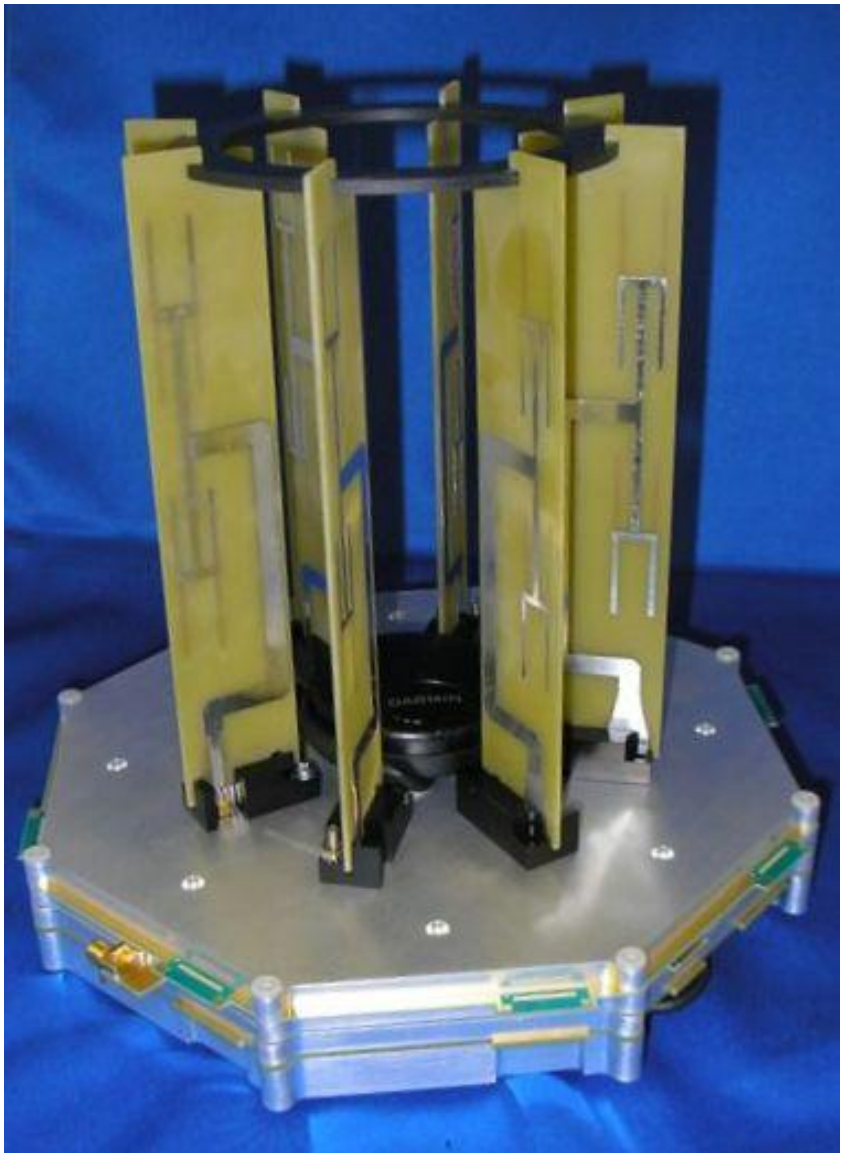

Figure 10. Interior Photograph of Third Generation Phocus Array

4.0 Conclusion

This paper has explored the evolution of a commercial phased array and some of the applications it has found. It has examined the way the technology has evolved to meet the emerging market needs that were not anticipated when the project was conceived. This paper has further explored the architecture of the overall array and the T/R Module in some detail.

A 8X8 WIDEBAND RIBCAGE-DIPOLE ARRAY FOR DIRECTED POWER APPLICATIONS AND ITS CHARACTERISTICS

D. D. Harty , B. Janice, and S. N. Makarov
Worcester Polytechnic Institute
100 Institute Road
Worcester, MA 01609-2280

F. Scirè Scappuzzo
Physical Sciences Inc.
20 New England Business Center
Andover, MA 01810-1077
fscire@psicorp.com

Abstract: The present study investigates a broadside relatively small linearly-polarized wideband UHF non-scanning array for directed power applications. The array radiator is a new volumetric ribcage dipole configuration. The array has a large impedance bandwidth and consistent front lobe gain over the wide frequency band. We present theoretical and experimental results describing the array performance.

Keywords: Broadband dipoles, Arrays, Finite arrays, Broadband arrays

1. Theoretical gain pattern of a finite 2D array

1.1. Gain of the main beam

The directive gain of a large finite mutually-coupled 2D phased array with *M* by *N* regularly-spaced elements is determined by the expression first suggested by Hannan [1] and repeatedly cited by Hansen [2],[3] and others. Namely, with reference to Fig. 1,

$$D(\theta,\varphi) = MN\frac{4\pi A}{\lambda^2}\cos\theta, \quad A = d_x d_y \tag{1}$$

Here, λ is the wavelength, θ is the *scan* elevation angle. This equation was suggested based on the "natural guess" that the directivity of the large array is exactly equal to the directivity of the large (compared to the wavelength) aperture. The directivity of the uniform-distribution aperture with the impingent electric field in the free space exactly

coincides with Eq. (1) [4]. Furthermore, since the effective area of an element should be proportional to its projected area in the direction of interest, the element gain should have a cosine variation with the angle in Eq. (1). Based on this intuitive reasoning, Eq. (1) has been stated.

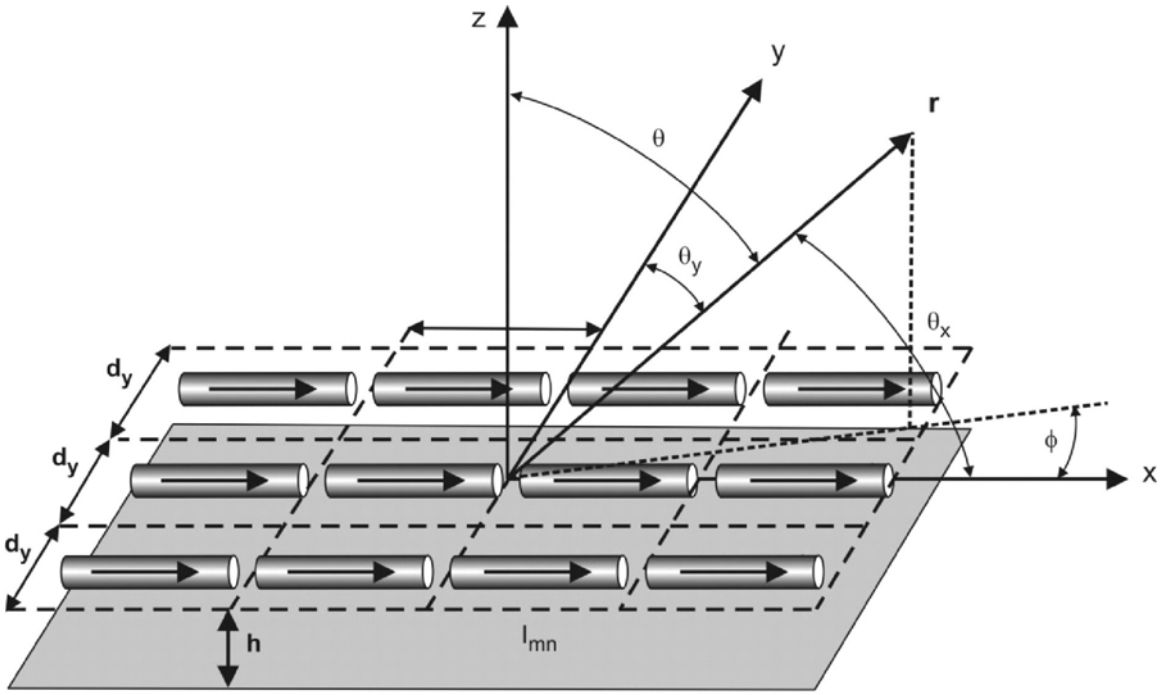

Fig. 1. Array geometry and unit cell dimensions.

Despite the lack of initial theoretical justification it was shown by Oliner and Malech [5] (and also mentioned by Hansen, Ref. [2]) that Eq. (1) can be proved for slots and dipoles. For our case of the non-scanning array pointing at zenith, $\theta = 0$, so that Eq. (1) can be used to predict the gain in dB at zenith (at broadside) in the form

$$D_0 = 10\log_{10}\left[MN\frac{4\pi d_x d_y}{\lambda^2} \right] \quad \text{dB} \tag{2}$$

1.2. Array factor and directivity

The amplitude pattern (array factor for isotropic radiators) of the scanning array in Fig. 1 is conveniently expressed in terms of direction cosines in Fig. 1 [6]. It is given by

$$AF(\theta,\varphi)=\left|\sum_{m=1}^{M}\sum_{n=1}^{N} I_{mn}\exp\left(j(md_{rx}\tau_x+nd_{ry}\tau_y)\right)\right|,\quad d_{rx}=\frac{2\pi d_x}{\lambda},\quad d_{ry}=\frac{2\pi d_y}{\lambda}$$
$$\tau_x=\cos\theta_x-\cos\theta_{xs},\quad \tau_y=\cos\theta_y-\cos\theta_{ys}$$
$$\cos\theta_{xs}=\frac{\psi_x}{d_{rx}},\quad \cos\theta_{ys}=\frac{\psi_y}{d_{ry}} \tag{3}$$

Here,

I_{mn} are (real) excitation weights; $I_{mn}=1$ with no taper;
θ_x and θ_y are the polar angles from the array axis (direction cosines) shown in Fig. 1;
ψ_x and ψ_y are the progressive phase shifts between elements.

When scanning at zenith, the direction cosines of the radius vector specifying scan direction (beam maximum) $\cos\theta_{xs}$ and $\cos\theta_{ys}$ are both equal to zero.

After some manipulations, the result from Eq. (3) is reduced to the form [4],[6]

$$AF(\theta,\varphi)=\frac{\sin x}{x}\frac{\sin y}{y},\quad x=\frac{1}{2}Md_{rx}\tau_x,\quad y=\frac{1}{2}Nd_{ry}\tau_y \tag{4}$$

which is the Fraunhofer scalar diffraction pattern of the corresponding rectangular aperture.

1.3. Gain of individual element

For vector fields or the array fields, Eq. (4) has to be further augmented with the pattern of an individual element. We omit this step though since the dipole pattern close to zenith is very uniform, and since we are only interested in the main beam of the large 8×8 array.

1.4. Total directive gain

We consider the array scanning at zenith. Combining the results of subsections 1.1 to 1.3 we obtain the directive gain of the array in the form

$$D_0 = 10\log_{10}\left[NM\,\frac{4\pi d_x d_y}{\lambda^2}\left(\frac{\sin x}{x}\frac{\sin y}{y}\right)^2\right] \text{ dB}, \qquad x = \frac{1}{2}Md_{rx}\cos\theta_x \quad y = \frac{1}{2}Nd_{ry}\cos\theta_y \quad (5)$$

For the *E*-plane scan (*xz*-plane in Fig. 1) $\theta_x + \theta = 90\text{deg}$, $\theta_y = 90\text{deg}$, and Eq. (5) simplifies to

$$D_0 = 10\log_{10}\left[NM\,\frac{4\pi d_x d_y}{\lambda^2}\left(\frac{\sin x}{x}\right)^2\right] \text{ dB}, \qquad x = \frac{1}{2}Md_{rx}\sin\theta \quad (6)$$

For the *H*-plane scan (*yz*-plane in Fig. 1) $\theta_y + \theta = 90\text{deg}$, $\theta_x = 90\text{deg}$, and Eq. (5) simplifies to

$$D_0 = 10\log_{10}\left[NM\,\frac{4\pi d_x d_y}{\lambda^2}\left(\frac{\sin y}{y}\right)^2\right] \text{ dB}, \qquad y = \frac{1}{2}Nd_{ry}\sin\theta \quad (7)$$

1.5. Application

The geometry of the unit cell in the array under study is shown in Fig. 2. The radiator is a ribcage dipole with a conical matching network close to the antenna feed to be connected to a balun. The overall size of the radiator is slightly less than the size of the unit cell.

In the particular case of the 8×8 array, with reference to Fig. 1, we use the following parameters in Eqs. (6) and (7):

$$N = 64,\ d_{rx} = d_{ry} = 240\text{mm},$$
$$k = 2\pi/\lambda, \quad \lambda = c_0/f \quad (8)$$

Fig. 3 shows the theoretical gain pattern for the array described by Eq. (7) at 500 MHz and 1 GHz, respectively.

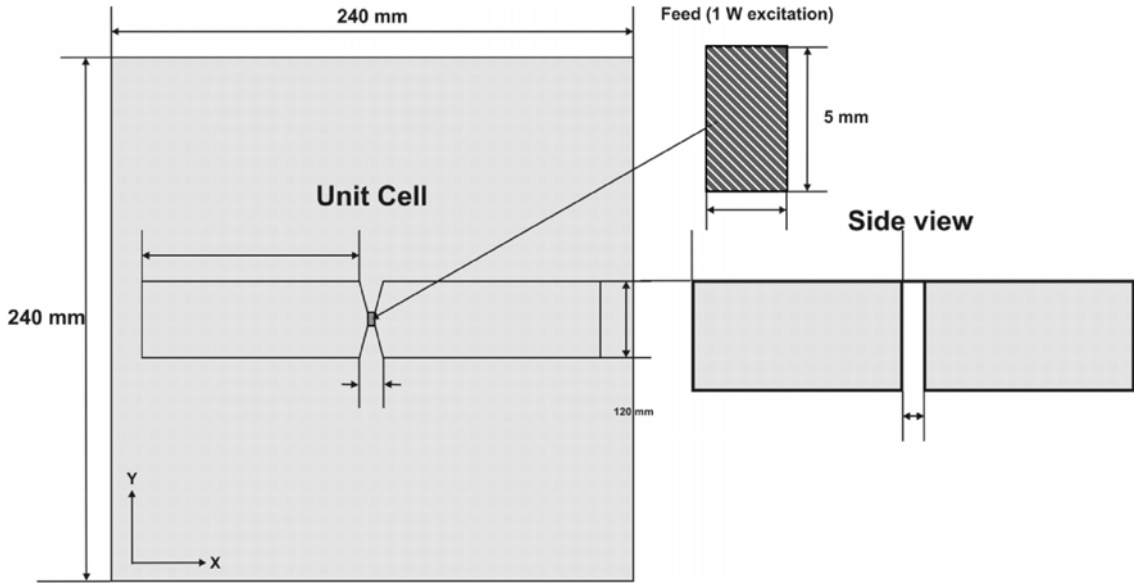

Fig. 2. The array unit cell on the size of 240mm by 240 mm.

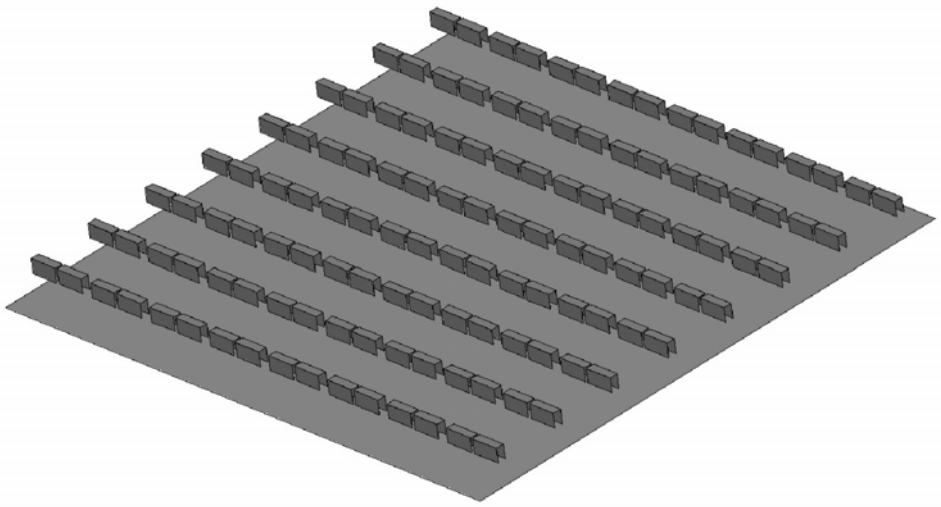

Fig. 3. Theory versus numerical simulations of an 8×8 array of dipoles on the total size of 1.96×1.96 m.

1.6. Comparison between theory and numerical simulations

The numerical simulations have been carried out for the array of center-fed ribcage dipoles (see the next section) with Ansoft HFSS v. 12. The spacing from the ground plane was 150mm. Fig. 3 shows the array structure. The solution was obtained with the PML box and used about 100,000 tetrahedra. Fig. 4 shows numerical directive gain (dashed curve) versus theoretical gain (Eq. (7) – solid curve) in the H-plane at two frequencies of interests.

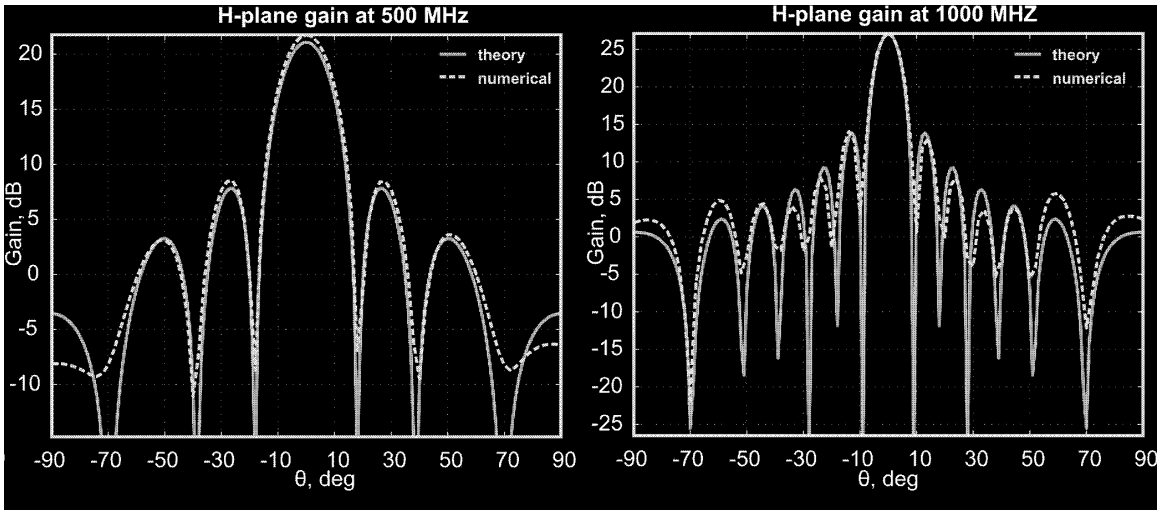

Fig. 4. Theory versus numerical simulations of an 8×8 array of dipoles on the total size of 1.96×1.96 m.

The theoretical and numerical data agree quite well despite the sophisticated nature of the dipole radiator. This confirms our estimates used to predict the behavior of the hardware prototype considered in the following text.

2. Array hardware

2.1. Radiator

As a single radiator we have chosen the ribcage dipole shown in Fig. 5a. Compared to its competitors – the blade dipole in Fig. 5b and the droopy dipole in Fig. 5c - the ribcage dipole is more versatile. It has been shown in our previous talk (AAS 2009) that, among other possible dipole configurations [10]-[30] it combines the advantages of both the blade dipole and the droopy dipole – the wider impedance bandwidth typical for the blade dipole and the better pattern uniformity over the frequency band typical for the droopy dipole.

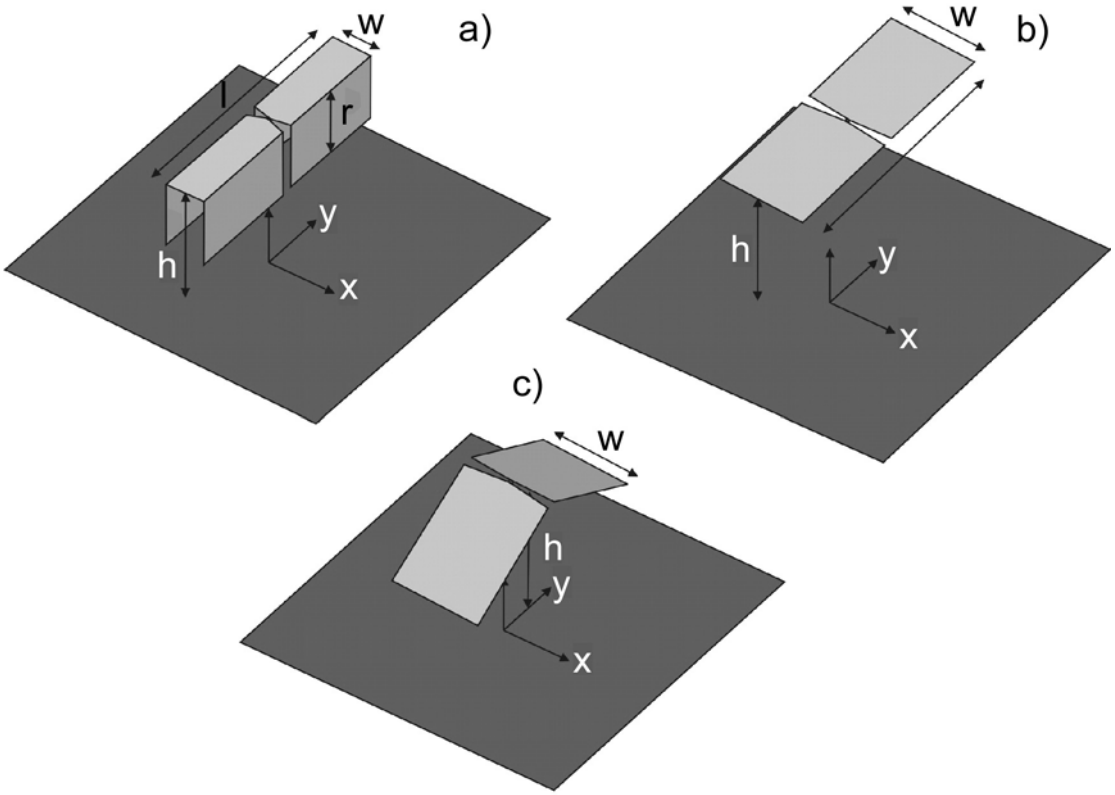

Fig. 5. Ribcage dipole versus its competitors: b) - the planar blade dipole; and c) - the droopy dipole.

2.2. Balun

A tapered microstrip balun shown in Fig. 6 has been employed. The use of this type of the balun is common for broadband linearly-polarized dipoles over a ground plane [10], [19]. The balun is printed on a 125 mil thick FR4 (using thick copper traces) and is soldered to an N-type male connector in the ground plane. The microstrip trace itself is either tapered or not. The typical trace width is 5-6mm.

We have investigated different tapering profiles including triangular, exponential, and Chebyshev's profiles, but did not find a significant improvement in the impedance bandwidth compared to the simple triangular profile.

Compared to the center-fed ribcage dipole, the isolated ribcage radiator with the balun may be optimized for a slightly lower or a similar impedance bandwidth.

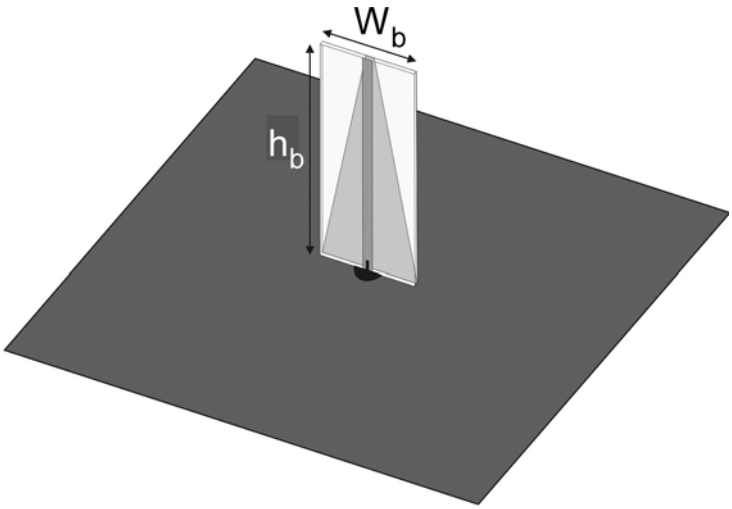

Fig. 6. Microstrip tapered balun and its dimensions.

2.3. Radiator with balun

Two isolated radiators including the printed balun shown in Fig. 7 have been tested prior to arrays assembly. Fig. 7 shows a comparison between simulations and experiments - the return loss measurements (calibrated 8722ETR Agilent network analyzer). The agreement is satisfactory, but not perfect. We partially explain the difference in the middle of the band by a detuning effect of two Teflon posts seen in Fig. 7. These posts have not been considered in the simulations. When the posts are removed, a better agreement is obtained.

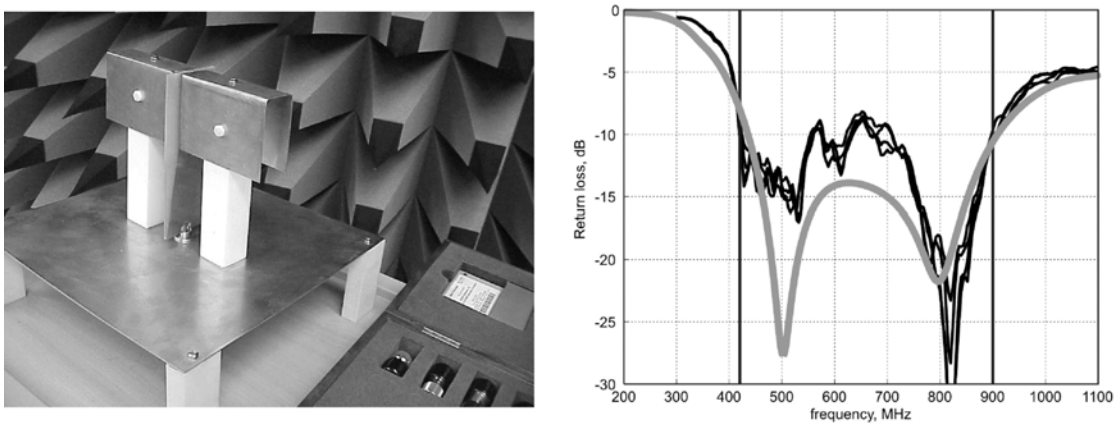

Fig. 7. Left - an isolated ribcage dipole antenna. Right - comparison between simulations and experiment - return loss of the isolated ribcage above 300×300mm ground plane. The thick curve indicates simulations; thin curves - experiment.

2.4. Feeding network with Wilkinson dividers

Corporate-fed networks are used to provide power splits of 2^n, such as n = 2, 4, 8… and so on. For an antenna array, this type of feed is more general and versatile because it provides the designer more control over the amplitude and phase of each element. For the 64-element antenna array a corporate feed network is constructed using 2:1, 4:1, and 8:1 Wilkinson dividers, shown in Fig.8. The array is divided into 4 sub-arrays having 16 elements in each 4x4 module. Within each module, each individual element is fed by two 8:1 power dividers, which in turn are fed by one 2:1 divider. Then, each module is fed by a master 4:1 divider. In total the feed network is composed of one 4:1 master divider, four 2:1 dividers, and eight 8:1 dividers.

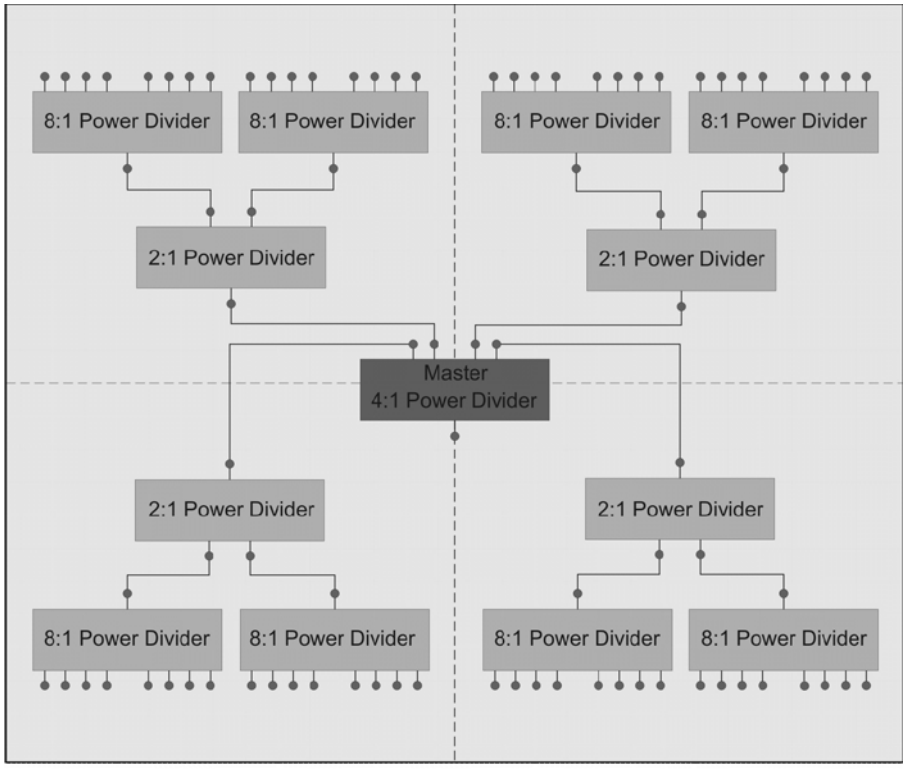

Fig. 8. Corporate-feeding network used for the 64-element antenna array.

2.5. Array assembly

The array is mounted on a 2D controlled mast shown in Fig. 9. The digitized motor controller allows for mechanical scanning in both azimuth and elevation plane, to within ±45 degrees. The array itself was built as a combination of four 4×4 individual blocks as shown in Fig. 8 and then tuned for the maximum impedance bandwidth.

Fig. 9. Array assembly. Top – front view; bottom – back of the array with the feeding network.

3. Array measurements

3.1. Path properties

The measurements of the directive gain have been performed in house, using a setup with two, A.H. Systems Inc. wideband ridged horns (AHS-570), shown in Fig. 10 for calibration purposes.

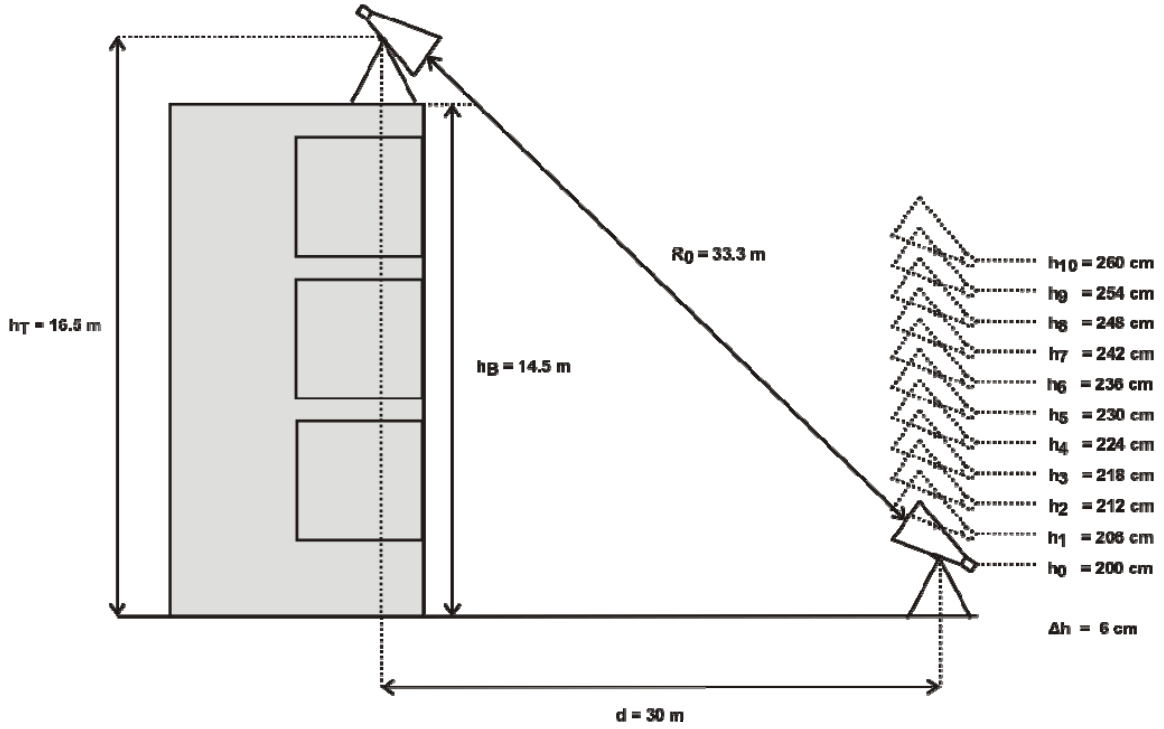

Fig. 10. Horn measurement setup at Physical Sciences Inc.

Horn-to-horn measurements were taken at 500 MHz and 1 GHz at the PSI building to calibrate the path and investigate the effects of ground reflections on the antenna gain.

The transmitting horn was set on the building's roof and the receiving horn was set in the parking lot in the arrangement shown above. Both horns stand 2 meters high when supported by tripod. The height of the receiving horn was varied by 6 cm increments and the received power was measured using an Agilent spectrum analyzer (E4402B ESA-E). Minimum and maximum values were taken because of the rapidly changing values shown on the spectrum analyzer. The minimum, maximum, and mean values are shown in Tables 1 and 2 that follow.

The results given in Tables 1 and 2 indicate that the gain remains nearly constant at 500 MHz and 1 GHz when the height is varying. The height of the receiving horn was varied sufficiently for one cycle of interference pattern at 500 MHz and two cycles at 1 GHz, so the effect of reflections appears to be minimal (on the order of ±1dB or less in pattern distortion) because of the stable gain values recorded.

Table 1: Received power at 500 MHz for increments of R.

ΔR **(m)**	**Max (dBm)**	**Min (dBm)**	**Mean (dBm)**
$R_0 = 33.32\ m$	-53.46	-57.02	-55.24
$R_1 = 33.34\ m$	-53.23	-56.94	-55.09
$R_2 = 33.37\ m$	-53.42	-56.72	-55.07
$R_3 = 33.40\ m$	-52.24	-56.91	-54.58
$R_4 = 33.43\ m$	-52.92	-56.03	-54.48
$R_5 = 33.45\ m$	-52.73	-56.18	-54.46
$R_6 = 33.48\ m$	-53.21	-56.13	-54.67
$R_7 = 33.51\ m$	-53.42	-56.11	-54.77
$R_8 = 33.53\ m$	-53.33	-56.82	-55.08
$R_9 = 33.56\ m$	-53.03	-56.72	-54.88
$R_{10} = 33.59\ m$	-53.01	-56.84	-54.93

Table 2: Received power at 1 GHz for increments of R.

ΔR **(m)**	**Max (dBm)**	**Min (dBm)**	**Mean (dBm)**
$R_0 = 33.32\ m$	-48.75	-52.36	-50.56
$R_1 = 33.34\ m$	-48.92	-52.38	-50.65
$R_2 = 33.37\ m$	-48.75	-52.46	-50.61
$R_3 = 33.40\ m$	-48.76	-52.38	-50.57
$R_4 = 33.43\ m$	-46.87	-52.12	-49.50
$R_5 = 33.45\ m$	-47.98	-51.20	-49.59
$R_6 = 33.48\ m$	-47.65	-51.38	-49.52
$R_7 = 33.51\ m$	-48.72	-52.22	-50.47
$R_8 = 33.53\ m$	-48.79	-52.06	-50.43
$R_9 = 33.56\ m$	-48.88	-52.43	-50.66
$R_{10} = 33.59\ m$	-48.93	-52.56	-50.75

3.2. Return loss of the array

The return loss of the array measured at the output of the 4:1 power divider is shown in Fig. 11 that follows. The array has a slightly better impedance bandwidth than initially simulated (Ansoft HFSS v. 12). This may be explained by extra loss in the feeding network, which become especially important at higher frequencies.

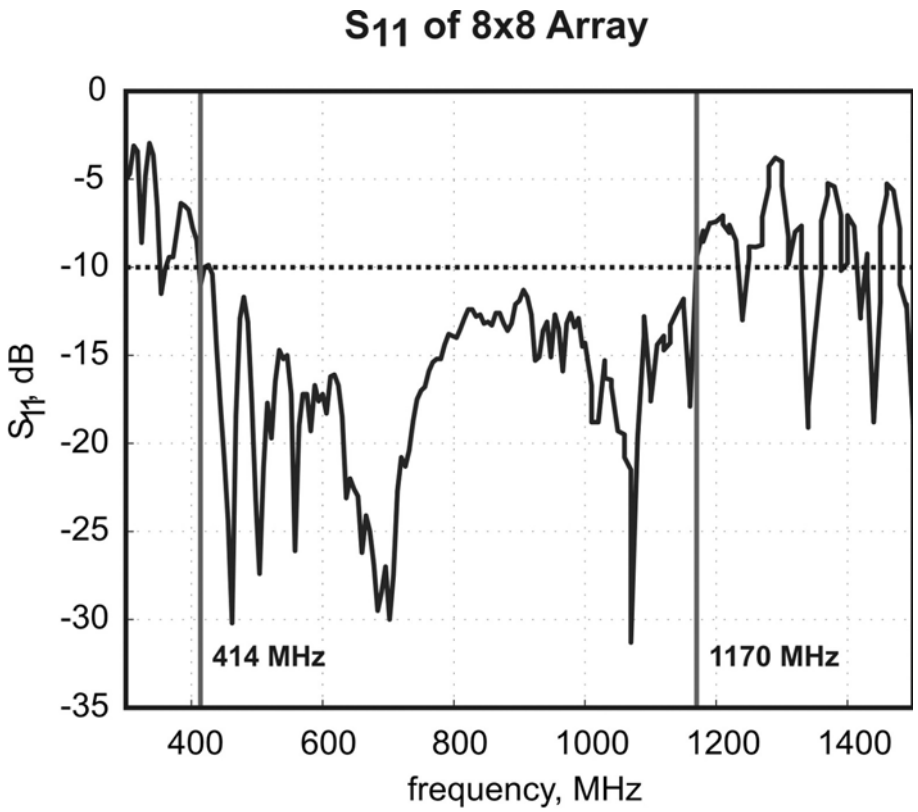

Fig. 11. Return loss of the array measured at the output of the 4:1 power divider.

3.3. Gain calibration with two horns

To calculate the absolute antenna gain from the received power measurements we performed measurements with two horns first, and then used the following expression:

$$G_{\text{Array}} = G_{\text{Horn}} + \left\{ P_{\text{Array/dBm}} - P_{\text{horn/dBm}} \right\} \tag{9}$$

where

G_{Array} - sought array directive gain at a given frequency (dB)

G_{Horn} - calibrated second horn gain at a given frequency from datasheet (dB)

$P_{\text{Array/dBm}}$ - measured array received power (dBm)

$P_{\text{Horn/dBm}}$ - measured second horn received power (dBm)

This estimate does not depend on the input power to the measurement setup.

3.4. Gain measurement results

The received power of the antenna array was measured after the horn-to-horn calibration. The array was mounted and positioned such that the face of the array was directed toward the roof of the PSI building. The phase center of the array was approximately 2 meters above the ground. The horn on the roof facing the array was excited with 20 dBm power. The array was then connected to the spectrum analyzer and rotated horizontally by 5 degree steps and scanned a total of 45 degrees. At each 5 degree step, the received power of the array was recorded.

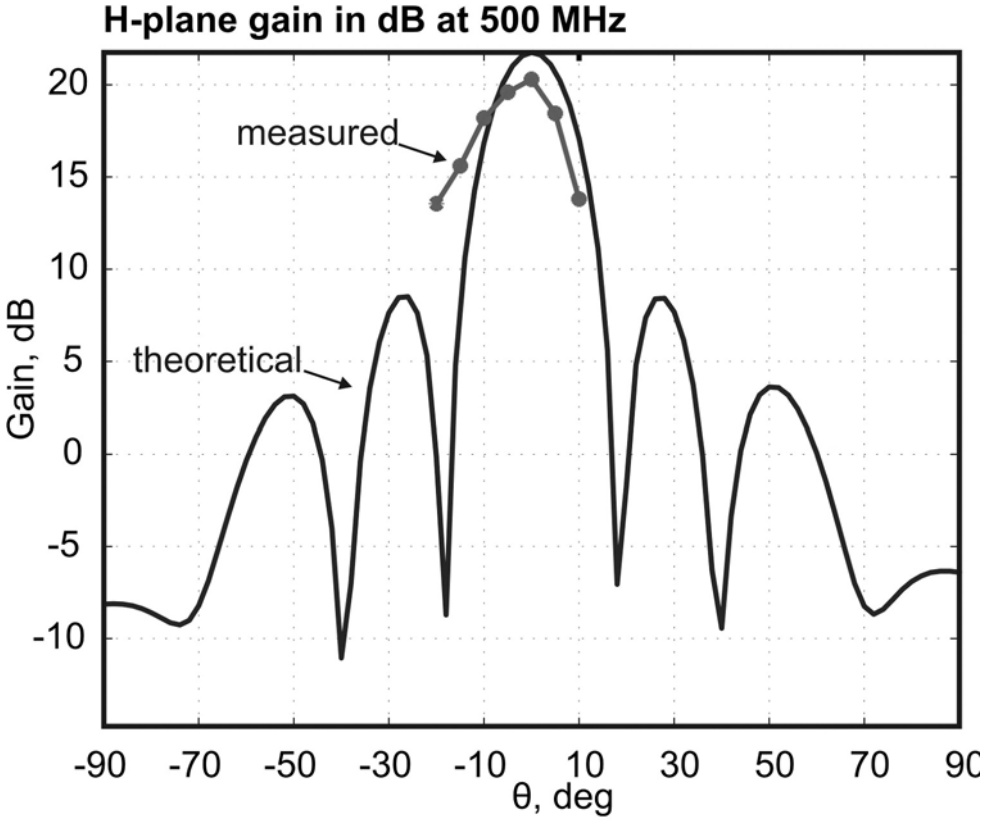

Fig. 12. Measured vs. numerical simulation - H-plane directive gain at 500 MHz.

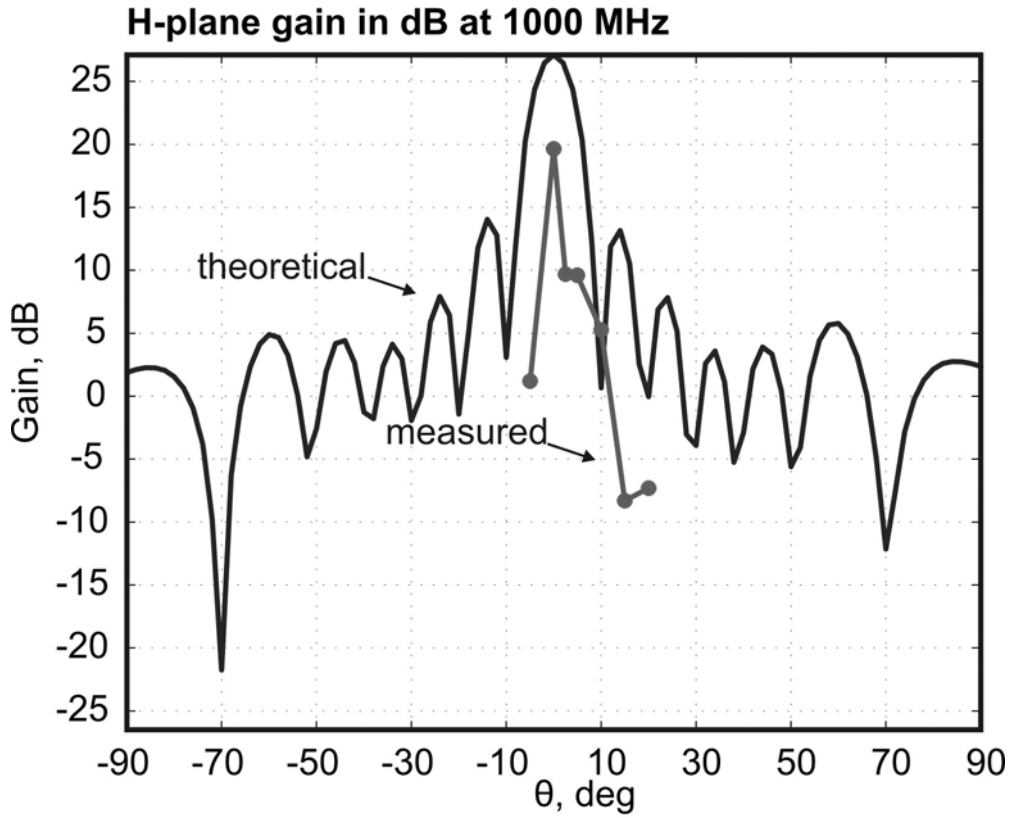

Fig. 13. Measured vs. numerical simulation - H-plane directive gain at 1000 MHz.

3.5. Discussion and conclusions

The array performance follows well theoretical prediction and assures that the array realized gain is at least 20 dB over the frequency band of interest. The gain degradation compared to the theory in Fig. 13 at 1 GHz is due to feeding network losses, which become especially important at the upper band edge. The corresponding losses include the losses of the 4:1, 2:1, and 8:1 Wilkinson dividers in Fig. 8. Their performance was simulated in Ansoft HFSS; it is shown in Fig. 14 that follows. The estimated divider loss at 1 GHz is 0.7+1+2=3.7dB. Another 1.5 dB is coming from cable adapters; the sum of those two numbers convincingly explains the deviation between theory and experiment in Fig. 13. Using a low loss substrate instead of the 130 mil FR4 would allow us to reduce the realized gain loss by about 3 dB.

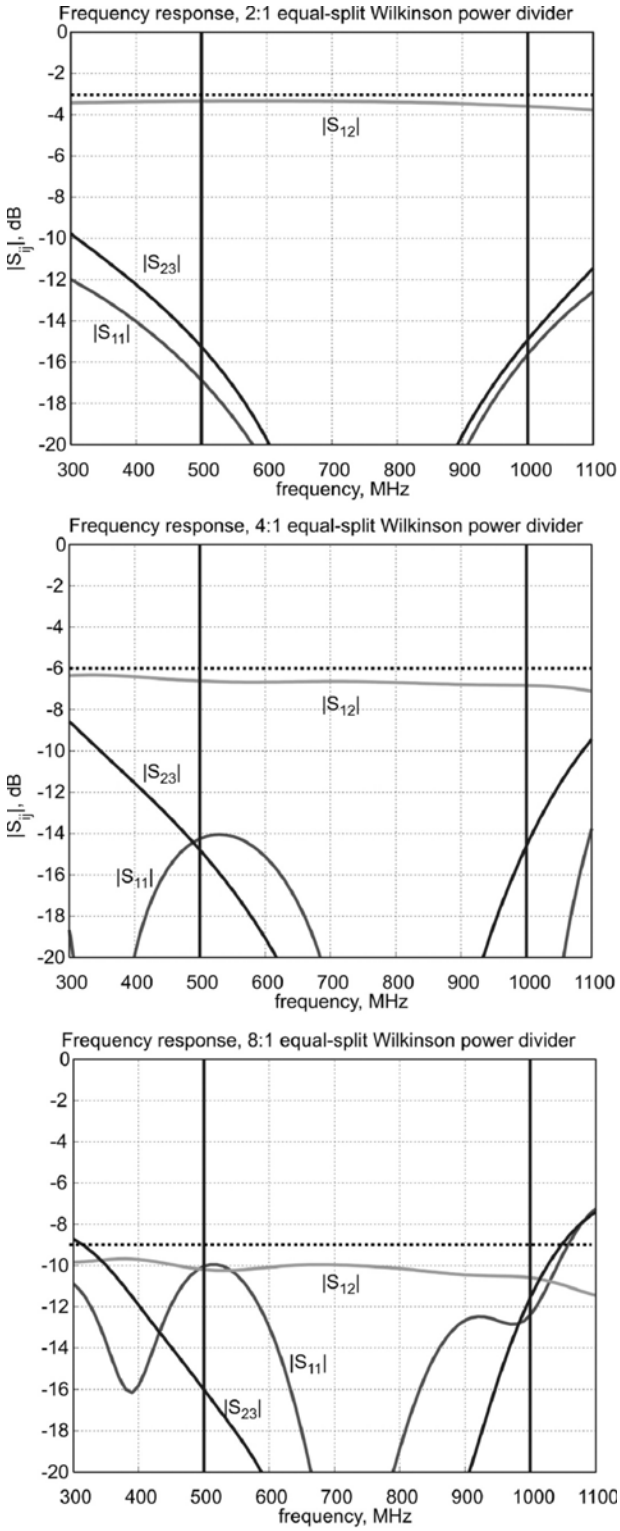

Fig. 14. Simulated behavior of three series Wilkinson dividers used in hardware prototype. The loss is given by the deviation of S_{12} from the theoretical dashed line.

4. Acknowledgement

This material is based upon work supported by the United States Army under Contract No. W15QKN 08 C 0493. Any opinions, findings and conclusions or recommendations expressed in this material are those of the author(s) and do not necessarily reflect the views of the United States Army.

5. References

[1] P. W. Hannan, "The Element-Gain Paradox for a Phased-Array Antenna," *IEEE Trans. Antennas Propagation*, vol. 12, no. 4, July 1964, pp. 423-433.

[2] R. C. Hansen, *Phased Array Antennas*, Wiley, New York, 1998, p. 222.

[3] R. C. Hansen, "Phased Arrays," in: *Antenna Engineering Handbook*, John L. Volakis, Ed., Mc Graw-Hill, 2007, fourth edition, p. 2-15.

[4] C. A. Balanis, *Antenna Theory. Analysis and Design*, Wiley, New York, 2005, third ed., p. 672-673.

[5] A. A. Oliner and R. G. Malech, "Mutual coupling in infinite scanning arrays," in *Microwave Scanning Antennas*, Vol. II, R.C. Hansen, ed., Academic Press, 1966, Chapter 3, pp. 195-335.

[6] W. H. Von Aulock, "Properties of phased arrays," *Proceedings of the IRE*, vol. 48, no. 10, pp. 1715-1727, 1960.

[7] S. Makarov and A. Puzella, "Scan impedance for an infinite dipole array: Hansen's formulas vs. Ansoft HFSS simulations," *IEEE Antennas and Propagation Magazine*, vol. 49, no. 4, Aug. 2007, pp. 143-156.

[8] A. Ishimary, *Electromagnetic Wave Propagation, Radiation, and Scattering*, Prentice Hall, Upper Saddle River, NJ, 1991.

[9] Chen-To Tai and S. A. Long, "Dipoles and monopoles," in: *Antenna Engineering Handbook*, John L. Volakis, Ed., Mc Graw Hill, 2007, fourth edition, pp. 4-3 to 4-32.

[10] Jeong Il Kim Joung Myoun Kim, Young Joong Yoon, and Cheol Sig Pyo, "Wideband printed fat dipole fed by tapered microstrip balun," *2003 IEEE AP-S International Symposium*, vol. 3, June 2003, pp. 32 – 35.

[11] M. I. Borgford and A. K. Kong, "Design of a very broadband dipole," *1988 IEEE AP-S International Symposium*, vol. 2, June 1988, pp. 812 – 815.

[12] A. Kerkhoff, and S. Ellingson, "A wideband planar dipole antenna for use in the long wavelength demonstrator array (LWDA)," *IEEE AP-S International Symposium*, July 2005, vol. 1B, pp. 553-556.

[13] S. Ellingson and A. Kerkhoff, "Comparison of two candidate elements for a 30-90 MHz radio telescope array," *IEEE AP-S International Symposium*, July 2005, vol. 1A, pp. 590-593.

[14] E. B. Rodal, M. C. Detro, D. R. Gildea, and J. M. Janky, *Antenna with Curved Dipole Elements*, US Patent # 5,173,715, Dec. 22nd, 1992.

[15] P. G. Elliot, "*Folded cross grid dipole antenna*," U.S. Patent #5796372, Aug. 18, 1998.

[16] Seong-Youp Suh, W. L. Stutzman, and W. A. Davis, “Low-profile, dual-polarized broadband antennas,” *2003 IEEE Antennas and Propagation Society International Symposium*, vol. 2, June 2003, pp. 256 – 259.

[17] Seong-Youp Suh, W. Stutzman, A. Davis, A. Waltho, K. Skeba, and J. Schiffer, “A novel low-profile, dual-polarization, multi-band base-station antenna element – the Fourpoint Antenna,” *2004 IEEE 60th Vehicular Technology Conference*, 2004. VTC2004-Fall, vol. 1, 26-29 Sept. 2004, pp. 225 – 229.

[18] Seong-Youp Suh, W. Stutzman, W. Davis, A. Waltho, K. Skeba, and J. Schiffer, “Bandwidth improvement for crossed-dipole type antennas using a tuning plate,” *2005 IEEE Antennas and Propagation Society International Symposium*, vol. 2A, July 2005, pp. 487 – 490.

[19] L. Akhoondzadeh-Asl, D. J. Kern, P.S. Hall, and D. H. Werner, “Wideband Dipoles on Electromagnetic Bandgap Ground Planes”, *IEEE Trans. Antennas Propagation*, vol. 55, no 9, Sept. 2007, pp. 2426-2434.

[20] S. Best, and D. Hanna, “Design of a broadband dipole in close proximity to an EBG ground plane,” *IEEE Antennas and Propagation Magazine*, vol. 50, no. 6, Dec. 2008, pp. 52 – 64.

[21] J. J. Lee, S. Livingston, and R. Koenig, "Performance of a wideband (3-14 GHz) dual-pol array," *IEEE AP-S International Symposium*, June 2004, vol. 2, pp. 551-554.

[22] J. J. Lee, S. Livingstone, and R. Koenig, “A low-profile wide-band (5:1) dual-pol array,” *IEEE Antennas and Wireless Propagation Letter*, vol. 2, 2003, pp. 46-49.

[23] P. Cerny and M. Mazanek, “Optimized Ultra Wideband Dipole Antenna”, *18th Int. Conf. on Applied Electromagnetics and Communications*, 2005, Oct. 2005, pp. 1-4.

[24] S. R. Best, "A Study of the Performance Properties of Small Antennas," *Antenna Applications Sym.*, Monticello, IL, 2007, pp. 193-219.

[25] M. Goettl and R. Kinker, "*Dual-polarized dipole antenna element*," U.S. Patent #6940465, Sep. 6, 2005.

[26] P. G. Elliot, "*Stacked crossed grid dipole antenna array element*," U.S. Patent #5418544, May 23, 1995.

[27] P. G. Elliot, “Octave Bandwidth Microwave Scanning Array”, *1995 Antenna Applications Symposium Proc.*, Monticello, IL, Sep. 1995, 19 p.

[28] P. G. Elliot and A. E. Rzhanov, “Octave bandwidth printed circuit phased array element,” *2006 IEEE Antennas and Propagation Society International Symposium*, July 2006, pp. 3743 – 3745.

[29] S. Makarov and F. Scire’ Scappuzzo, “Multipath rejection by virtue of a choke ring for a broadband droopy turnstile antenna,” *2007 Antenna Applications Symposium Proc.*, Monticello, IL, Sep. 2007, pp. 467-507.

[30] B. Kaswarra, W. Quddus, F. Scire' Scappuzzo, and S. Makarov, "Circular Polarization Bandwidth for a Bowtie Turnstile Over a Ground Plane," *Proc. IEEE AP-S International Symposium on Antennas and Propagation*, Honolulu, June 2007, pp. 3544-3547.

POLYOMINO SUBARRAYS FOR TIME-DELAY INSERTION: RECENT RESULTS

Robert J. Mailloux (1), Scott G. Santarelli (2), Thomas M. Roberts (2)

(1) Department of Electrical and Computer Engineering, University of Massachusetts, Amherst MA, 01003, USA, Ph. 781-377-3710, Robert.Mailloux.ctr@hanscom.af.mil

(2) Sensors Directorate, Electromagnetics Technology Division, Antenna Technology Branch, Air Force Research Laboratory, Hanscom AFB, MA 01731, USA, Ph. 781-377-6854, Scott.Santarelli@hanscom.af.mil

Abstract-- This paper presents data and a procedure for the use of irregular subarrays in planar, wideband arrays. Using element-level phase shifters and time delay at subarray ports, the procedure substitute's polyomino subarrays in place of conventional rectangular subarrays to eliminate quantization lobes. Included in this paper are new results for four-element subarrays of up to 6,400 elements and eight-element subarrays of up to 16,000 elements, in addition to rules for extending these results to much larger arrays.

INTRODUCTION:

Large phased arrays have severely limited instantaneous bandwidth because the scanned beam location changes with frequency. This effect can be removed by using time-delay units at every element instead of phase shifters, but time-delay units are too expensive, heavy, or bulky for many radar and communications applications.

One alternative solution is to use short time delays at each element, and after grouping these elements together, provide longer time delays digitally or with a tree like arrangement of switched delay lines. This may be an acceptable solution at frequencies where low-loss integrated circuits can include several wavelengths of time delayed line, and it has the advantage of maintaining good sidelobes.

A commonly used alternative is to reduce the total number of required time delays by using phase shifters at the element level and time delay at the subarray inputs. This reduces the beam deviation, but if the subarrays are regularly spaced it causes large quantization lobes in the array pattern.

A second approach for the very wide-band problem is to use element level phase shifters in an aperiodic arrangement of irregular subarrays to replace the short time delays. Longer time delays are provided digitally. Since the quantization lobes are a consequence of the periodic lattice, the use of irregular subarrays removes much of the periodicity and reduces peak sidelobes. We have chosen to use polyomino subarrays because of their ability to tile (i.e., fill) rectangular areas leaving no voids. In this study, we have restricted our choice to tetrominos (4 elements) and octominos (8 elements) [1,2].

RECTANGULAR AND POLYOMINO SUBARRAYS:

Figure 1 shows an array with phase shifters at the element level and time delays at each subarray input. The phase shifters provide all elements with the correct phase at center frequency, but introduce errors at frequencies away from center frequency. If rectangular subarrays are used, the errors become periodic, and cause quantization lobes. The right hand side of the figure shows an L-shaped tetromino subarray and two octomino subarrays- one L-shaped and one that we have called “point-up.” When these are rotated, flipped, and placed in an array, the resulting time-delayed array has no quantization lobes and only slightly higher average sidelobes than the same array filled with rectangular subarrays.

Figure 2 shows far-field radiation patterns for arrays of eight-element subarrays at a frequency ratio of r = 1.3, where $r = f/f_0$, f is the operational frequency, and f_0 is the center frequency. The left figure represents an array of rectangular subarrays (2 x 4 elements), while the right figure represents an array of L-octomino subarrays. The array is scanned using phase shifters at the element level and time delays at each subarray. The scan direction is (u,v) = (0.5, 0.5) in direction cosine coordinates, where $u_0 = \sin\theta_0\cos\varphi_0$ and $v_0 = \sin\theta_0 \sin\varphi_0$. It is apparent that the use of polyomino subarrays eliminates the large quantization lobes, which are present in the array pattern of the array of rectangular subarrays. In effect, the quantization lobes of the rectangular pattern are replaced by a large number of discrete sidelobes at lower signal levels in the case of the polyomino array. Although not apparent in the figures, the average sidelobe level is very nearly the same for both cases. The actual level of the largest peak is about -9 dB for the array of rectangular subarrays and -30 dB for the array of polyominos.

Figure 3 provides a basis for choosing the subarray size subject to gain requirements and/or peak quantization level. The figure shows results for three linear arrays of uniformly illuminated subarrays scanned to $u_0 = 0.707$. This linear model uses element-level phase shifters with progressive phase set at frequency f_0 and implements time delay at each subarray. The results are independent of array taper. We have found that the gain variation with array size and frequency for polyomino subarrays is almost the same as for rectangular subarrays; therefore, one can use Figure 3 as a first approximation of the relative gain at any selected maximum frequency ratio. In this figure the gain is normalized to broadside scan.

The abscissa is the maximum frequency ratio $r_{max} = f/f_0$, and the curves show gain and peak sidelobe levels at any given maximum frequency. The term 'maximum frequency' instead of simply 'frequency' is used in Figure 3, because each point on the abscissa represents an element spacing chosen to be half wavelength at that particular ratio $r_{max.}$

The number of elements in each subarray is M (M = 2, 3, 4), and the figure compares relative gain and quantization lobe level for the three subarray sizes scanned in the principal plane ($u = \sin\theta$, $v = 0$). Each linear array consists of 20 subarrays, so the arrays are different lengths, but the gain data is normalized.

The figures in this paper show behavior for $r_{max} > 1$ because the sidelobe levels for $r < 1$ are very similar if one takes $r = 1 - r_{max}$ as the lowest frequency ratio. The exception to this local symmetry about r=1 is for very wideband cases where the element spacing for the low frequencies is so small that the quantization lobes do not radiate. In these cases there is no low frequency limit for the technique. This means that in general the bandwidth is at least $2(r_{max}-1)$. For $r_{max} = 1.3$, the lowest maximum frequency chosen, this is nearly a two to one bandwidth.

Figure 4 compares the gain of an array of rectangular (2 x 2) subarrays with an array of L- tetromino subarrays. The three sets of data show gain as a function of array size for both rectangular subarrays (solid lines) and L-tetromino subarrays (dotted lines) at maximum frequency ratios of 1.6, 2.0 and 2.4. In all cases, the gain decreases with increasing maximum frequency, even though the arrays are the same size measured in wavelengths. This is caused by increased phase error at the higher frequencies. A significant conclusion is that the gain for polyomino subarrays is less than that of the array filled with rectangular subarrays, but within about one dB at the highest frequency. It is within about one-eighth dB at the frequency ratio 1.6.

Figure 5 shows the peak sidelobe level for arrays of rectangular and L-tetromino subarrays as the array size is varied and for several frequency ratios. The maximum array size is 80 x 80 or 6,400 elements. The rectangular subarray peak sidelobes are quantization lobes and are almost independent of array size. They are produced by the

product of the narrow grating lobes and the subarray pattern. As such, their size is determined by the narrow array factor sampling the subarray pattern, which occurs at the same point regardless of array size. The peak sidelobes of the L-tetromino array cannot be considered residual quantization lobes, since they decrease continually with increasing array size and have a slope of -4 to -5 dB per quadrupling of array size. We have observed that the average sidelobes of the polyomino arrays decay approximately as 6 dB per quadrupling as would be expected for a random phase error; therefore, the peak sidelobes do exhibit a degree of structure that increases their level beyond that of the more random average sidelobes.

Most notable about the results of Figure 5 is that for each frequency, the difference between the peak sidelobes of rectangular and L-tetromino subarrays is relatively constant. This difference, the sidelobe reduction achieved by the irregular subarrays, is plotted in Figure 6 and is constant to within ±0.5 dB over the chosen wide frequency band. This advantage ranges from about 12 db for a 32^2 size array to approximately 18 dB for an array of 80^2 elements.

Figures 7 through 9 repeat the data of figures 4 through 6, but using a 2 x 4 element rectangular subarray and L-octomino subarrays in an array of up to 128 elements on a side, or 16,384 elements.

Figure 7 shows the gain of an array with time delay set to be perfect at the element level. The other three sets of data show results of using rectangular (4 x 2) subarrays shown in dotted red vs L-octomino subarrays with data shown in dotted green at maximum frequencies ratios of 1.3, 1.5, and 1.7. As was the case for the four-element subarrays, the phase error causes the gain to decrease with frequency. In this case however, the gain of the array with polyomino subarrays is nearly identical to that with rectangular subarrys. This is a result of the decreased bandwidth and resulting decreased phase error for this combination.

Figure 8 gives the peak sidelobes for rectangular and L-octomino arrays for r = 1.3, 1.5, and 1.7. The array size is varied from 32 elements to 128 elements on a side with the sidelobe level falling at about 4.5 dB per 6 dB change in array area. The sidelobe reduction data is again relatively constant (within ±0.75 dB) with frequency and ranges from 12 db to about 20 dB with the array size increase. As previously stated, the behavior for r<1 is not included in these figures because the sidelobe ratios at $r = 1\text{-}r_{max}$ are very similar to those at r_{max}. For example, this figure shows that the peak sidelobe level is –31.5 dB for $r_{max} = 1.3$ with the array of 128 elements on a side, and (not shown) the computed results for $r_{max} = 0.7$ are -32.5 dB.

The sidelobe reduction data of Figure 9 are quite similar to that of Figure 6 over the range of 32 elements on a side to 80 elements on a side signifying that with double the frequency offset, the four-element and eight-element irregular subarrays yield nearly the same quantization-lobe suppression. This fact can also be useful in defining array size.

CONCLUSION

This paper introduces new results that compare the gain and sidelobe levels of rectangular subarrays and irregular polyomino subarrays when used to introduce time delay into wideband phased arrays. The intent of the paper is to present data that enables the design of arrays with polyomino subarrays. Two facts make engineering judgments possible. The first is that an array of polyomino subarrays has nearly the same gain as an array of rectangular subarrays. This allows the selection of subarray size using Figure 3 on the basis of gain falloff. The second fact is that the quantization levels of Figure 3 are higher than those of the polyomino-based array – this can be attributed to a single parameter that is related to array size and only weakly related to the frequency displacement. This allows the quantization lobe data of Figure 3 to be a predictor of the polyomino array peak sidelobe level by subtracting the data of Figures 6 or 9 from the Figure 3 sidelobe levels. Figures 6 and 9 show that any given quantization level shown in Figure 3 can be reduced by a significant number that is related to the array size, and only slightly related to frequency displacement.

ACKNOWLEDGMENT

This work was supported in part by the Air Force Office of Scientific Research under Dr. Arje Nachman and in part by the Center for Advanced Sensor and Communications Antennas, Department of Electrical and Computer Engineering, University of Massachusetts, Amherst, MA, USA. The work was conducted at the Antenna Technology Branch, Sensors Directorate, Air Force Research Laboratory, Hanscom AFB, MA, USA.

References:

1. R. J. Mailloux, S. G. Santarelli, T. M. Roberts, “Wideband arrays using irregular (polyomino) shaped subarrays,” Electronics Letters, 31 Aug 2006, Vol. 42, No. 18, pp. 1019-1020.

2. R. J. Mailloux, S. G. Santarelli, T. M. Roberts and D. Luu, “Irregular Polyomino Shaped Subarrays for Space-Based Active Arrays,” International Journal on Antennas and Propagation, Hindawi Publishing Corporation, Volume 2009, Article ID 956254, March 2009.

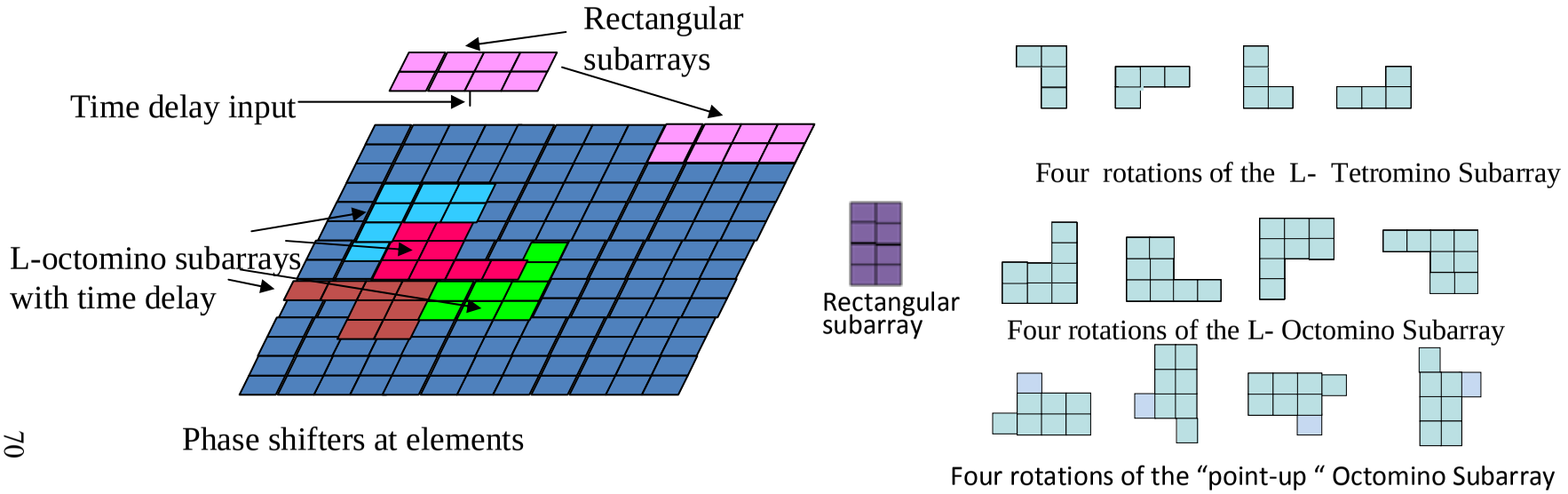

Figure 1. Rectangular, tetromino and octimino subarrays for time delayed wideband arrays

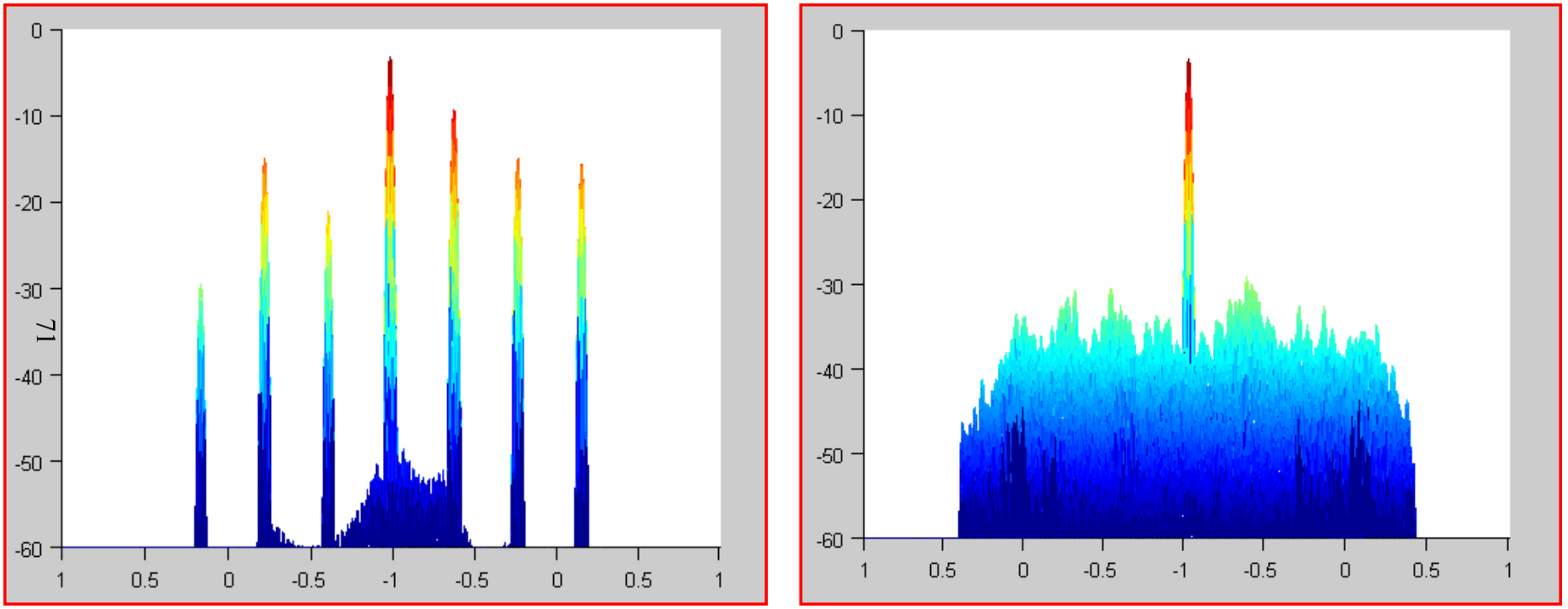

Figure 2. Radiated patterns of 128 x 128 element array with eight element rectangular (left) and L-octomino (right) subarrays

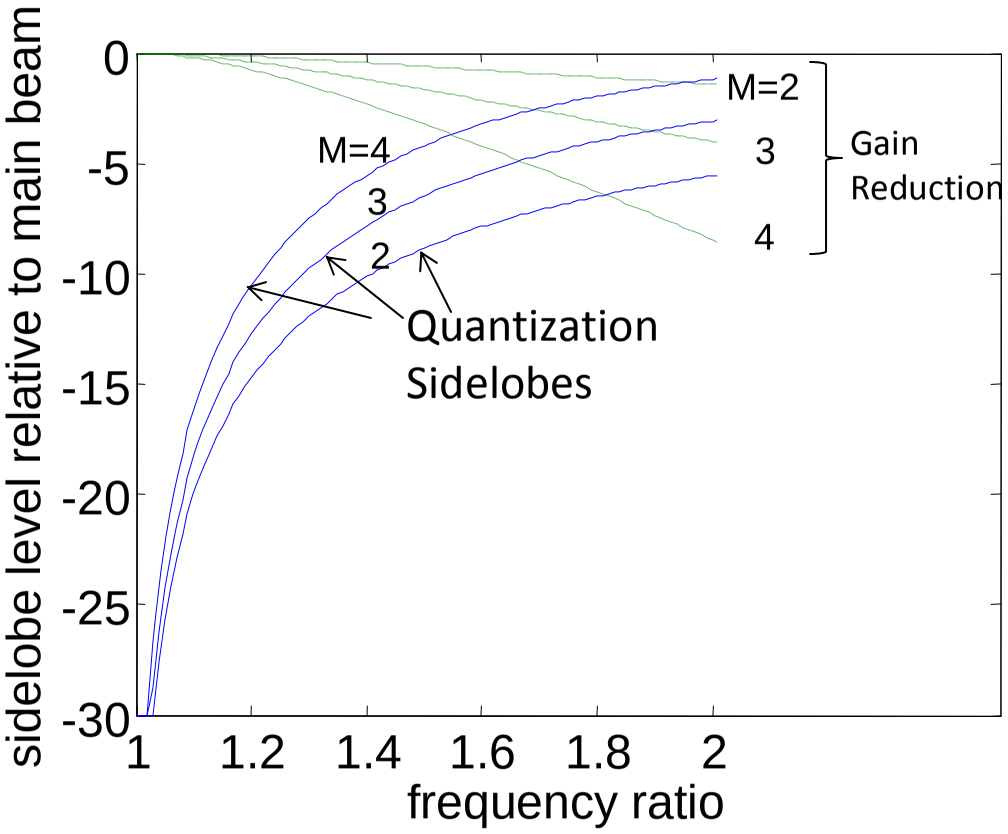

Figure 3. Peak quantization lobe level (solid) and approximate gain reduction (dashed) for planar array of rectangular subarrays

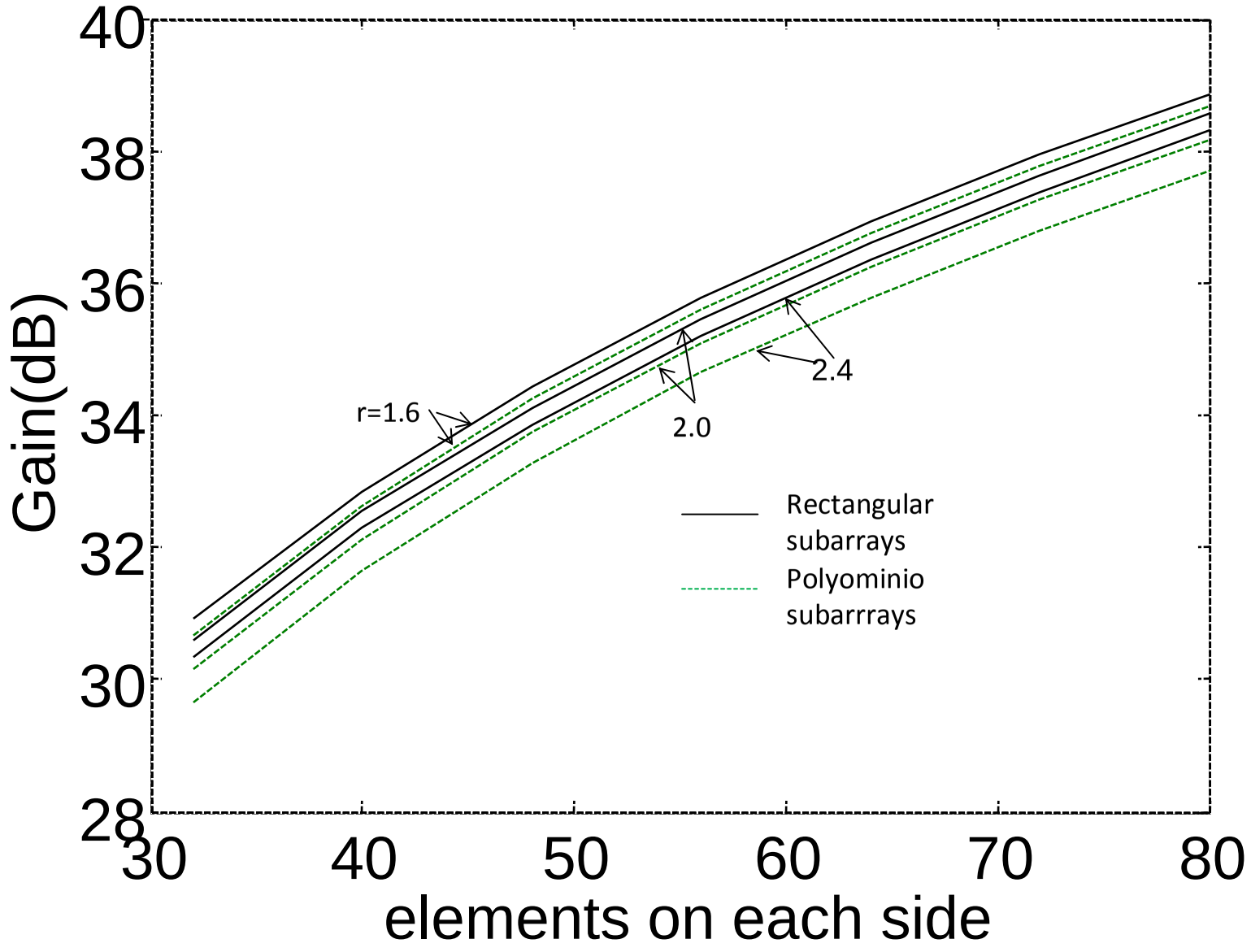

Figure 4. Gain of 128 x 128 element arrays using rectangular and polyomino (tetromino) subarrays, for various frequency ratios (r)

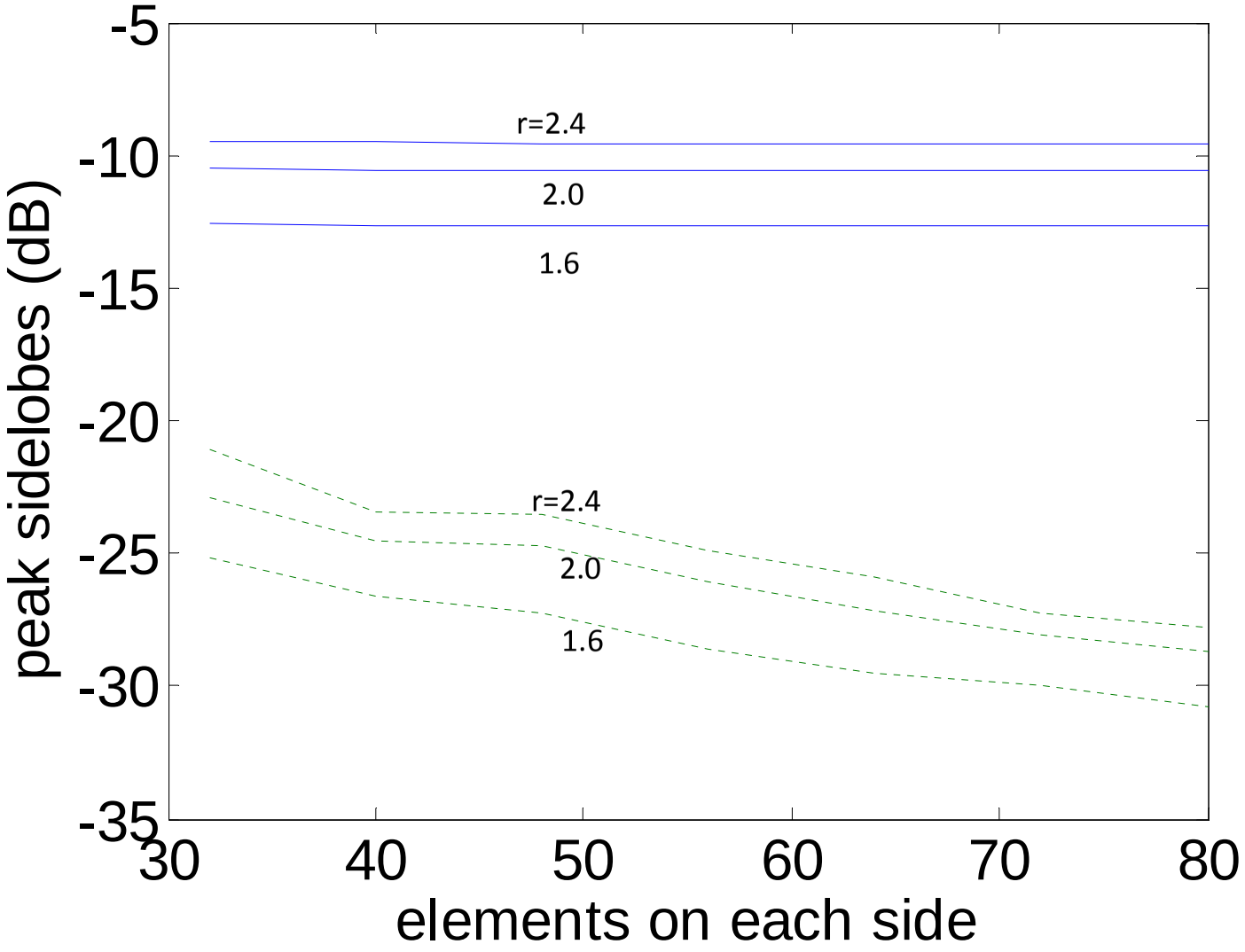

Figure 5: Peak sidelobe levels for arrays of rectangular and tetromino subarrays

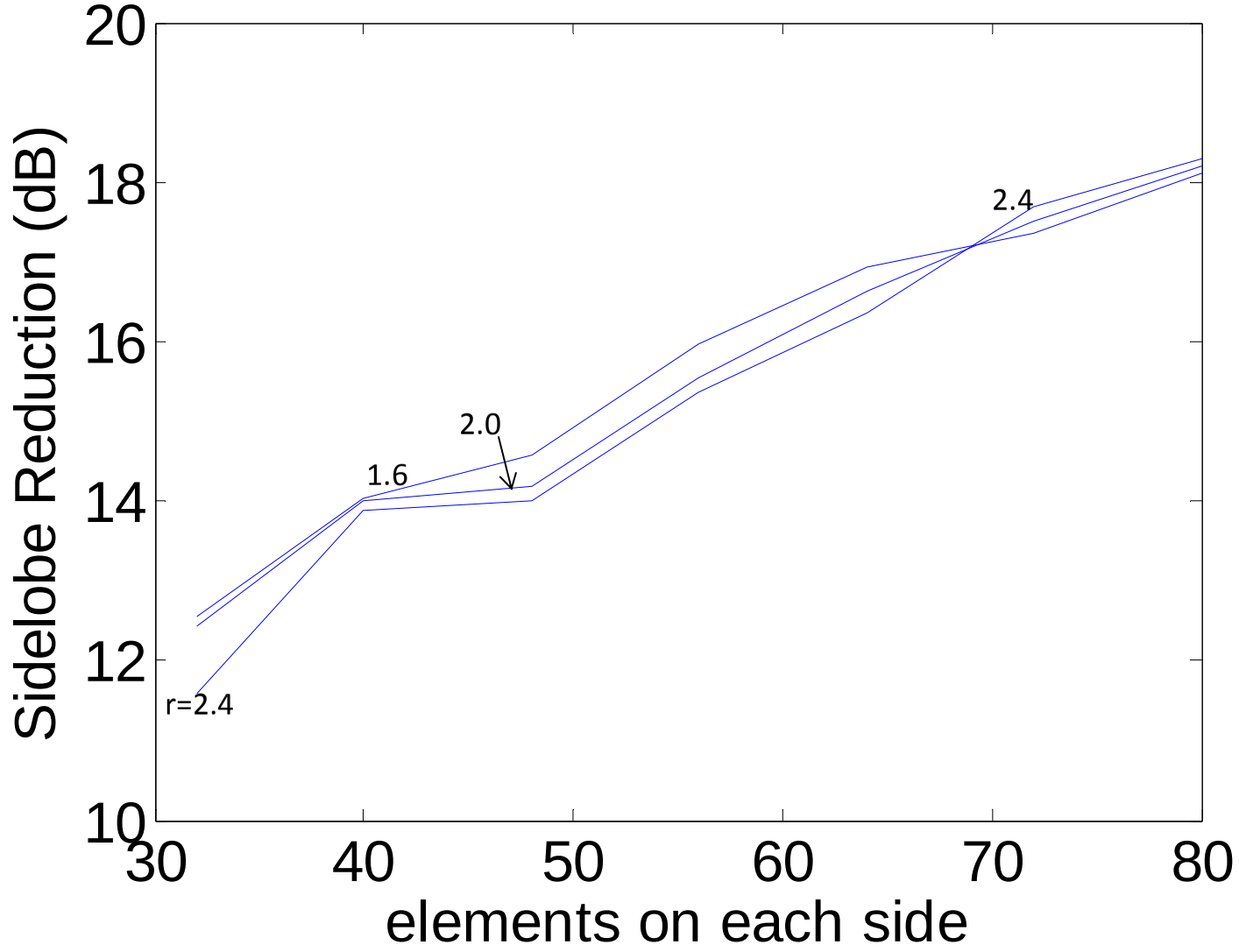

Figure 6. Sidelobe reduction achieved by tetromino subarrays

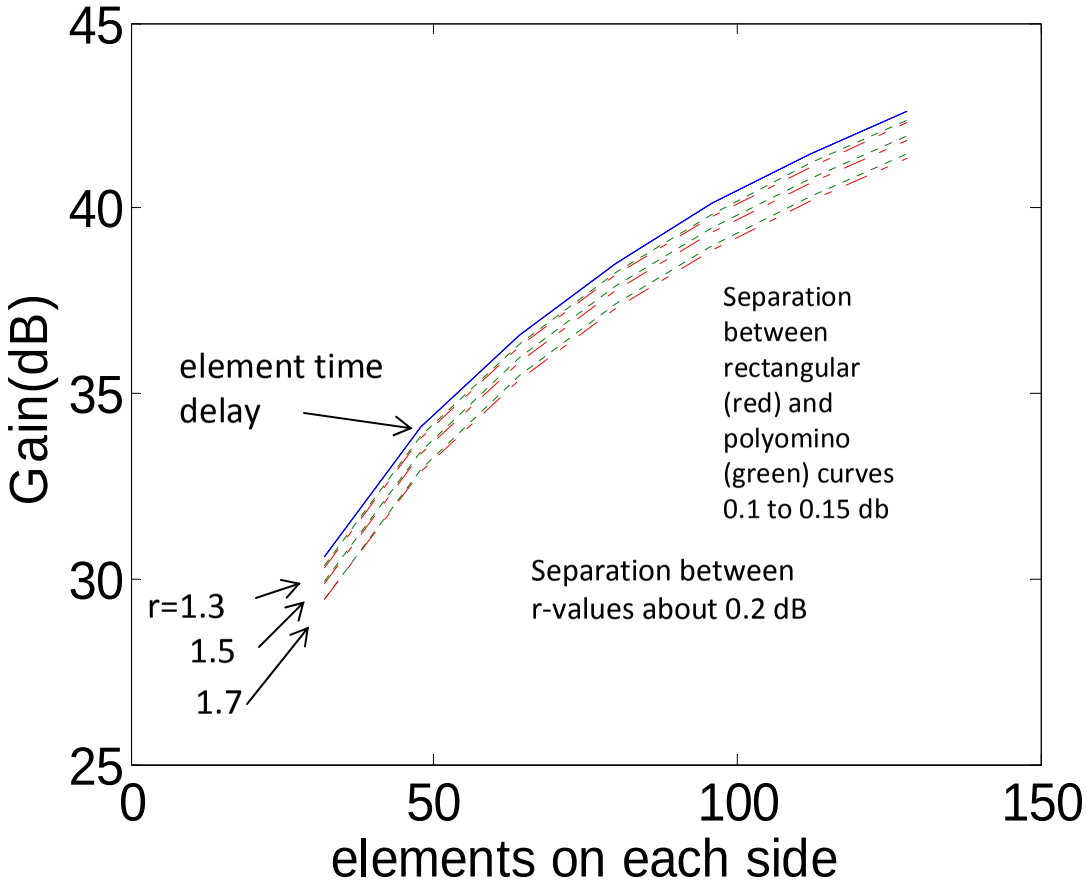

Figure 7. Gain of 128 x 128 element arrays using rectangular and polyomino (octomino) subarrays, for various frequency ratios (r)

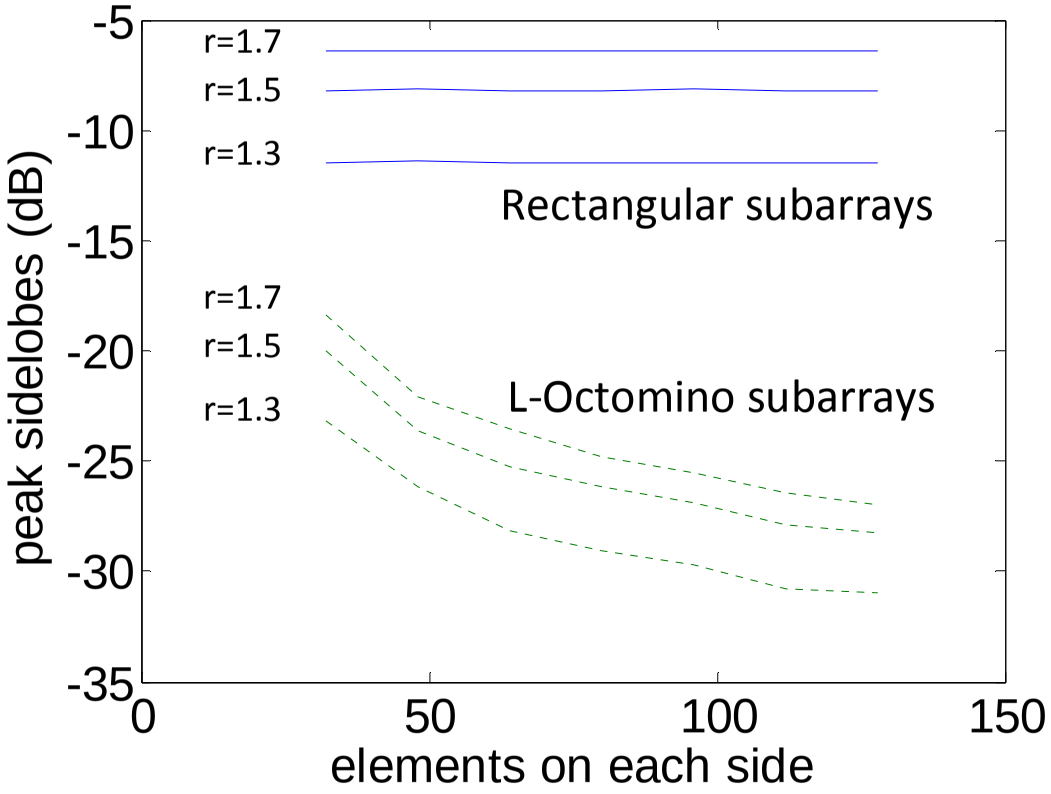

Figure 8. Peak sidelobe levels for arrays of rectangular and octomino subarrays

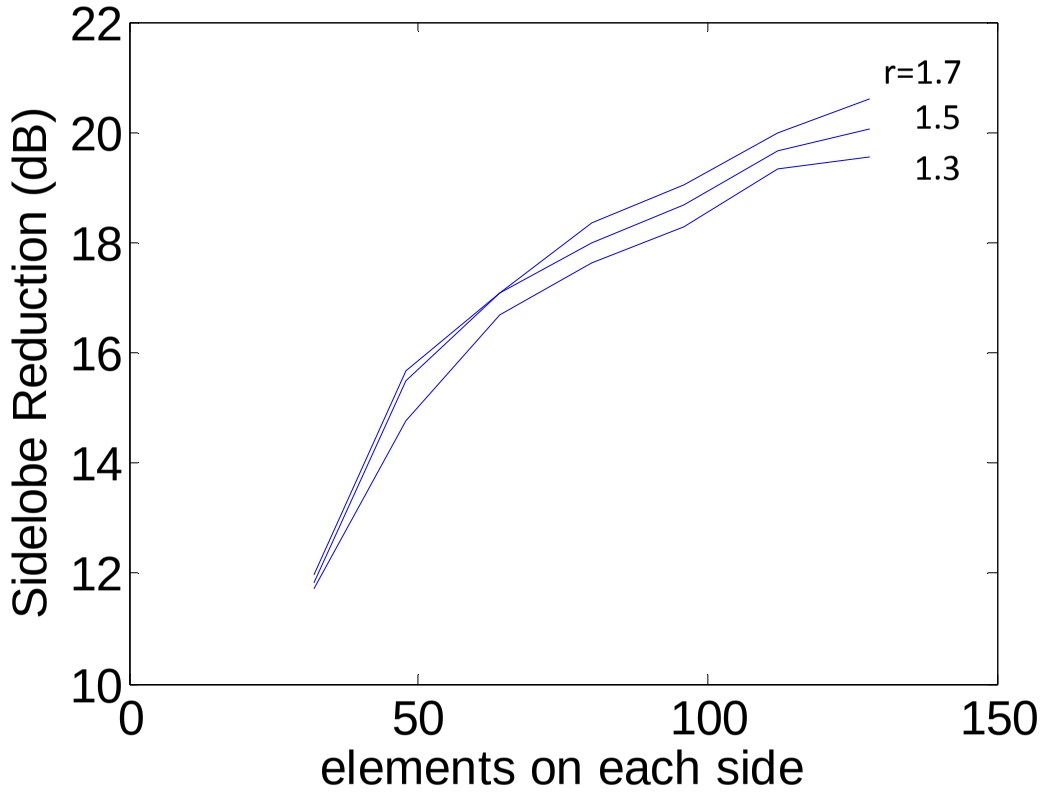

Figure 9. Sidelobe reduction achieved by octomino subarrays

A COMPACT STACKABLE ANTENNA FOR MULTIBAND SYSTEMS

J.P. Doane and R.J. Legge

Advanced Technology Center
Rockwell Collins, Inc. Cedar Rapids, IA 52402 USA
jpdoane@gmail.com, rjlegge@rockwellcollins.com

Abstract: A new low profile, compact antenna design for multiband systems is described. The antenna employs a stacked aperture architecture in which each antenna layer is independently sized for different frequency bands. The antenna that comprises each layer achieves a 40% VSWR 2:1 bandwidth and is only λ/10 tall at the low end of the band. The antenna is comprised of a four element circular array of electrically small wideband radiators fed in phase, each connected to an upper metallic disk. A central post connects the upper disk to the ground plane and simultaneously serves to inductively tune the antenna while allowing additional signals to be passed through the antenna. This topology allows multiple antennas tuned to different bands to be easily stacked, creating an aggregate multiband aperture with >15dB isolation between bands. This antenna is therefore especially suited for radio systems with multiple bands and limited available antenna footprint. The radiation pattern of the antenna is omnidirectional and monopole like. A specific implementation covering L, S, C, and Ku bands is presented with simulated and measured results. Adjustments to the design to mitigate scattering and facilitate manufacturing are also discussed.

1.0 Overview

Advanced radio systems covering multiple RF bands, such as software defined radios, are increasingly common and pose a challenging problem for antenna engineers. In many cases, there is insufficient space for separate antennas for each band, especially as the radios themselves become more compact. Therefore, there is a great need for small, low profile antenna designs that can support multiple frequency bands.

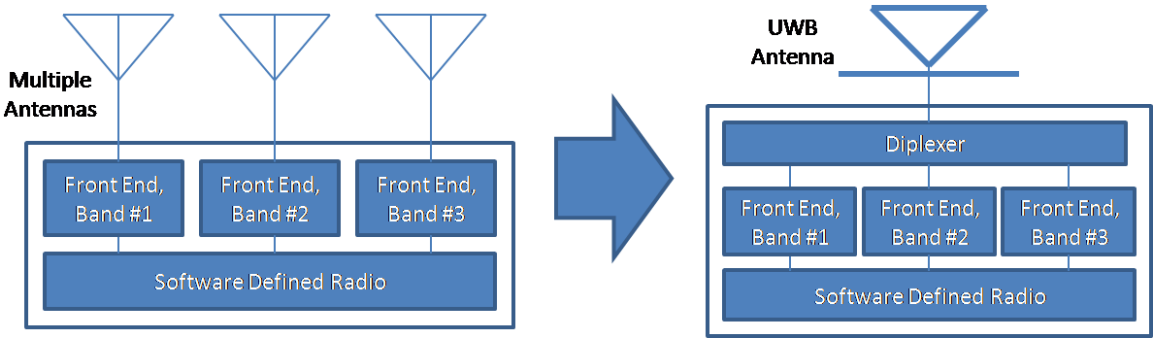

Fig 1. Ultra Wide Band (UWB) Antenna for multiband radio system

Combining multiple antennas into a single ultra-wideband (UWB) antenna is often an attractive option for reducing antenna volume and footprint (Figure 1). However, there are several drawbacks of using a single UWB antenna for a multiband radio application. Because all bands share a common feed, a diplexer must be used to separate each band to its front end. Many UWB antennas are not necessarily electrically small at the low end of the band. Omnidirectional UWB antennas often have degraded pattern coverage at the higher end of the band, which may be problematic for some applications. Different bands may also have different polarization or pattern requirements. Finally, if the bands are too far apart in frequency, a single UWB antenna may not have sufficient bandwidth.

A solution to these problems is to stack separate antenna apertures on top of each other to create a composite multiband antenna, for example stacked bi-conical dipoles. The disadvantage of this approach is that it requires feeding the upper apertures through the active radiating volume of the lower apertures by wrapping the feed of the upper antennas around the exterior of lower antennas[1], as shown in Figure 2. This adds length and signal loss to the feed for the upper antennas and deteriorates the polarization and the uniformity of the lower antenna pattern.

These problems can be resolved if the aperture is designed with an internal conduit running through the antenna. The feed lines for the upper antenna layers could be fed through this conduit without disrupting the performance of the other antennas, as shown in Figure 3.

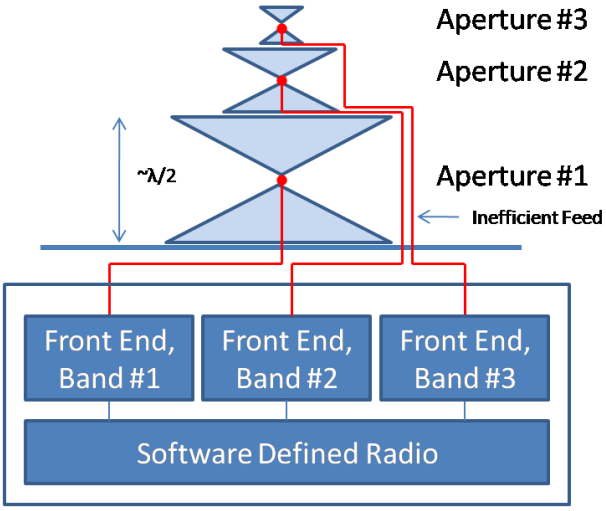

Fig 2. Stacked Biconical Dipoles with sub-optimal Feed

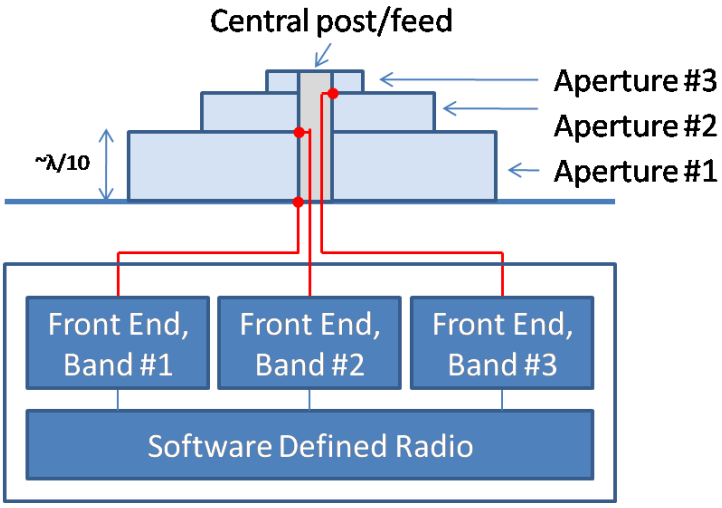

Fig 3. Proposed Stacked Antenna with Central Feed

In this paper, we present such a design for a stackable multiband antenna, where each 'layer' radiates omnidirectionally and can be vertically stacked without interference. The antenna is designed to support a small mobile radio unit with the four bands of operation shown in Table 1.

Band	Frequency Range
L	1.75-1.85 GHz
S	2.2-2.5 GHz
C	4.4-6.0 GHz
Ku	14.4-15.3 GHz

Table 1. Frequencies for Radio System of Interest

Each layer on its own can cover a 40% 2:1 VSWR bandwidth and is only λ/10 tall at the low end of the band, a significantly lower profile than the biconical dipole design. Additionally, because of the central conductive post, this antenna can be mounted partway up a mast without loss of performance.

2.0 Design of a Stackable Multiband Antenna Layer

Each layer of the stackable antenna consists of a four element array on a circular ground plane. The array element is a wideband monopole, which is tuned with a central inductive post that is shared between all four elements and serves as the bypass conduit. A large conductive disk is connected to each element and to the central conductive post.

A microstrip 4 way splitter network is constructed over the ground plane, and delivers equal amplitude and phase to each element. While each element pattern is somewhat directional due to the inductive post, the summed circular array produces an omnidirectional, monopole-like beam. The antenna is fed by a coax transmission line connected to the microstrip near the center of base of the antenna.

Because the antenna is covered with a large conductive disk, a smaller antenna can be stacked on top of this antenna, with the disk becoming the ground plane for the smaller antenna. The smaller antenna can then easily be fed through the conductive post. In this manner, increasingly smaller antennas can be vertically stacked for a composite multiband antenna with as many bands as necessary.

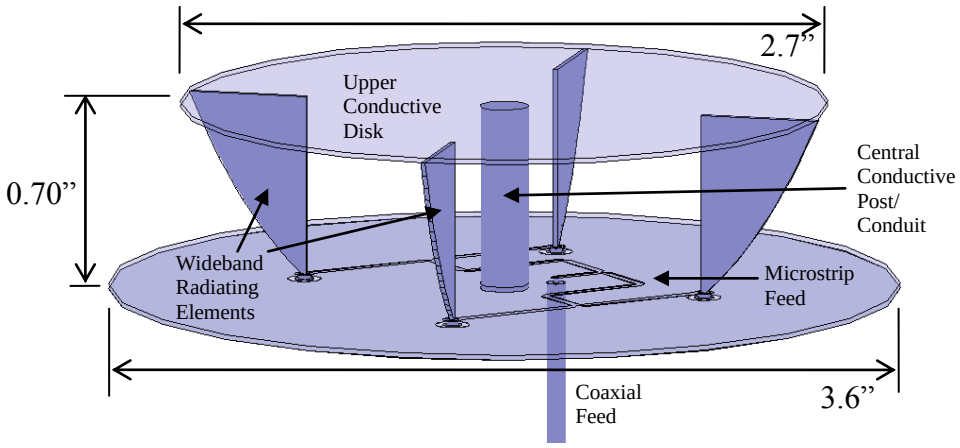

Fig 4. Stackable Antenna ‘Layer’ covering 1.75-2.5GHz

The first layer is resonant from 1.7-2.5 GHz, covering both the L and S bands of interest, and is pictured in Figure 4. It is 0.7” tall (0.1 λ at 1.7GHz), and 2.7” wide (0.39λ at 1.7GHz), on a 3.6” (0.52λ at 1.7GHz) diameter ground plane.

The design of a C band layer covering 4.4-6.0 GHz is merely a matter of frequency scaling the L/S band antenna and tweaking to optimize performance. The C band antenna is .3" tall and its upper conductive disk diameter is 1".

The final Ku layer does not need to pass any additional feeds through it, so it can be of whatever design is convenient. For this application, a simple quarter-wave monopole is used (0.2" tall). However, a more sophisticated antenna could easily be used instead, such as a Ku Band parasitic array as described in [2].

2.1 Design of a Stacked Multiband Antenna

The combined multiband antenna covering L, S, C, and Ku band is shown in Figure 5. The coaxial feeds for the C band and Ku band layers are fed through the central post of the L/S layer. Likewise, the Ku feed is fed through the post of the C band layer. In fact, the C band post simply is the Ku band rigid coax cable. The total antenna is only 1.25" tall.

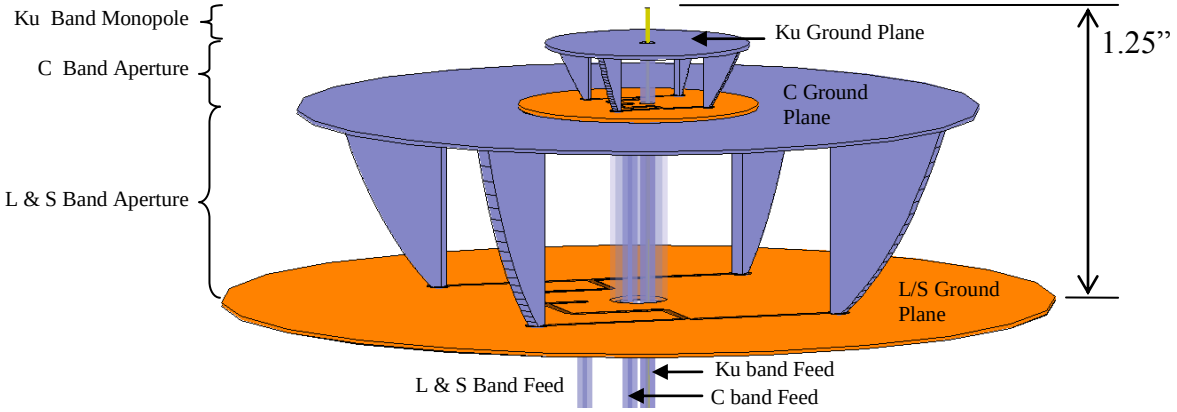

Fig 5. Stacked Multiband Antenna Concept covering L, S, C, and Ku bands

The simulated return loss and gain patterns of the L/S band and C band layers are plotted in Figures 6-8. The patterns are omnidirectional and monopole-like. Note that the C band patterns have a higher peak gain which falls off more rapidly towards the horizon. This is because the C band ground plane is much larger electrically than the L/S band ground, and is similar to a monopole's pattern on a ground plane of that size.

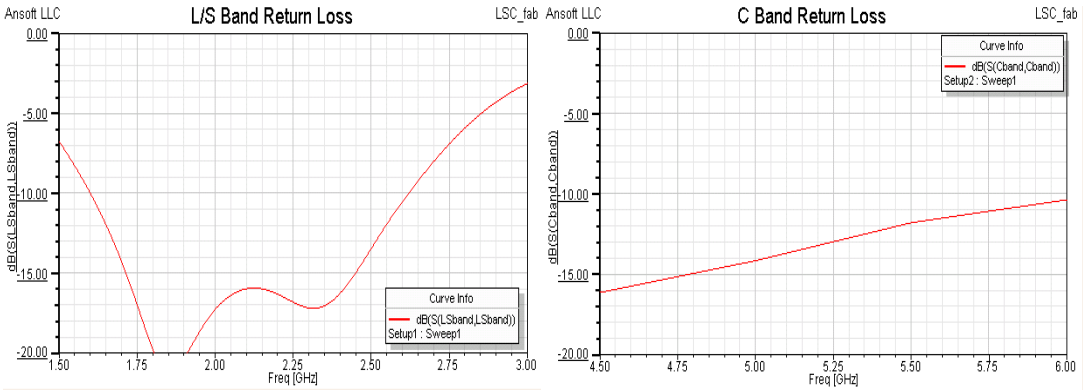

(a) **(b)**

Fig 6. Simulated Return Loss of (a) L and S band layer and (b) C band layer

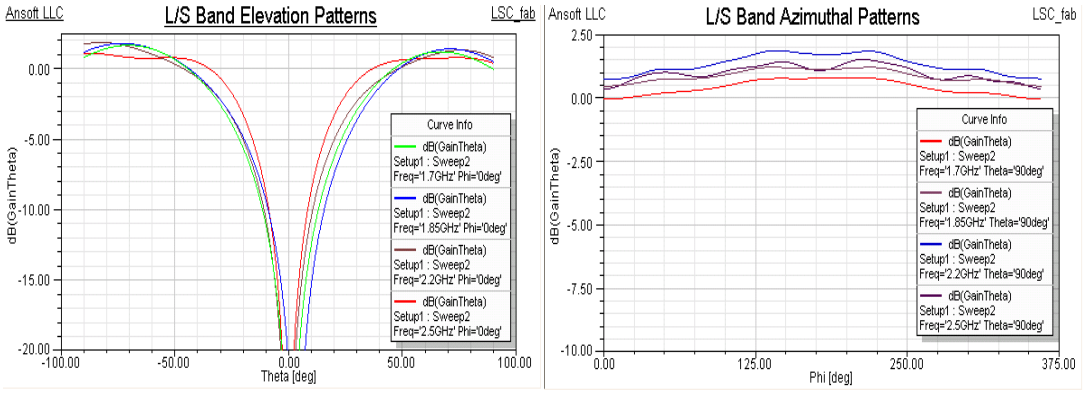

(a) **(b)**

Fig 7. Simulated L/S band (a) Elevation and (b) Azimuthal Gain Patterns

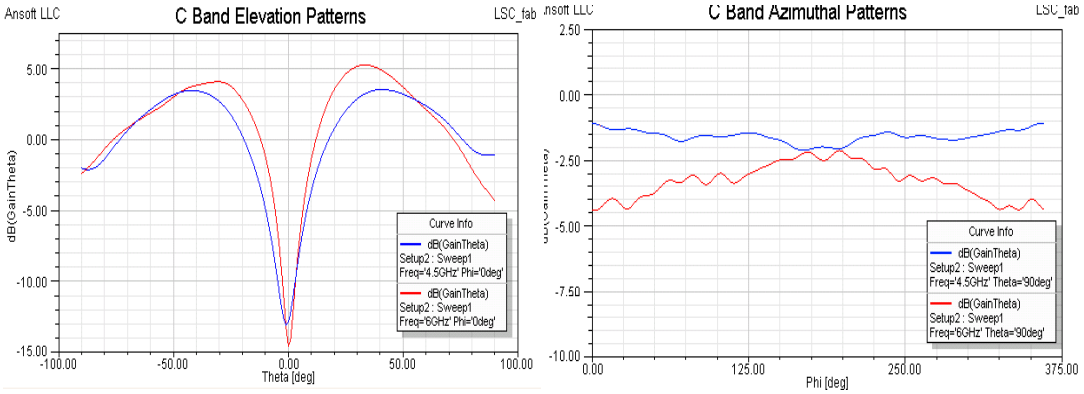

(a) **(b)**

Fig 8. Simulated C band (a) Elevation and (b) Azimuthal Gain Patterns

One complication of stacking the antennas in this manner is that the multiple ground planes can scatter the fields and distort the radiation patterns of the higher frequency antennas. In this design, the L, S, and C band patterns are relatively unaffected, but the

Ku pattern is distorted because the C band ground plane extends into its field of view and becomes a scatterer. The result is a -5dB null in the Ku pattern, as seen in Figure 10.

To alleviate this issue, a high impedance surface can be added to the C band ground plane, as shown in Figure 9. This high impedance surface is constructed by thickening the ground plane and cutting circumferential grooves a quarter-wave deep (0.2" at Ku band). Of course lower profile high impedance surfaces could also be used to reduce total height. With this adjustment, the Ku band reflected phase of the C band ground was altered enough to significantly reduce the destructive interference and mitigate the null in the Ku band elevation pattern. The Ku band patterns with and without the high impedance surface are plotted in Figure 10.

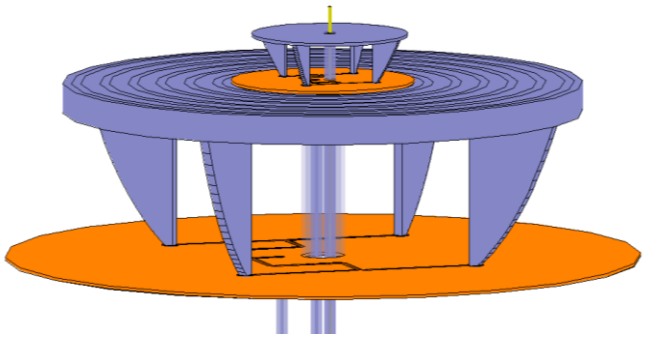

Fig 9. Stacked Antenna with High Impedance Surface for Improved Ku Band Coverage

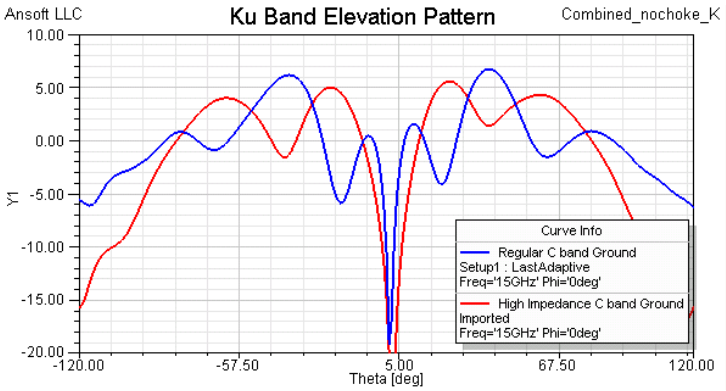

Fig 10. Simulated Elevation Gain patterns for the Ku band monopole with and without the High Impedance surface on the C band ground plane

An advantage of separating each band into its own aperture (vs. a single UWB element), is that the antenna itself provides isolation between bands, removing the need for a diplexer and easing the requirements of the front end filtering of each band. The isolation between each aperture is plotted in Figure 11.

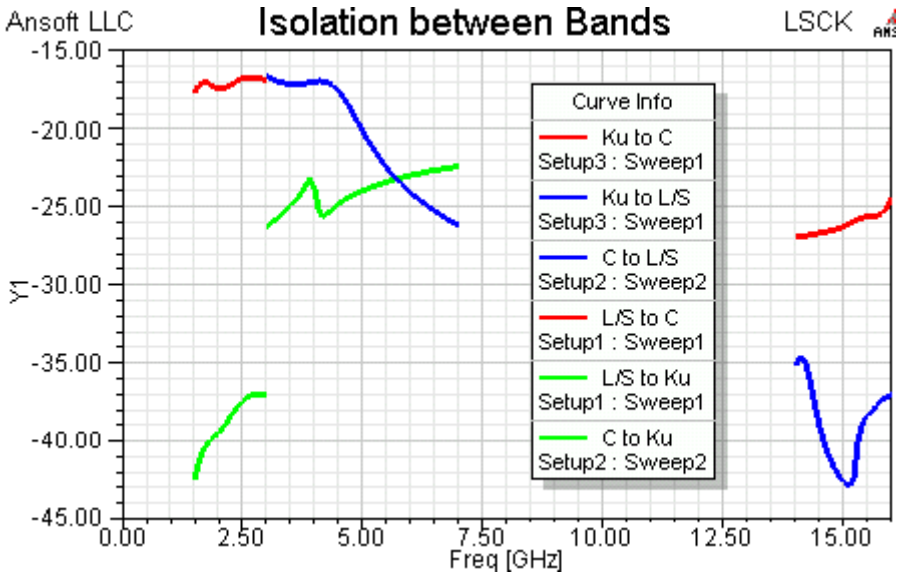

Fig 11. Simulated Isolation between Apertures

3.0 Initial Antenna Prototype Measurements

A prototype of the stacked multiband antenna was built and tested and is shown in Figure 12. Because of a change in the design of the radio, the Ku band aperture was not included in the final design. The measured return loss of the antenna over L, S, and C band is plotted in Figure 13, and the measured antenna gain is plotted in Figure 14. The antennas are matched with VSWR <2:1 over the bands of interest and the patterns are effectively monopole-like, with very good agreement between measurement and simulation.

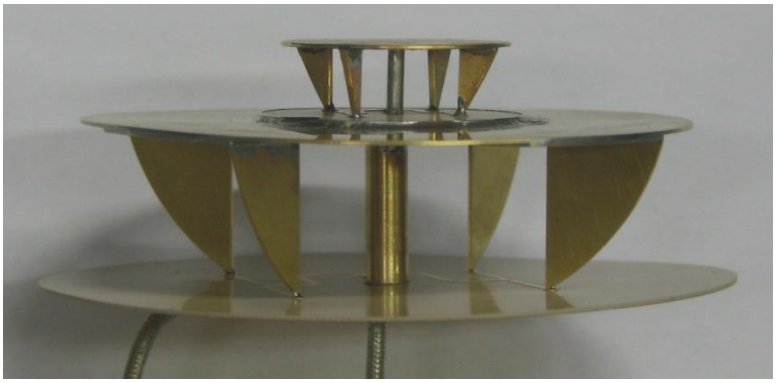

Fig 12. Stacked Multiband Antenna Prototype

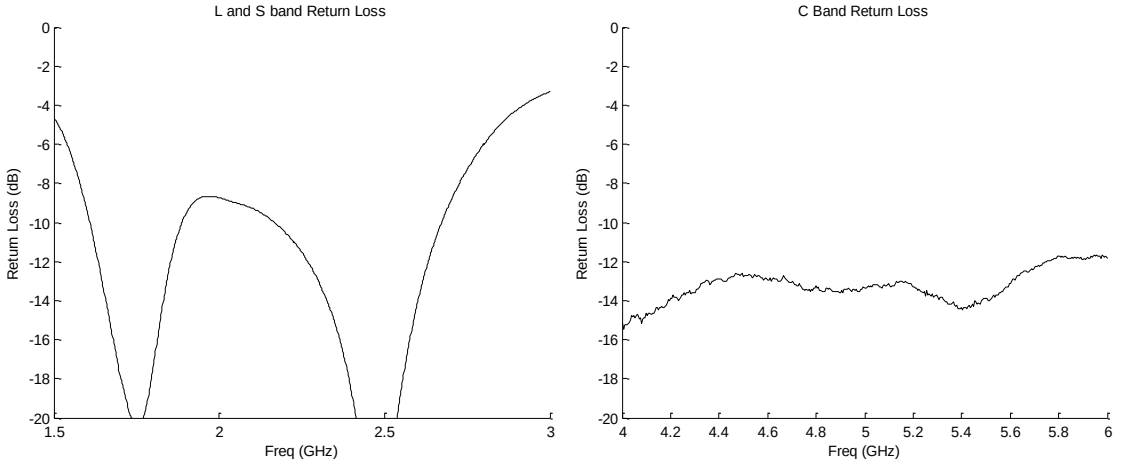

(a) **(b)**

Fig 13. Measured Return Loss of (a) L/S band layer and (b) C band layer

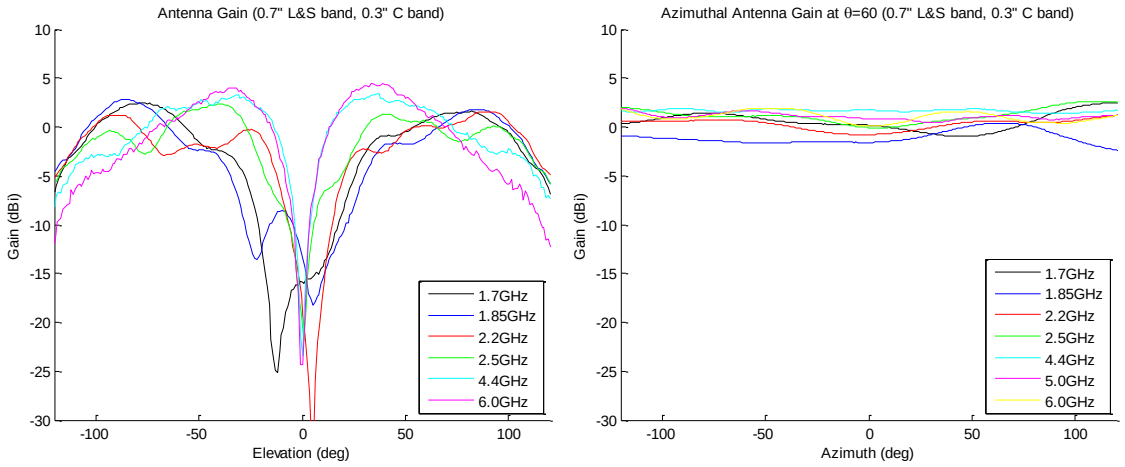

(a) **(b)**

Fig 14. Measured Antenna Gain patterns of L, S, and C bands (a) Elevation Pattern (b) Azimuthal Pattern

3.1 Design Modifications for Improved Manufacturability

As part of system level tradeoffs of the overall radio, it was recognized that the L and S bands had excess link margin because for the same range, there is less path loss vs. the C band link. It was decided that the overall height of the antenna could be reduced at the expense of L and S band realized gain. Figure 15 shows the measured gain of the antenna with a 0.3" tall L/S band layer and 0.3" tall C band layer. Comparing with Figure 14, it can be seen that the L and S band gain has been reduced by several dB while the antenna height was reduced by 0.4". This was determined to be an advantageous tradeoff for the radio system.

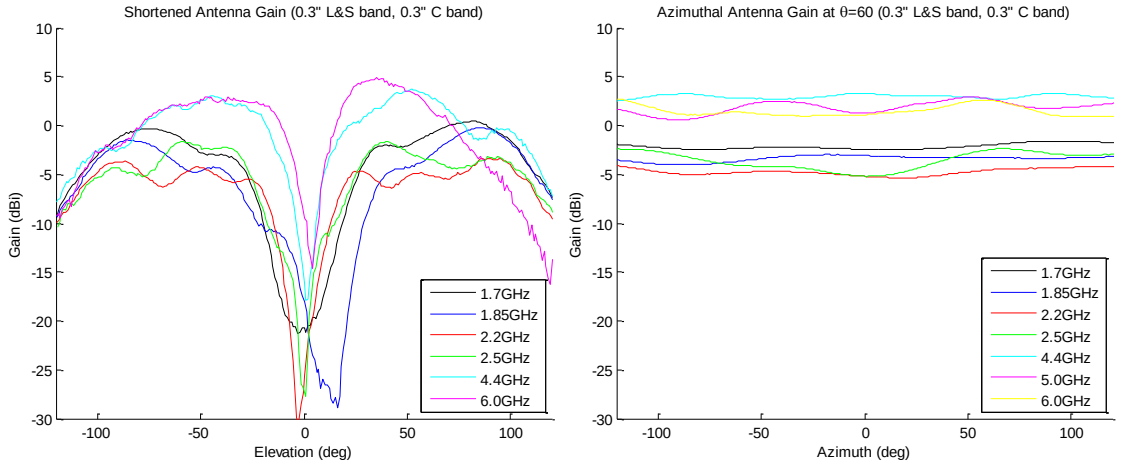

(a) **(b)**

Fig 15. Measured Antenna Gain of Final Stacked Multiband Antenna with 0.3" tall L/S band layer (a) Elevation Pattern (b) Azimuthal Pattern

The working prototype design had multiple components and required considerable time and care to properly assemble. Each radiating element was aligned by hand and soldered to the microstip feeds and conductive disks. The center posts and conduits were also hand positioned and soldered into place. Several modifications were created to improve the ease of manufacture of the antenna. Figure 16 shows the L/S band layer design features that will be discussed further in the next several paragraphs.

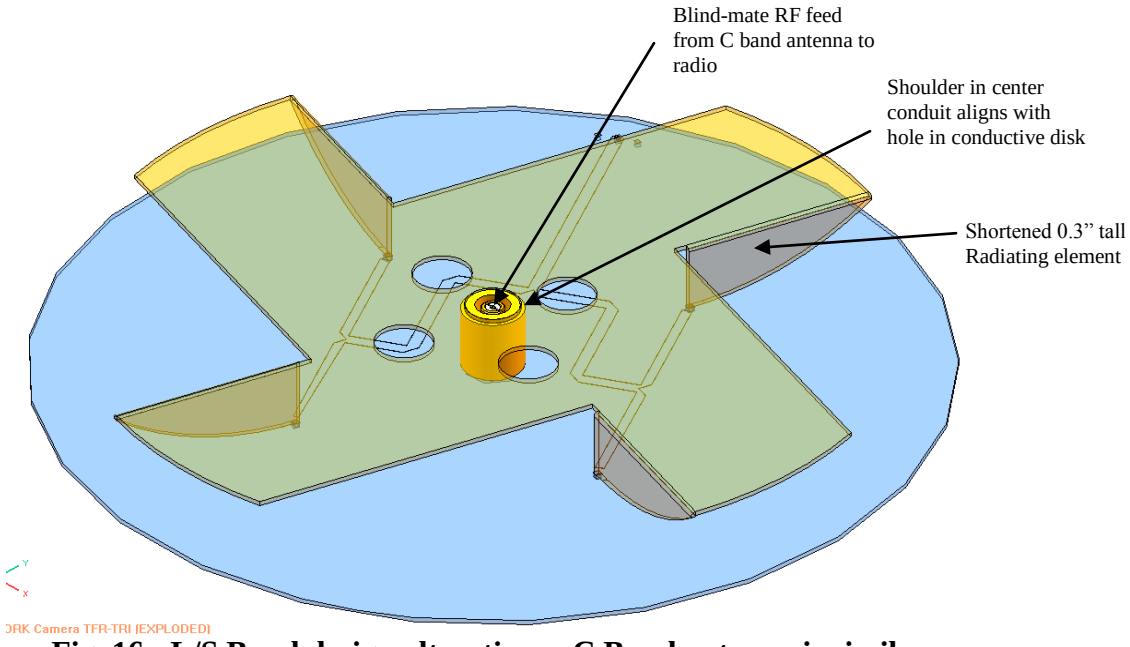

Fig. 16: L/S Band design alterations. C Band antenna is similar

The most influential design change was to combine the radiating elements with the upper conductive disk into one part. This was accomplished by using a chemical etching process to create the profile, then bending the elements down at a 90 degree angle from the conductive disk. This created a 'pinwheel' appearance in the part. The altered design was tested in the lab and found to have minimal impact to the antenna performance. Alignment tabs on the ends of the elements aligned the component to the microstrip feeds to aid the soldering process.

To ease assembly of the center conduits, alignment shoulders were created on each end that fit into corresponding holes in the conductive disks and circuit boards. This fixtured the parts in place and improved the ease of soldering the parts together.

In order to maintain a low profile for integration into the radio electronics, the rigid coax cable feed through the center conduit of the L/S band aperture needed to be replaced. This was accomplished by using blind-mate RF connectors and adaptors. This eliminated the need for cabling and the room necessary for bend radius clearance of the cable.

Figure 17 shows the final antenna assembly. The quantity of parts was reduced from 14 pieces to 6, and the ease of assembly was considerably improved.

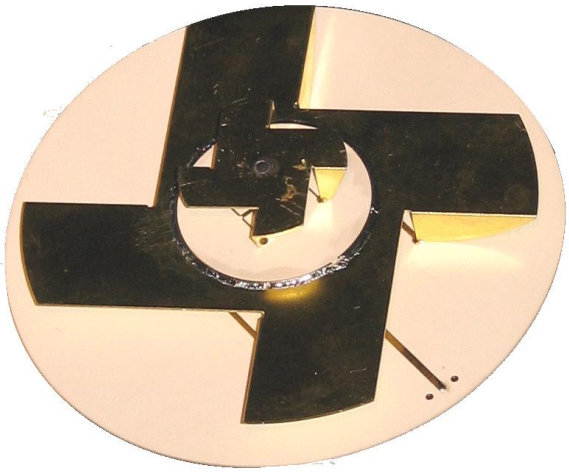

Fig 17. Final Stacked Multiband Antenna used in L/S/C Band Radio

4.0 Conclusion

The stackable antenna design provides an efficient manner of combining multiple apertures into a single low profile antenna with a small footprint. Compared to the common practice of stacking biconical antennas, this novel antenna concept affords significant height reduction while improving feed efficiency. Several manufacturing

concepts are presented which simplify the antenna construction for a production environment.

A specific design covering L, S, C, and Ku bands is presented, with good agreement between measurement and simulation. This antenna is integrated with a small handheld multiband radio, which is housed directly underneath it. The overall radio system was able meet the size, weight and volume requirements because all of the required bands were integrated into a single compact, low profile multiband antenna.

After this work was completed, the authors became aware of the Goubau Multielement Monopole [3], which is a very similar design using an array of 4 top loaded monopoles to achieve a low profile and wide bandwidth. Although the original Goubau antenna uses segmented disks above the monopoles, later modifications use a solid upper ground plane [4,5]. This antenna has the same electrical height as the stackable monopole array described in this paper (~λ/10) but demonstrates a superior 2:1 VSWR bandwidth of one octave (2:1). Because of the large upper conducting disk and grounding posts, this antenna ought to be able to be stacked for multiband operation in the manner described above. Analysis and design of such a configuration are recommended for further work.

5.0 References

[1] D.D. Button, W.D. Wyatt, J.F. McGrath, "Stacked Biconical Omnidirectional Antenna" U.S. *Patent 5,534,880,* Jul. 1996

[2] J.P. Doane, L.M. Paulsen, "A Ku Band Parasitic Array for Data Link Systems", *34th Allerton Antenna Symposium,* Sept 2010

[3] G. Goubau, "Multi-element monopole antennas" *Proc. ECOM-ARO Workshop on Electrically Small Antennas,* Ft. Monmout, NJ, May 1976, pp. 63-67

[4] C.H. Friedman, "Wide Band Matching of a Small Disk-Loaded Monopole", *IEEE Trans. Antennas Prop*, vol. 33, no. 10, Oct. 1985, pp. 1142-1148

[5] C.B. Ravipati, C.J. Reddy, "Low Profile disc and Sleeve Loaded Monopole Antenna," *Proc IEEE Antennas & Prop Soc. Int. Symp.*, vol 2A, 2005, pp. 160

Self-Supporting Coaxial Antenna with an Integrated Balun and a Linear Array Thereof

Vishwanath Iyer, Andrew Cavanaugh, Sergey N. Makarov, R. J. Duckworth,
and David Cyganski
Worcester Polytechnic Institute, Worcester, MA, USA
vishiyer@wpi.edu

Abstract: A new coaxial dipole-like wideband UHF antenna is proposed and tested consisting of two wide concentric cylindrical shells. A short transmission line is used in order to accommodate an off-center probe feed, with one shell serving as a transmission line ground plane. The antenna typically has a wide bandwidth (60-90%) and maintains a very consistent pattern over the band. Its advantage is the integration with a balun. Furthermore, the feeding cable always runs within the antenna body. The last circumstance allowed us to suggest an extendable endfire array (3×1 and 5×1) of independently fed coaxial antennas in the form of a telescopic cylinder. Standard low-cost acrylic tubing and press-fit aluminum/brass cylinders have been used for this purpose. All feeding cables run within the array body, and do not disturb the array pattern. Such an array is intended for indoor geolocation purposes in the UHF band. Its major feature is the minimum crosstalk between individual radiators.
Keywords: Broadband Dipoles, Arrays, Finite arrays, Broadband arrays

1. Problem Statement and Antenna Radiator Design

A RF multicarrier indoor geolocation method [1]-[7] developed by a group of researchers at Worcester Polytechnic Institute, MA requires multiple UHF RX antenna radiators assembled in a broadside array with the following properties:

1. Omnidirectional radiation pattern over the band;
2. Low phase center variation (low time delay variation) of the radiator over the band of interest and for different azimuthal angles;
3. Built-in broadband balun;
4. Low crosstalk between individual radiators, which makes the present array different from the canonic arrays with the strong mutual coupling [8]-[11].

In view of requirements 1-3 we will not use the standard broadband dipole with a coaxial cable running out of the antenna and generally perturbing the radiation pattern. More promising is the *coaxial dipole*, for which the feeding cable is located exactly on the antenna axis and thus introduces minimum pattern distortion.

One possible candidate from the family of coaxial dipoles – see [12]-[25] – is shown in Fig. 1 [21] . This antenna does not need the external balun and has a perfect axial symmetry. It also has a reasonable bandwidth of about 40%, which is indeed higher than the bandwidth of the wire dipole, but still has room for improvement. Another potential problem with the dipole in Fig. 1 is an assembly of a number of such dipoles in an echelon array, which will require multiple cable passing through the feeding volume and the feeding metal disk of an individual dipole in Fig. 1.

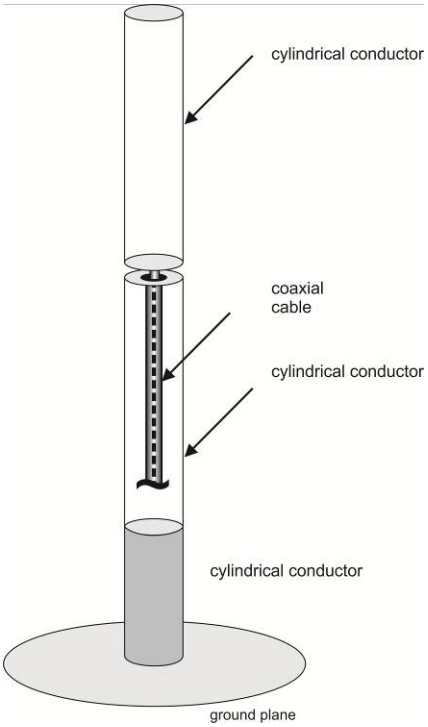

Fig. 1. Coaxial dipole from Ref. [21].

Keeping in mind this and foregoing observation we suggest a modification of the coaxial dipole (which also may be called the ribcage dipole for an obvious reason) shown in Fig. 2. This modification mostly concerns the antenna feed, which now resembles a microstrip probe feed with one wing (or cylinder) of the dipole being the ground plane. The symmetry is thus slightly distorted. However, such a distortion is expected to have a minor influence on the pattern since it only occurs in the inner volume surrounded by the metal cylinders.

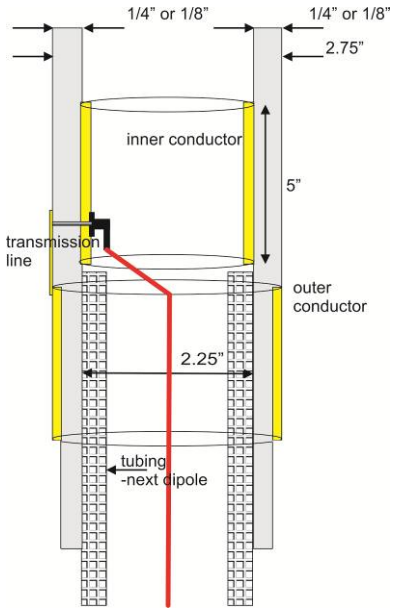

Fig. 2. Cross-section of the suggested coaxial dipole setup.

At the same time, we have created enough free space in order to run cables for other coaxial dipoles within the inner volume of the antenna. Moreover, the microstrip feed provides a great flexibility in antenna tuning and increasing the impedance bandwidth as will be shown in what follows. Similar to the coaxial antenna in Fig. 1, the antenna in Fig. 2 does not need a balun: one dipole wing plays the role of the ground plane for the microstrip feed.

Last but not least, the setup in Fig. 2 allows us to create a *telescopic* expandable dipole array as indicated in the same figure. Though the present bulky feed adapter (SMA type) limits the degree of expandability – see Fig. 2 – we believe that there is a possibility to overcome this problem.

2. Performance of a Single Radiator

2.1. Numerical simulations

Fig. 3 that follows shows critical geometry parameters of the radiator. They are the outer diameter of a dielectric cylinder (standard Plexiglas low-cost tubing from McMaster-Carr with ¼" and 1/8" wall thickness), spacing between metal cylinders, *g*, length of one metal cylinder, *L*, width of the TL, *w*, and length of the TL, *h*.

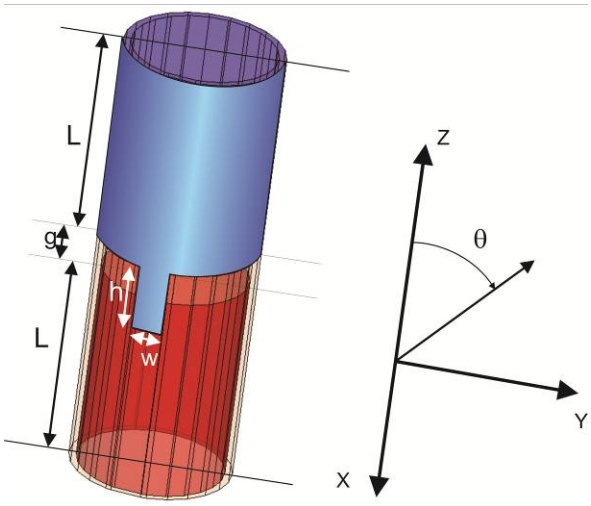

Fig. 3. Major dimensions of the coaxial radiator.

The radiator in Fig. 3 has been carefully optimized using multiple parametric sweeps in Ansoft HFSS in order to achieve maximum impedance bandwidth. The results for coaxial dipoles with different outer diameters (keeping in mind the telescopic design) and with Plexiglas wall thickness of 1/8" are given in Table 1 that follows. Similar results for ¼" thick Plexiglas dipoles are shown in Table 2.

One can see that the impedance bandwidth of 2.3:1 is routinely achieved, which is a remarkable result for simple dipole antennas. The shadowed rows in Tables 1 and 2 indicate the radiators, which may be directly used for our frequency band of interest that extends from 500 MHz to 750 MHz.

Table 1. Parameter set for thin telescopic dipoles (1/8" Plexiglas wall tubing thickness) optimized for maximum impedance bandwidth.

Outer diameter (standard)	Spacing between metal cylinders, *g*, mm	Length of one metal cylinder, *L*, mm	Width of the TL, *w*, mm	Length of the TL, *h*, mm	BW, MHz
3.00"	15	130	14.6	29	**371-701 1.9:1**
2.75"	20	140	13.3	34	**336-742 2.2:1**
2.50"	20	140	12.05	34	**337-791 2.3:1**
2.25"	15	130	10.8	29	**380-875 2.3:1**
2.00"	15	110	9.6	29	**435-982 2.3:1**
1.75"	10	100	8.4	24	**501-1090 2.2:1**
1.50"	10	90	7.2	24	**550-1140 2.1:1**

Table 2. Parameter set for thick telescopic dipoles (¼" Plexiglas wall tubing thickness) optimized for maximum impedance bandwidth.

Outer diameter (standard)	Spacing between metal cylinders, *g*, mm	Length of one metal cylinder, *L*, mm	Width of the TL, *w*, mm	Length of the TL, *h*, mm	BW, MHz
3"	25	180	20	29	**263-615 2.3:1**
2.75"	25	140	20	29	**336-690 2.1:1**
2.50"	25	150	20	29	**307-728 2.4:1**
2.25"	15	140	20	29	**353-761 2.2:1**
1.75"	15	110	20	29	**436-920 2.1:1**

The next point of interest is the radiation pattern. As a sample result, Fig. 4 presents the radiation patterns of the 1.75" dipole with the Plexiglas wall thickness of 1/8" in the H- and E-planes, respectively. Dipole parameters are those from the second last row in Table. 1. One could mention a nearly omnidirectional pattern, the shape of which is slightly distorted when frequency varies. It is interesting to note that largest pattern variations with frequency appear in the direction opposite to the antenna feed.

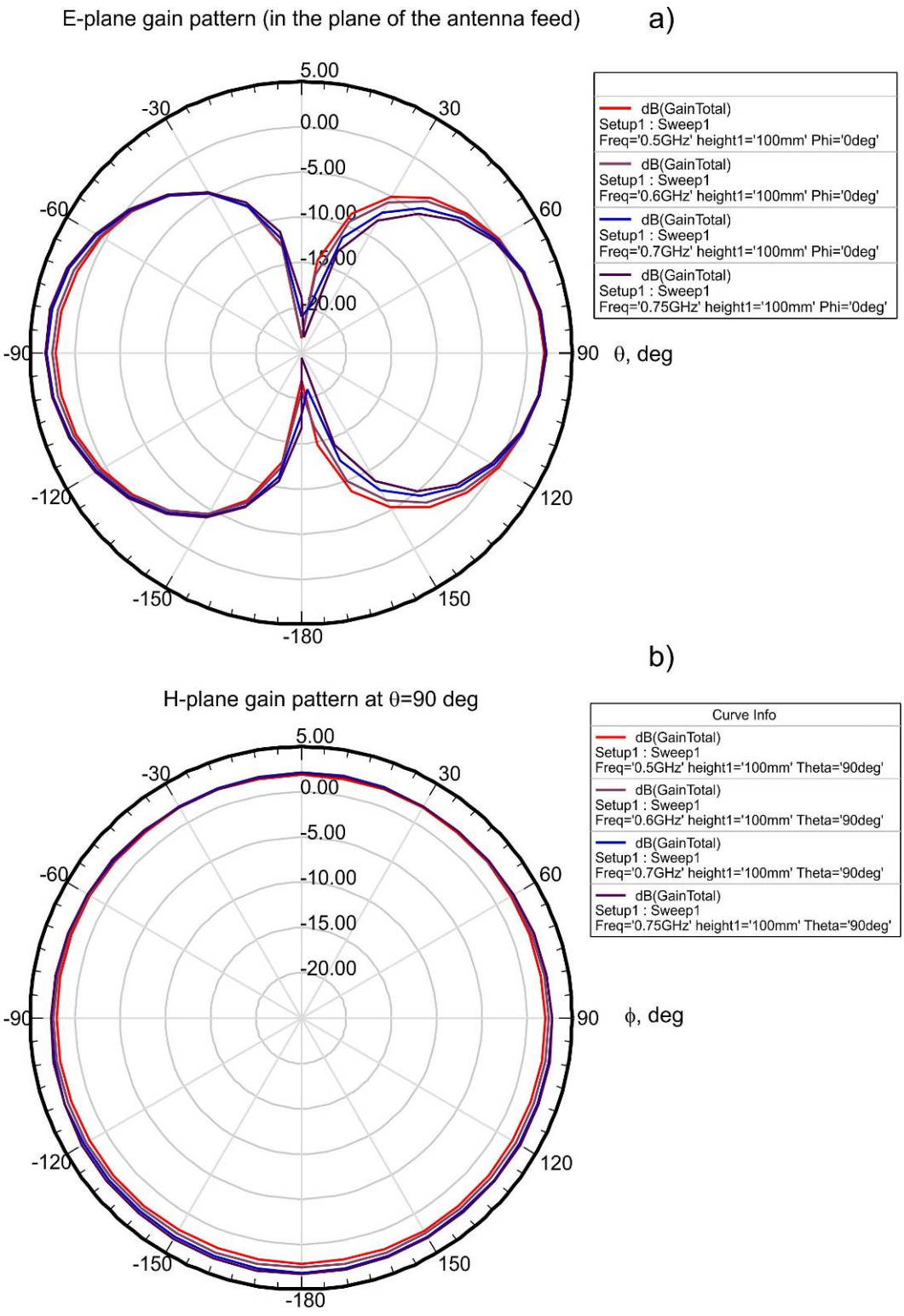

Fig. 4. E- and H-plane patterns at different frequencies within the band 500-750 MHz for the 1.75" dipole with the Plexiglas wall thickness of 1/8" – see the second last row in Table 1. Largest pattern variations with frequency occur on the side that is opposite to the antenna feed.

2.2. Experiment

Fig. 5 shows one sample antenna – the 1.75" dipole with the Plexiglas wall thickness of 1/8". Its parameters are those from the second last row in Table. 1. Fig. 6 gives the measured reflection coefficient versus the simulated reflection coefficient curve in dB. The agreement between two sets of data is acceptable keeping in mind a possible deviation of the generic relative dielectric constant of Plexiglas (3.4) in Ansoft HFSS from the real value.

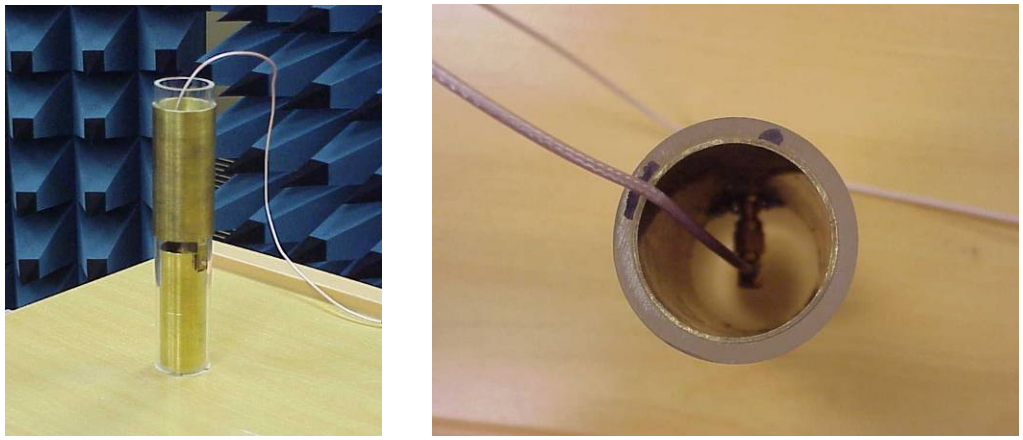

Fig. 5. 1.75" dipole with the Plexiglas wall thickness of 1/8" – see second last row of Table. 1.

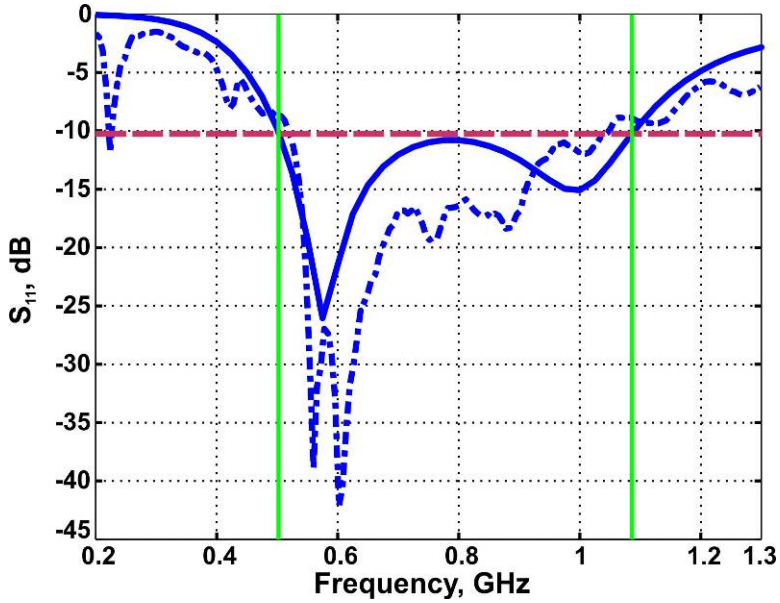

Fig. 6. Measured (dashed) versus simulated (solid) reflection coefficient for a 1.75" dipole with the Plexiglas wall thickness of 1/8".

3. Phase Center

3.1. Phase center of a dipole antenna

The phase center of an antenna is the local center of curvature of the far-field phase front – in other words, it is the center of a sphere that is tangent to the far-field phase front for a given observation angle. In general an antenna phase center *location* can vary with the elevation angle

and frequency of operation, and its dynamics are critical for high-precision GPS applications [26]. We note that:

1. For an ideal dipole antenna *without* ground plane, the phase front is angle-independent and frequency-independent. The phase center coincides with the physical center of the antenna at all frequencies.
2. For a dipole (and any other antenna) *with an infinite reflector* the phase center is the center of the reflector ground plane, for any frequency and for any dipole height. In other words, it is located exactly in the middle between the dipole and its image.
3. When the ground plane is of finite size or just small, the phase center is expected to be located somewhere between the ground plane and the dipole, since the effect of the ground plane is less profound. It is also expected to have an angular dependence, especially at low elevation angles.
4. When the dipole does not have the ground plane, but is not symmetric, a phase center variation with angle and frequency is expected again. This is also valid for the present antenna, indeed.

3.2. Effect of phase center variation on time delay variation

A dipole oriented along the z-axis radiates at the distance R a diverging spherical wave of the form (in spherical co-ordinates R,φ,θ - see Fig. 3)

$$E_\theta = \frac{E_0(\theta)}{R}\cos(\omega t - kR + \psi) \tag{1}$$

with the local phase

$$\angle E_\theta = -kR + \psi = \psi - \frac{\omega}{c_0}R \quad [\text{rad}] \tag{2}$$

where ψ is the initial phase shift. We will assume $\psi = 0$ for any angular frequency ω for simplicity. A *time delay between two harmonic signals* ω_U, ω_L is important for the present geolocation method. Such a delay is defined in the form

$$d(\varphi,\theta) \equiv \frac{\angle E_\theta\big|_{f_L} - \angle E_\theta\big|_{f_U}}{\omega_U - \omega_L} \quad [\text{sec}] \tag{3}$$

When the phase center does not vary with frequency/angle, Eq. (3) predicts the obvious dependence

$$d(\varphi,\theta) = d_0 = \frac{R}{c_0} \tag{4}$$

However, when the phase center moves, $d(\varphi,\theta)$ will be a function of φ,θ and ω_U, ω_L. Our goal is to estimate the resulting *time delay variation*,

$$\Delta d(\varphi,\theta) \equiv d_0 - d(\varphi,\theta) \quad [\text{sec}] \tag{5}$$

about d_0 as a function of the radiation direction and over the band of interest. More specifically, we are only interested in the estimate for the maximum possible swing, ΔD, of $\Delta d(\varphi,\theta)$ about zero.

3.3. Time delay variation from Ansoft HFSS simulations

Ansoft HFSS provides a convenient way to estimate the time delay variation. The starting point is the plot of the phase of E_θ in the far field at ω_U, ω_L, respectively, as a function of the polar angle. One such plot is shown in Fig. 7 in the H-plane ($\theta = 90°$). Further, we either export data to MATLAB or use the Ansoft Field Calculator. Since d_0 typically remains unknown, the maximum possible swing ΔD of $\Delta d(\varphi,\theta)$ about zero is found in the equivalent form using the original Ansoft HFSS data from Fig. 7:

$$\Delta D(\theta) = \max_\varphi\big(d(\varphi,\theta)\big) - \min_\varphi\big(d(\varphi,\theta)\big) \quad [\text{sec}] \tag{6}$$

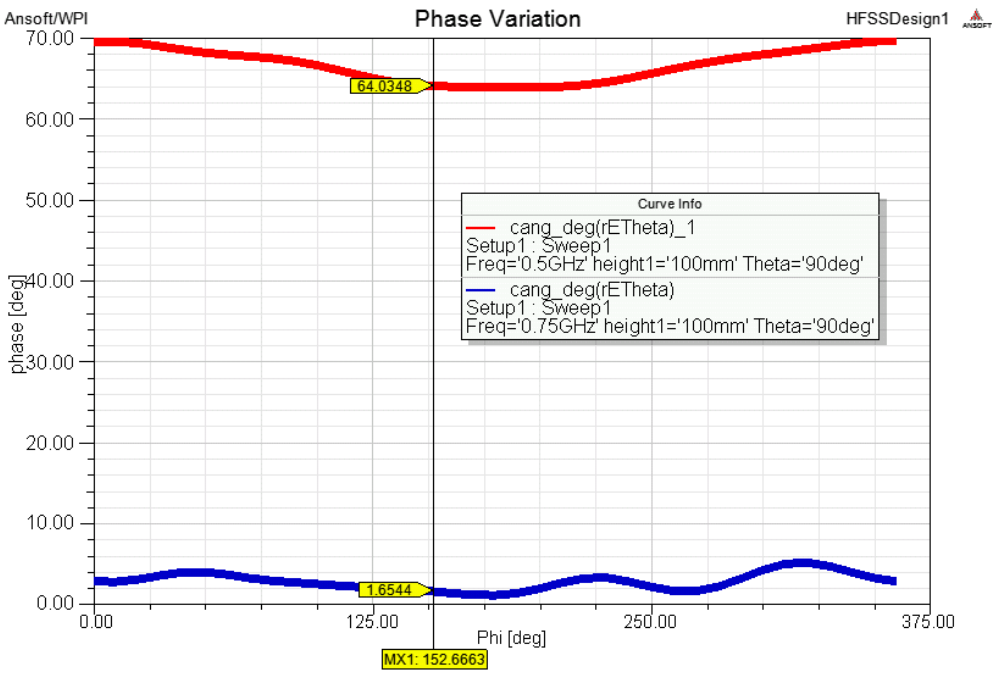

Fig. 7. Phase of the radiated field for the 1.75" thin-walled dipole in the H-plane ($\theta = 90°$) for lower and upper band frequencies of 500 MHz and 750 MHz, respectively. The difference between two phases is approximately the same; its variation is of note.

In MATLAB, the script that accomplishes the task reads

```
clear all
a = csvread('thick_250_30.csv');
angle         = a(:, 1);
phase_omegaL  = a(:, 2);
phase_omegaU  = a(:, 3);
```

```
plot(angle, phase_omegaL, 'r');
hold on; grid on;
plot(angle, phase_omegaU, 'b');

delta_d = max(phase_omegaL-phase_omegaU) - min(phase_omegaL-phase_omegaU)
delta_d = pi*delta_d/180/(2*pi*(750e6-500e6))
delta_d = delta_d*1e12   % in ps
```

Table 3 that follows is the extension of Table 1 for thin dipoles by the time delay data found according to Eq. (6). Similarly, Table 4 that follows is the extension of Table 2 by the time delay data found according to Eq. (6). For all shadowed rows, the time delay swing does exceed 160ps, over all azimuthal angles changing from 90 degrees (horizontal plane) to 30 deg (from zenith). This information is important for the subsequent geolocation algorithm.

Table 3. Complete parameter set for thin telescopic dipoles (1/8" Plexiglas wall tubing thickness).

Outer diameter (standard)	Spacing between metal cylinders, g, mm	Length of one metal cylinder, L, mm	Width of the TL, w, mm	Length of the TL, h, mm	BW, MHz	Maximum time delay swing, ΔD, over the band of interest (500-750 MHz) in ps
3.00"	15	130	14.6	29	**371-701**	**187.9ps for** $\theta = 90°$ **75.5ps for** $\theta = 60°$ **1088.6ps for** $\theta = 30°$
2.75"	20	140	13.3	34	**336-742**	**138.9ps for** $\theta = 90°$ **37.4ps for** $\theta = 60°$ **76.4ps for** $\theta = 30°$
2.50"	20	140	12.05	34	**337-791**	**107.4ps for** $\theta = 90°$ **23.7ps for** $\theta = 60°$ **42.6ps for** $\theta = 30°$
2.25"	15	130	10.8	29	**380-875**	**89.8ps for** $\theta = 90°$ **60.1ps for** $\theta = 60°$ **160.0ps for** $\theta = 30°$
2.00"	15	110	9.6	29	**435-982**	**70.0ps for** $\theta = 90°$ **51.1ps for** $\theta = 60°$ **38.9ps for** $\theta = 30°$
1.75"	10	100	8.4	24	**501-1090**	**65.5ps for** $\theta = 90°$ **46.0ps for** $\theta = 60°$ **78.4ps for** $\theta = 30°$
1.50"	10	90	7.2	24	**550-1140**	**51.7ps for** $\theta = 90°$ **37.4ps for** $\theta = 60°$ **51.8ps for** $\theta = 30°$

Table 4. Complete parameter set for thick telescopic dipoles (1/4" Plexiglas wall tubing thickness).

Outer diameter (standard)	Spacing between metal cylinders, g, mm	Length of one metal cylinder, L, mm	Width of the TL, w, mm	Length of the TL, h, mm	BW, MHz	Maximum time delay swing, ΔD, over the band of interest (500-750 MHz)
3"	25	180	20	29	**263-615 2.3:1**	**Not in the band**
2.75"	25	140	20	29	**336-690 2.1:1**	**Not in the band**
2.50"	25	150	20	29	**307-728 2.4:1**	**128.1ps for** $\theta = 90°$ **23.7ps for** $\theta = 60°$ **46.3ps for** $\theta = 30°$
2.25"	15	140	20	29	**353-761 2.2:1**	**117.6ps for** $\theta = 90°$ **77.6ps for** $\theta = 60°$ **92.4ps for** $\theta = 30°$
1.75"	15	110	20	29	**436-920 2.1:1**	**69.7ps for** $\theta = 90°$ **57.2ps for** $\theta = 60°$ **68.5ps for** $\theta = 30°$

4. Array Setup

4.1. Geometry

Fig. 8 that follows outlines the geometry setup for an echelon telescopic array of the coaxial dipoles designed previously. One unsolved problem is the radiator feed – see Fig. 2 – that will not yet allow the array to be collapsed into a single section.

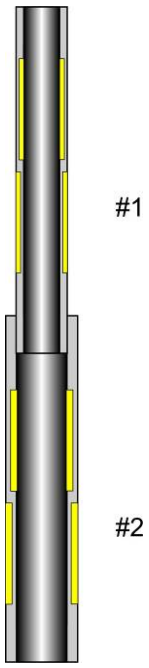

Fig. 8. Two elements of an echelon array.

The array should include five coaxial radiators and have the vertical length of about 10m. Therefore, the distance between array elements is expected to be 1-2m. The mutual coupling between the array radiators is the subject of the further investigation. For simplicity, we will only consider two neighbor radiators.

4.2. Estimate of mutual coupling

As indicated in the list of design requirements mentioned in section 1, the level of crosstalk between individual radiators of the broadside array needs to be low. Crosstalk essentially quantifies the perturbation of the currents on an individual radiator due to the presence of a neighboring identical/non-identical radiator. This is also known as mutual coupling and in the case of typical finite arrays as studied in [8]-[11], its influence is significant. Of particular importance is the physical arrangement of the radiators. It is our expectation that placing the present individual radiators 1-2 meter apart in collinear fashion should minimize crosstalk. To determine this we may study the 2x1 array of the same radiators and calculate the crosstalk as a function of frequency for the fixed distance of separation.

In [10], a possible approach for calculating the maximum coupling between a pair of radiators is suggested that is based on the equivalent 2-port network representation of the coupled system. Widely known in RF amplifier design community as the Linville method, it makes use of the Y-parameters and is suggested in [27]. Coupling calculations can also be done by using the S-parameters as suggested in [28], [29]. However, for the purposes of this study, we will utilize the Z-parameter based approach as explained in [30]-[32]. It is our hope that by doing so and later introducing a simple transfer function also based on the Z-parameters, we can gain better intuitive understanding of the problem.

Consider a pair of radiators driven by voltage source V_{g1}, V_{g2} having internal resistance R_g. This setup is shown in Fig. 9 with the radiators in a collinear arrangement and the distance of separation being d. It needs to be noted that the analysis technique does not depend on the physical arrangement of the radiators, nor do the radiators themselves need to be identical.

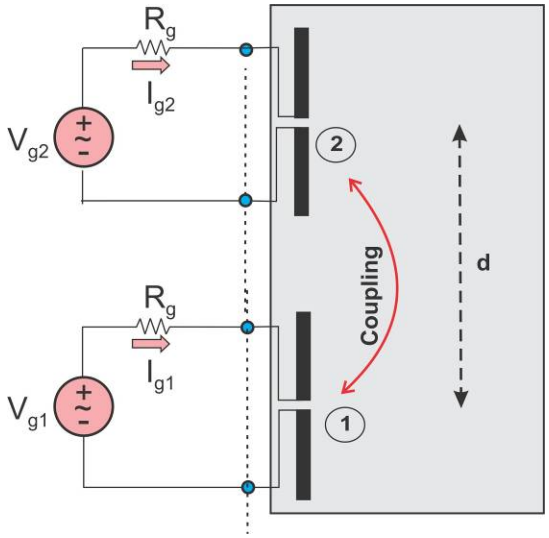

Fig. 9. A 2x1 collinear array shown with the voltage sources with internal resistance R_g. The antennas 1 and 2 are separated by a distance d.

Ultimately reducing this system to an equivalent two-port network, where all the self and mutual impedances can be captured in the Z-parameters of this system, will allow us to quantify the crosstalk [10], [30] - [34]. This reduction is shown in Fig. 10. In this figure, the voltages V_1 and V_2 are the feed point voltage of the antennas.

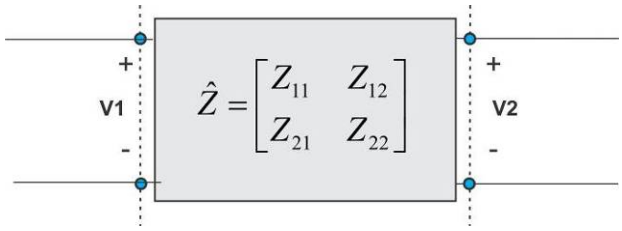

Fig. 10. The two-port equivalent Z-parameter representation of the system in Fig. 9.

As shown in [30]-[32], the complex coefficient of coupling between two antennas can be defined in terms of the equivalent Z-parameters as,

$$k = \frac{Z_{12}}{\sqrt{Z_{11} Z_{22}}} \tag{7}$$

In addition, it is mentioned in [32] that when antenna 1 is driven and open circuit condition is maintained at the second antenna, the coefficient of coupling becomes,

$$k = \frac{V_2}{V_1} \tag{8}$$

To study Eq. (7) and Eq. (8) we terminate the antenna 2 (from Fig. 9) or which is to say the port 2 of the network in Fig. 10, into a resistive load R_L. This setup is shown in Fig. 11 and follows from [10], [32], [33], wherein the *Z*-parameter description of the coupled antenna system is replaced with an equivalent T-network representation.

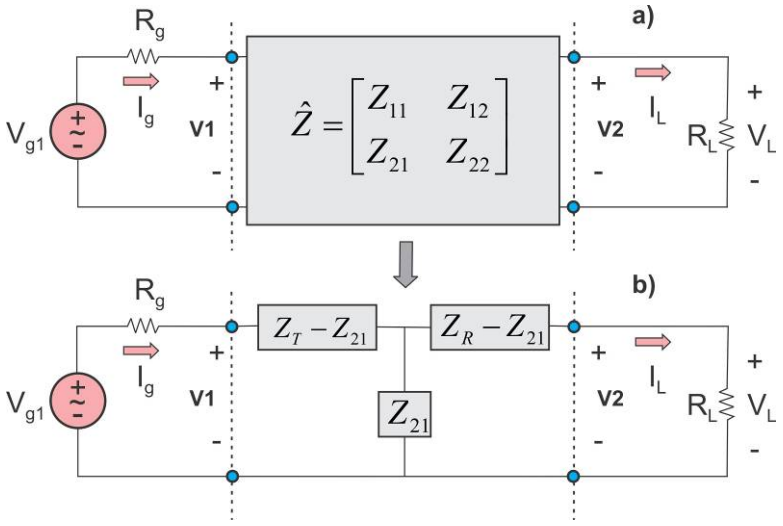

Fig. 11. Transformation of Z-parameters of the coupled antenna system into a T-network description with port 1 (antenna 1) being driven by voltage source V_{g1}, and port 2 (antenna 2) terminated into a resistive load R_L.

In Fig. 11, the impedance $Z_T = Z_{11}$ and $Z_R = Z_{22}$. By using circuit analysis techniques, we can derive the voltage transfer function as [33],

$$\frac{V_L(\omega)}{V_{g1}(\omega)} = \frac{R_L Z_{21}}{(Z_R + R_L)(Z_T + R_g) - Z_{21}Z_{21}} \tag{9}$$

While the voltage transfer function is an important quantity, the coefficient of coupling as defined in Eq. (8) requires that we calculate V_2/V_1. To do so we argue that,

$$\frac{V_L(\omega)}{V_1(\omega)} \approx \frac{V_2(\omega)}{V_1(\omega)} \text{ when, } R_L \to \infty \tag{10}$$

Therefore we calculate,

$$\frac{V_L(\omega)}{V_{g1}(\omega)} \times \frac{V_{g1}(\omega)}{V_1(\omega)} = \frac{V_L(\omega)}{V_1(\omega)} = \frac{R_L Z_{21}}{(Z_R + R_L)(Z_T + R_g) - Z_{21}Z_{21}} \times \frac{Z_{eq} + R_g}{Z_{eq}} \tag{11}$$

Here, $Z_{eq} = \left[\left(Z_R - Z_{21} + R_L\right) \| \, Z_{21}\right] + Z_T - Z_{21}$.

4.3. Results

To extract the Z-parameters, we simulated the 2x1 collinear array in Ansoft HFSS. The antennas were placed 1 meter apart (feed to feed) as shown in Fig. 8 and were excited using the lumped port. The PML (Perfectly Matched Layer) was used in the Ansoft HFSS simulations and the resulting mesh had a large number of tetrahedral (about 100,000) and a good solution convergence. The resulting Z-parameter matrix for the frequency band 500 - 750 MHz was exported from Ansoft HFSS and post processing was done in MATLAB. The first experiment we consider implies a load resistance of $R_L = 50\Omega$ connected to the feed terminals of antenna 2 while antenna 1 is driven by a 50Ω source ($V_{g1} = 1\,\text{V}$). The result of Eq. (7) and Eq.(11) are plotted in Fig. 12.

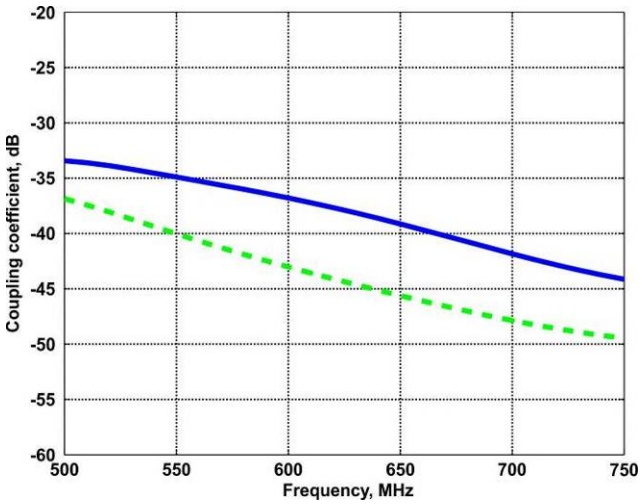

Fig. 12. Solid blue curve - theoretical coefficient of coupling from Eq. (7); dashed green curve is the result of Eq. (11).

We note the following:

i. The coupling between the antennas is less than -30 dB over the band thus ensuring a low cross talk between the antennas.
ii. The coefficient of coupling decreases with increasing frequency since the electrical separation in terms of wavelengths increases.
iii. The theoretical coefficient of coupling calculated using Eq. (7) is higher over the band as compared to that calculated by using Eq. (11), mainly because the open circuit condition is not realized at antenna 2.

Our next experiment is to illustrate the change in coupling as the load resistance is changed at antenna 2. Specifically we seek to show that as R_L increases, the coefficient of coupling curve in Fig. 12 (dashed green curve) will approach the theoretical curve (solid blue) and thereby justify Eq. (8).

Fig. 13 verifies the fact that as the load resistance increases, the coefficient of coupling tends towards the theoretical result. At $R_L = 1\,\mathrm{M}\Omega$, there is good agreement between the theoretical result from Eq. (7) and the result obtained through circuit analysis techniques in Eq. (11).

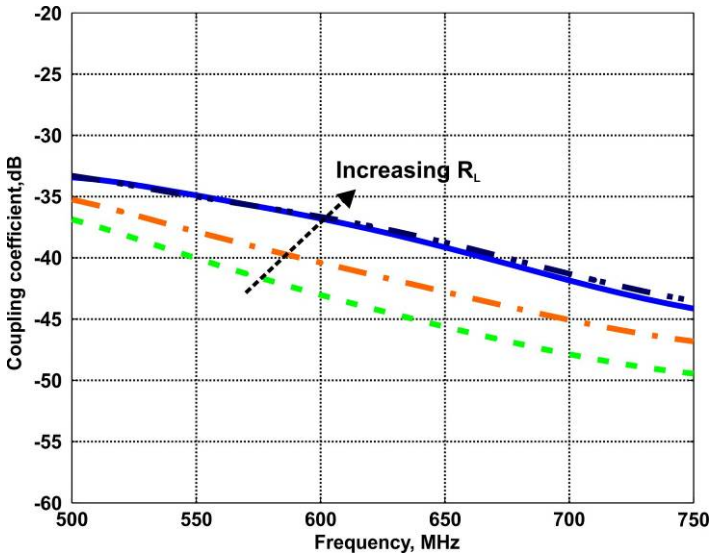

Fig. 13. Change in coefficient of coupling as the load resistance increases from 50Ω to 100Ω, and finally to $1\,\mathrm{M}\Omega$. The solid blue curve is theoretical result of Eq. (7) while the rest of the curves are generated by Eq. (11) using simulated data from Ansoft HFSS.

We also plot the voltage transfer function between the two antennas. This is shown in Fig. 14 together with the coefficient of coupling for the sake of comparison. We expect this to be lower since there is additional loss in the form of R_g present in the network. In fact the voltage transfer function can be related to the coupling coefficient, indeed under the condition that we have an ideal zero internal resistance voltage source at the input to antenna 1 and an open circuit at antenna 2 as shown in Eq. (12). Fig. 15 precisely shows the result of enforcing this condition and validates Eq. (12).

$$\frac{V_L(\omega)}{V_{g1}(\omega)} = \frac{kZ_{eq}}{\left(Z_{eq} + R_g\right)} = k \tag{12}$$

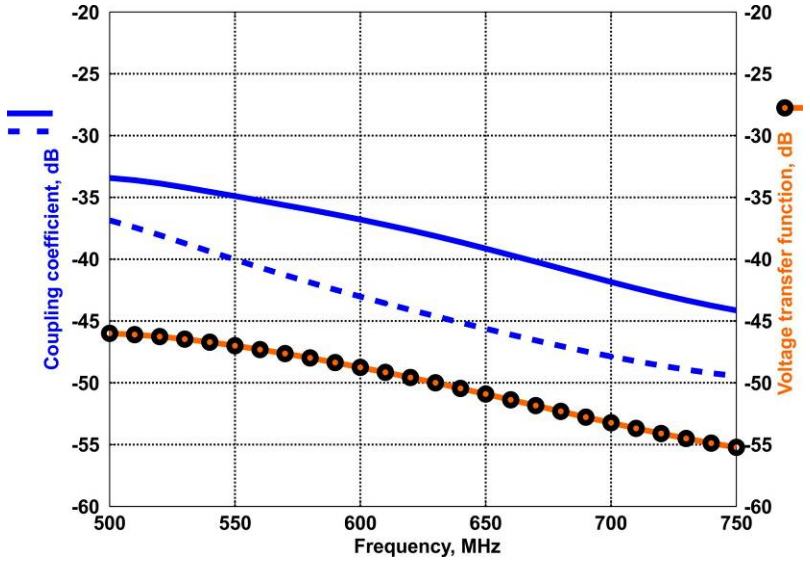

Fig. 14. Comparison between the coefficient of coupling (solid blue curve follows Eq. (7); dashed blue curve follows Eq. (11)) and the voltage transfer function for the 2x1 collinear array (circles). As before, the solid blue curve is the theoretical result calculated using Eq. (7), while the dashed blue curve is calculated using Eq. (11). The voltage transfer function is calculated using Eq. (9). The load resistance is fixed to R_L = 50Ω.

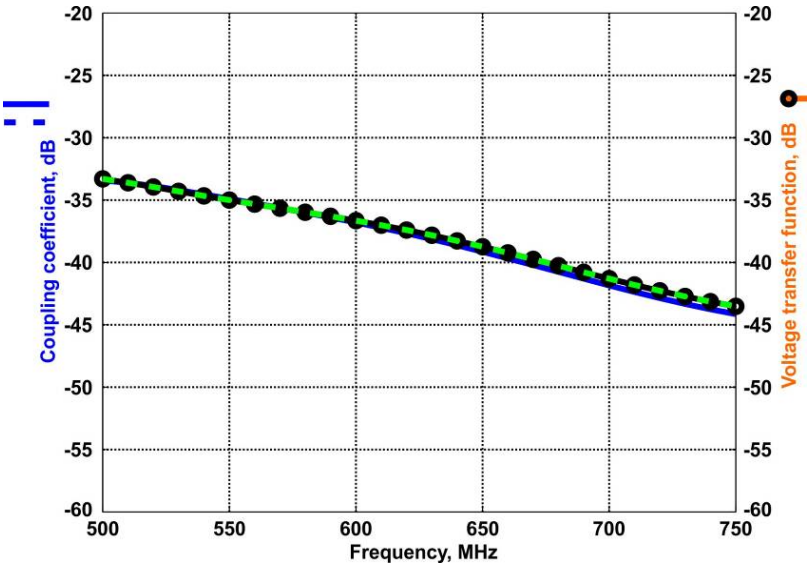

Fig. 15. Equality of the coefficient of coupling (solid blue curve and dashed blue curve) and the voltage transfer function for the 2x1 collinear array (circles). As before, the solid blue curve is the theoretical result calculated using Eq. (7), while the dashed blue curve is calculated using Eq. (11). These curves are plotted assuming that R_g = 0Ω and R_L =1MΩ, thus confirming Eq. (12).

4.4. Preliminary array assembly

Mechanical assembly of a long 5x1 echelon array is currently underway. It has met considerable difficulties. As a base we use a commercial fiberglass telescopic pole purchased from GeoData Systems Management Inc., OH. The expanded pole is 40 ft long and is mounted on a heavy-duty tripod. The major problem appears to be the antenna weight, which should be reduced to a minimum by using copper foil instead of the initial choice – brass, and possibly replacing Plexiglas tubing by a lower-weight material or reducing overall tubing length. As an example, Fig. 16 on its left shows the telescopic pole in the ECE shop with partially assembled coaxial antennas whereas the telescopic pole in its full length and in the vertical position with most of antennas removed is shown in Fig. 16 -right.

Fig. 16. Left - telescopic pole in the ECE shop with partially assembled coaxial antennas; right - telescopic pole in its full length and in the vertical position with most of antennas removed.

5. Conclusions

A new coaxial dipole-like wideband UHF antenna has been proposed and tested consisting of two wide concentric cylindrical shells. A short transmission line is used in order to accommodate an off-center probe feed, with one shell serving as a transmission line ground plane. The antenna typically has a wide bandwidth (60-90%) and maintains a very consistent pattern over the band. Its advantage is the integration with a balun.

We further suggested an extendable endfire array (3×1 and 5×1) of independently fed coaxial antennas in the form of a telescopic cylinder. Further work is being pursued toward the final array design. Authors thank Daniel D. Harty and Yi-Yu Tsai for help.

References

[1] A. Cavanaugh, M. Lowe, D. Cyganski, R. J. Duckworth, "WPI Precision Personnel Location System: Rapid Deployment Antenna System and Sensor Fusion for 3D Precision Location," *Proceedings of the 2010 International Technical Meeting of The Institute of Navigation*, pp. 214-219, San Diego, CA, Jan. 2010.

[2] B. Woodacre, D. Cyganski, R. J. Duckworth, V. Amendolare, "WPI Precision Personnel Locator System: Antenna Geometry Estimation using a Robust Multilateralization Technique," *Proceedings of the 2009 International Technical Meeting of The Institute of Navigation*, pp. 822-828, Anaheim, CA, Jan. 2009.

[3] J. Coyne, D. Cyganski, R. J. Duckworth, "FPGA-Based Co-processor for Singular Value Array Reconciliation Tomography," *16th International Symposium on Field-Programmable Custom Computing Machines,* pp.163-172, 14-15 April 2008.

[4] V. Amendolare, D. Cyganski, R. J. Duckworth, S. Makarov, J. Coyne, H. Daempfling, B. Woodacre, "WPI precision personnel locator system: Inertial navigation supplementation," *IEEE/ION Position, Location and Navigation Symposium,* pp.350-357, 5-8 May 2008.

[5] D. Cyganski, J. Duckworth, S. Makarov, W. Michalson, J. Orr, V. Amendolare, J. Coyne, H. Daempfling, J. Farmer, D. Holl, S. Kulkarni, H. Parikh, B. Woodacre, "WPI Precision Personnel Locator System," *Proceedings of the 2007 National Technical Meeting of The Institute of Navigation*, pp. 806-814, San Diego, CA, Jan. 2007.

[6] D. Cyganski, J. Duckworth, S. Makarov, W. Michalson, J. Orr, V. Amendolare, J. Coyne, H. Daempfling, S. Kulkarni, H. Parikh, B. Woodacre, "WPI Precision Personnel Locator System – Indoor Location Demonstrations and RF Design Improvements," *Proceedings of the 63rd Annual Meeting of The Institute of Navigation*, pp. 511-521, Cambridge, MA, April 2007.

[7] J. Duckworth, D. Cyganski, S. Makarov, W. Michalson, J. Orr, V. Amendolare, J. Coyne, H. Daempfling, D. Hubelbank, H. Parikh, B. Woodacre, "WPI Precision Personnel Locator System - Evaluation by First Responders," *Proceedings of the 20th International Technical Meeting of the Satellite Division of The Institute of Navigation (ION GNSS 2007)*, pp. 1427-1435, Fort Worth, TX, September 2007.

[8] R. C. Hansen, *Phased Array Antennas*, Wiley, New York, 1998, p. 222.

[9] R. C. Hansen, "Phased Arrays," in: *Antenna Engineering Handbook*, John L. Volakis, Ed., Mc Graw-Hill, 2007, fourth edition, p. 2-15.

[10] C. A. Balanis, *Antenna Theory. Analysis and Design*, Wiley, New York, 2005, third ed., p. 672-673.

[11] A. A. Oliner and R. G. Malech, "Mutual coupling in infinite scanning arrays," in *Microwave Scanning Antennas*, Vol. II, R.C. Hansen, ed., Academic Press, 1966, Chapter 3, pp. 195-335.

[12] Xiangyu Cao, K. M. Luk, Changhong Liang, Jun Gao, "Accurate analysis of cylindrical dipole arrays for base station antenna," *IEEE Antennas and Propagation Society International Symposium,* vol.3, pp. 678- 681, 22-27 June 2003.

[13] G. Dubost, "A tuneable thick folded-dipole operating in two octaves," *Antennas and Propagation Society International Symposium,* vol.13, pp. 248- 251, June 1975.

[14] C. L. Goodzeit, M. J. Ball, R. B. Meinke, "The double-helix dipole - a novel approach to accelerator magnet design," *IEEE Transactions on Applied Superconductivity,* vol.13, no.2, pp. 1365- 1368, June 2003.

[15] K. Saito, S. Hosaka, Y. Hayashi, H. Yoshimura, K. Ito, "Localized heating by the coaxial-dipole antenna for microwave coagulation therapy," *5th International Symposium on Antennas, Propagation and EM Theory*, pp.406-409, 2000.

[16] H. Miyashita, H. Ohmine, K. Nishizawa, S. Makino, S. Urasaki, "Electromagnetically coupled coaxial dipole array antenna," *IEEE Transactions on Antennas and Propagation,* vol.47, no.11, pp.1716-1726, Nov. 1999.

[17] Peng Wang, M. C. Converse, J. G. Webster, D. M. Mahvi, " "Improved" Calculation of Reflection Coefficient for Coaxial Antennas With Feed Gap Effect," *IEEE Transactions on Antennas and Propagation,* vol.57, no.2, pp.559-563, Feb. 2009.

[18] Tam Do-Nhat, R. MacPhie, "Effect of gap length on the input admittance of center fed coaxial waveguides and infinite dipoles," *IEEE Transactions on Antennas and Propagation,* vol.35, no.11, pp. 1293- 1299, Nov. 1987.

[19] C. Ozzaim, C. M. Butler, "Coupling to a probe in a metal can by an electric dipole," *IEEE Antennas and Propagation Society International Symposium,* vol.2, pp.838-841, Aug. 1999.

[20] R. Hansen, "Evaluation of the Snyder dipole," *IEEE Transactions on Antennas and Propagation,* vol.35, no.2, pp. 207- 210, Feb. 1987.

[21] K. Nishizawa, N. Yamamoto, M. Tanakar, H. Miyashita, S. Makino, "Self-supported wide-band dipole antennas with a constant gain characteristic," *IEEE Antennas and Propagation Society International Symposium,* vol.1B, pp.426-429, 2005.

[22] T. J. Judasz, B. B. Balsley, "Improved theoretical and experimental models for the coaxial collinear antenna," *IEEE Transactions on Antennas and Propagation*, vol.37, no.3, pp.289-296, Mar. 1989.

[23] H. Wheeler, "A vertical antenna made of transposed sections of coaxial cable," *IRE International Convention Record* , vol.4, pp. 160- 164, March 1956.

[24] K. Ito, "Recent Small Antennas for Medical Applications," *International Workshop on Antenna Technology: Small Antennas and Novel Metamaterials,* pp.1-4, 4-6 March 2008.

[25] M. Bailey, F. Beck, W. Croswell, "Vertically polarized stacked arrays of omnidirectional antennas," *IEEE Transactions on Antennas and Propagation,* vol.18, no.2, pp. 285- 290, March 1970.

[26] J. M. Tranquilla and B. G. Colpitts, "Development of a class of antennas for space-based NAVSTAR GPS applications," *6th Int. Conference on Antennas and Propagation, ICAP 89*, Conf. Publ., No. 301, vol. 1, pp. 65-69, April 1989.

[27] D.Rubin, The Linville Method of High Frequency Transistor Amplifier Design, Naval Weapons Center, NWCCL TP 845, Coronal Labs., Corona, CA, March 1969.

[28] J. -P. Daniel, "Mutual coupling between antennas for emission or reception--Application to passive and active dipoles," *IEEE Transactions on Antennas and Propagation*, vol.22, no.2, pp. 347- 349, Mar 1974.

[29] E. Saenz, I. Ederra, R. Gonzalo, S. Pivnenko, O. Breinbjerg, P. de Maagt, "Coupling Reduction Between Dipole Antenna Elements by Using a Planar Meta-Surface," *IEEE Transactions on Antennas and Propagation*, vol.57, no.2, pp.383-394, Feb. 2009.

[30] R. King, "Coupled Antennas and Transmission Lines," *Proceedings of the IRE*, vol.31, no.11, pp. 626- 640, Nov. 1943.

[31] E. A. Blasi, "The Theory and Application of the Radiation Mutual-Coupling Factor," *Proceedings of the IRE*, vol.42, no.7, pp.1179-1183, July 1954.

[32] J. Dyson, "The coupling and mutual impedance between conical log-spiral antennas in simple arrays," *IRE International Convention Record* , vol.10, pp. 165- 182, March 1962.

[33] D. M. Pozar, *Microwave Engineering*, Wiley, New York, 2005, 3rd ed.

[34] S. Makarov, U. Khan, M. Islam, R. Ludwig and K. Pahlavan "On Accuracy of Simple FDTD Models for the Simulation of Human Body Path Loss" in the *29th IEEE International Performance Computing and Communications Conference*, 2010.

Fabrication and Performance of Broadband, Waveguide-to-Stripline Transition for Phased Arrays

Michael J. Buckley, Wajih Elsallal, Brian J. Herting,
John Mather, Jeremiah Wolf, James West

Advanced Technology Center
Rockwell Collins, Inc.
400 Collins Rd. NE. M/S: 108-102
Cedar Rapids, IA 52498

***Abstract* – A novel aperture coupled stripline-to-waveguide (SL/WG) transition is designed using two metamaterial layers. The SL/WG transition has a 28% bandwidth at Ku-band with a VSWR < 1.22. The total thickness of the transition is less than 150 mils. The SL/WG metamaterial transition is compared to a SL/WG transition with one of the metamaterial layers replaced with a patch transducer. A Floquet mode analysis is done on the two SL/WG transitions in order to understand the effects of the metamaterial layers. Floquet mode analysis of the two SL/WG transitions shows that the metamaterial structure scatters the incident Floquet mode into higher order Floquet modes than the SL/WG patch transition. The higher order Floquet modes present in the metamaterial SL/WG transition minimize reflections over a broader bandwidth than lower Floquet modes present in the patch SL/WG transition.**

Key Words: broadband metamaterial, Floquet modes, waveguide to stripline transition.

1. Introduction

Parabolic reflector antennas are currently used as high directivity antennas for Satellite Communication (SatCom) systems. Major drawbacks of the reflector antennas are large size, lengthy setup time, and weight. There is an increased demand for man-portable, high-gain and high-efficiency terminals to replace the parabolic dishes with flat panel array technology; see figure 1. Our flat panel array terminal includes a printed circuit board aperture of meta-material enabled phased array (MEPPA), novel stripe-to-waveguide transition, and two combiners of stripline and waveguide feeds. The total thickness of the entire stack-up is less than 1″.

[a]

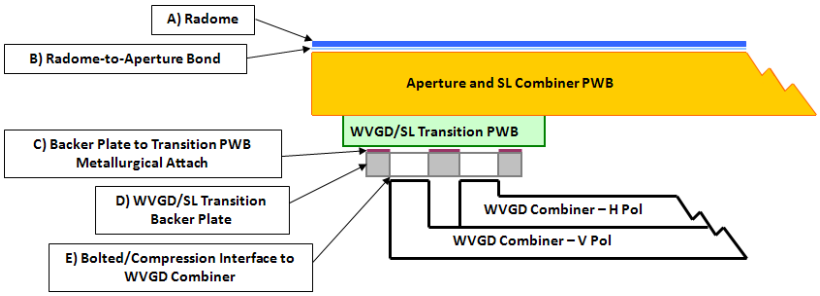

[b]

Figure 1 Evolution to flat panel SatCom apertures. [a] Flat panel aperture replacement for the parabolic dish enables low-profile man-portable suitcase. [b] Stack-up of the proposed flat panel technology.

The MEPPA aperture design and performance is discussed in reference [1]. In this paper, a simple, innovative and efficient solution for the stripline-to-waveguide (SL/WG) transition is discussed.

In the open literature, several SL/WG transitions for phased arrays were introduced [2] – [7]. The major aspects limiting the use of those design concepts for our system are as follows:

- The need to operate over a 28% bandwidth at Ku-band, with low insertion loss.
- The SL/WG transition must be compact such that the entire stack-up of the flat panel aperture is less than 1″, figure 1.
- The design must be easy to fabricate. Hence, a probe-fed waveguide is not possible for an array that has 1,024 radiating elements.

The proposed SL/WG transition with metamaterial matching circuit is less than 150 mils thick, and operates between 10 GHz – 15 GHz with a VSWR < 1.22.

2. Description of the Waveguide to Stripline Transition

The proposed SL/WG transition consists of a stripline transmission line with an aperture slot in the ground plane. The energy couples from the stripline stub into the waveguide through layers of metamaterials, see figure 2. To simplify the analysis of the proposed SL/WG transition, the following approximations are assumed, see figure 3:

- The stripline to waveguide transition can be analyzed as planar radiating element in an H plane waveguide simulator
- The ground vias in the stripline to waveguide transition function as PEC waveguide walls

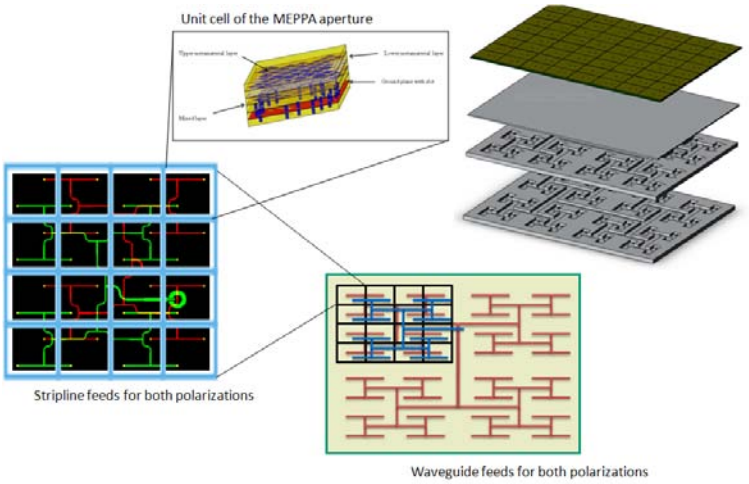

Figure 2 Illustration of the flat panel array terminal showing the proposed SL/WG transition.

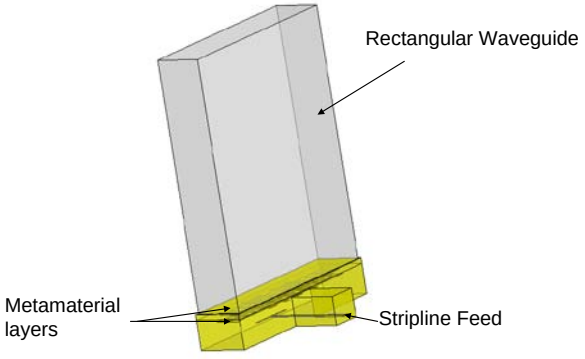

Figure 3 An Ansys HFSS diagram of an H plane waveguide simulator. The stripline to waveguide transition is essentially a waveguide simulator.

It is known from phased array antenna aperture design theory that the largest lateral dimension of a waveguide simulator controls the scan angle of the radiating element [8]. A plot of an "equivalent" scan angle for a waveguide simulator using the dimensions of our waveguide combiner's aperture cross section of 750 mils × 170 mils is shown in figure 4. These dimensions are based on the required waveguide manifold's operational bandwidth and mechanical registration to the MEEPA aperture's stripline combiner layers.

The waveguide simulator data suggests a relatively large H plane scan angle (~ 30 degrees) at which the design must be optimized. The required return loss criteria of better than -20dB across the bandwidth, is a challenging design problem.

Waveguide simulator theory indicates that in order to improve radiating element performance, the grid should be tightened [8]. However, since we are analyzing a fixed waveguide cross section based on our waveguide manifold design, we do not have this degree of freedom. We improved radiating element performance through the use of MEPPA metamaterials in the WG/SL transition. We define a metamaterial as an electrically small set of periodic structures in a unit cell. The metamaterial performance is analyzed through the use of a Floquet modal decomposition technique within the waveguide simulator, as discussed below.

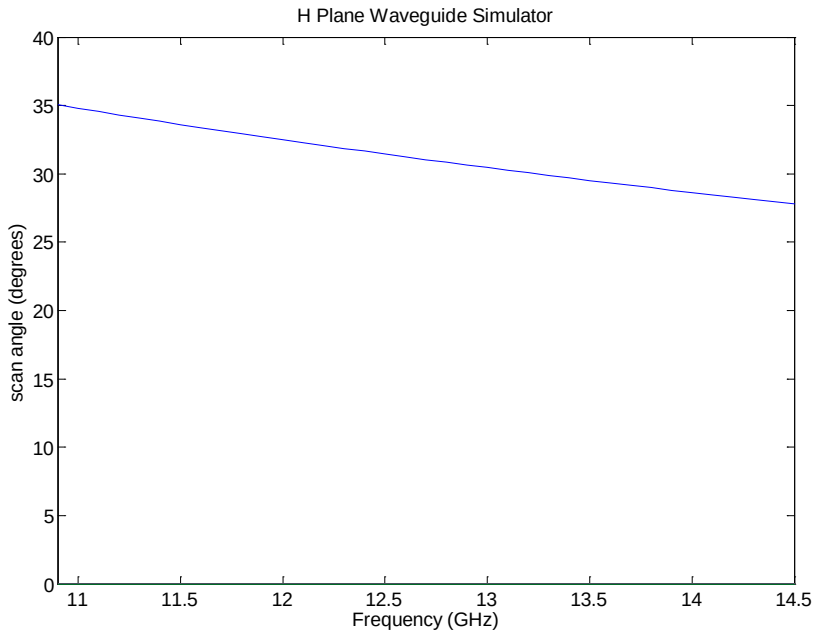

Figure 4 H Plane Waveguide Simulator Scan Angle Variation as a function of frequency for the waveguide simulator.

It is obvious from the constraints mentioned in section 1 that the traditional probe-fed waveguide transition is not a viable solution to this problem. It will suffer from a larger profile and is not practical relative to fabricating a large aperture with a large number of interconnects.

In order to understand the effect of the metamaterial layers, the SL/WG metamaterial transition is compared to a SL/WG transition with one of the metamaterial layers replaced with a patch transducer (see figure 5). The patch dimensions were chosen such that the return loss of the alternative structure was minimized over the frequency band. A Floquet mode analysis is done on the two SL/WG transitions in order to understand the effects of the metamaterial layers.

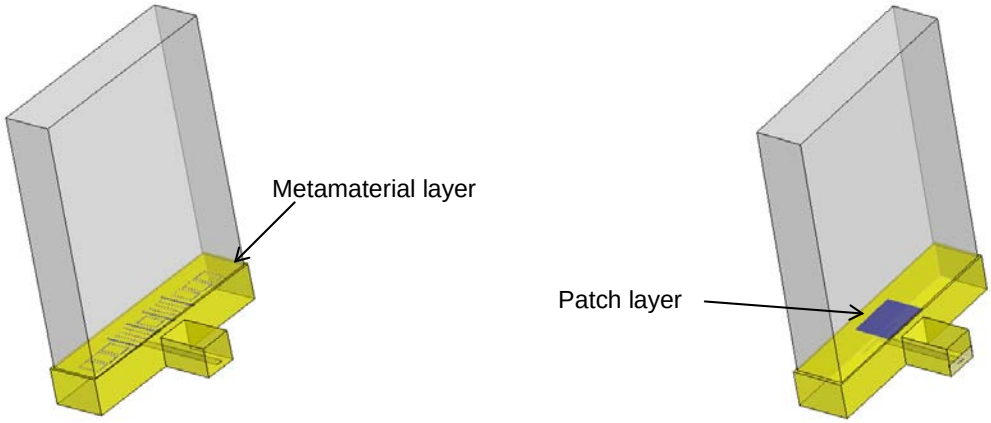

(A) Metamaterial **(B) Patch**

Figure 5 The waveguide simulator with (A) metamaterial layer The detail of the coupling slots in the stripline stub's ground plane is not shown. (B) with top patch layer.

3. Simulated Performance

The performance of the two waveguide simulators is shown in figure 6 thru figure 8. The metamaterial transition achieves close to 28% bandwidth at Ku-band with a -20dB return loss criteria and less than <1dB of insertion loss across the band of interest.

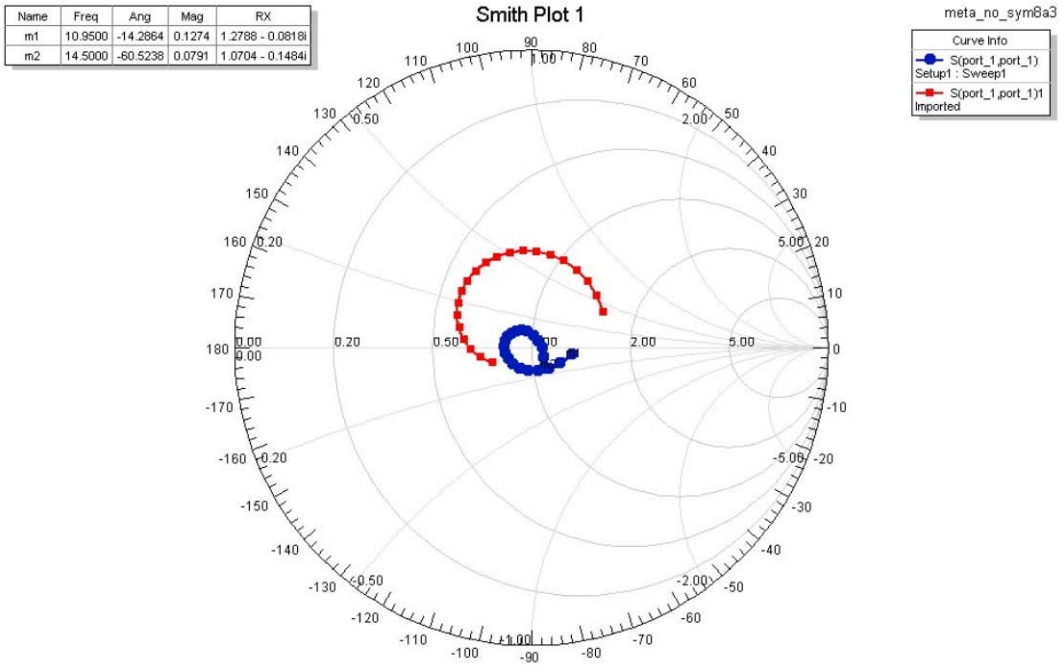

Figure 6 Smith chart plot of the waveguide simulator with the metamaterial layer (circle) and top patch layer (square).

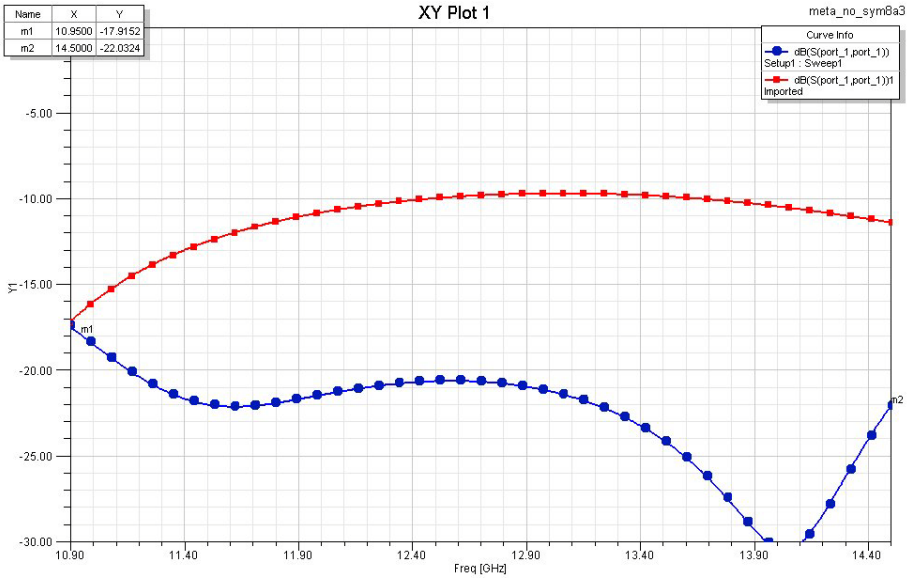

Figure 7 Waveguide Simulator: $|S_{11}|$ Metamaterial (circle) / Patch (square) Comparison. The vertical axis is for the return loss [dB].

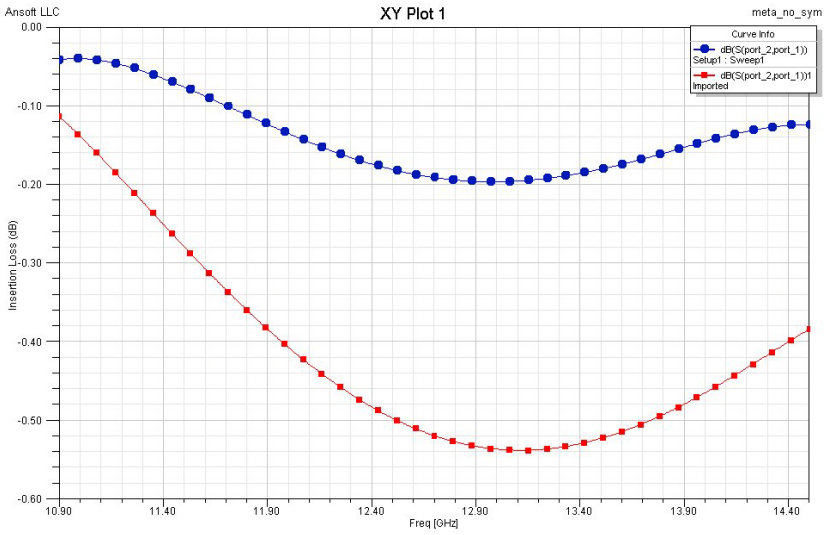

Figure 8 Waveguide Simulator: $|S_{21}|$ Metamaterial (circle) / Patch (square) Comparison.

4. Floquet Mode Decomposition

The difference in performance between the metamaterial and patch radiators can be understood by considering the fields scattered by the metamaterial compared to the fields scattered by the patch. Figure 9 shows a plot of the tangential E fields two mils above the top patch and a plot of the tangential E field two mils above the top metamaterial.

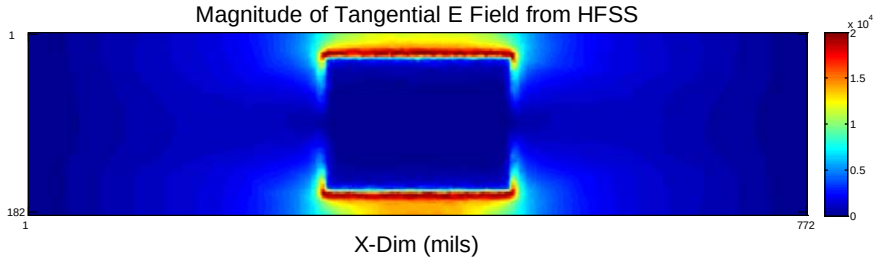

(A) Patch Radiator

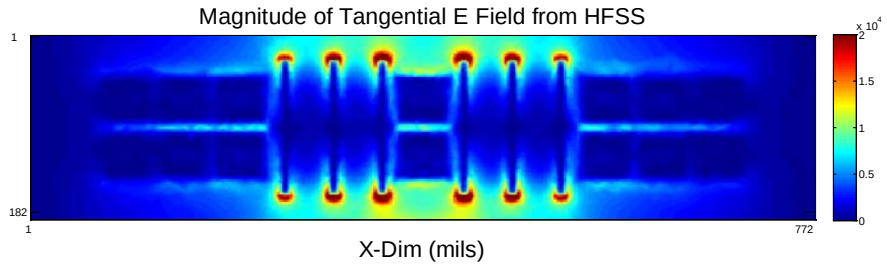

(B) Metamaterial Radiator

Figure 9 E-Field 2 mils above patch or metamaterial, calculated in HFSS.

In order to analyze the respective E fields, the fields calculated using HFSS are exported into MATLAB and a modal decomposition into the TE and TM PEC wall waveguide modes is performed. It should be noted that the TE and TM waveguide modes can be considered as a superposition of Floquet modes. The tangential E fields can be expressed in terms of the TE and TM eigenmodes as:

$$\sum_{m,n} V_{TEmn} * \hat{e}_{TEmn} + \sum_{m,n} V_{TMmn} * \hat{e}_{TMmn} = \overrightarrow{E_{HFSS}} \quad (1)$$

V_{TEmn} and V_{TMmn} are the modal voltages and $\hat{e}_{TEmn}$ and $\hat{e}_{TMmn}$ are the orthonormal eigenmodes of the rectangular waveguide. V_{TEmn} and V_{TMmn} can be solved for with the result:

$$V_{TEmn} = \iint \vec{E}_{HFSS} * \hat{e}_{TEmn} \quad (2)$$

and

$$V_{TMmn} = \iint \vec{E}_{HFSS} * \hat{e}_{TMmn} \quad (3)$$

The integration is over the waveguide cross section.

The number of eigenmodes required to adequately represent the E-field 2 mils above the metamaterial or patch can be determined by comparing the eigenmode and voltage superpositions with the HFSS results.

Figure 10 plots the superposition of TE and TM eigenmodes weighted by the voltage modal amplitudes. It is important to realize that only the TE_{10} and TE_{20} modes are propagating in the in the waveguide 2 mils above the metamaterial. The waveguide two mils above the metamaterial is filled with dielectric constant 3.0 material. All other modes are evanescent.

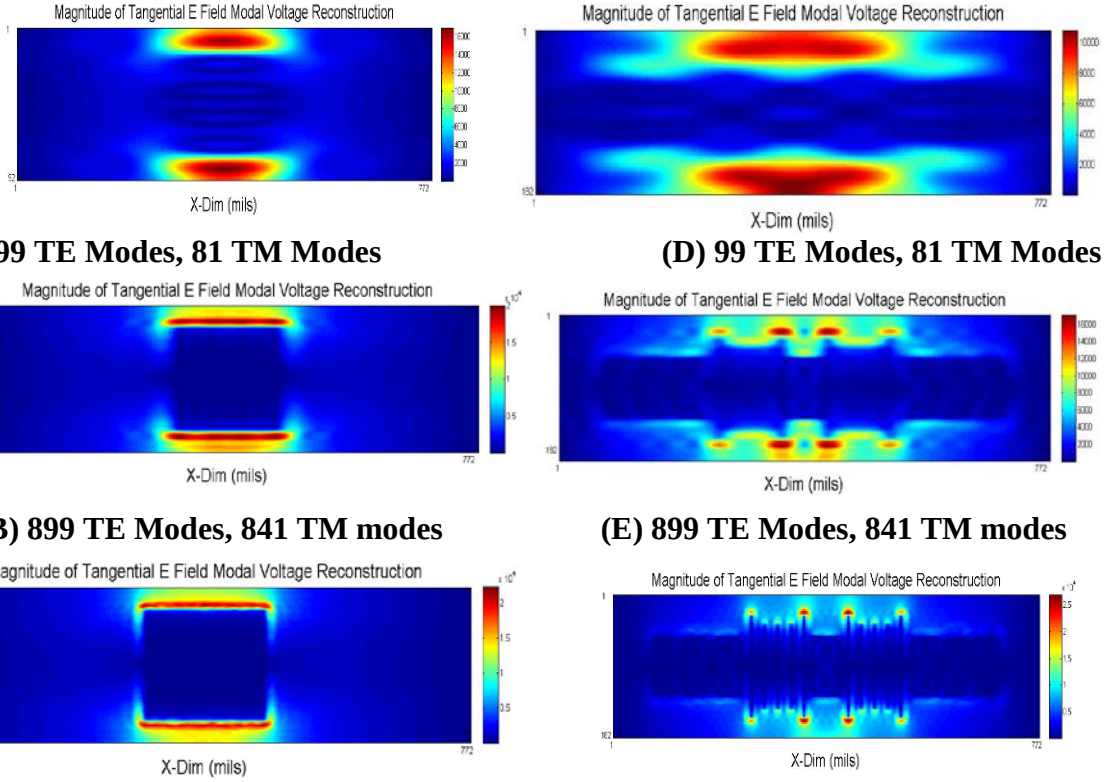

(A) 99 TE Modes, 81 TM Modes **(D) 99 TE Modes, 81 TM Modes**

(B) 899 TE Modes, 841 TM modes **(E) 899 TE Modes, 841 TM modes**

(C) 8099 TE Modes, 7921 TM Modes **(F) 8099 TE Modes, 7921 TM Modes**

Figure 10 A plot of the tangential E field reconstruction using TE and TM modes for the waveguide simulator with patch geometry on the left (A,B,C) and with the metamaterial geometry on the right (D,E,F).

The E-field two mils above the patch can be well represented by the first 899 TE and 841 TM modes, whereas the metamaterial requires 8099 TE and 7921 TM modes. The metamaterial scatters significant higher order Floquet mode content which proves to be key in obtaining broadband performance, as will be discussed in the next section.

5. Discussion

The reason for the superior performance of the metamaterial can be seen by examining the modal decompositions of the metamaterial and patch configurations shown in figures 11 through 14. Figure 11 and 12 contrast the normalized TE modal voltages for the patch and our SL/WG with metamaterial respectively at 12.5 GHz. Likewise, figure 13 and figure 14 contrast the normalized TM modal voltages for the patch and our WG/SL with metamaterial respectively at 12.5 GHz. Similar modal content distributions are observed across the bandwidth of interest.

The study involves up to 9000 Floquet modes. The TE and TM modes form a complete set of orthonormal modes. Due to polarization of the incident field, the higher order scattered modes are predominately TM.

In figures 11 through 14, the modes scattered by the metamaterial compared to the patch have lower voltage amplitudes for lower modal numbers and higher voltage amplitudes for higher modal numbers. Since the wave number in the z direction (z is normal to the metamaterial surface) is a function of the modal indices, k_{zmn} , and can be written as

$$k_{zmn} = \sqrt{k^2 - (m\pi/a)^2 - (n\pi/b)^2} \tag{4}$$

k is the wave number in the dielectric medium and a and b are the dimensions of the rectangular waveguide.

Based on these observations, it is evident the larger the modal indices, the more evanescent the mode is. The more evanescent the mode is, the more stable the mode is over frequency. Hence, a larger operational bandwidth can be achieved.

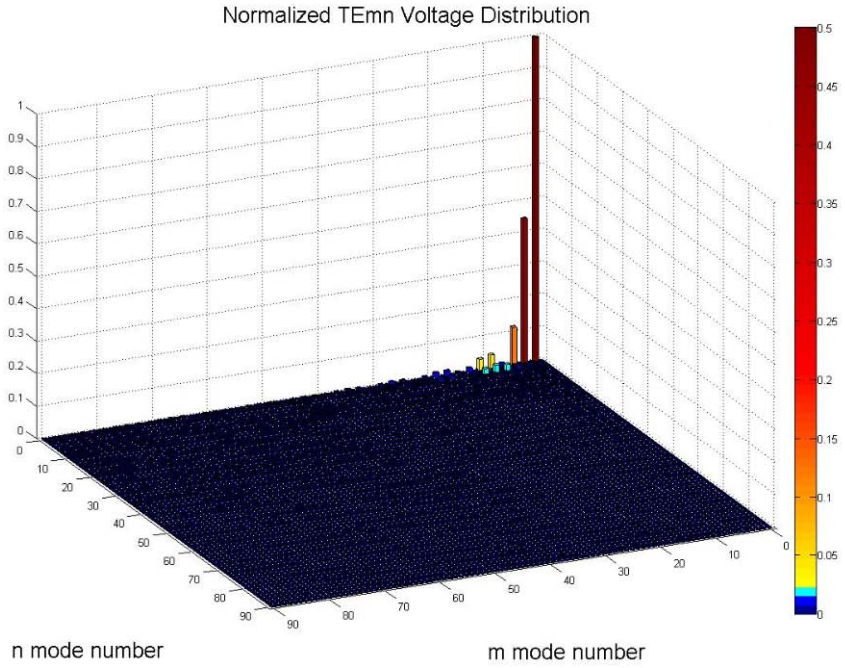

Figure 11 A plot of the first 8099 TE modes for the waveguide simulator of the **patch.**

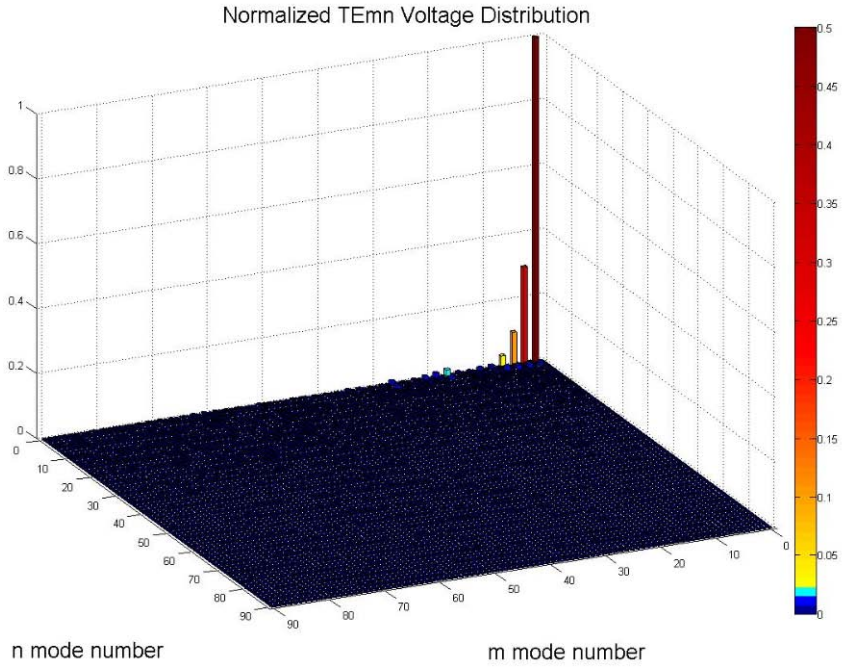

Figure 12 A plot of the first 8099 TE modes for the waveguide simulator of the metamaterial.

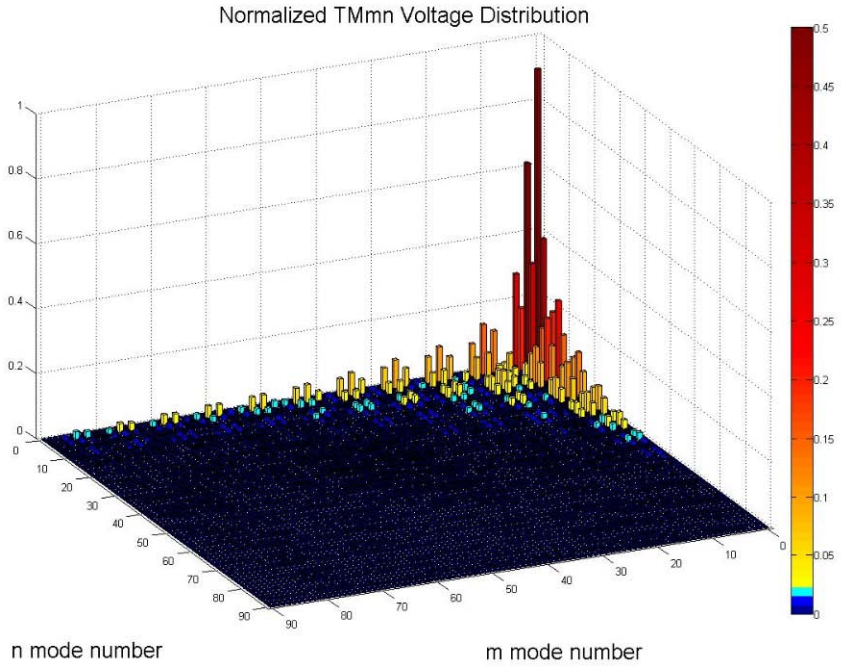

Figure 13 A plot of the first 7921 TM modes for the waveguide simulator with patch.

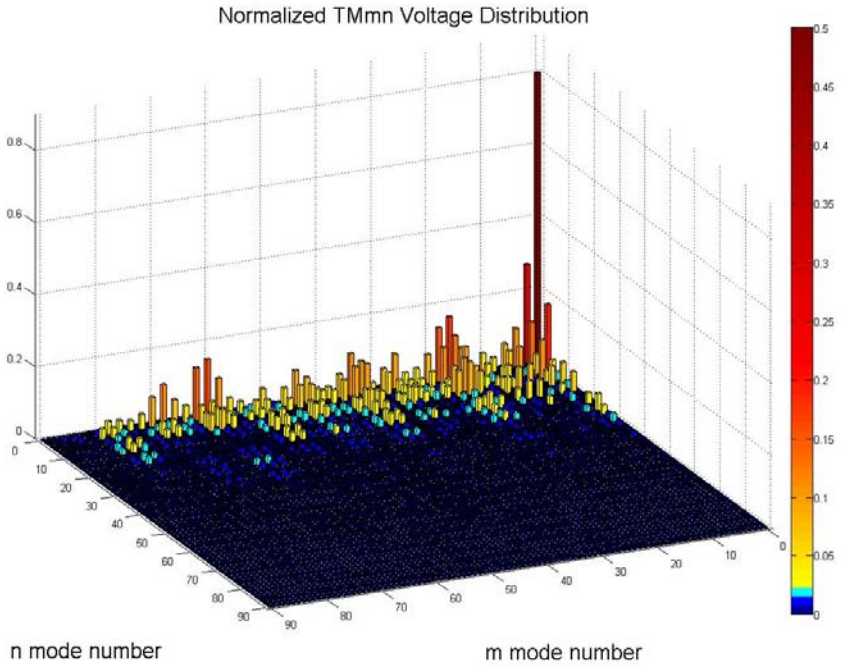

Figure 14 A plot of the first 7921 TM modes for the waveguide simulator with metamaterial.

6. Measured Performance

The corporate waveguide feed combiner, figure 15, is made from a nonstandard rectangular waveguide that has a cross-section area of 0.750″×0.170″. To measure the S Parameter matrix [S] of the proposed waveguide-to-stripline transition, a custom-made waveguide TRL calibration kit is made, as shown in figure 16. The kit consists of two WR75 waveguide to coaxial adapters, two tapered WR75 to the custom waveguide, a thorough line of the custom waveguide, and a short. A calibration routine of Thru/Reflect/Line was implemented.

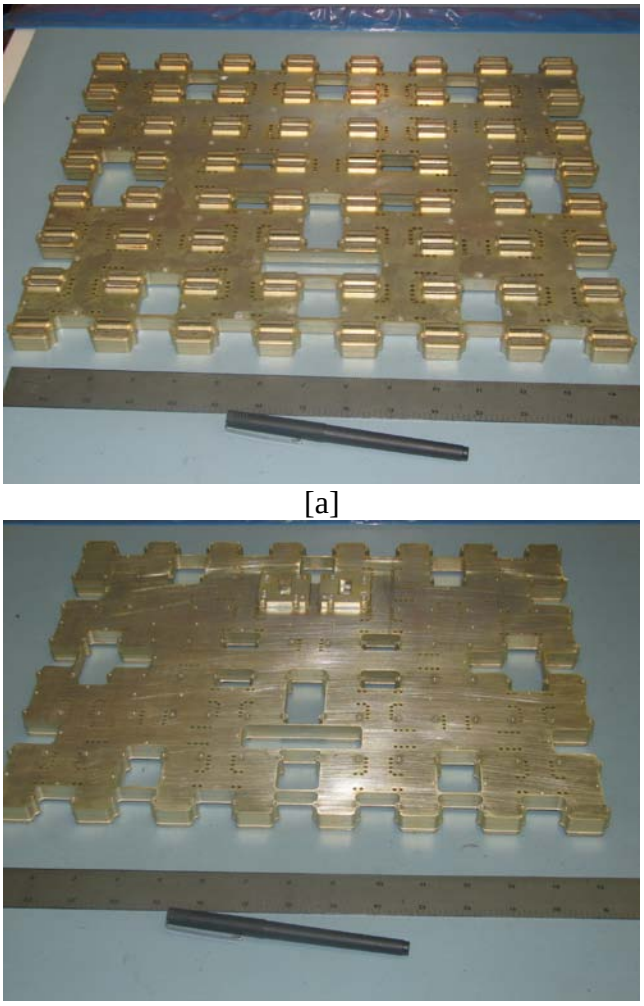

[a]

[b]

Figure 15. Aluminum dip-brazed waveguide feed manifold consists of [a] two straddled 64:1 waveguide corporate combiners (VP & HP) , as depicted in figure 1. The waveguide cross section is 0.750″×0.170″. [b] Two WR75 flanges to be connected to the SATCOM system.

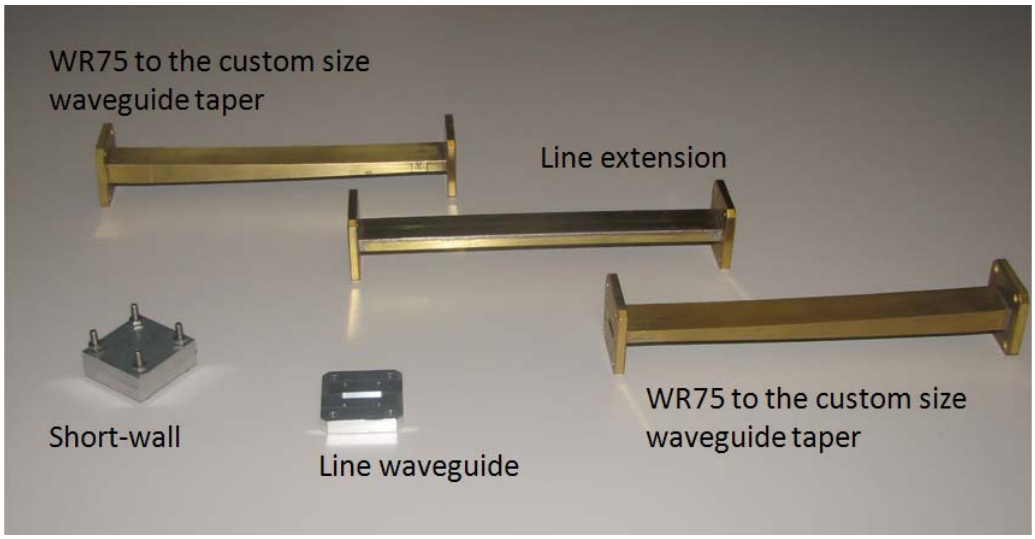

[a]

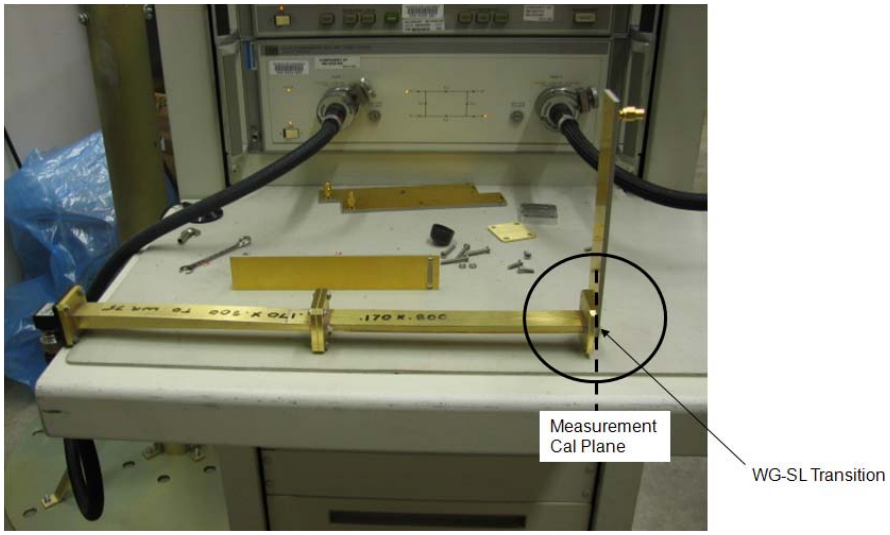

[b]

Figure 16. Custom made TRL calibration kit to measure the performance of the stripline-to-waveguide transition.

A test article of the metamaterial loaded WG/SL was fabricated with a coaxial to stripline adapter at one side, and the open-ended aperture at the other side, see figure 16a. The tapered waveguide section is attached to that test article to measure “stripline-to-waveguide” transition using time-gating. The measured data is not yet available at the time of print, but they will be presented in the symposium.

7. Conclusion

A novel wideband and low profile metamaterial stripline to waveguide (SL/WG) transition has been designed for use as an array manifold to aperture transition. The SL/WG transition was analyzed as an H plane waveguide simulator. The performance of the SL/WG transition was optimized through the use of metamaterial layers. The SL/WG transition exhibits significantly improved bandwidth because the metamaterial layers scatter the incident energy into higher order Floquet modes compared to the scattering that takes place from a conventional patch layer. The higher order Floquet modes are more stable over frequency. Measured results will be presented at the symposium.

References

[1] M. Buckley, J. Wolf, B. J. Herting, S. Patten, J. Mather, D. Manson, and J. West, " Wide Band and Wide Scan Metamaterial Loaded Radiating Elements," To appear at the 2010 Antenna Applications Symposium, Allerton Park, Monticello, Illinois, Sept 21 – 23, 2010

[2] D. E. Anagnostou, M. Morton, J. Papapolymerou and C. Christodoulou, "A 0 – 55 GHz Coplanar Waveguide to Coplanar Strip Transition," IEEE Transactions on Microwave Theory and Techniques, vol. 56, pp. 1 – 6, January 2008.

[3] H. Akel, "Broadwall-Side Stripline-to-Waveguide Transition," Proceedings of Asia-Pacific Microwave Conference, pp. 1 – 4, 2007.

[4] A. Zaghloul, R. Gupta, E. Khols, L. Sun, R. Allnutt, "Low Cost, Flat Antennas for Commerical and Military SATCOM terminals," IEEE Military Communications Conference, Vol. 2, pp. 795-799, 2001.

[5] A. Lait, "Waveguide to Stripline Transition," U.S. Patent# 4,716,386

[6] D. Sedivec, "Transition from Stripline to Waveguide," U.S. Patent# 4,562,416

[7] L. Joefsson, M. Eriksson, L. Malm and J. Bergendahl, "Microwave Antenna Transmission Device Having a Stripline to Waveguide Transition Via A Slot Coupling," U.S. Patent# 6,081,241

[8] A. Oliner and R. G. Malech, "Simulation of infinite arrays by waveguide," R.C. Hansen, Ed., "Microwaveg Scanning Antennas," vol. 2, pp. 322-335, 1966.

Wide Band and Wide Scan Metamaterial Loaded Radiating Elements

M.J. Buckley, J. Wolf, B.J. Herting, S. Patten, J. Mather, D. Manson, and J.B. West
Advanced Technology Center
Rockwell Collins, Inc.
400 Collins Rd. NE. M/S: 108-102
Cedar Rapids, IA 52498

Abstract – **Wide band and wide scan metamaterial loaded radiating elements are discussed. In order to illustrate the effect of a metamaterial structure on a linearly polarized radiating element performance, a comparison is made with a non metamaterial loaded linearly polarized radiating element. The Floquet modal distribution is calculated for the metamaterial radiating element and the conventional patch radiating element. The metamaterial loaded and non metamaterial radiating elements have significantly different Floquet modal distributions.**

1. Introduction

Modern phased arrays suffer from a variety of technical and practical shortcomings. Wider bandwidth is required to enable multifunction network-centric communication systems and radar systems, and lower-SWAP and low profile solutions are required for interface with many platforms, particularly UAV's. In addition, array scan angle must be increased and module count reduced in order to reduce array costs.

Our approach to address these shortcomings is to use metamaterials. We will define a metamaterial as an electrically small set of periodic structures in a phased array unit cell. The rationale for using a metamaterial can be explained by considering a plane wave incident on a phased array antenna. Assuming a large number of radiating elements in the array, the interior elements can be treated as if they are in an infinite array. This allows analysis to be completed with only one radiating element. The interactions with the other radiating elements are accounted for by using periodic boundary conditions. In the infinite array case, the Floquet modes are the complete set of modes that describe the interaction of the incident plane wave with the phased array radiating elements. The Floquet modes are an excellent approximation for the modes of an interior element in a large finite array. The dominant Floquet mode is a plane wave. When the incident electromagnetic plane wave scatters from the structure in a periodic array, it scatters into other Floquet modes.

By using a metamaterial instead of, for example a patch, the incident electromagnetic radiation will scatter into higher order rather than lower order Floquet modes. The periodic metamaterial structure is arranged symmetrically about the radiating element unit cell in order to excite symmetric Floquet modes at array normal and to minimize cross polar radiation. The higher order Floquet modes are more evanescent and hence more stable over scan and frequency variation. The higher order Floquet mode excitation

can be used to design radiating elements with a larger unit cell size and/or a larger frequency band and scan volume.

In this paper, we will compare a metamaterial phased array radiating element with a conventional patch phased array radiating element

2. Metamaterial and Conventional Phased Array Radiating Element

A cross sectional view of the metamaterial phased array radiating element is shown in figure 1. The metamaterial phased array radiating element consists of a stripline feed layer, a ground plane with a slot, a mixed metal layer, and two metamaterial layers. The dielectric material consists of six Rogers 3003 layers and five Speedboard C layers.

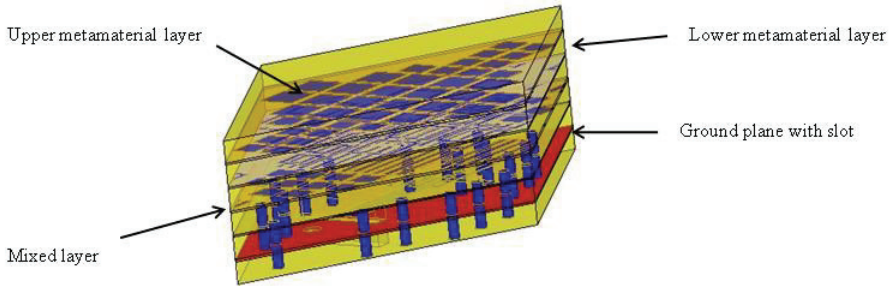

Figure 1. Cross sectional view of the Rockwell Collins metamaterial loaded radiating element.

A cross sectional view of the patch radiating element [1] is shown in figure 2.

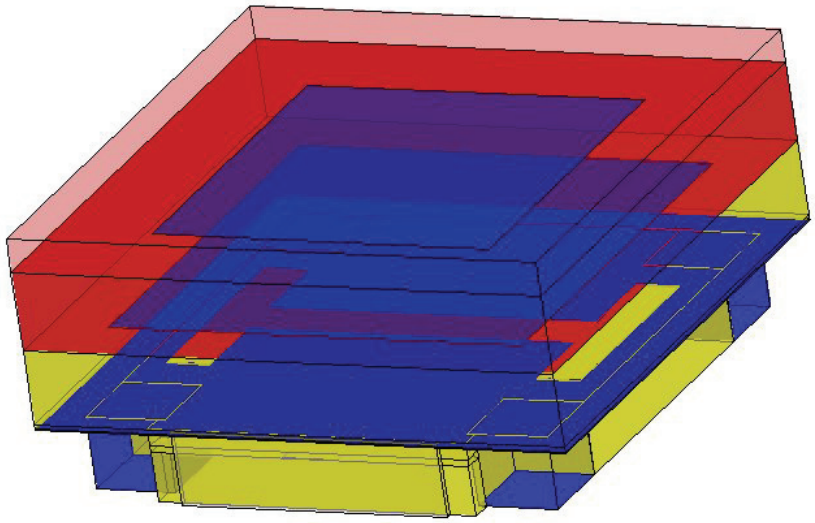

Figure 2. A view of a conventional patch radiating element presented at EuCap 2007 [1].

Table 1 is a comparison of the performance of the metamaterial radiating element and the conventional patch radiating element.

Table 1 Comparison of the Rockwell Collins radiating element and a recently published radiating element. The use of metamaterials significantly improves performance.

Radiating Element	Maximum scan angle (half conical scan angle)	Bandwidth at max scan angle	Unit cell size (Lambda)^2	Comments
Rockwell Collins 2010	70 degrees 2D scan n <1.3	39% 12-17.8 GHz	.1667	Extensive use of metamaterials
R. Erickson et al [ ]	60 degrees 2D scan n = 1.3 H plane scan @ 60 degrees	32 % 8-11 GHz	.093414	Use of patches, poor return loss H plane, EuCap 2007

The unit cell size of the Rockwell Collins metamaterial loaded radiating element is 1.76 times larger than the unit cell size of the EuCap 2007 radiating element. The substantially larger unit cell size is a critical parameter in radiating element performance. Consider an array consisting of 1760 EuCap 2007 radiating elements. A metamaterial loaded array of the same size would consist of only 1000 radiating elements. Assuming one module costs $100, the metamaterial loaded array would cost $80,000 less. There are additional savings from DC power and logic devices and reduced cooling

requirements. In addition, there is a significant weight reduction. A properly scaled top down view of the metamaterial loaded radiating element and the EuCap 2007 radiating element is shown in figure 3.

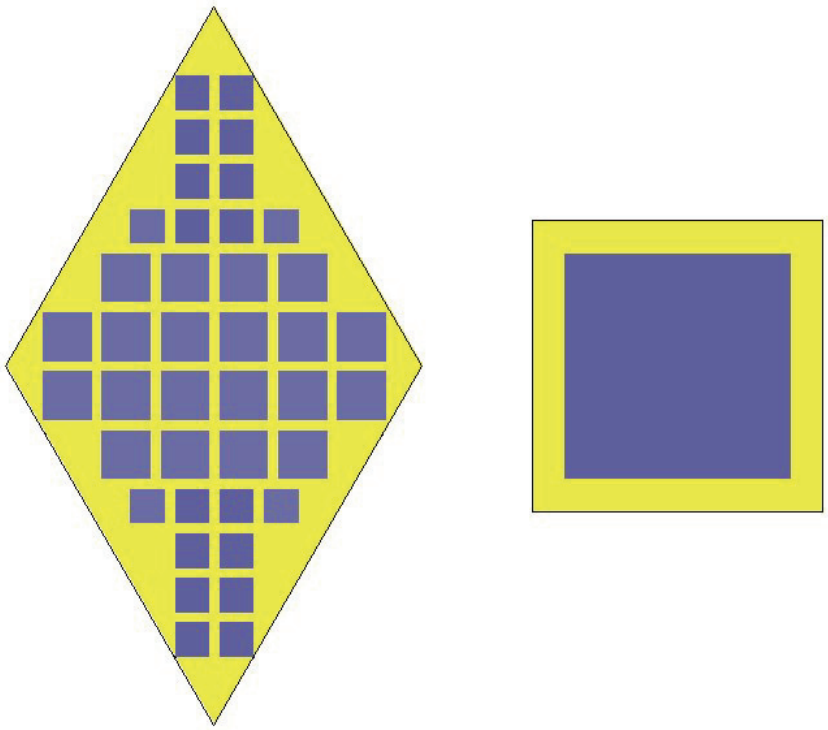

Figure 3 A top down view of the metamaterial loaded radiating element and the EuCap 2007 radiating element is shown above. The metamaterial loaded radiating element is 1.76 times larger than the EuCap 2007 radiating element. The increased size of the metamaterial radiating element is significant advantage in a radar or communication system. In addition, as shown in Table 1, the metamaterial radiating element performs better than the patch radiating element.

The impact of the metamaterial layers on the metamaterial loaded radiating element is shown in figures 4, 5, and 6. Figure 4 is a Smith chart plot of the metamaterial loaded radiating element with both layers of metamaterial. Figure 5 is a Smith chart plot of the metamaterial loaded radiating element with only the lower layer of metamaterial. Figure 6 is a Smith chart of the metamaterial radiating element with both metamaterial layers omitted.

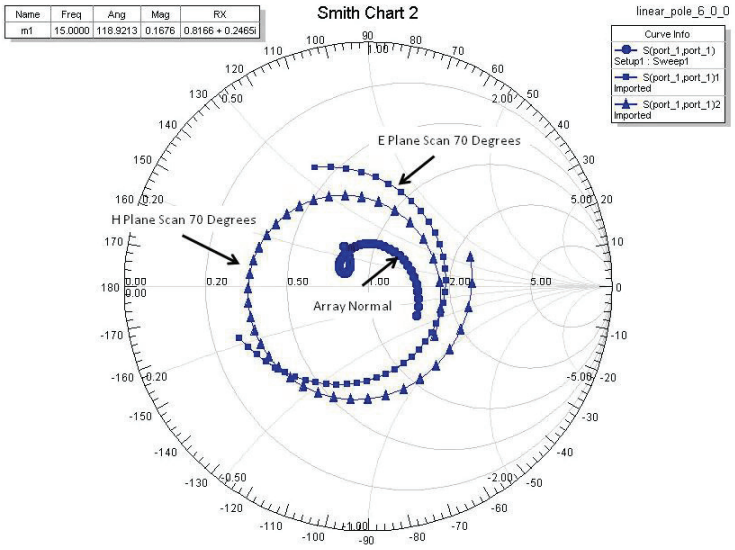

Figure 4. A Smith chart plot of the metamaterial loaded radiating element with both layers of metamaterial is shown.

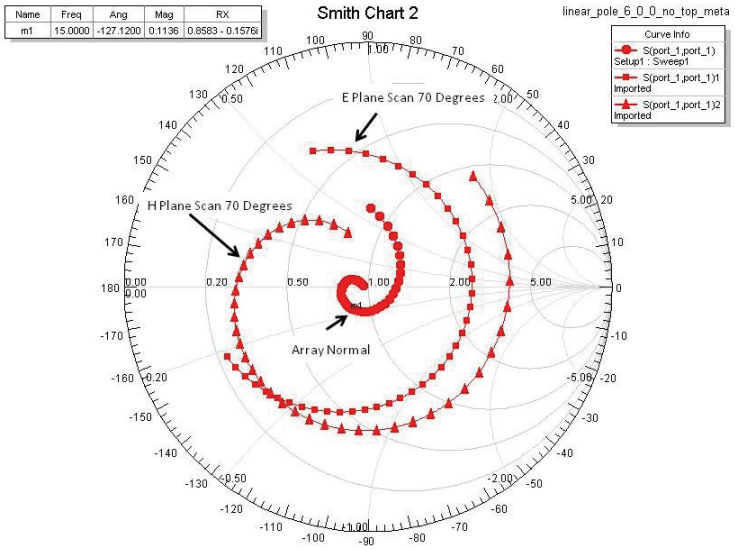

Figure 5. A Smith chart plot of the metamaterial loaded radiating element without the top layer of metamaterial is shown.

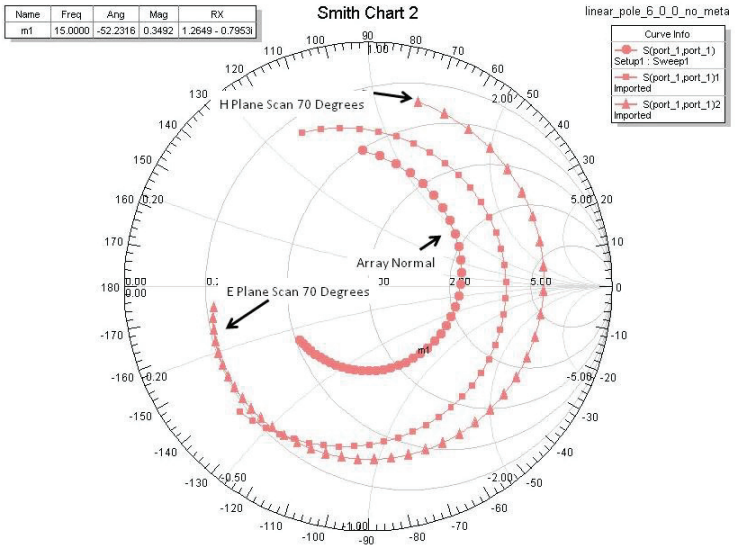

Figure 6. A Smith chart plot of the metamaterial loaded radiating element without both layers of metamaterial is shown.

3. Floquet Mode Analysis

In order to understand the performance advantage of the metamaterial loaded radiating element, the fields scattered by the top metamaterial layer are compared to the fields scattered by the EuCap 2007 top patch layer. Figure 7 is a plot of the tangential E fields two mils above the top metamaterial and two mils above the top patch layer. The fields scattered by the top metamaterial layer are substantially different from the fields scattered by the top patch layer. The eigenmodes of a periodic structure with planar substrates are the Floquet modes. At array normal scan, the Floquet modes consist of TEM modes, TE modes, and TM modes. The TEM modes are the dominant modes and have no cutoff frequency. In order to calculate the Floquet mode content for the metamaterial and patch layers, the fields were exported from Ansoft HFSS [2] and analyzed in MATLAB [3]. The tangential E fields, expressed in terms of the Floquet eigenmodes, can be written as:

$$\sum_{m} V_{TEMm} * \hat{e}_{TEMm} + \sum_{m,n} V_{TEmn} * \hat{e}_{TEmn} + \sum_{m,n} V_{TMmn} * \hat{e}_{TMmn} = \overline{E_{HFSS}}$$

V_{TEMm} , V_{TEmn} , and V_{TMmn} are the modal voltages and $\hat{e}_{TEMm}$, $\hat{e}_{TEmn}$, and $\hat{e}_{TMmn}$ are the orthonormal Floquet modes.

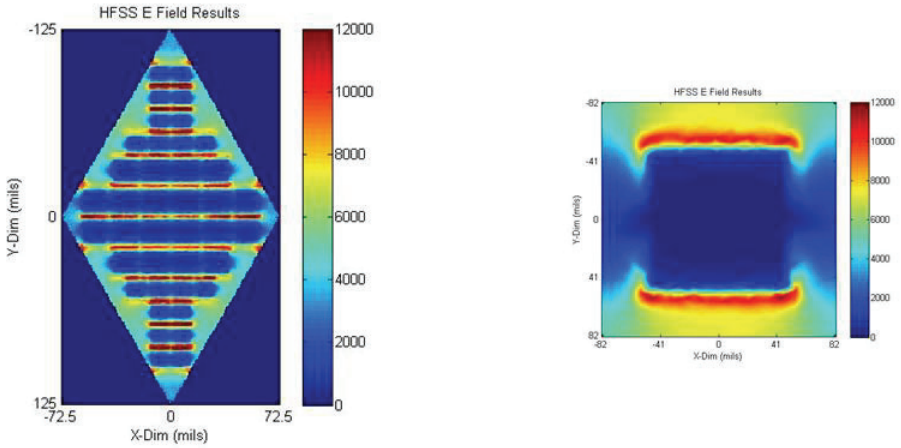

Figure 7. The tangential E fields two mils above the top metamaterial layer of the Metamaterial radiating element and two mils above the top patch of the EuCap 2007 patch radiating element.

The modal voltages can be solved for with the result:

$$V_{TEMm} = \iint \vec{E}_{HFSS} * \hat{e}_{TEMm}$$

$$V_{TEmn} = \iint \vec{E}_{HFSS} * \hat{e}_{TEmn},$$

and

$$V_{TMmn} = \iint \vec{E}_{HFSS} * \hat{e}_{TMmn}$$

The number of Floquet modes required to adequately represent the E-field two mils above the metamaterial or patch layer can be determined by comparing the Floquet mode and voltage superpositions with the Ansoft HFSS results. Figure 8 plots one linearly polarized TEM Floquet mode, 120 TE Floquet modes and 120 TM Floquet modes for the E-fields two mils above the top metamaterial layer and two mils above the patch layer.

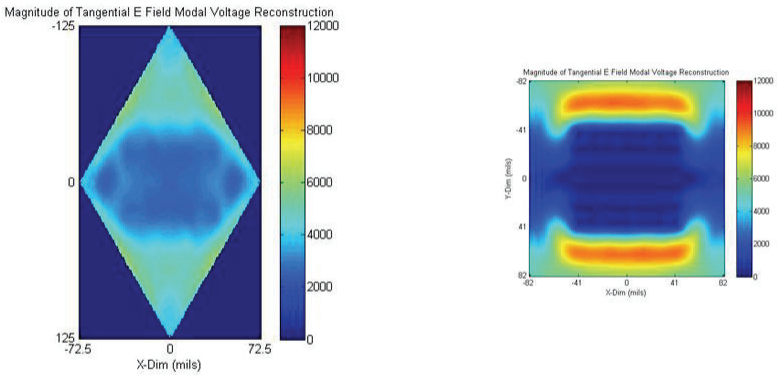

Figure 8 A plot of the tangential E field recontruction two mils above the metamaterial layer and patch layer using a linearly polarized TEM mode and 120 TE and 120 TM modes. The fields above the patch layer are approximated much better than the fields above the metamaterial layer by the relatively small Floquet mode reconstruction.

Figure 9 plots one linearly polarized TEM Floquet mode, 960 TE Floquet modes, and 960 TM Floquet modes for the E-fields two mils above the top metamaterial layer and one linearly polarized TEM Floquet mode, 440 TE Floquet modes, and 440 TM Floquet modes 2 mils above the patch layer.

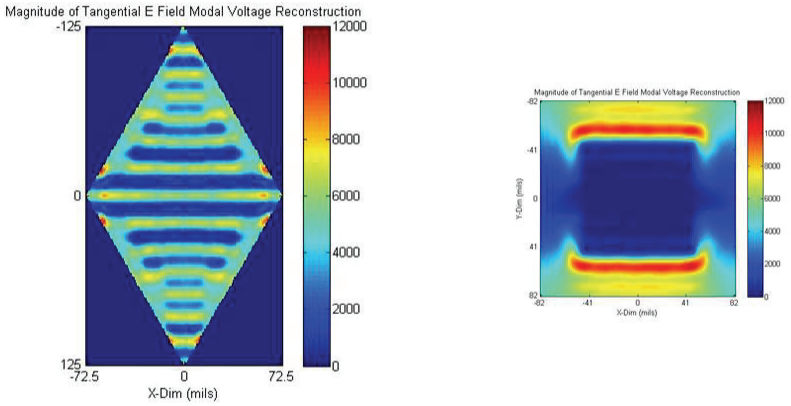

Figure 9. A plot of the tangential E field recontruction two mils above the metamaterial layer using a linearly polarized TEM mode and 960 TE and 960 TM modes. The fields above the patch layer are approximated by one linearly polarized TEM mode and 440 TE and 440 TM modes

Figure 10 plots one linearly polarized TEM Floquet mode, 3720 TE Floquet modes, and 3720 TM Floquet modes for the E-fields two mils above the top metamaterial layer and one linearly polarized TEM Floquet mode, 899 TE Floquet modes, and 899 TM Floquet modes 2 mils above the patch layer. The fields two mils above the metamaterial layer can be well represented by one linearly polarized TEM mode, 3720 TE, and 3720 TM Floquet modes. The fields two mils above the metamaterial layer can be well represented by one linearly polarized TEM mode, 960 TE, and 960 TM Floquet modes.

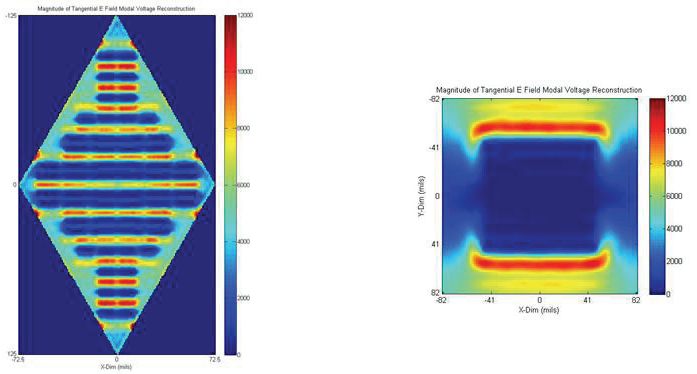

Figure 10. A plot of the tangential E field recontruction two mils above the metamaterial layer using a linearly polarized TEM mode and 3720 TE and 3720 TM modes. The fields above the patch layer are approximated by one linearly polarized TEM mode and 960 TE and 960 TM modes

4. Discussion

The reason for the superior performance of the metamaterial loaded radiating element is due to the modal voltage amplitude distribution difference between the metamaterial loaded radiating element and the patch radiating element. Figures 11 and 12 are plots of the absolute value of the modal voltage amplitudes for the metamaterial loaded radiating element for the TE and TM modes respectively at 18 GHz. Figures 13 and 14 are plots of the absolute value of the modal voltage amplitudes for the EuCap 2007 patch radiating element the TE and TM modes respectively. The modal voltage amplitudes for the TE modes are small for both the metamaterial and patch cases. The TM modal voltage amplitude distributions are substantially different for the metamaterial and patch cases. In figures 12 and 14, the modes scattered by the metamaterial compared to the patch have lower voltage amplitudes for lower modal numbers and higher voltage amplitudes for

higher modal numbers. The wave number in the z direction (z is normal to the metamaterial surface), k_{zmn} , can be written as

$$k_{zmn} = \sqrt{k^2 - \left(m\pi/a\right)^2 - \left(n\pi/b\right)^2} \tag{4}$$

k is the wave number in the dielectric medium and a and b are the dimensions of the rectangular waveguide. The larger the modal indices, the more evanescent the mode is. The more evanescent the mode is, the more stable the mode is over frequency. For comparison, figure 15 is a plot of the absolute value of the TM voltage modal distribution at 12 GHz. The absolute value of the TM voltage modal distribution at 12 GHz is quite similar to the voltage modal distribution at 18 GHz, which suggests that the metamaterial effects are not strongly frequency dependent.

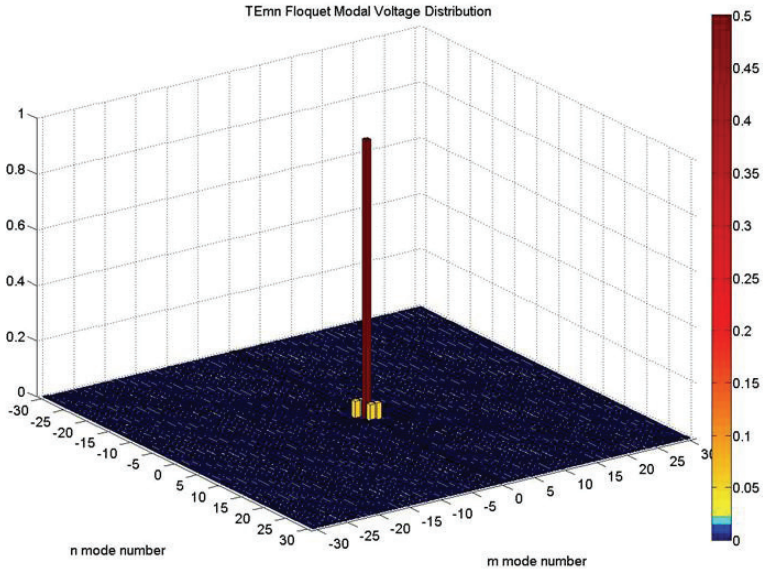

Figure 11. A plot of the linearly polarized TEM modal voltage amplitude (mode number 0,0) and 3600 TM Floquet modal voltage amplitudes for the metamaterial loaded radiating element.

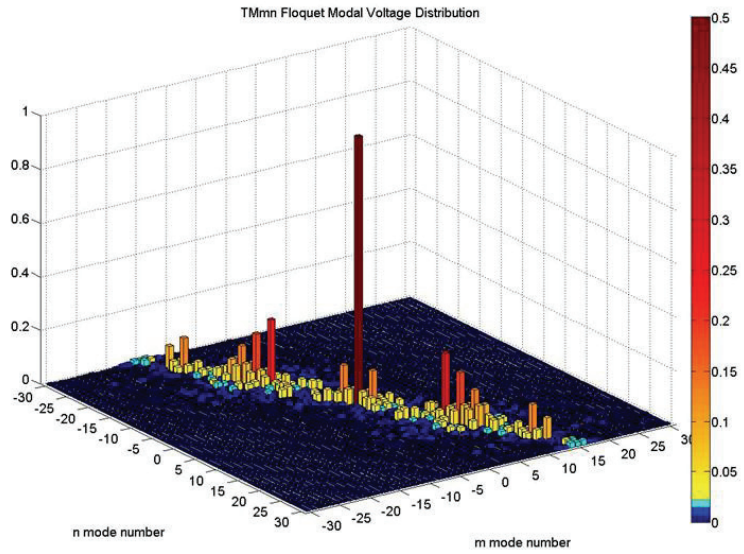

Figure 12. A plot of the linearly polarized TEM modal voltage amplitude (mode number 0,0) and 3600 TM Floquet modal voltage amplitudes for the metamaterial loaded radiating element at 18 GHz.

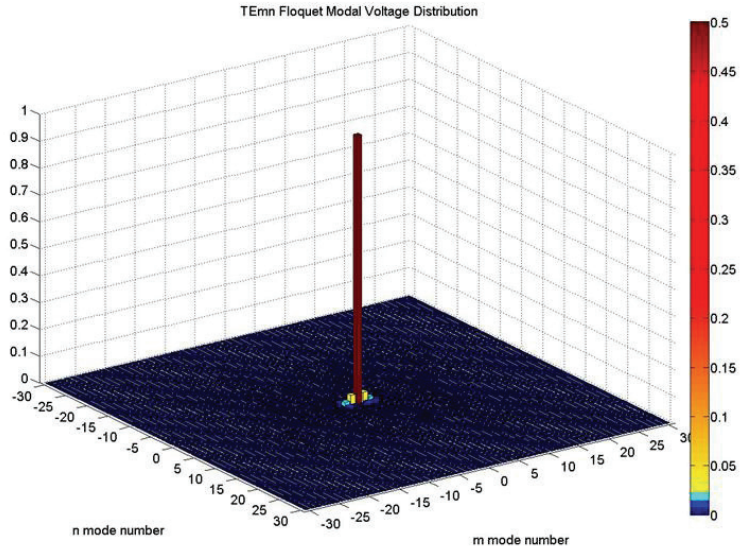

Figure 13. A plot of the linearly polarized TEM modal voltage amplitude (mode number 0,0) and 3600 TE Floquet modal voltage amplitudes for the EuCap 2007 patch radiating element.

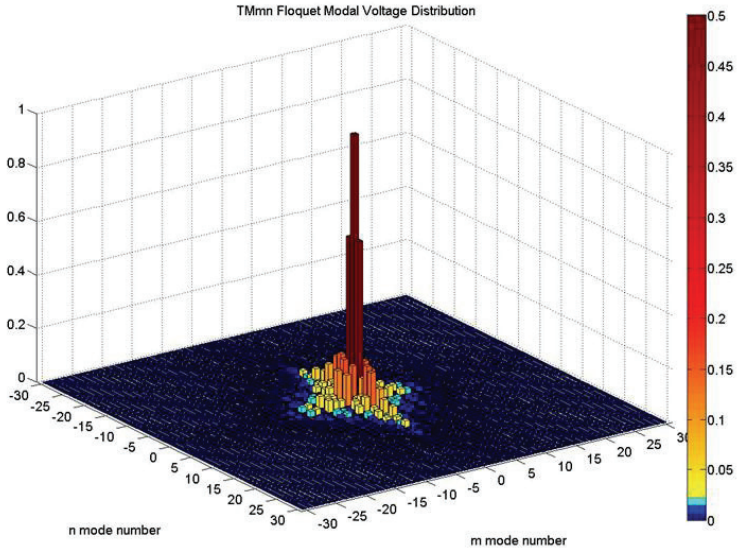

Figure 14. A plot of the linearly polarized TEM modal voltage amplitude (mode number 0,0) and 3600 TM Floquet modal voltage amplitudes for the EuCap 2007 patch radiating element.

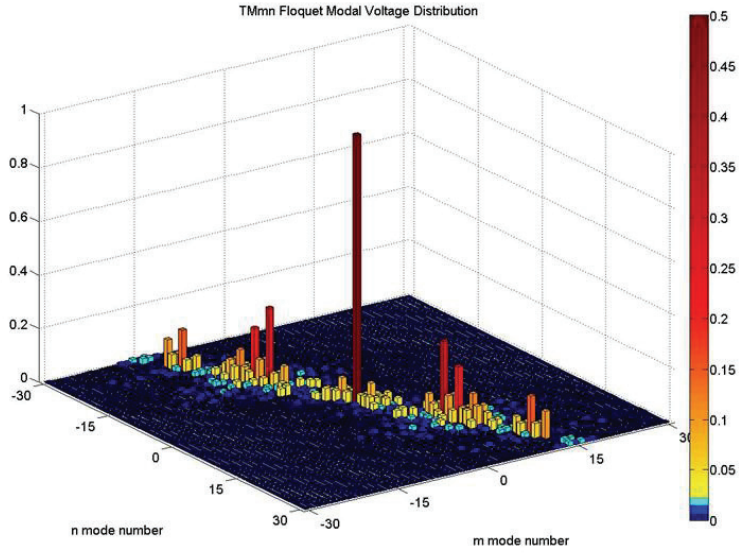

Figure 15. A plot of the linearly polarized TEM modal voltage amplitude (mode number 0,0) and 3600 TM Floquet modal voltage amplitudes for the metamaterial loaded radiating element at 12 GHz.

5. Measured Results

A picture of a fractional array for the metamaterial loaded radiating element is shown below. The fractional array will be tested and results will presented at the 2010 Allerton Antenna Symposium.

6. Future Work

We are currently extending our linearly polarized radiating element to a dual polarized radiating element. Figure 16 is a plot of the tangential electric field magnitude 2 mils above the top layer of metamaterial with the dual polarized radiating element excited with slant linear polarization. Also shown on Figure 16 is a plot of the tangential electric field magnitude produced by 960 TE modes, 960 TM modes, and 1 TEM mode. Figure 17 is a plot of the absolute value of the voltage modal amplitudes of 960 TE modes and 1 TEM mode. Figure 18 is a plot of the absolute value of the voltage modal amplitudes of 961 TM modes and 1 TEM mode.

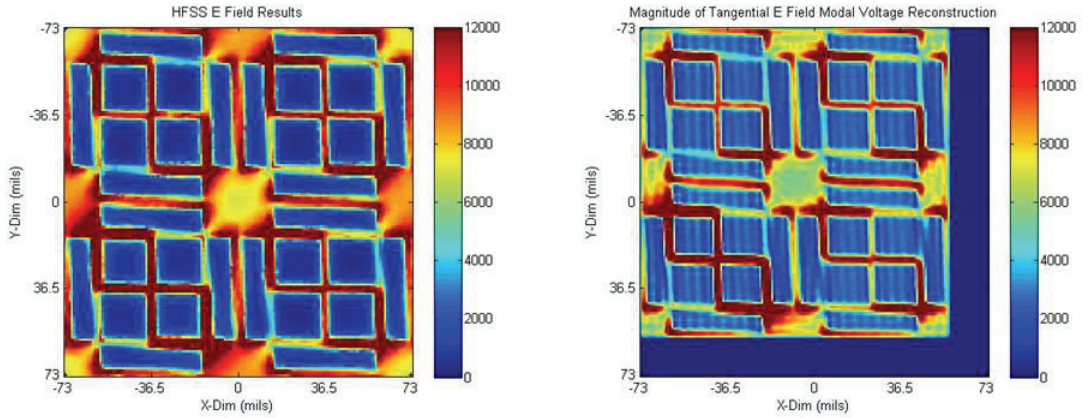

Figure 16. The left figure is a plot of the tangential electric field magnitude 2 mils above the top layer of metamaterial with the dual polarized radiating element excited with slant linear polarization. The right figure is a plot of the tangential electric field magnitude produced by 960 TE modes, 960 TM modes, and 1 TEM mode 2 mils above the top metamaterial layer.

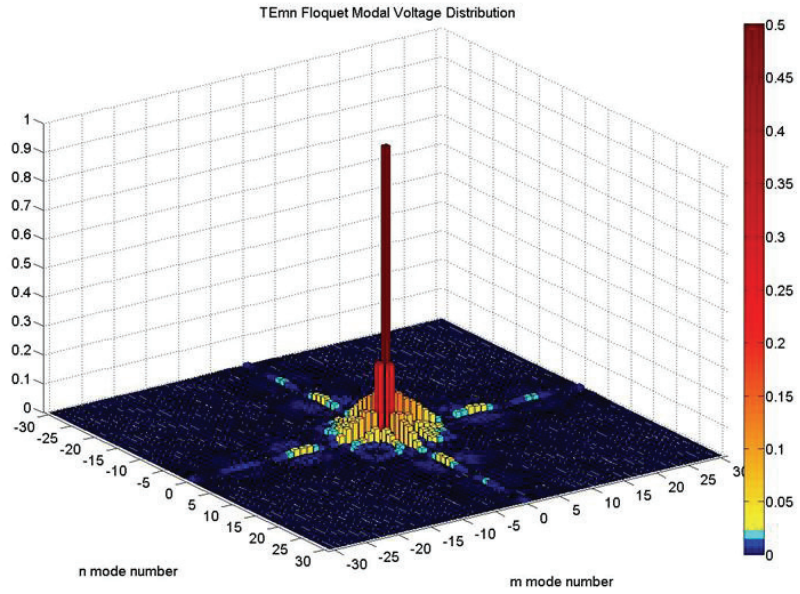

Figure 17. A plot of the TEM modal voltage amplitude (mode number 0,0) and 3720 TE Floquet modal voltage amplitudes for the dual polarized metamaterial loaded radiating element.

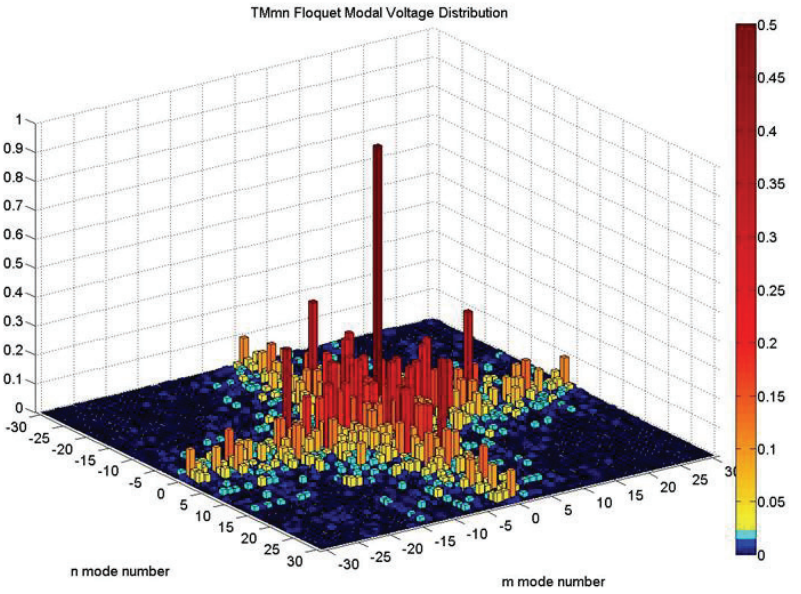

Figure 18. A plot of the TEM modal voltage amplitude (mode number 0,0) and 3720 TM Floquet modal voltage amplitudes for the dual polarized metamaterial loaded radiating element.

7. Conclusion

Metamaterial phased array radiating elements offer significant advantages compared to conventional phased array radiating elements. A planar metamaterial phased array radiating element has increased unit cell size, larger scan volume, and larger frequency band compared to a conventional patch radiating element. The increased unit cell size results in lower costs, lower weight, reduced cooling requirements, and lower packaging complexity. The increased scan volume and frequency band results in improved system performance. The metamaterial advantages are because the metamaterial element scatters into higher order Floquet modes than the conventional patch radiating elements.

8. References

[1] R. Erickson, R. Gunnarsson, T. Martin, L. –G. Huss, L. Pettersson, P. Andersson, A. Ouacha, "Wideband and Wide Scan Phased Array Microstrip Patch Antennas for Small Platforms," Antennas and Propagation, 2007 EuCAP 2007 The Second European Conference on, 11-16 Nov. 2007 Page(s):1-6

[2] www.ansoft.com

[3] www.mathworks.com

Antenna Design Using a Metamaterial Ground Plane

Hugh L. Southall[ab], Terry H. O'Donnell[ac], John S. Derov[a], and Jeffery W. Allen[a]
[a] Air Force Research Laboratory, 80 Scott Drive, Hanscom AFB, MA USA 01731
[b] On-site Consultant, Solid State Scientific Corp., 27-2 Wright Road, Hollis, NH 03049
[c] On-site Consultant, ARCON Corp., 260 Bear Hill Road, Waltham, MA 02451

ABSTRACT

In this paper we use multi-parameter optimization to design a wideband, single-element antenna over both metamaterial (MM) and perfect electric conductor (PEC) ground planes. The PEC ground plane design includes an optimized balun/feed. We describe how the Efficient Global Optimization (EGO) algorithm can be interfaced with a full-wave computational electromagnetics (CEM) simulation. EGO is an evolutionary, data-adaptive algorithm which can be useful with expensive cost functions.

Keywords: Efficient global optimization (EGO), computational electromagnetics (CEM), evolutionary computation, antenna design optimization, design and analysis of computer experiments (DACE), metamaterials, folded triangular bowtie antenna (FTBA) element, wideband antenna element

1. INTRODUCTION

A cavity-backed antenna has the desirable radiating properties of high gain, low side lobes, and low back lobes. Reduced radiation in the backward direction makes it attractive for a large number of applications. If the radiating element in front of the cavity is wideband, the antenna can be wideband. Qu[1] proposed a bowtie dipole as the element[2] (Figure 1). The dipole has two narrow folding arms on either side of the driven bowtie and exhibits good performance over more than an octave bandwidth at UHF (Ultra High Frequency) and SHF (Super High Frequency) frequencies (2 to 5 GHz). It is referred to as a cavity-backed folded triangular bowtie antenna (FTBA) in the literature[1] and is more compact than the short backfire antenna used for similar applications [1, 3, 4] however the gain of the FTBA is lower.

In this paper we propose a structure which is potentially simpler and more compact than either the cavity-backed FTBA or the short backfire antenna. The concept is shown in Figures 2 and 3. We use the FTBA element over a backing structure which is a flat disk composed of a special metamaterial (MM) called an indefinite material.[5, 6] The bottom surface of the disk is a conducting plate. The six design parameters (variables) are shown in Table 1. Design optimization requires a multi-parameter algorithm suitable for expensive cost functions since each proposed antenna design (combination of the six parameters) is analyzed using a full-wave CEM simulation[7] which can be very expensive in terms of computation time. To demonstrate the feasibility of our design approach, the emphasis in this paper is on coupling the optimization algorithm to the CEM engine.

Table 1. The six antenna design variables.

Design Variable	
t_m	MM Thickness (mm)
$D_m/2$	MM Radius (mm)
h	Dipole height (mm)
L	Dipole length (mm)
α	Bowtie angle (degrees)
W_a	Folding arm width (mm)

In **Section 2** we discuss the indefinite material and in **Section 3** we briefly describe the EGO algorithm and the modifications required for multi-parameter optimization. In **Section 4** we describe the optimum design of the FTBA over a finite PEC ground plane with a balun/feed. We present results in **Section 5** for designs using both MM and PEC ground planes and summarize in **Section 6**.

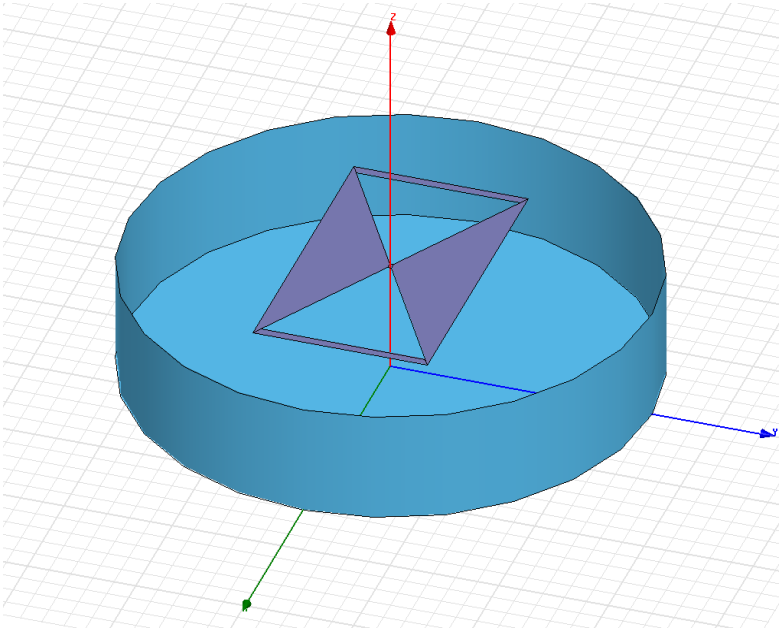

Figure 1. FTBA element backed by a metal cavity. The coordinates are x,y,z counterclockwise from the lower left arrow. Two narrow folding arms are at either side of the bowtie element.

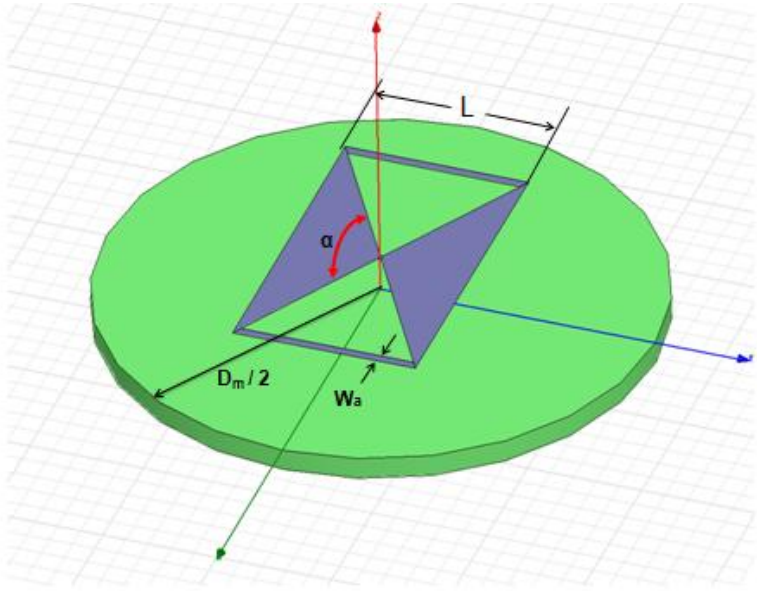

Figure 2. FTBA element backed by a disk of indefinite material. Principal design parameters are shown. The bottom surface of the disk is covered by a conducting plate (not visible).

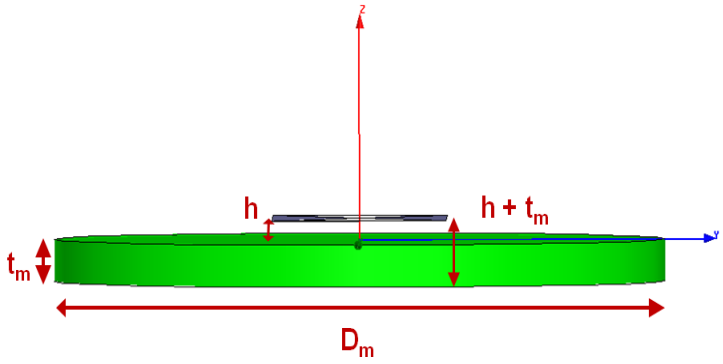

Figure 3. Side view of the FTBA element backed by an indefinite material. Principal design parameters are shown.

2. THE INDEFINITE MATERIAL (METAMATERIAL)

Metamaterials are artificial, structured, composite media with unit cell dimensions much smaller than a wavelength.[5] They are composed of periodically positioned scattering elements (conductors), and have been shown to exhibit simultaneously negative effective permittivity and negative effective permeability.[5, 6] A homogenization process allows this complicated composite medium to be described by effective permittivity and permeability tensors rather than by band diagrams.[5]

In Figure 4, the semi-infinite region to the left is free space and the MM is represented by the cross-hatched region to the right. The constitutive parameters are defined by relative permittivity tensor $\varepsilon_r = \mathrm{diag}[\varepsilon_{xr}\ \varepsilon_{yr}\ \varepsilon_{zr}]$ and relative permeability tensor $\mu_r = \mathrm{diag}[\mu_{xr}\ \mu_{yr}\ \mu_{zr}]$, where diag[ ] represents a diagonal matrix. In free space the diagonal elements are equal to one. An indefinite material is an MM where the diagonal elements have different signs.[5] We consider a special indefinite material called *unit magnitude anti-cutoff*[5] which has $\varepsilon_{yr}\mu_{xr} = -1$ and $\mu_{xr}/\mu_{zr} = -1$.

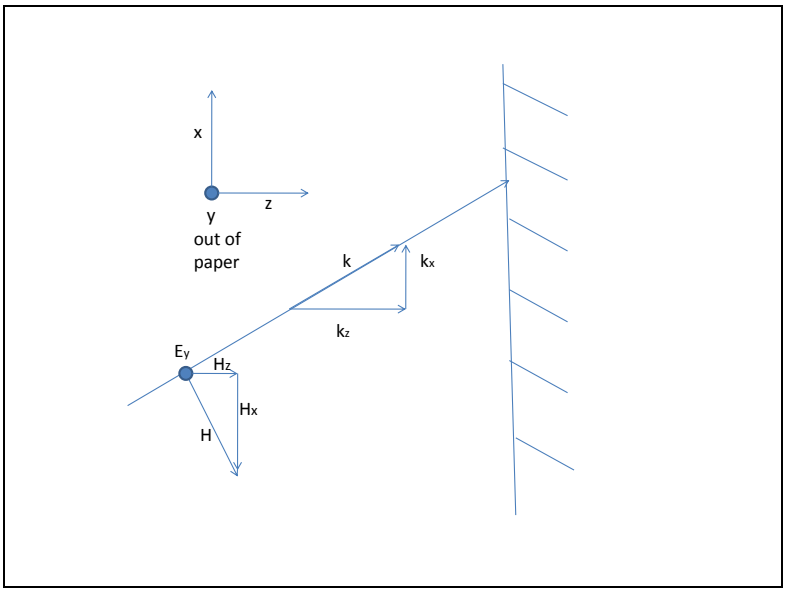

Figure 4. A Transverse Electric (TE_{xz}) wave incident on a MM.

Our ideal indefinite material has homogenized constitutive parameters that are constant over the band (2 to 5 GHz). In real materials there would be dispersion, or frequency variation. We also assume that the primary field produced by the dipole is transverse electric. A transverse electric (TE) wave will encounter a unit magnitude reflection coefficient at the surface of the indefinite material as discussed below. Of course the full-wave CEM code includes all field components (including TM_{xz} waves). We consider TM waves in the paragraph after Equation (2) below.

In Figure 4, the polarization vector in Figures 2 and 3 is in the y direction (to the right). The electric field is therefore primarily transverse to the MM surface in the x-y plane. For TE_{xz} plane waves, $\mathbf{E} = \mathbf{y} \exp[j(\omega t - k_x x - k_z z)] = \mathbf{y}\, E_y$ and propagation vector, **k**, has components k_x and k_z. For plane wave solutions, the dispersion relation for TE wave propagation is: [5]

$$k_z^2 = \varepsilon_{yr}\mu_{xr}\frac{\omega^2}{c^2} - \frac{\mu_{xr}}{\mu_{zr}}k_x^2 \ , \qquad (1)$$

and the surface reflection coefficient is:

$$\rho = (\mu_{xr}k_z - q_z)/(\mu_{xr}k_z + q_z). \qquad (2)$$

k and **q** are the wave vectors in free space and the MM, respectively. Using Equations 1 and 2 and the fact that k_x represents a transverse variation and is continuous across the interface, Smith and Schurig[5] show that for TE waves the reflection coefficient $\rho = +j$, *independent of the angle of incidence*.[5] Therefore the TE reflection coefficient has unit magnitude and a 90^o phase shift. The surface impedance is equal to $+j377\ \Omega$. It can be shown that ρ is also unit magnitude for TM waves if $\varepsilon_{xr}\mu_{yr} = -1$ and $\varepsilon_{xr}/\varepsilon_{zr} = -1$. In **Section 5** we consider indefinite materials with unit magnitude ρ for: (1) TE waves and (2) both TE and TM waves.

For a perfect electric conductor (PEC) and a perfect magnetic conductor (PMC), $\rho = -1$ and $\rho = +1$ respectively. As the dipole height approaches zero a PEC ground plane shorts out the dipole and the radiated power vanishes. For a PMC ground plane, image currents are in phase and reinforcement occurs. For the anti-cutoff indefinite material the effect is intermediate; however, a significant amount of power is radiated when the dipole is moved closer to the surface.[7] This suggests that the radiating element can be located closer to the surface without inducing field-cancelling image currents which occur in metallic ground planes and may create opportunities for more compact, lower profile antennas. The purpose of our research is to investigate this possibility using multi-parameter design optimization, which we now discuss.

3. MULTI-PARAMETER OPTIMIZATION

The fundamentals of EGO were presented in References 8 and 11. We described our Matlab implementation of EGO in previous papers.[7, 9, 10] There is a fundamental difference between our previous papers and the current one. Previously we used two design variables for demonstrating feasibility and ease in visualizing results. The current problem requires six design variables as shown in Table 1. Larger dimensionality causes the following steps in the EGO algorithm to be much more difficult: (1) determination of correlation parameters[8, 9, 10, 11] and (2) maximization of a quantity called expected improvement.[8] We will briefly describe the modifications to EGO required to address these two problems.

EGO models the deterministic output (cost function) of a complex computer code as the realization of a stochastic process.[7, 8, 10] The output is deterministic since replicate observations for identical input are uninformative. The stochastic model represents the fact that we do not know the outcome until we perform a simulation. The stochastic nature is captured in an "error correlation matrix" which depends on the current design points, the values of the cost function at the design points, and a set of correlation parameters. The number of correlation parameters is equal to the dimensionality and accurate and efficient determination of these parameters is essential. Values for the correlation parameters are found by maximizing the sample data set likelihood function relative to these parameters. The data set includes the current set of n input vectors, **x,** (i.e. current set of designs) and the $n \times 1$ output vector, **y,** representing the corresponding n cost function values.[8, 11] The number of input vectors, n, is given by the number of

initial data samples (input vectors) plus the current number of iterations. One new design is produced per iteration of the algorithm. Maximizing the data set likelihood function is *nontrivial* for large dimensionality. We now discuss a technique which can deal with this problem.

Following Welch[11] we use an algorithm which sequentially introduces the correlation parameters. The algorithm is called a "screening algorithm" since it gives an indication of the importance of each design variable. The design variables with larger correlation parameters are more active, or important. The ones with very small values for their correlation parameters are not important. The algorithm performs a series of less expensive one-dimensional line searches. Correlation parameters are used to construct a DACE predictor,[8, 9, 10] a cheap surrogate model of the response surface. The DACE predictor uses very fast and simple matrix operations to calculate a quantity called "expected improvement."[8] The location (in the input space of design variables) of the maximum value of this quantity is used as the new design point. Finding this location is very difficult and time consuming for large dimensionality. We now discuss the modification required to address this problem.

For small dimensionality, a search technique described by Cox and John[12] which uses exhaustive search, along a multi-dimensional grid, has proven successful.[9, 10] For large dimensionality this is impractical. We implemented a multi-dimensional, continuous-parameter, genetic algorithm (CPGA) which is both efficient and sufficiently accurate in finding the combination of design parameters where the expected improvement is maximized.[13] This new design point is passed to the CEM simulation for cost function evaluation. The new design point and cost function value are then added to the data set.

Coupling an optimization engine with a cost function evaluation engine can be one of the more challenging aspects in setting up a design optimization. For our problem, a full-wave CEM simulator was required. We selected the 3D full-wave, finite element code HFSS (High Frequency Structure Simulator).[14] One attractive feature of this code is its ability to export results directly into Matlab.[15] We also required external control of the program, in this case from our Matlab implementation of EGO. Initially, we submitted requests to HFSS using Ansoft's Visual Basic Scripting (vbs) language and the HFSS batch job command line interface. The values of the design variables selected by EGO for the next design point were coded into appropriate vbs commands, along with commands to open the project, run the analysis, and export results. This script was then called by a command line execution of HFSS, which launched the program, ran the script (which analyzed the appropriate antenna configuration and exported results) and then terminated HFSS. While this method yielded acceptable results, it suffered from the overhead of repeatedly launching and terminating HFSS. Since our ability to run HFSS also depended on acquiring a floating-license at runtime, a major drawback to this method was the continual acquiring and surrendering of the license and the potential loss of the license.

A better method was suggested by Dr. Eric Zheng, a technical services engineer at Ansys Inc. Using an Active X Server opened to the HFSS Script Interface we could open and control HFSS directly from Matlab. This had two major benefits over the batch-file interface. First, the program could be opened once and maintained open throughout the entire optimization which eliminated the overhead of opening and closing the program many times. More importantly, HFSS results, such as numbers of meshing cycles before convergence, overall model size, and program errors, could be reported back to Matlab and then used to guide or terminate the design optimization.

Antenna Z parameters were exported from HFSS to Matlab. Using the Z parameters we could determine the best voltage standing wave ratio (VSWR) of the antenna when matched to feed line impedance Z_0 which we allowed to have any value from 20 to 250 Ω. The cost function penalized the design by summing the squared difference, i.e. $(\text{VSWR}-1.25)^2$, at any frequency where the VSWR was larger than 1.25:1. Minimizing this cost function provides the best impedance match.

4. FTBA OVER A PEC GROUND PLANE (ANTENNA BALUN/FEED)

The indefinite material described in **Section 2** is not currently available. Therefore, to obtain measured data for an optimized antenna design generated using EGO/HFSS we designed a simpler antenna using a finite PEC ground plane. This antenna structure is the FTBA element over a conducting disk (PEC) shown in Figure 5 below. The structure has been fabricated and tested. It is a special case of the short backfire antenna without the front reflector. In Reference 5 on page 111, reflector #1, i.e. R_1, is absent and on reflector #2, the rim height, w, is zero. Since a feed will be required when the antenna structure is built using a MM, we also use this simpler antenna structure to design and optimize the feed. This will help us learn more about designing the feed. The balun/feed structure goes through the ground plane and differentially drives the dipole (Figure 5 below).

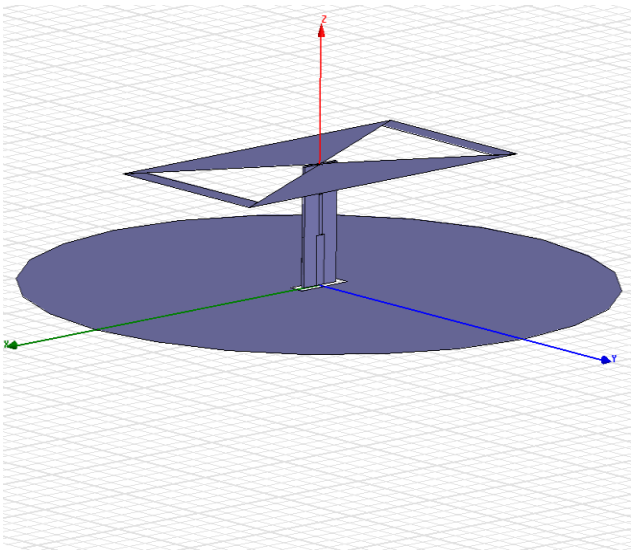

Figure 5. FTBA over a finite PEC ground plane.

A front view of the balun/feed structure is shown in Figure 6 below and is similar to the one used by Qu, et al.[1] The structure is a double-sided Rogers 5880 substrate (ϵ_r = 2.2) which is 31 mils (0.787 mm) thick and 10 mm wide. We use a coaxial SMA connector to couple a source to the feed. Since the coax is unbalanced we require a balun to feed the balanced dipole. The first (bottom) trace in Figure 6 is unbalanced 50 ohm microstrip with an appropriate ground on the back side of the Rogers substrate. The length of the trace is determined through optimization. The middle trace is a transition section of balanced double-sided parallel stripline (DSPSL). The length and width of this trace is determined through design optimization. The top trace is 120 ohm DSPSL. The transition and the top traces have identical traces on the back side of the substrate. As discussed in the last paragraph in **Section 3,** the 120 ohm value was found by optimizing the design of the FTBA over the PEC ground plane using a lumped port (voltage gap) excitation and no feed structure. Therefore, we separated the design of the feed (having only three design parameters) from the antenna design.

The length of the top trace depends on the lengths of the first two traces since the height of the antenna above the ground plane has been determined in the antenna design optimization. We again used EGO/HFSS to find optimum values for: (1) the length of the 50 ohm microstrip trace, (2) the length of the DSPSL transition trace, and (3) the width of the transition trace. The values are: 11.37 mm 10.71 mm and 1.57 mm, respectively.

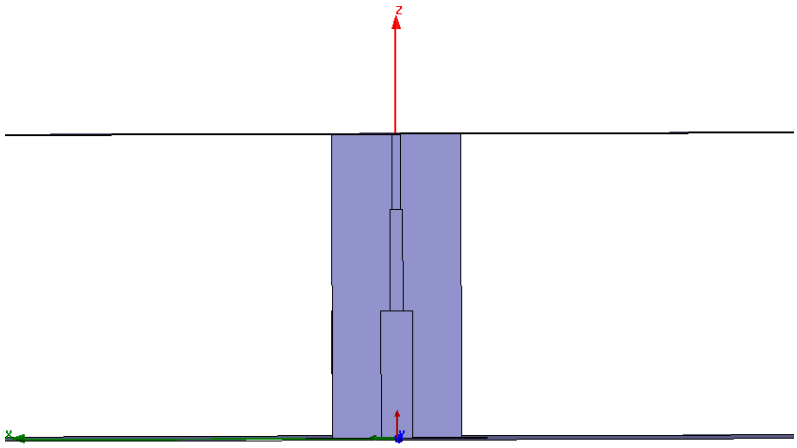

Figure 6. Front view of the balun/feed structure.

5. RESULTS

The three designs are shown in Table 2. The first design has relative permittivity tensor ε_r = diag[1 -1 1] and relative permeability tensor μ_r = diag[1 1 -1] which has a unit magnitude surface reflection coefficient for TE waves only. The second design has relative permittivity tensor ε_r = diag[-1 -1 1] and relative permeability tensor μ_r = diag[1 1 -1] and has a unit magnitude reflection coefficient for both TE and TM waves. The MM thickness for the FTBA over the finite PEC ground plane is zero since there is no MM.

Table 2. Antenna design variables selected by EGO design optimization for the three designs.

Design Variable		MM-Backed (TE case)	MM Backed (TE/TM case)	FTBA over Finite PEC
t_m	MM Thickness (mm)	15.94	14.10	0
$D_m/2$	MM Radius (mm)	63.11	63.65	70.00 (PEC)
h	Dipole height (mm)	8.47	10.00	23.94
L	Dipole length (mm)	41.30	39.54	43.31
α	Bowtie angle (degrees)	119.53	119.89	125.32
W_a	Folding arm width (mm)	1.56	1.01	5.00

We show the predicted and measured return loss for the FTBA over a finite PEC ground plane in Figure 7. The measured results agree very well with the predicted results. The predicted realized gains for the two MM-backed designs are shown in Figure 8. Also shown is the predicted realized gain for the cavity-backed FTBA.[1] The gains for the MM designs are comparable to the cavity-backed antenna but have more variation across the band. For the TE case there is a blind spot near 3.75 GHz. The gain for the combined TE/TM case shows less variation and has higher gain in the region of 3.75 GHz where the cavity-backed FTBA has decreased gain. Both designs had acceptable VSWR (< 2:1) over the frequency band. The predicted realized gain of the FTBA over a finite PEC ground plane is

shown in Figure 9. There is significant gain reduction at the higher end of the frequency band. The gain for our optimized design is generally higher across the band than the gain for the same case reported by Qu.[1] The gain for our optimized design is lower near 4 GHz.

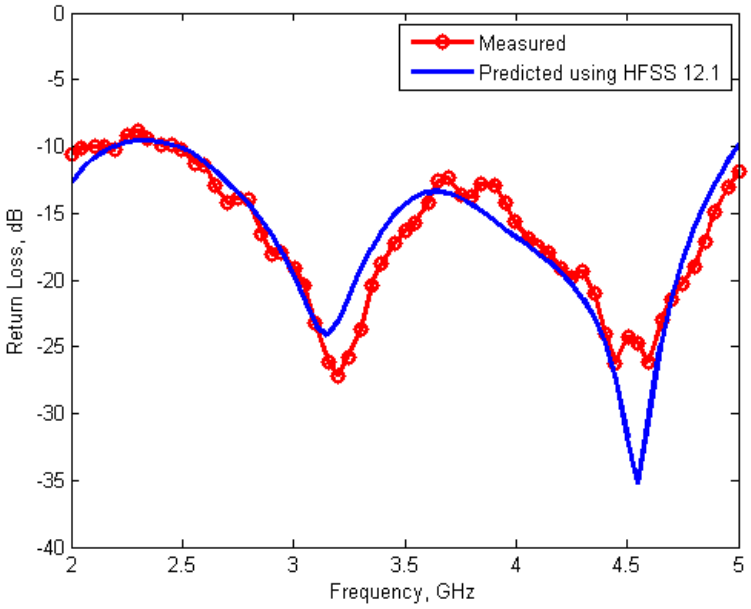

Figure 7. Measured and predicted return loss for the FTBA over a finite PEC ground plane (Figure 5). The optimized design is shown in the last column of Table 2.

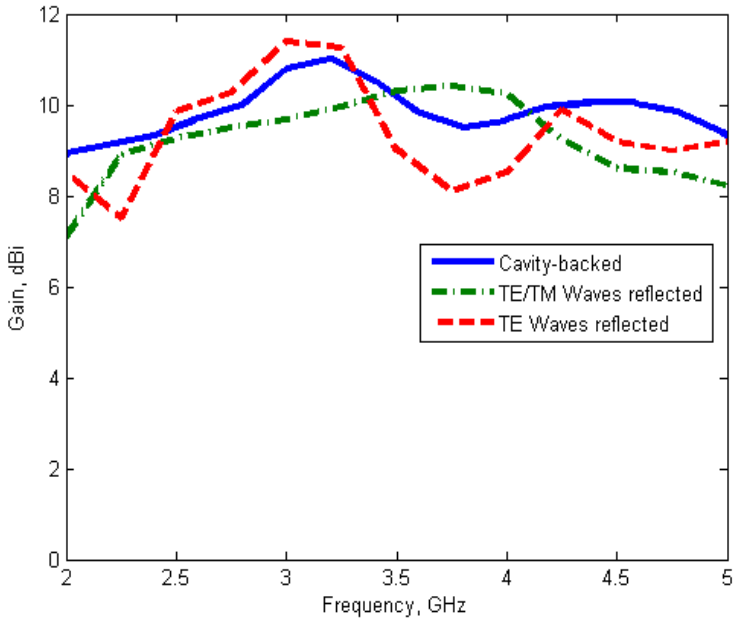

Figure 8. Predicted gains for: (1) the cavity-backed FTBA (Solid); (2) MM-backed FTBA TE Case (Dashed); and (3) the MM-backed FTBA TE/TM Case (Dot-Dashed).

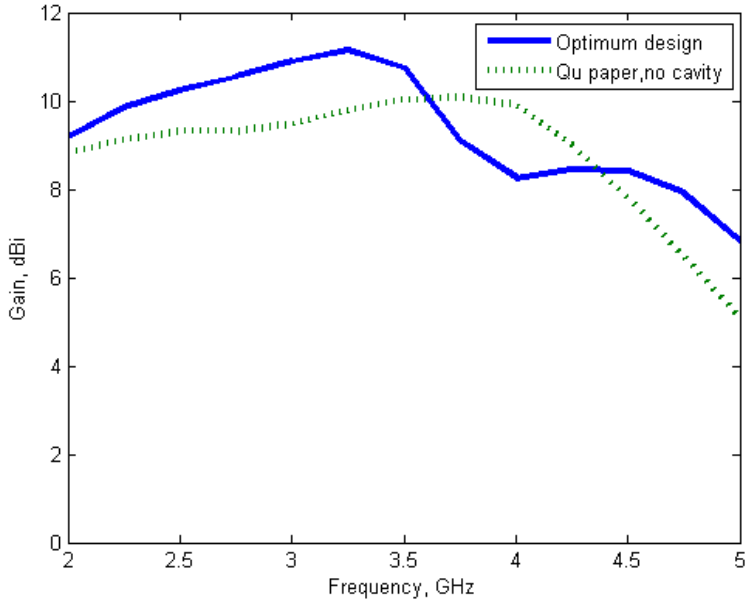

Figure 9. Gains for: (1) the optimized design of the FTBA over a finite PEC ground plane and (2) the same case from Qu (Figure 8 (b), without rim).[1]

Design optimization was accomplished using the Matlab implementation of EGO coupled with the full wave CEM capabilities of HFSS. Each new design from EGO (in the initial data set and in each algorithm step) was analyzed as an individual HFSS project. The convergence criterion in the HFSS **Solution Setup Window** under the **General** tab for Maximum Delta S per Pass was 0.01. Each HFSS project required between four and 15 adaptive meshing passes. Some designs failed to converge but all of the "good designs," i.e. designs with low values for the cost function, converged. Simulations were performed on a 2.66 GHz Dell Precision PWS 490 using four HFSS distributed solve engines in parallel and 32 GB of RAM.

The initial data set was 30, 30, and 50 for the three cases in Table 2. The recommended number of initial data samples is 11k-1, where k is the dimensionality.[8] This is equal to 65 for our antenna design case, therefore we are undersampling initially. We have, however, had success in the past using a smaller number of initial samples. The design parameters for each sample in the initial data set were selected using a standard Latin Hypercube technique.[8]

The total number of cost function evaluations (one evaluation requires the complete run and analysis of an HFSS project with a given set of design variables) was 138, 133, and 97 for the three designs. The computation time per design varied for the different MM configurations but was between 40 and 70 minutes per sample. Approximately 1/3 of the time was required for the evaluation of the expensive cost function using HFSS and 2/3 was required by EGO to find a new design. Therefore the overhead of the optimization algorithm is not trivial. Computation time is saved in the long run by reducing the total number of expensive cost function evaluations. Including the number of samples in the initial data set, design optimization takes approximately 150, 89, and, 48 hours respectively for the three antenna designs in Table 2.

6. SUMMARY AND CONCLUSIONS

We showed how the EGO algorithm could be used to design an FTBA over a MM ground plane. Two enhancements were required for large dimensionality: (1) a "screening" algorithm which sequentially introduces correlation parameters and (2) a GA which replaces exhaustive gridding for finding new design points. We were able to seamlessly couple our Matlab EGO code with HFSS using the Active X Server interface. EGO successfully found MM-backed FTBA designs with acceptable VSWR across the frequency band with realized gains comparable to the cavity-backed FTBA. These designs are still almost as large vertically (about $\lambda/4$ at the band center) as the cavity-backed FTBA. Our antenna design optimization technique was proven on a simpler antenna design where we also optimized the design of the balun/feed.

ACKNOWLEDGMENTS

We thank the Air Force Office of Scientific Research (AFOSR), Dr. Harold Weinstock, for funding portions of this work. We acknowledge the outstanding support of Ms. Michelle Champion in fabricating the FTBA and the balun/feed. The antenna was expertly assembled and tested by personnel at the Ipswich Antenna Test Site, Ipswich, MA, including: Jim Kenney, Ed Martin and Richard Demasi. We express our deep appreciation to Dr. David Smith of Duke University for expert advice on metamaterials and Dr. Eric Zheng at Ansys Incorporated in helping us understand the scripting required for interfacing Matlab with HFSS and for advice on modeling the antenna.

REFERENCES

[1] Qu, S-W., Li, J-L., Chan, C.H. and Li, S., "Wideband and Unidirectional Cavity-Backed Folded Triangular Bowtie Antenna," IEEE Transactions on Antennas and Propagation, 57(4), 1259-1263 (2009).
[2] Balanis, C.A., [Antenna Theory: Analysis and Design], John Wiley and Sons, Inc., New York, 449 (1997).
[3] Li, R., Thompson, D., Tentzeris, M.M., Laskar, J. and Papapolymerou, J., "Development of a Wideband Short Back Fire Antenna Excited by an Unbalance-fed H-Shaped Slot," IEEE Transactions on Antennas and Propagation, 53(2), 662-671 (2005).
[4] Kirov, G.S., "Design of Short Back Fire Antennas," IEEE Transactions on Antennas and Propagation Magazine, 51(6), 110-120 (2009).
[5] Smith, D.R. and Schurig, D., "Electromagnetic Wave Propagation in Media with Indefinite Permittivity and Permeability Tensors," Physical Review Letters, 90(7), 077405-1 - 077405-4 (2003).
[6] Smith, D.R., Padilla, W.J., Vier, D.C., Nemat-Nasser, S.C. and Schultz, S., "Composite Medium with Simultaneously Negative Permeability and Permittivity," Physical Review Letters, (84)18, 4184-4187 (2000).
[7] Southall, H.L., O'Donnell, T.H. and Derov, J.S., "Optimum Design of Antennas Using the Efficient Global Optimization (EGO) Algorithm," Evolutionary and Bio-Inspired Computation: Theory and Applications Conference IV Proceedings of SPIE Defense Security and Sensing Symposium, 7704, 770408 (2010).
[8] Jones, D.R., Schonlau, M. and Welch, W.J., "Efficient Global Optimization of Expensive Black-Box Functions," Journal of Global Optimization, 13, 455-492 (1998).
[9] Southall, H.L., O'Donnell, T.H., and Kaanta, B., "Efficient Global Optimization for Antenna Design," Proceedings of the 2008 Antenna Applications Symposium at Robert Allerton Park, IL (2008).
[10] O'Donnell, T.H., Southall, H.L. and Kaanta, B., "Efficient Global Optimization of a Limited Parameter Antenna Design," Evolutionary and Bio-Inspired Computation: Theory and Applications Conference II Proceedings of SPIE Defense & Security Symposium, 6964, 69640J (2008).
[11] Welch, W.J., Buck, R.J., Sacks, J., Wynn, H.P., Mitchell, T.J. and Morris, M.D., and Jones, D.R., "Screening, Predicting, and Computer Experiments," Technometrics, 34, 15-25 (1992).

[12] Cox, D.D. and John. S. “SDO: A Statistical Method for Global Optimization,” [Multidisciplinary Design Optimization: State of the Art; N.Alexandrov and M.Y. Hussaini eds.], SIAM, Philadelphia, 315–329 (1997).
[13] O’Donnell, T.H., Southall, H.L., Santarelli, S., and Steyskal, H., “Applying EGO to Large Dimensional Optimizations: A Wideband Fragmented Patch Example,” Evolutionary and Bio-Inspired Computation: Theory and Applications Conference IV Proceedings of SPIE Defense Security and Sensing Symposium, 7704, 770407 (2010).
[14] http://www.ansoft.com/products/hf/hfss/
[15] http://www.mathworks.com/products/matlab/

VARIABLE UHF-BAND ARTIFICIAL MAGNETIC CONDUCTORS

D.J. Gregoire, C.R. White and J.S. Colburn
HRL Laboratories LLC
3011 Malibu Canyon Rd.
Malibu, CA 90265

G.P. Johnson
The Boeing Company
Seattle, WA

Artificial magnetic conductors (AMC) are laminated structures that reflect incident radiation with a zero degree phase shift at their resonant frequency. An AMC enables low-profile antennas because it allows the antenna to be mounted with its polarization parallel to the surface. AMCs are typically composed of a periodic grid of metallic elements on a grounded dielectric substrate. Reactive elements can be used to load the grid in order to tune the resonant frequency. In this paper, we present methods for designing reactively-loaded AMCs using analytic methods and full-wave simulation, highlighting the effects of electrical loss in components and materials on performance. We compare simulations and measurements of a variable UHF-band AMC that uses varactors to load its grid and tune its resonant frequency from *200* to *500* MHz. Its ±*90˚* bandwidth varies from *4* to *12%* respectively. Measurements indicate more loss is present in the AMCs than expected by simulations. The source of the additional loss is unknown at this time and continues to be under investigation.

1. Introduction

A magnetic conductor is a hypothetical material that is the magnetic analog to the electrical conductor. Its boundary conditions dictate that transverse components of magnetic field vanish at the boundary, and image charges and currents have the same polarity as their sources. Such a material, if it exists, can be useful for antenna applications because it would allow antennas to be placed with their radiation currents parallel to a surface, expanding the design space of low-profile conformal antennas.

In recent years, many authors [1-6] have published methods of making artificial magnetic conductors (AMC) by using resonant structures that create magnetic-conductor boundary conditions at a given frequency . A typical AMC is realized with a laminated structure composed of a periodic grid of reactive elements distributed on top of a grounded dielectric layer. The reactive elements come in many shapes and sizes [2-5]. They may have vias to the ground plane wherein each element resembles a mushroom[3], or they may be designed with complex fractal shapes to reduce their size or tailor their frequency response and bandwidth. Lumped reactive elements are often used to tune AMC response, or variable elements such as varactors actively modify AMC response[6] .

a.)

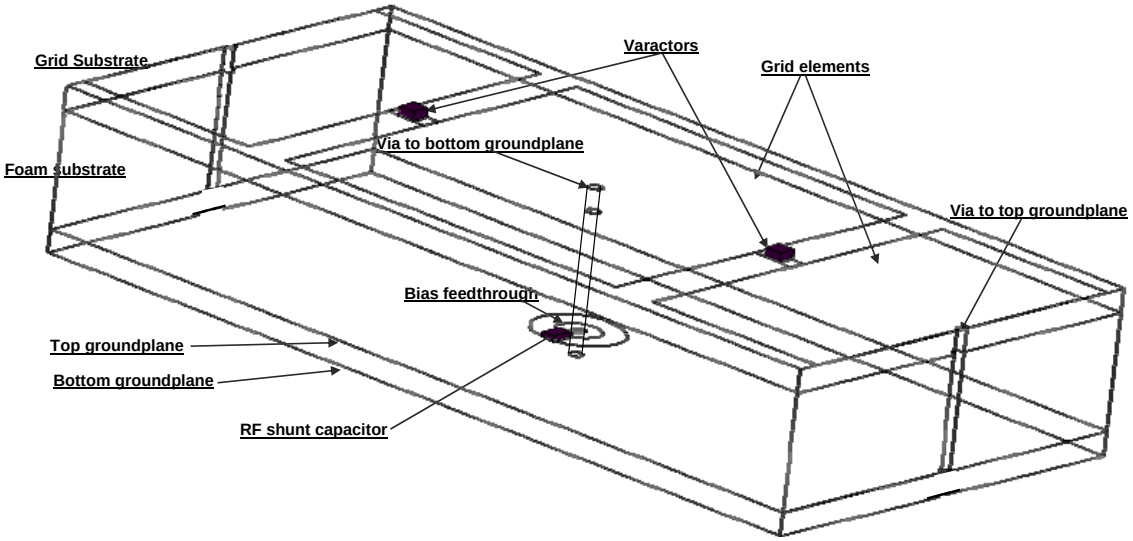

b.)

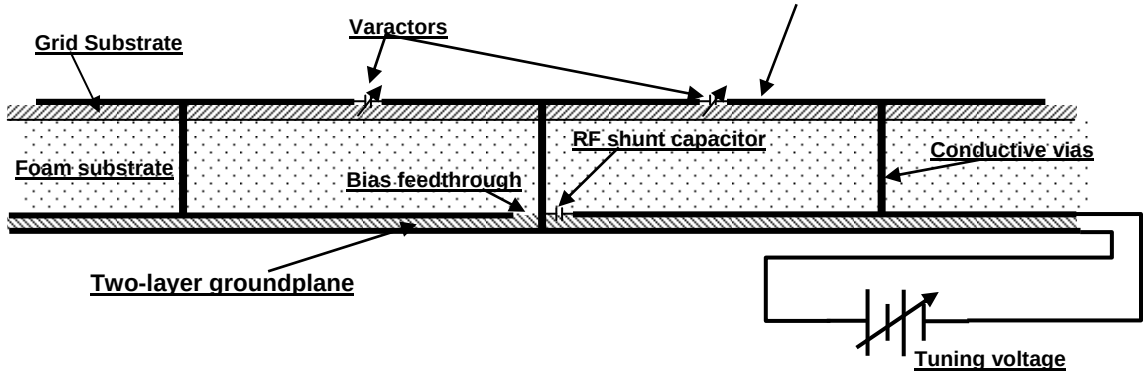

Figure 1. Variable UHF AMC Schematic The variable AMCs are composed of periodic metallic patches distributed on a dielectric substrate with variable capacitors between grid elements. The bulk of the substrate thickness is made of the lightweight rigid foam. Thicknesses of 0.500" and 0.750" were used in the fabricated AMCs. Bias voltage is applied between the two groundplanes and conducted to the varactors through alternating grid elements and vias. Feedthroughs with RF shunt capacitors in the top groundplane allow the vias to connect to the bottom groundplane without RF leakage.

In this paper, we present the simulations and measurements of an artificial magnetic conductor (AMC) design that scales to the UHF range (200 to 400 MHz) by loading the AMC grid with capacitive elements that reduce the resonant frequency by a factor of 3. We also present a variable AMC loaded with variable capacitance varactor diodes whose resonant frequency can be tuned within a range from 200 to 450 MHz.

Scaling microwave AMCs designs to VHF/UHF frequencies is problematic because of the long wavelength and the corresponding large AMC unit cell size. AMCs have been fabricated and demonstrated for many different frequency bands greater than 1.0 GHz. In order to realize AMCs at lower frequencies, such as in the VHF band (30 – 300MHz) and in the lower end of the UHF band (300 MHz – 3 GHz), the size must be scaled proportionally. AMC bandwidth is proportional to substrate thickness[11]. So, while a 10 GHz AMC is easily fabricated using thin (0.025 – 0.050" thick) substrates of standard electronic circuit board material, a VHF AMC requires substrate thickness 0.500" to 1.00" and greater. Therefore, using standard electronic substrates is prohibitive for practical application because of availability, cost and weight. Also standard circuit board substrates typically have relative permittivities of 2.0 or more. The higher the substrate permittivity, the lower the bandwidth of the AMC because the capacitance between the grid and the groundplanes is proportional to the substrate permittivity.

The AMCs presented in this paper overcome those limitations by laminating a thin layer of circuit board material with thick structural foam (See Figure 1).The top layer supports the AMC's metallic structures, while the foam layer provides a thick, light weight and rigid substrate that enables the high-bandwidth, low-cost, lightweight AMC. The foam enables larger AMC bandwidth because its relative permittivity is typically ~ 1.05, much lower than most circuit board substrates.

2. AMC Design Principles

An AMC is most readily characterized by the phase shift it imposes on the reflection of an incident electromagnetic wave. Whereas an electric conductor imposes a 180° phase shift to the reflected wave, the analogous phase shift is 0° for the magnetic conductor. For the AMC, the phase shift is 0° at the resonant frequency, f_o . It is generally accepted that the operating range of the AMC is where its reflected phase shift is within the range $|\phi_r| \leq 90^\circ$. It has been suggested that a more restrictive range, e.g. $|\phi_r| \leq 45^\circ$, is more appropriate for antenna applications[7].

Figure 2 shows the reflected phase and magnitude as simulated for an example AMC with various capacitive loadings. An equivalent parallel LRC circuit can be used to exactly describe the AMC response over a wide range around the resonant frequency. Therefore, the LRC circuit model is useful for understanding the broad characteristics of AMCs. THE LRC impedance is

$$Z = \frac{j\omega L}{1 - \omega^2 LC + j\omega L / R} \tag{1}$$

The resonant frequency is

$$f_o = \frac{1}{2\pi\sqrt{LC}} \tag{2}$$

The refection coefficient of an incident wave with impedance Z_o is

$$\Gamma = \frac{Z - Z_o}{Z + Z_o} \tag{3}$$

In the limit $R \ll \omega L$, $\phi_r = \angle\Gamma = 0°$ at $f = f_r$, and the fractional bandwidth defined by the range where $|\phi_r| \leq 90°$ is

$$BW = \frac{\sqrt{L/C}}{Z_o} \tag{4}$$

AMCs are often formed by lamination of a metallic grid on a grounded dielectric substrate. The grid can be loaded with lumped reactive elements to tune the AMC frequency and/or bandwidth to values not achievable with the grid alone. The loaded AMC can be represented by the transmission line model [8,9] of Figure 3, where the AMC impedance seen by the incident wave is parallel combination of the grid impedance, Z_g in series with grid loading Z_{load}, with the dielectric impedance $Z_d = jZ_2 \tan(k_{2z}d)$.

$$Z = \frac{j\left(Z_g + Z_{load}\right) Z_2 \tan\left(k_{2z}d\right)}{\left(Z_g + Z_{load}\right) + jZ_2 \tan(k_{2z}d)} \tag{5}$$

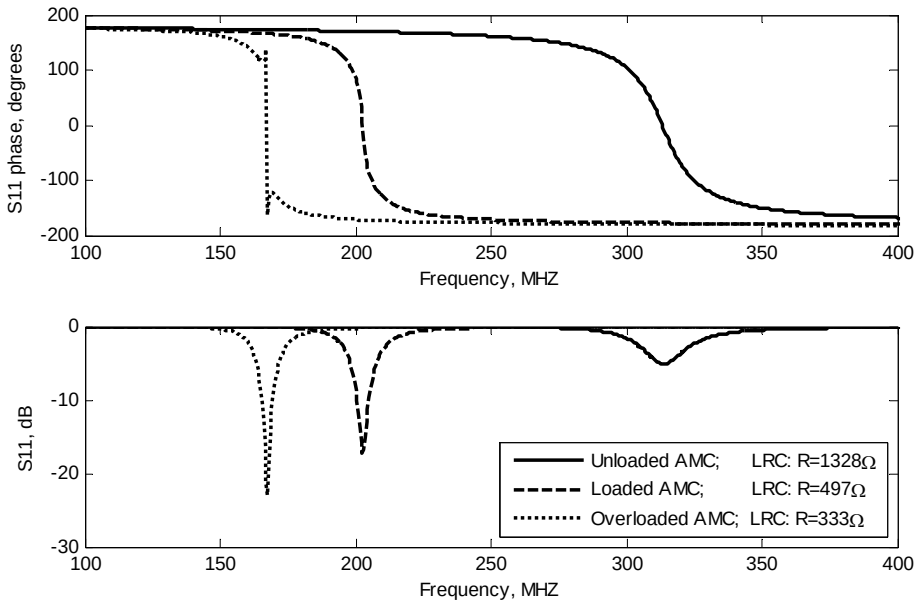

Figure 2. Loaded-AMC response. The top and bottom graphs show the phase and amplitude response of a wave reflected from a variable. As the loading is increased, the resonant frequency is shifted lower and the bandwidth is decreased. If losses in the system are controlled as in the middle trace, the resistance of the equivalent LRC circuit is greater than Z_o, and the phase response maintains a smooth transition through $0°$. If AMC is overloaded to the point where the resistance of the equivalent LRC circuit is less than Z_o, then the phase response at $0°$ is very abrupt.

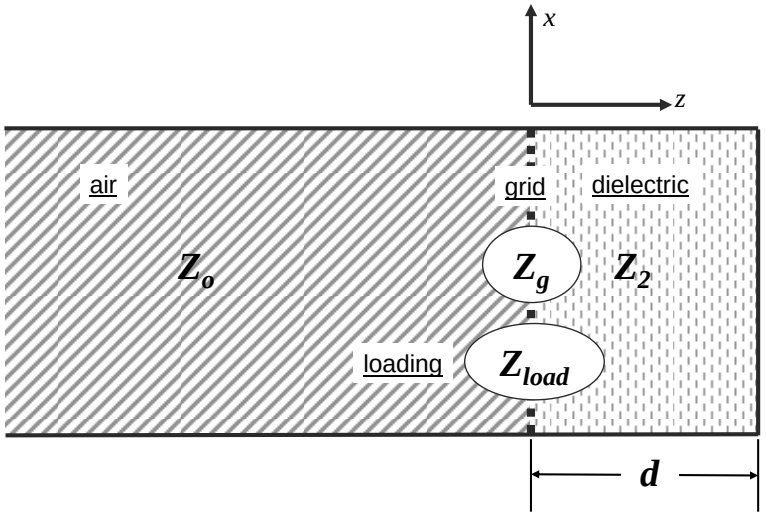

Figure 3 AMC transmission line model for a loaded AMC. The loaded AMC can be modeled as an incident wave with impedance Z_o incident on a grounded dielectric with impedance Z_2 and in parallel with a combination of the grid impedance Z_g and the load impedance Z_{load}.

Where $Z_2=\eta_2=\eta_o\sqrt{\mu_2/\varepsilon_2}$ is the wave impedance in the dielectric, $k_{2z}=k\sqrt{\mu_2\varepsilon_2}$ is the longitudinal wavenumber in the dielectric, *d* is the dielectric thickness, *k* is the free-space wavenumber, and ε,μ and η refer to relative permittivity, relative permeability and wave impedance respectively. For the lossless case, $\Gamma=1$ at the resonant frequency; that occurs when $Z=\infty$ which occurs when the denominator of Eqn. (5) goes to zero.

If the grid is formed by an array of metallic squares, then the grid impedance can be expressed as being due to a grid capacitance, $Z_g=-j/(\omega C_g)$. The grid capacitance can be estimated in a number of ways [8,9]. For more complex grids, the grid impedance can be estimated by simulating wave reflection Γ on the unloaded grid on a grounded dielectric substrate. Using equations (3) and (5), one can obtain a numerical value for Z_g that can be plugged back into equations (5) to obtain an AMC impedance that is valid over a wide range of substrates and grid loading.

The quantities in the simple LRC model can be related to the transmission line model by

$$\omega L = Z_2 \tan(k_{2z}d) \text{ and } C=C_g+C_{load} \tag{6}$$

in the case where the grid loading is purely capacitive as in the case where a capacitor or an ideal varactor diode is inserted between grid elements. From equations (1), (4) and (6), it is seen that capacitive loading leads to a decrease in the resonant frequency and the AMC bandwidth by the factor $\sqrt{C_g/(C_g+C_{load})}$. This is illustrated in Figure 2.

Effects of Loss on AMC Phase Response

An AMC is by definition a surface where the phase of a reflected wave decreases smoothly from 90° to -90° as the frequency increases. If losses in the dielectric substrate, the grid or in the grid loading are too high, then the phase curve does not pass through the 90° to -90° range making it useless as an AMC. On the Smith chart, this condition is represented as a curve that never crosses into the high-impedance region where $Z>Z_o$, and we therefore designate this as the low-impedance condition.

In the simple LRC model, the transition to the low-impedance condition occurs when the equivalent resistance decreases to less than the incident wave's impedance $R \le Z_o$. As *R* decreases towards Z_o, the bandwidth decreases more and more from Eqn. (4) until at $R=Z_o$, the phase shift at f_o becomes very sharp and the bandwidth is zero. This is because at the resonant frequency, $Z=R$, and if $R=Z_o$, then $\phi_r = atan(0/0)$ is undefined.

In general, the transition to the low-impedance condition is found by writing equation (3) as

$$\Gamma = \frac{Z - Z_o}{Z + Z_o} = \frac{|Z|^2 - Z_o^2 + 2jZ_o \,\mathrm{Im}(Z)}{|Z|^2 + Z_o^2 + 2Z_o \,\mathrm{Re}(Z)} \tag{7}$$

and the phase of the reflected wave as

$$\phi_r = \mathrm{atan}\left(\frac{\mathrm{Im}(\Gamma)}{\mathrm{Re}(\Gamma)}\right) = \mathrm{atan}\left(\frac{2Z_0 \,\mathrm{Im}(Z)}{|Z|^2 - Z_o^2}\right) \tag{8}$$

At the resonant frequency, $\phi_r(f_o)=0$, and it follows from Eqn. (8) that $\mathrm{Im}(Z(f_o))=0$ and $|Z(f_o)| = \mathrm{Re}(Z(f_o))$. So if $\mathrm{Re}(Z(f_o))=Z_o$ at the resonant frequency, then $\phi_r(f_o)=\mathrm{atan}(0/0)$ is undefined. Therefore, the low-impedance condition occurs when

$$\mathrm{Re}(Z(f_o)) \le Z_0 . \tag{9}$$

This expression can be used in conjunction with the grid-loaded dielectric slab model and equivalent circuit models to determine the point where material loss causes the low-impedance condition in an AMC.

Consider the AMC model of Figure 3 where the dielectric includes loss in terms of complex permittivity and permeability. We use an equivalent circuit model where the material loss is represented by a resistance in series with the inductance. The low-impedance condition of Eqn. (9) applied to this model occurs when

$$R \ge \frac{L}{CZ_o} \qquad \text{at} \qquad f_o = \frac{1}{2\pi\sqrt{LC}}\sqrt{1 - R^2C/L} \tag{10}$$

Where the equivalent circuit parameters are defined in terms of the AMC geometry and the material properties as

$$\omega L = \mathrm{Im}(A) \quad \text{and} \quad R = \mathrm{Re}(A) \quad \text{where} \quad A \equiv jZ_o\sqrt{\mu/\varepsilon}\,\tan\left(kd\sqrt{\mu\varepsilon}\right) \qquad (11)$$

An interesting consequence of this result is that in the limit where the substrate is electrically thin, then $A \approx jZ_o\mu kd$, and ε has no effect on the phase response, and the resistance in series with the inductor can be neglected. Another circuit model to consider is one where the resistance is included as being in series with the grid capacitance. Simulations and calculations show this to have a major effect on AMC phase response.

3. AMC Simulation

We used a combination of simulation and analytic modeling to evaluate the AMC design and loading for operation at 300 MHz. Figure 1a shows the basis for the AMC model used in simulations with Ansoft's HFSS. In the simulations, the varactor structures in the figure are represented by lumped RLC boundaries that directly include the grid loading into the model. The structure is excited by an incident plane wave from a waveport boundary, and the resulting S11 contains the simulated AMC phase response for the given RLC loading.

In another method, the lumped RLC boundaries are replaced with a lumped port. Then the simulation will produce an S2P matrix between incident wave and the lumped port. The AMC phase response with the lumped port replaced by an arbitrary impedance can then be computed from the S2P [10].This method gives nearly identical results to the HFSS simulation with the RLC boundary and has the advantage that a broad range of grid loading can be quickly calculated from a single simulation. The AMC phase response can also be estimated by using equations (5) and using a grid capacitance that is either obtained through simulation or by various analytic methods [8,9].

Figure 4 graph the effects of grid loading on AMCs geometries. In Figure 4a, the resonant frequency, sensitivity to loading and bandwidth are computed as a function of loading for various unit cell sizes. In Figure 4b, the same quantities are computed for various substrate foam thickness, including the configurations of the two AMC test panels that were fabricated and tested with grid loading of *10* and *8 pF* respectively to tune them approximately to the target frequency of *300 MHz*.

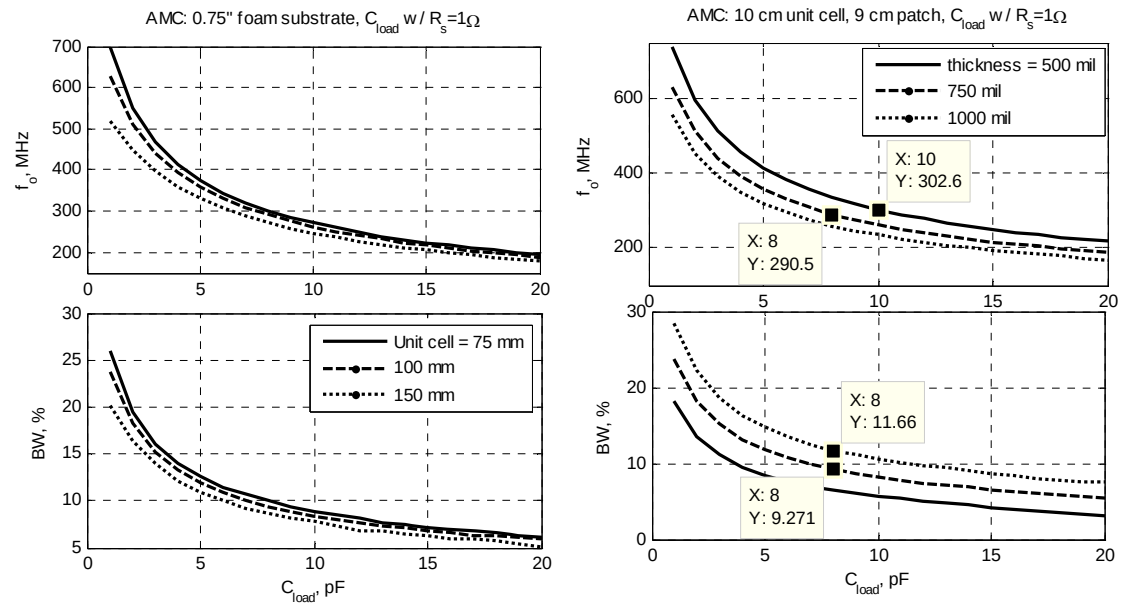

a.) b.)

Figure 4. Effects of AMC Geometry on Grid Loading.
a.) The top and bottom graphs plot the resonant frequency and bandwidth respectively vs. grid loading for AMC cell size of 75, 100 and 150 mm. b.) The same graphs for substrate foam thickness of 0.500, 0.750, and 1.000". As expected, since *L* is proportional to thickness, the bandwidth is proportional to thickness while the resonant frequency increases inversely with thickness$^{1/2}$. The cursors indicate the design loading for the two fixed-frequency test panels fabricated and measured.

4. AMC Fabrication

Three AMC test panels were fabricated and measured with the basic design shown in Figure 1 and illustrated in the photographs of Figure 5. The grids are composed of 9-cm square patches spaced periodically every 10 cm, and etched onto 0.030" thick Rogers 3003 substrate material. Rohacell 31 structural foam ($\varepsilon=1.05$), 0.500" or 0.750' thick is laminated between the grid PCB and the groundplane. Vias connect the center of each grid element to the groundplane. The test panels were 3 x 6 units cells in extent, and approximately 12" x 24". The dimensions were chosen to be compatible with the UHF TEM cell that was used to measure the phase response.

Two of the AMCs, with 0.500" and 0.750" foam substrate spacers respectively, were configured as fixed-frequency devices by loading the grid with capacitors, 10 pF and 8 pF respectively, between grid elements that tuned the resonant frequency to be near 300 MHz. The third AMC had 0.750" foam spacer and was configured to be tunable by loading the grid with Skyworks SMV-1213-004LF varactor diodes that tune the resonant frequency from 200 to 450 MHz. The grid is loaded along one polarization only that matches the TEM cell's field polarization. Installing load capacitors between all edges of the grid elements will make the AMC work in both polarizations.

In the tunable AMC, the varactors are tuned to between 4 and 30 pF by applying low and high voltage to alternating grid elements. The bias voltage is applied to the varactors through conductive vias from each grid element to a two layer groundplane. Each layer of the groundplane is at a different bias voltage. In order to rout the vias from the bottom groundplane to the grid elements without shorting to the top groundplane, the vias pass through holes cut into the top groundplane. The holes disrupt the AMC performance, because RF radiation leaks through the holes into the layer between the groundplanes. We prevent RF leakage by using shunt capacitors between the vias and the top groundplane, effectively shorting the holes to RF radiation.

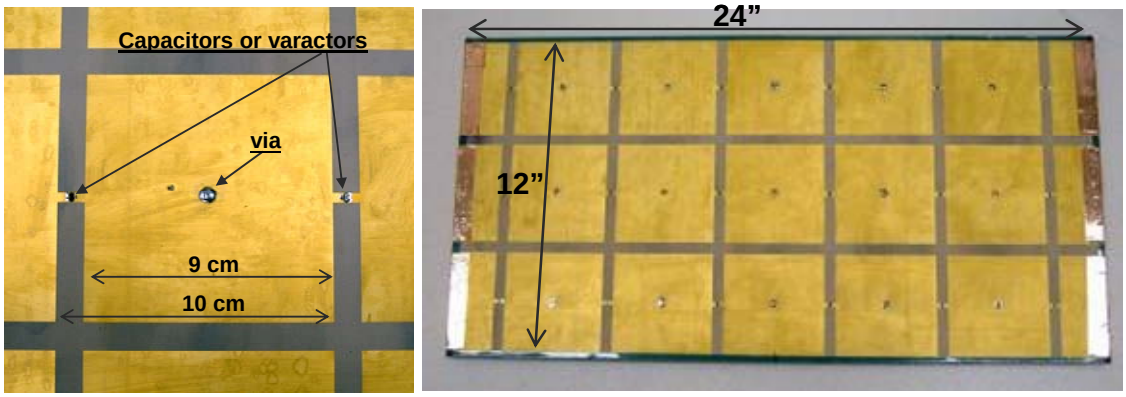

a.) b.)

Figure 5. AMC Test Panel.

5. AMC Measurement

Directly measuring an AMC’s phase response requires launching an incident TEM plane wave at AMC of infinite extent and measuring the phase of the reflection. In practice, AMCs are measured with a variety of methods that approximate this and/or use post-processing to remove edge effects and extract the plane-wave response. High-frequency (> 3 GHz) AMCs are readily made to be several wavelengths in size and can be easily measured in small laboratory antenna ranges. Another method is to insert an AMC sample into a waveguide, and account for the effects of frequency-dependent, non-normal incidence. Measuring UHF AMCs poses a problem because of their inherent unit-cell large size that makes fabrication of a large-enough AMC for antenna range measurements or a large-enough waveguide (WR 2000) intimidating.

We measured the AMC test panels in a UHF/VHF TEM cell (See Figure 9), a large parallel-plate, open-sided waveguide where the sample is radiated with a cylindrical TEM wave, and the reflected wave is measured and post-processed to extract the AMCs impedance boundary condition. The TEM cell plates are separated by 24” and the E field is aligned normal to those plates. The TEM cell provides the equivalent of an infinitely long plane wave, in the E-field direction, from 100 to 1000 MHz.

Prior to inserting the AMC into the TEM cell, a series of calibration procedures are performed using PEC and absorbing boundaries on the test fixture. Background noise is

minimized with vector subtraction of the cell in its open, no target condition. The AMC is designed to fit onto the front face of the test fixture which is a triangular metal wedge whose front face is 12' wide by 24" high.

The data measured in the TEM cell is analyzed using a non-linear fitting routine that compares the data to methods-of-moments simulations of impedance surfaces with known LRC equivalent circuit parameters. In this analysis, we used a simple parallel LRC circuit for the non-linear fitting. A more accurate AMC circuit model would include resistance and inductance in series with the grid loading, and resistance in series with the substrate inductance. Future work will apply more complex circuit models to the TEM cell optimization procedure

Figure 6 shows the results of the TEM measurements of the fixed-frequency AMC test panels and compares them to simulations. For the 0.500" thick AMC with 10-pF loading (Figure 6a), the resonant frequencies of the measured vs. simulation are close, 292 MHz vs. 302 MHz, but the measured phase exhibits the low-impedance condition. If the load capacitor's series resistance is raised to 4Ω (much higher than the quoted value of less than 1Ω) in the simulation, then the simulated phase response closely matches the measured, but the S11 magnitudes don't agree. As of this writing, we don't know the source of this discrepancy and are continuing to investigate it. It may be due to actual loss in the AMC not included in the simulations. It may also be affected by the choice of circuit model used in the TEM cell non-linear fit procedure.

The simulated phase response for the 0.750" thick AMC (Figure 6b) with 8-pF grid loading (f_o*=291 MHz, BW =27 MHz)* nominally agrees with the TEM-cell measurements (f_o*=276 MHz, BW =47 MHz).* However, there is considerable variation in the bandwidth and the magnitude. Adjusting the load capacitor's series resistance to 3Ω in the simulation forces the S11 magnitudes to match

Figure 7 compares the TEM cell results and simulations of the variable AMC test panel. The measured data shows that there is much more loss in the AMC than expected by the simulations. The source of this loss remains unknown and continues to be under investigation. The result of the unexpected loss is that the AMC's tuning range is reduced to *275 to 400 MHz*; below *275 MHz* the equivalent *LRC* resistance falls below 377Ω. Figure 7a graphs the phase response vs. frequency for various loadings, while Figure 7b plots the resonant frequency, S11 at the resonant frequency and the bandwidth vs. the grid loading. As seen in the figures, the measured values agree very well with the simulation when $R_s=5.4\Omega$ is used in the simulations. When the quoted value of $R_s=1.0\Omega$ is used, the agreement suffers. Figure 8 plots the equivalent LRC circuit parameters. The *L, R* and *C* values extracted from the measurement are close to what is expected from the simulations, especially when $R_s=5.4\Omega$.

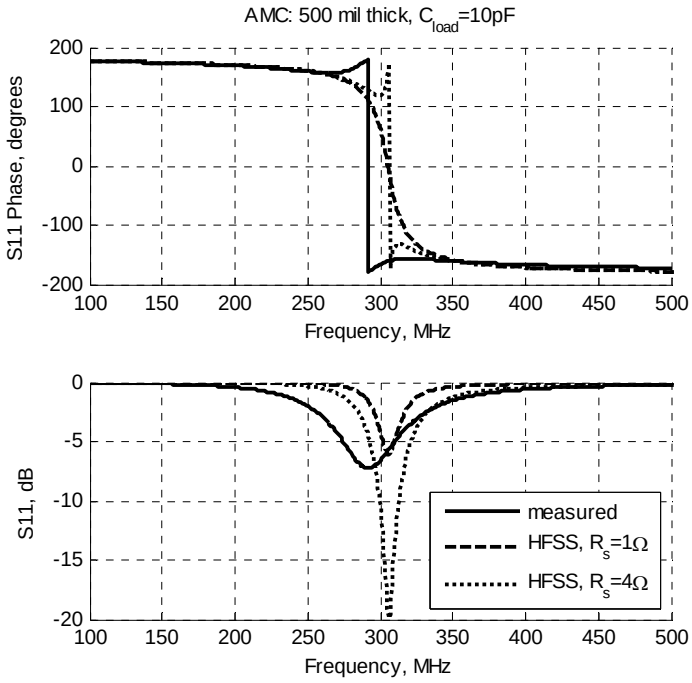

a.)

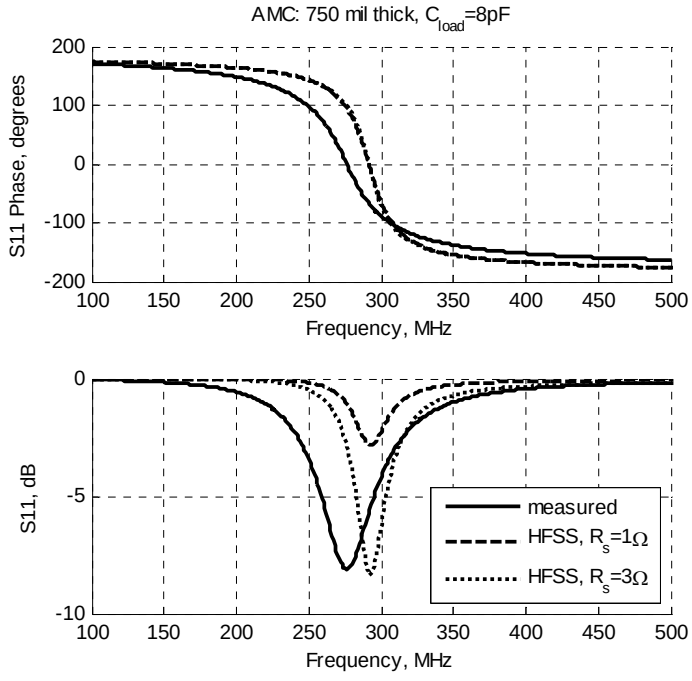

b.)

Figure 6. Measurement of passively-loaded AMCS. Measured and simulated reflection for the fixed-frequency AMCs a.) for the low-bandwidth, 0.500" thick AMC and b.) the high-bandwidth, 0.750" thick AMC (bottom right)

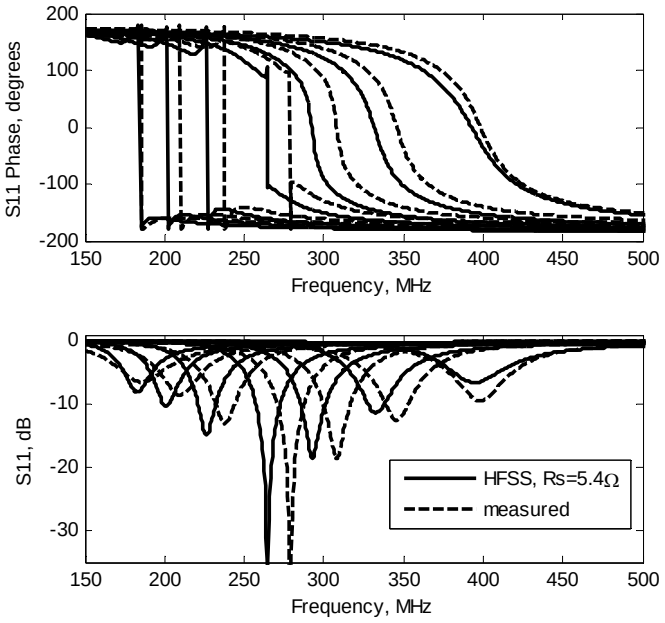

a.)

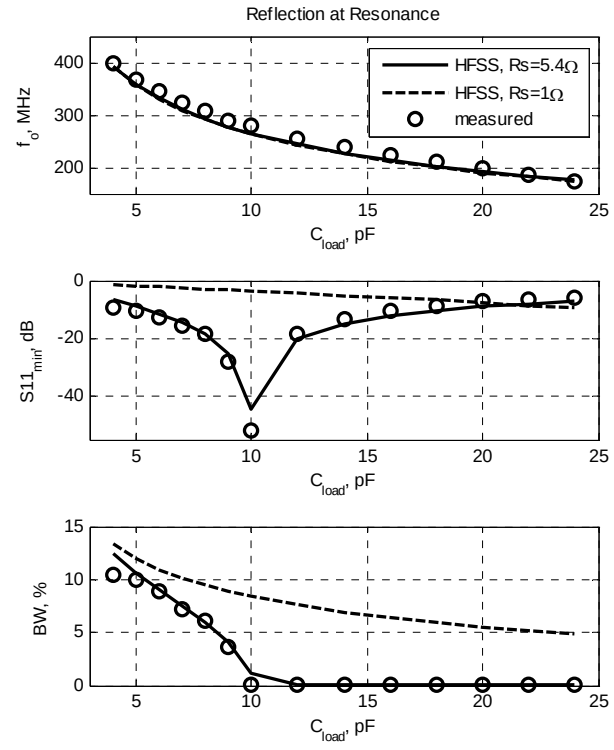

b.)

Figure 7. Measurement of the Variable AMC a.) The simulated (solid lines) vs measured (dashed lines) reflection from the variable AMC for various grid loadings. b.) The resonant frequency, S11 magnitude at the resonant frequency and the bandwidth vs. load capacitance.

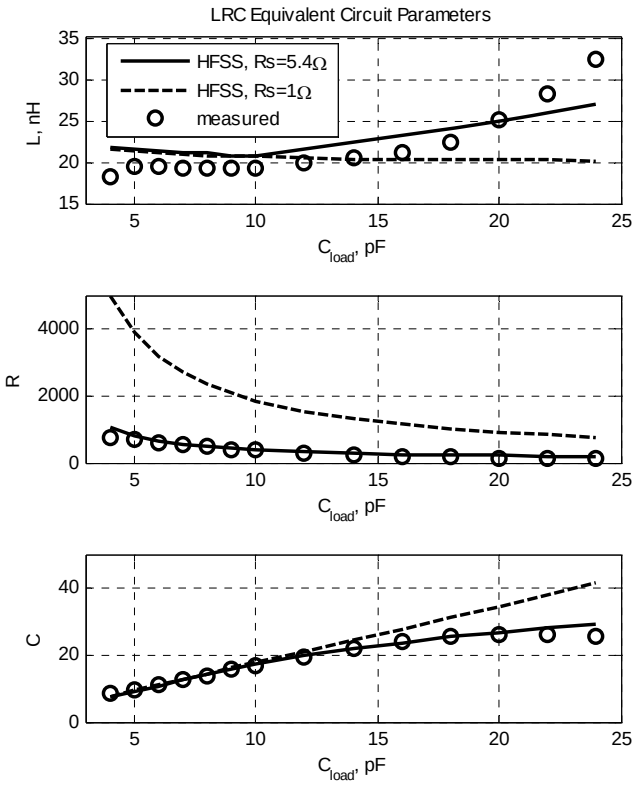

Figure 8 Measured Equivalent LRC Circuit Parameters.

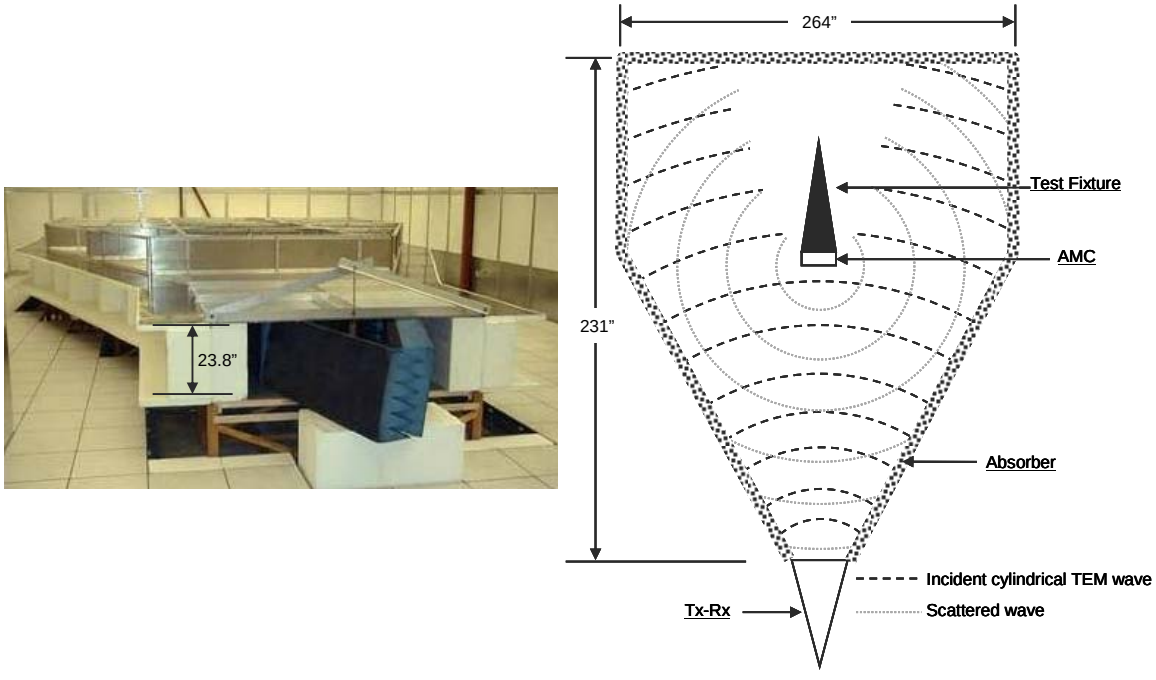

Figure 9. TEM cell photo and schematic

6. Conclusion

We have designed, fabricated and measured fixed-frequency and variable VHF-UHF AMCs. The test panels are 12” wide by 24” tall and either 0.530” or 0.780” thick, and are composed of 9-cm square metal patches with 10-cm spacing on a 0.030” Rogers 3003 substrate laminated to Rohacell RH31 foam. Capacitors or varactors are connected between adjacent grid patches. In the tunable AMC, the varactors are biases with vias connected to a dual ground-plane designed to prevent RF leakage. The AMC test panels are measured in a TEM cell that uses post processing to extract equivalent LRC circuit parameters using a non-linear fitting routine.

The measured values suggest more loss is present in the AMCs than is expected by HFSS simulations. When additional loss is introduced into the simulations, they agree very well with the measurements. The source of the additional loss is unknown at this time and continues to be under investigation. The variable AMC was demonstrated to have a usable tuning range between 275 and 400 MHz using Skyworks SMV1213-004 varactors for tuning.

7. References

[1] F. Yang and Y. Rahmat-Samii, “Electromagnetic Band-Gap Structures in Antenna Engineering”, ser. The Cambridge RF and Microwave Engineering Series. Cambridge, U.K.: Cambridge Univ. Press, 2008.

[2] J.R. Sohn, K.Y. Kim, and H.-S. Tae, “ Comparative study on various artificial magnetic conductors for low-profile antenna”, Prog. Elect. Res., **61**, 27, 2006

[3] M.E. de Cos, F. Las Heras, and M. Franco, “Design of Planar Artificial Magnetic Conductor Ground Plane Using Frequency-Selective Surfaces for Frequencies Below 1 GHz”, IEEE Ant. Wireless Prop. Letters, **8**, 951, 2009

[4] Y. Kim, F. Yang and A.Z. Elsherbeni, “Compact Artificial Magnetic Conductor Designs Using Planar Square Spiral Geometries”, Prog. Elect. Res., **77**,43 ,2007

[5] L Akhoondzadeh-Asl, D.J. Kern, Peter S. Hall, and D.H. Werner, “Wideband Dipoles on Electromagnetic Bandgap Ground Planes”, IEEE Trans. Ant. Prop., **55**, 2426, 2007

[6] T.H. Hand, “Design and Applications of Frequency Tunable and Reconfigurable Metamaterials”, Ph.D. dissertation, Duke University, 2009

[7] S.R. Best and D.L. Hanna, “ Design of a roadband dipole in close proximity to an EBG ground plane”, “ IEEE Ant. And Prop. Mag., **50**, 52, 2008

[8] C. Simovskii et al, “High-impedance surfaces having stable resonance with respect to polarization and incidence angle”, IEEE Trans. Antennas Prop., **53**, 908, 2005

[9] O. Luukkonen et al, “Simple and accurate analytical model of planar grids and high-impedance surfaces comprising metal strips or patches”, IEEE Trans. Antennas Prop., vol. 56, 1624, 2008

[10] D.M. Pozar, “Microwave Engineering, 3rd ed.”, Wiley, N.Y., 2005

[11] C.R. Brewitt-Taylor, “Limitation on the bandwidth of artificial perfect magnetic conductor surfaces,” IET Microw. Antennas Propag., 1, 255,2007

Resonant Antennas Based on Coupled Transmission-Line Metamaterials

Christopher Merola and Do-Hoon Kwon

Department of Electrical and Computer Engineering
University of Massachusetts Amherst

Transmission-line metamaterials are realized by conventional transmission lines loaded with lumped/distributed reactive elements such that the phased velocity of the guided wave can be designed. In this paper, resonant-type printed antennas based on coupled transmission-line metamaterials are presented. Using a single feed for a coupled line, both even- and odd-mode resonances can be excited to radiate efficiently at their respective design frequencies. The efficiency of the odd-mode radiation is enhanced by separating the two metamaterial lines, while strong coupling is maintained by inserting a series of narrowly-separated thin loops between them. Several example resonant antenna designs at the 2.4 GHz band are presented.

1. Introduction

Development of metamaterials theory and technology in recent years has inspired various novel antenna designs as well as application of metamaterials to conventional antennas. Adding metamaterial superstrate layers to small antennas has been demonstrated to enhance maximum directivities significantly [1]–[4]. Various metamaterial-inspired electrically small antennas have been reported [5]–[8].

Transmission-line (TL) metamaterials [9], [10] are reactively loaded microwave transmission lines such as microstrips or co-planar waveguides. Periodic reactive loading can modify the propagation constant of the transmission line from that of the unloaded value. The composite right/left-handed (CRLH) TL metamaterials [11] can support propagating waves with a propagation constant ranging from positive values (right-handed), through zero, to negative values (left-handed). Leaky-wave antennas with backward propagations have been designed and demonstrated [12], [13]. Subsequently, electrically steerable leaky-wave radiation was reported [14]. Dual-band and multi-band antennas have been designed [15], [16]. In addition, the zeroth-order resonance was observed and exploited for resonant antenna designs [17], [18]. Designed to have an infinite phase velocity at the desired frequency, a properly-designed structure can resonate independent of its physical length.

Coupled TL-metamaterials have been applied to microstrip directional coupler designs. By combining even-/odd-mode analysis with metamaterial theory, a directional coupler with arbitrary coupling coefficient has been designed [19]. Microwave couplers using both positive-index and negative-index transmission lines have been presented [20]. However, to date, no one has applied metamaterial coupled line structures to antenna applications.

In this paper, resonant antennas based on coupled-TL metamaterials are presented. The novel antenna design utilizes a coupled TL-metamaterial structure in order to obtain two un-coupled resonances whose frequencies can be easily adjusted. Any currents flowing on the coupled structure are described as a properly weighted superposition of an even (parallel) and odd (anti-parallel) current modes. We present a method to independently control the phase velocities of these modes in order to obtain a structure with two resonances. Several resonant printed antennas are designed based on the design approach, featuring either dual-band, wide-band, or pattern-reconfigurable characteristics. Prototype antennas are fabricated and their measured characteristics are compared with numerically simulated predictions.

2. Unit cell design and analysis

Following a typical TL-metamaterial antenna design approach [9], we begin our design with the analysis of wave propagation properties over a coupled transmission line. Using dispersion analysis, we are able to determine the even- and odd-mode phase velocities along this structure. A difference in phase velocities, or propagation constants, between the two modes translates into a frequency separation between the even- and odd-mode resonances.

Fig. 1(a) shows the top view of typical coupled transmission lines of finite length. The even- and odd-mode currents exhibit the distinctly different radiation patterns shown in Fig. 1(b). In the even-mode, the symmetric current distribution has the radiation pattern characteristic of a two-element broadside array. Since the odd mode requires currents on the two patches to be 180° out of phase, the resulting pattern has a broadside null with two lobes steered to an angle determined by separation between elements. This quality can be of use for certain applications. Changing radiation pattern to avoid interference or eavesdroppers is possible by switching between modes. Additionally, an antenna for a mono-pulse radar can be designed with this technique. By spacing the two resonances closely, both modes can be made to radiate efficiently at the same frequency. When the modes radiate simultaneously the result is two asymmetrical lobes with a null close to broadside. Adjusting the spacing between the resonances affects the level of asymmetry. By comparing voltages received at the two ports placed on both patches, the direction to a target could be determined.

Computationally, the even- and odd-mode coupling can be efficiently modeled and analyzed using either a perfect magnetic conductor (PMC) or perfect electric conductor

(PEC) boundary down the symmetry plane between the lines as illustrated in Fig. 1(a). As the spacing between the lines becomes narrower, the distance from either transmission line to this symmetry plane decreases and coupling is increased. The electric (odd mode) or magnetic (even mode) coupling can be represented as periodic, shunt reactive elements. Differences in these element values can cause the even- and odd-mode phase velocities to be different.

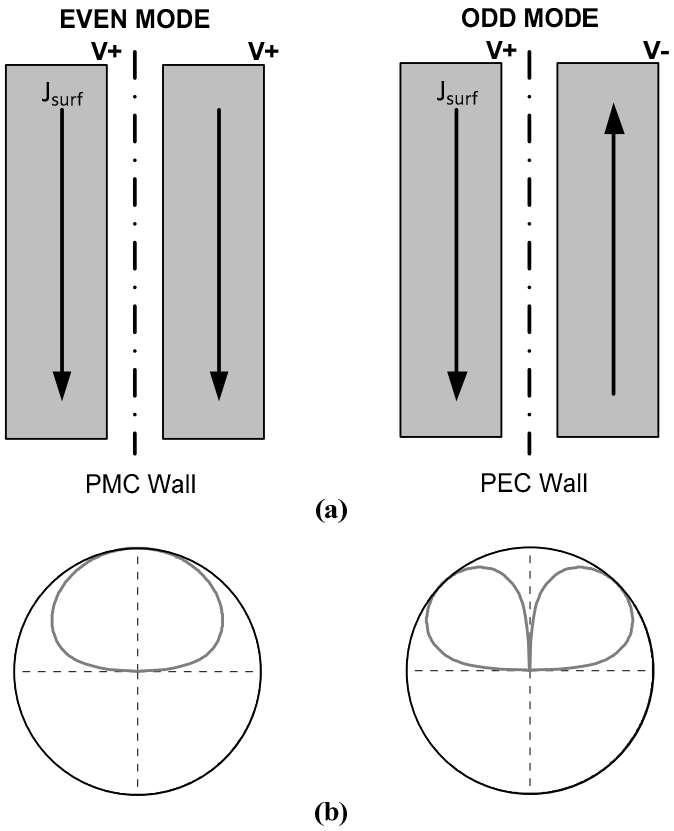

Figure 1: Current flow and radiation characteristics of the even- and odd-modes of a coupled structure. (a) Top view of the even- and odd-mode currents, and the effective boundary conditions from symmetry. (b) Typical H-plane radiation patterns associated with these current modes.

In this study, the overall antenna structure is obtained by cascading several identical building blocks, or unit cells. By cascading unit cells to attain a total 180° of phase progression, a resonant antenna is constructed. The phase velocity along the transmission line is analyzed using a single unit cell under periodic boundary conditions. Fig. 2 shows the top view of the unit cell employed in this study. The symmetrical structure consists of two lines of the width W, separated by the distance s. Between these lines are coupling loops with the line width w_{loop}, separated by a narrow gap g, along the symmetry plane. The length of the closely coupled edge between these loops is defined as l_{couple}. Short-

circuited shunt stubs of the width w_{stub} and the length l_{stub} extend from each side of the lines along at center of the unit cell length.

This design approach relies on strong coupling between the two transmission lines in order to have appreciable phase constant separation between the modes. Unfortunately, odd-mode currents for two very closely spaced elements do not radiate efficiently. For efficient radiation to occur in both modes, strong coupling must be maintained between the lines across a wide separation. To accomplish this, a coupling structure was placed between two wide transmission line segments, or patches. Narrow loops were placed between the patches, separated by a small gap g, along the symmetry plane. The narrow line forces the currents to flow close to the coupling edge, increasing the coupling. Additionally, the narrow line width reduces unwanted radiation from this portion of the antenna. From a circuit perspective, the coupling loop loads the patch similarly to a open-circuited shunt stub. The stub used is less than λ/4 long, giving it a capacitive input reactance. The separation in the even- and odd-mode phase velocities comes from the difference in the capacitances that this structure exhibits in each of these modes. In the even mode, the symmetry plane results in the end of the stub being closely spaced to a PMC boundary. This effective open forces the fringing field to zero, slightly shortening the electrical length of the stub. This has little effect on its capacitance versus the stub with no PMC boundary. In the odd mode, however, the PEC boundary places an effective ground plane very close to the end of the stub. The close spacing between the end of the stub and the ground plane creates a significant increase in the capacitance of the stub. This increase in capacitance only affects propagation of the odd mode, separating even- and odd-mode electrical lengths for the same physical length L_{cell}.

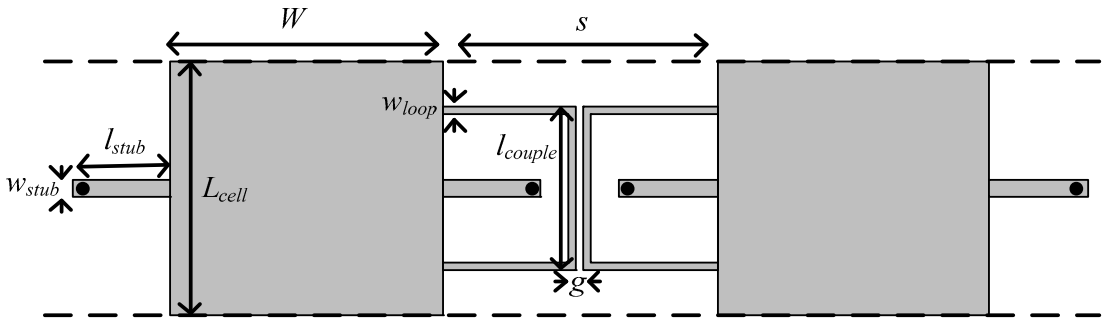

Figure 2: Unit cell diagram. Dashed lines indicate periodic cell boundaries.

The difference in electrical lengths can be controlled by adjusting the ratio of the even-to-odd mode capacitances. This is primarily controlled by two parameters: the gap g between the coupling loops and the length l_{couple} of the coupling edge. Figs. 3 and 4 plot the dispersion curves for different values of l_{couple} (for a fixed g) and for different values of g (for a fixed l_{couple}), respectively. Decreasing g or increasing l_{couple} will increase the phase constant separation. Changes in g have a negligible effect on the even-mode capacitance. A larger l_{couple} lowers the impedance of the equivalent open-circuit stub. This

has some effect on the even-mode capacitance, but much less than that of the odd mode. By adjusting these two parameters, it is possible to tune the difference in even- and odd-mode phase velocities. The phase velocities are represented by (1)–(3). Intrinsic microstrip values of the series inductance per-unit-length and the shunt capacitance per-unit-length are represented by L_{MS} and C_{MS}, respectively.

$$v_p = \frac{\omega}{\beta} = \frac{1}{\sqrt{\mathrm{Im}\{Z_{series} Y_{shunt}\}}} \tag{1}$$

$$v_{p,even} = \frac{1}{\sqrt{L_{MS}(C_{MS} + C_{loop})}} \tag{2}$$

$$v_{p,odd} = \frac{1}{\sqrt{L_{MS}(C_{MS} + C_{loop} + C_{loop,odd})}} \tag{3}$$

In (2)-(3), C_{loop} and $C_{loop,odd}$ denote the per-unit-length values of the shunt capacitance introduced by the coupling loops.

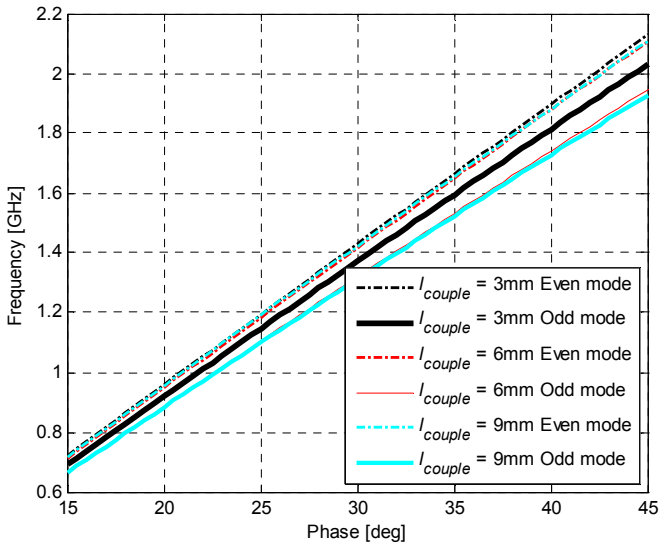

Figure 3: Effect of the coupled edge l_{loop} on the dispersion relation. The gap g is fixed at 0.3 mm.

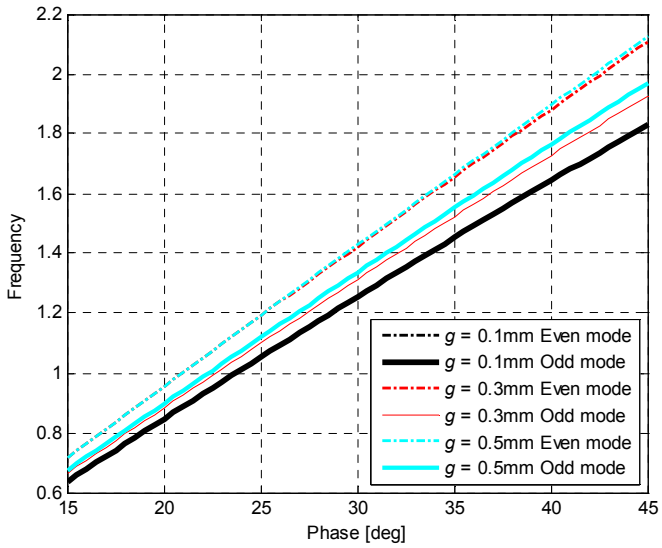

Figure 4: Effect of the coupled loop separation g on the dispersion relation. The coupled edge l_{loop} is fixed at 9 mm.

In addition to the coupling loops, our design also uses short-circuit shunt stubs of the width w_{stub} and the length l_{stub} as illustrated in Fig. 2 to improve the antenna gain. These stubs, which introduce a per-unit-length shunt inductance L_{stub}, affect both even and odd modes equally. They are used to increase the phase velocity by effectively decreasing the shunt capacitance of each transmission line, which increases the physical resonant length. The gain improvement can be understood intuitively. The shunt stubs increase the resonant length of the antenna, effectively increasing the distance between the elements of a two-element array formed by the radiating slots at each end of the patch. The directivity of the two-element array is maximized when the patch length is equal to λ/2 in free space. For typical patch antennas, built on a dielectric substrate, the resonant length is shorter than λ/2, leading to sub-optimal gain values. By introducing inductive shunt stubs, we are able to increase the patch length close to a free-space half wavelength, improving the antenna gain. The input impedance of the stub Z_{stub} and the effect of its inductance on the phase velocity are given by

$$Z_{stub} = jZ_0 \tan \beta_d l_{stub} \tag{4}$$

$$v_p = \frac{1}{\sqrt{L\left(C - \frac{1}{\omega^2 L_{stub}}\right)}} \tag{5}$$

where Z_0 is the characteristic impedance of the microstrip forming the stub and β_d is the propagation constant along the stub. The values of L and C in (5) denote per-unit-length values for either mode used in (2)-(3).

The limitation in increasing phase velocity using this technique lies in manufacturing tolerances when constructing the inductive stubs. From (5), it is seen that a smaller value of L_{stub} has a greater effect on v_p. To realize a smaller inductance, the stub must become either shorter in length or wider in width. As w_{stub} increases and approaches l_{stub}, the stub's input impedance behavior begins to deviate from the transmission line model of a shunt stub. Additionally, as the stub becomes extremely short, small variations in the l_{stub} cause a large change in L_{stub}. In extremely short stubs, manufacturing tolerances can have a large effect on the resonant frequency. One method used to create such small inductances is to place one stub on each side of the underlying transmission line. This way, the inductance of a single stub needs to be a twice that of the desired value, increasing the range of realizable inductances by a factor of two. Another solution is to narrow the width W of the patch, decreasing the inherent shunt capacitance of the microstrip structure.

3. Resonant antenna

Building a resonant antenna from a unit cell involves cascading cells to an electrical length of 180° at the desired frequency, as illustrated in Fig. 4. Since the coupled structure has two separate phase velocities, the antenna will have resonances at two different frequencies. There are several considerations in building an antenna from this coupled structure: the patch width W affects the radiation efficiency and frequency bandwidth; the use of inductive stubs allows the overall patch length L_{ant} to be adjusted to an arbitrary length independent of the design frequency; and the value of L_{ant} is chosen based on either desired gain or space constraints. Additionally, the spacing s between the patches controls the ratio between the even- and odd- mode gains. The spacing also controls the length of the coupling loops l_{couple}, adjusting the capacitance seen by both modes.

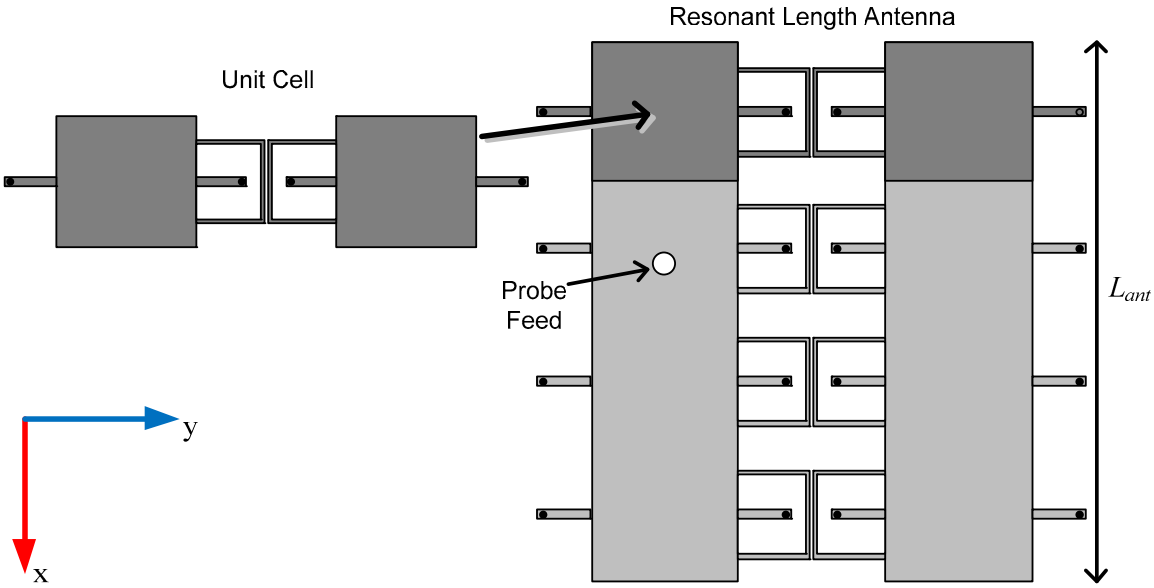

Figure 4: Cascading unit cells to form a resonant antenna.

The first consideration is to determine how many unit cells to use, and then design the unit cell phase progressions to achieve the desired even- and odd-mode phase difference. First, choose the two desired resonant frequencies. Next, choose the length of the antenna L_{ant} to be close to half of the free space wavelength in the operating band. Dividing this length by the number of unit cells gives the unit cell length L_{cell}. The designs presented in this paper use either 4 or 5 unit cells. The number of unit cells will be decided by the desired separation between resonances. For a greater separation between resonances, l_{loop} must be made longer. It is desirable to make the unit cells as short as possible, while fitting in the necessary length of l_{loop}.

The spacing s between the two patch elements will control the gain of both modes. If the elements are very close together, the odd mode will not radiate efficiently. As the elements are spaced further apart, the gain for both modes will increase, although the even-mode gain will increase more than the odd-mode gain. The designs presented were optimized to keep the gains of the two modes as close as possible. For this purpose, elements are spaced just far enough for the odd mode to radiate efficiently. As the value of s is increased beyond this point, the gain imbalance between the two modes is also increased.

Once the general dimensions of the unit cell have been decided, the HFSS eigenmode solver is used to determine the even- and odd-mode electrical lengths of the unit cell. This is accomplished by placing a master/slave boundary condition along the dashed lines in Fig. 2. The phase is set to the resonant length divided by the number of unit cells. Due to the H-plane symmetry of the design, the even mode is computationally equivalent to simulating one half of the unit cell with a PMC boundary placed along the symmetry plane. Replacing this with a PEC boundary is computationally equivalent to the odd

mode excitation. This simulation will predict the even- and odd-mode resonant frequencies of the antenna.

The electrical length of a patch antenna at the fundamental-mode resonance is slightly shorter than 180° [21]. This difference in length may be taken into account in order to have a good agreement between the unit-cell predicted frequency and the actual antenna resonant frequency. This difference in length is due to the fringing fields which extend beyond the edges of the patch. For a fixed design frequency, the additional electrical length due to the fringing field was found to be nearly independent of the phase velocity along the length of the patch. The added fringing phase Δ_{phase} depends primarily on W, the permittivity of the dielectric substrate, and the substrate thickness. The value of Δ_{phase} was determined by simulating a standard, probe-fed, microstrip patch which resonates at the mid-band frequency using the same dielectric material and patch width. Subtracting Δ_{phase} from 180° and dividing the resulting electrical length by the number of unit cells was found to give a good agreement between the unit cell predictions and the resonant frequencies when applied to coupled patch designs.

In order to use this patch as a dual-resonance antenna, both modes must be simultaneously excited. Use of a probe feed on each patch allows an arbitrary excitation of the two modes. It is shown in (6)–(9) that exciting the antenna only at one port with the second port open-circuited makes the antenna input impedance Z_{in} to be simply a sum of the individual mode impedances Z_{ee} and Z_{oo} for the even and odd modes, respectively. Due to the uncoupled nature of the two modes, it follows that $Z_{eo}=Z_{oe}=0$. Using this arrangement, the antenna can be fed with a single feed probe to either patch.

$$\begin{bmatrix} V_1 \\ V_2 \end{bmatrix} = \begin{bmatrix} Z_{11} & Z_{12} \\ Z_{21} & Z_{22} \end{bmatrix} \begin{bmatrix} I_1 \\ I_2 \end{bmatrix} \tag{6}$$

$$Z_{ee} = \frac{1}{2}\left(Z_{11}+Z_{12}+Z_{21}+Z_{22}\right) \tag{7}$$

$$Z_{oo} = \frac{1}{2}\left(Z_{11}-Z_{12}-Z_{21}+Z_{22}\right) \tag{8}$$

$$Z_{in} = \frac{1}{2}\left(Z_{ee}+Z_{oo}\right) \tag{9}$$

It should be noted that there is a limit on the resonant frequency separation when this method is used. As the resonances are pushed further apart in frequency, the input impedances of the two modes at their respective resonances become further separated. A dual-band antenna design presented below demonstrates approximately how far the two resonances can be spaced in frequency under the particular set of geometrical parameters

considered. For instance, using a wider patch will improve the ability to impedance-match both modes, but decreases the resonant length and therefore the antenna gain.

4. Antenna Designs

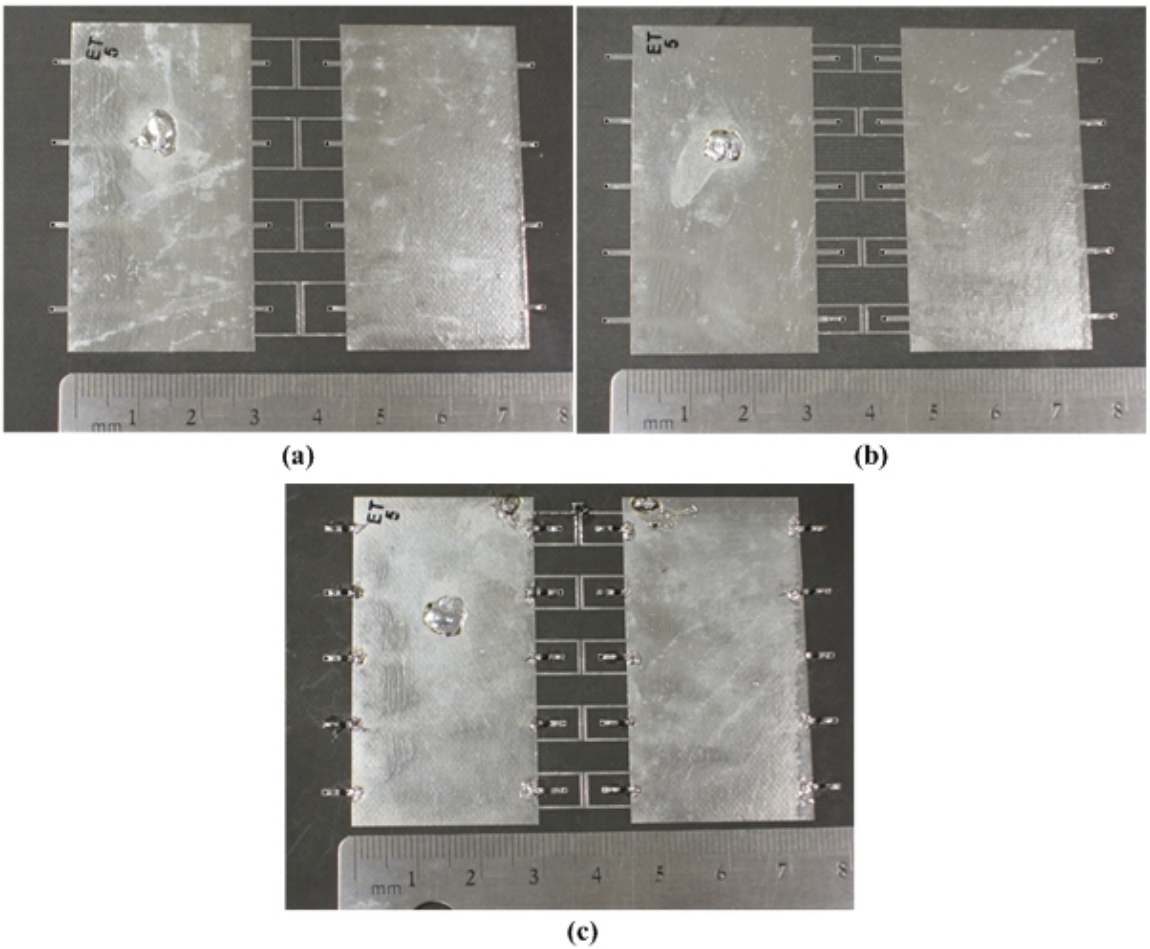

Figure 5: Photographs of the (a) dual-band, (b) wide-band, and (c) pattern-reconfigurable antenna designs.

Three antenna designs based upon the described technique are presented. They were chosen to operate in the 2.4-GHz band. All of the designs were built on a Rogers RT/Duroid 5880 (ε_r=2.2, tanδ=0.0009) substrate of thickness 62 mil (1.57 mm) and a 0.5-oz (thickness of 0.017 mm) of copper cladding. A patch width of W=30 mm and spacing of s=15 mm were kept the same for all three designs. For the coupling structure and stubs in the unit cell defined in Fig. 2, the trace widths for the loop and the stub were set to w_{loop}=0.5mm and w_{stub}=1 mm. The size of the ground plane of the fabricated prototypes is 127 mm×203 mm.

Dual-band Antenna

A dual-band antenna was designed for resonances at 2.405 GHz (odd mode) and 2.849 GHz (even mode), spaced by 84 MHz within the 2.4 GHz band. Four unit cells of length L_{cell}=13.75 mm were cascaded to realize the antenna. The specific values of the unit-cell parameters are given by l_{couple}=9 mm, g=0.254 mm, and l_{stub}=3 mm. A photograph of the prototype is shown in Fig. 5(a). The overall antenna dimensions are 55 mm×81 mm. A feed-probe is positioned 7 mm away from the patch center along the center line bisecting one patch in the x direction.

The input impedance of the prototype was measured from 2.3 to 2.6 GHz in the lab using a vector network analyzer. The magnitudes of the input reflection coefficient $|S_{11}|$ are compared between simulated and measured results in Fig. 6, where an excellent agreement is observed in the entire measurement frequency range. Far-zone radiation gain patterns were measured in an anechoic chamber. Fig. 7 plots the H-plane (the y-z plane) realized gain patterns at the two resonance frequencies with respect to the angle θ measured from the +z axis. Excellent agreement is observed at both frequencies except at angles close to θ=90° at the odd-mode frequency in Fig. 7(a). Characteristic differences in the even- and odd-mode patterns illustrated in Fig. 1(b) are clearly observed in Fig. 7. At the odd-mode frequency of 2.405 GHz, note that the magnitudes of the two major lobes are not equal and the pattern null is not located at θ=0 due to the presence of a residual even-mode component at this frequency. In contrast, the even-mode pattern in Fig. 7(b) is observed to be almost free of any odd-mode characteristic. This is due to a narrower bandwidth of the odd-mode resonance compared with the even-mode resonance.

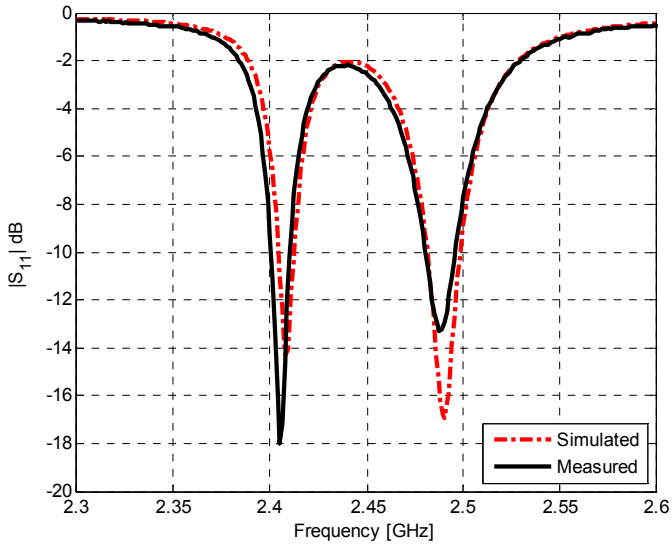

Figure 6: The input reflection coefficient response for the dual-band design referenced to 50 Ω.

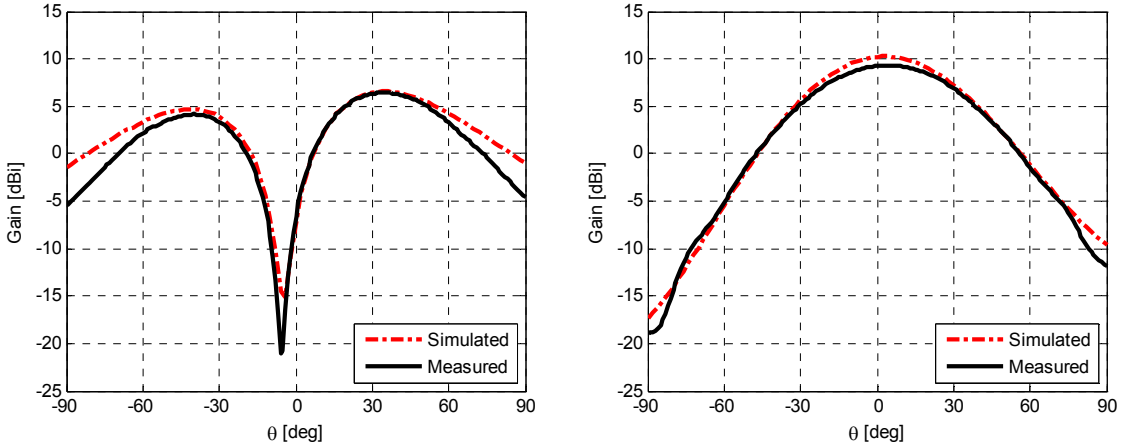

Figure 7: Dual-band design co-pol absolute gain in H-plane at (a) the odd mode resonance (2.405 GHz) and (b) the even mode resonance (2.489 GHz).

Wide-band Antenna

The antenna design method allows the two resonance frequencies to be separated by an arbitrarily small difference due to the uncoupled nature of the even and odd modes of coupled transmission lines. By bringing the two resonance frequencies closer to each other, an antenna can be designed to have a wider impedance bandwidth than a similar single resonance patch. A wide-band antenna was designed around the center frequency of 2.45 GHz by cascading five unit cells with L_{cell}=11 mm. The unit-cell geometrical parameters were chosen to be l_{couple}=5 mm, g=0.3 mm, and l_{stub}=4.5 mm. The overall dimensions of the antenna are 55 mm×84 mm. A single probe feed is located at 6.5 mm away from the center of the excited patch. A photograph of the prototype is shown in Fig. 5(b). From Figs. 3–4, weaker coupling between the two patches leads to a narrower separation between the two resonance frequencies. For this wide-band design, note that g is larger and l_{loop} is shorter than their respective counterpart in the dual-band design. In addition, a shorter l_{loop} allows a shorter unit cell size, leading to a five-cell structure rather than a four-cell geometry of the previous design.

Fig. 8 compares the simulated and measured reflection coefficient for the wide-band antenna. An excellent agreement is obtained over the entire frequency range. Two resonances are clearly visible and $|S_{11}|$ stays below –10 dB over the merged band. The 2:1 VSWR bandwidth of the merged resonances is found to be 36MHz , or 1.46%. The H-plane gain patterns for the co-polarized component are plotted at three different frequencies in Fig. 9. Good agreement is obtained between simulation and measurement at each frequency. For this design, the radiation pattern is a strong function of frequency within the band. Frequency points in the low, mid, and high range in the band were chosen in Fig. 9. At the low frequency of 2.436 GHz, Fig. 9(a) shows a pattern

characteristic of the odd mode. At the mid-band frequency of 2.457 GHz, a highly asymmetric pattern is obtained. At the high-band frequency of 2.471 GHz, the even-mode radiation characteristics dominate as shown in Fig. 9(c).

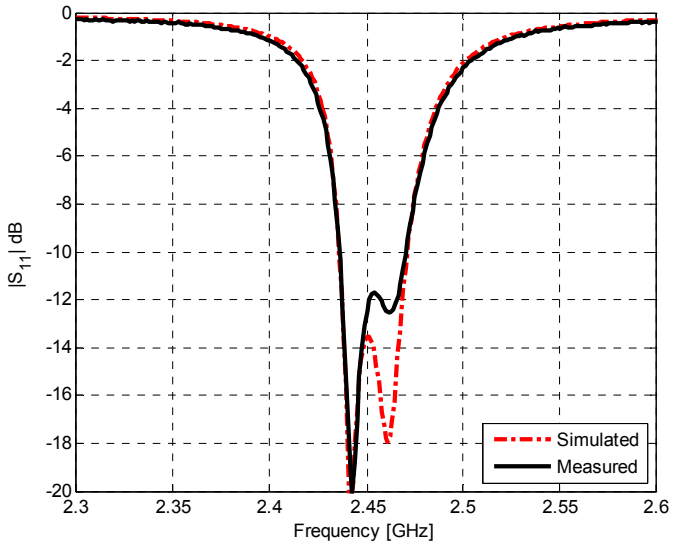

Figure 8: The input reflection coefficient response for the wide-band design referenced to 50 Ω.

The asymmetric radiation pattern on the two sides of the H plane suggests an interesting application of the coupled TL-metamaterial antenna design approach to mono-pulse radars [22]. One could design a coupled antenna having one feed on each patch and have the even- and odd-mode resonances merged to form a wideband resonance. Within the operation band, the radiation pattern transitions smoothly from the anti-symmetric odd-mode pattern to the symmetric even-mode pattern with increasing frequency. At some frequency, the total radiation pattern will become highly asymmetric with respect to the H plane, having a strong main lobe and a weak minor lobe on opposite sides. Then, the magnitudes of the received voltages from the two probes will indicate on which side of the H plane a target is positioned. Therefore, the output signals from the two receiving ports could directly drive servo motors to track a target. This way, there will be no need to implement separate sum and difference feed networks of conventional mono-pulse radar systems, reducing system complexity, saving space, and lowering manufacturing cost.

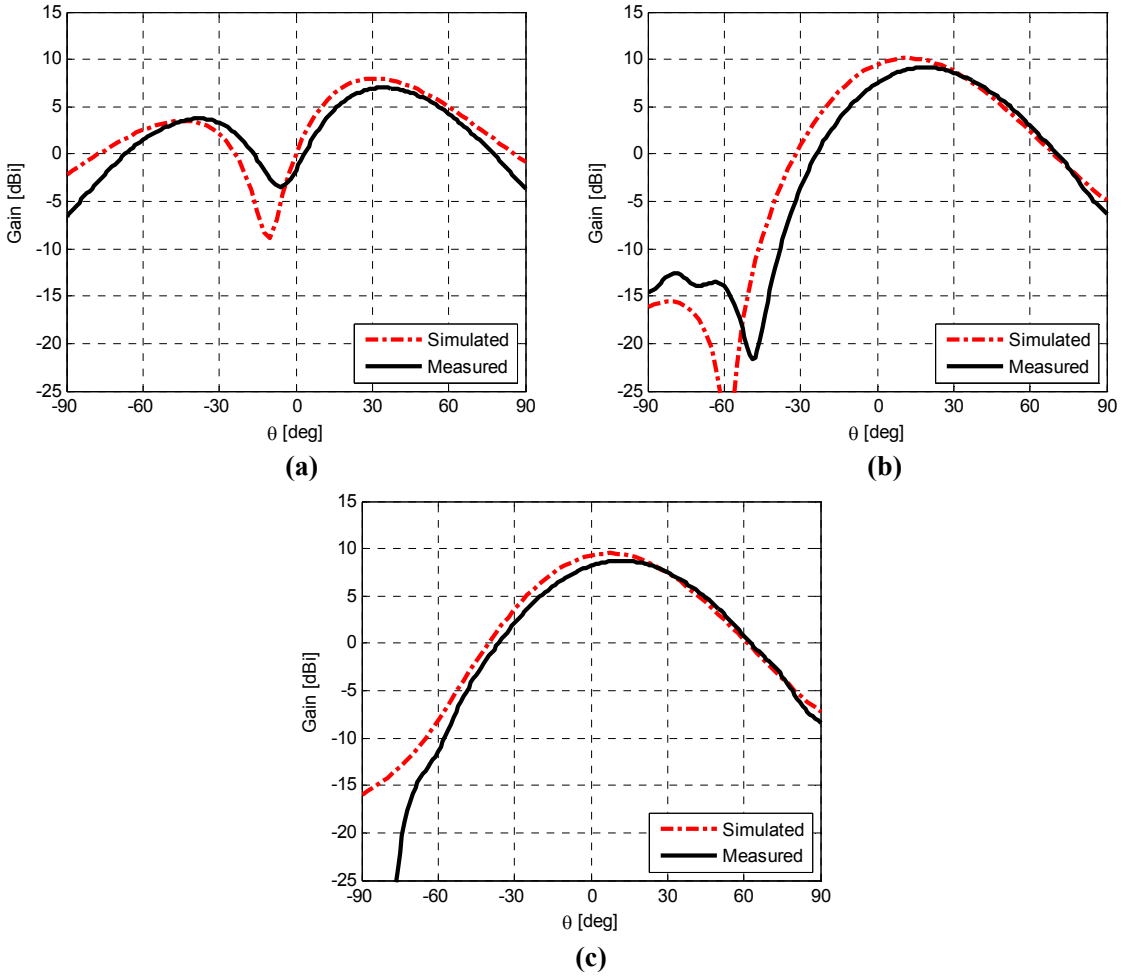

Figure 9: The H-plane realized gain patterns for the co-polarization component for the wide-band design. (a) At 2.436 GHz. (b) At 2.457 GHz. (c) At 2.471 GHz.

Pattern-Reconfigurable Antenna

For the resonant coupled-patch antennas under consideration, changing the shunt capacitance of the patches, C_{MS} in (2)–(3), will change the resonance frequencies accordingly. The shunt capacitance can be reconfigured using variable capacitors in a shunt path from a patch to the ground. At the design frequency under consideration, reverse-biased varactor diodes can be used as variable capacitors [23]. We chose to place a series of varactor diodes along the length of the patch in the shunt path (four varactors per unit cell) to control the shunt capacitance. The value of the capacitance can be adjusted easily by varying a DC bias voltage. Note that this arrangement of varactor diodes affects the even and odd modes almost equally. Therefore, the entire resonance curve that includes both resonances will shift up or down in the frequency axis as a function of the DC bias voltage. Increasing the shunt capacitance lowers both resonance frequencies. At a fixed design frequency, the patch can be made to radiate in the odd

mode at one DC offset. By decreasing voltage (increasing capacitance), the even mode can be configured to resonance at the design frequency.

A pattern-reconfigurable antenna at 2.45 GHz was designed by cascading five unit cells with L_{cell}=11mm. The unit-cell geometry is specified by l_{couple}=6 mm, g=0.3 mm, and l_{stub}=4.7 mm (including the diode package length of 0.9 mm). The overall dimensions of the antenna are 55 mm×84 mm. The probe is located 6.5 mm away from the center of the excited patch. In a cell, one varactor diode was placed for each shunt stub. The design presented uses Skyworks Sollutions, Inc's hyperabrupt tuning varactor diodes (model SMV1234-079LF). These diodes provide documented variable capacitance up to and above 2.5GHz according to the data sheet.

Using different varactor capacitance values, the input impedance responses from simulation and measurement are compared in Fig. 10. Simulation predictions using HFSS indicated that the even- and odd-mode resonance frequencies can be aligned to 2.45 GHz using the varactor capacitance values of 5 pF and 4.2 pF, respectively. During the experiment, adjusting the capacitances to the predicted values did not align the resonance frequencies to 2.45 GHz. Different capacitance values were needed (according to the data sheet) for proper alignment of resonance frequencies. The measured responses in Fig. 9 reflect these adjusted capacitances of 7.53 pF and 5.39 pF, respectively.

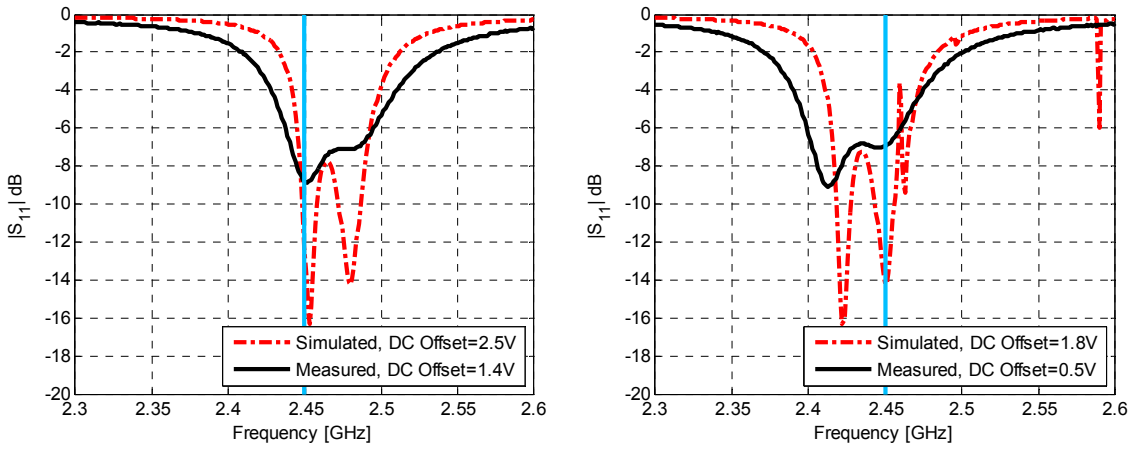

Figure 10: Predicted and measured input reflection coefficient response for the pattern-reconfigurable design, referenced to 50 Ω. (a) Odd mode resonance at 2.45 GHz. (b) Even mode resonance at 2.45 GHz. The design frequency is indicated by a solid vertical line in cyan in each plot.

The observed discrepancy between the simulated and measured results can be attributed to approximations made in modeling the diode in HFSS. The diode response was linearized and modeled as sheets of series L and C elements. The inductance and capacitance values from the data sheet were measured at a lower frequency than the

operating frequency of the reconfigurable antenna. It should be possible to obtain a better agreement between simulation and measurement if a more accurate diode model is available. It may be obtained by simulating the SPICE model of the diode available from the data sheet and extracting the *RLC* parameters at the antenna design frequency. Nevertheless, the capacitive tuning range of the diode still allowed for either resonance to be adjusted to occur at 2.45 GHz. The results shown overlay simulated and measured results when the DC offset is adjusted for even- or odd-mode resonance occurring at 2.45 GHz. Although the resonance frequencies were aligned, Fig. 10 shows that the impedance match of the fabricated antenna is poorer in both cases than the simulation results.

At 2.45 GHz, the H-plane gain patterns for the co-polarized field are plotted and compared between simulated and measured results in Fig. 11. Although some discrepancies exist, measured and simulated patterns follow the same overall trend. The generally lower measured gains compared with the simulated gains are attributed to larger impedance mismatches shown in Fig. 10 and also to efficiency degradation, mainly due to the resistive element in the varactor diodes.

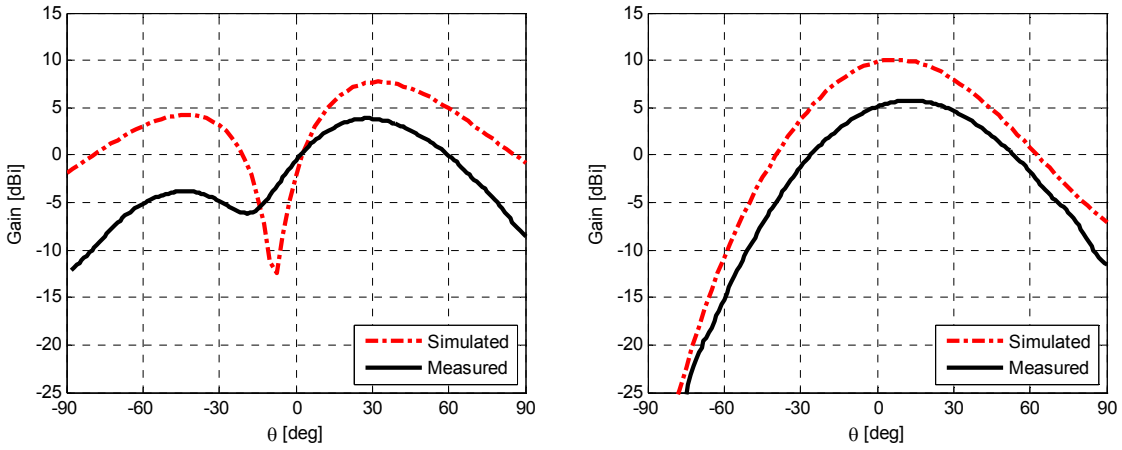

Figure 11: Pattern-reconfigurable design co-pol absolute gain in H-plane at (a) odd mode resonance and (b) even mode resonance.

5. Conclusion

Novel resonant printed antenna designs based on coupled TL-metamaterial structure have been presented. The design exploits the uncoupled nature of coupled transmission lines of symmetric construction to configure the even- and odd-mode resonance frequencies independent of each other. In particular, a coupling structure based on thin loops allows the two transmission lines to be separated so that the odd-mode current can radiate efficiently. A series of shunt inductive stubs can modify the phase constants such that the

overall length of the antenna can be adjusted closer to a half free-space wavelength, leading to a high gain. Three antennas – a dual-band antenna, a wide-band antenna, and a pattern-reconfigurable antenna – were designed, fabricated, and experimentally characterized. Excellent agreement was obtained between simulated and measured results for the dual-band and wide-band antenna designs, validating the proposed design approach. Inaccuracies in the varactor diode model at the design frequency of 2.45 GHz resulted in some discrepancy between predicted and measured responses for the pattern-reconfigurable antenna. The proposed antenna design approach may find applications where a choice is desired in the radiation pattern among the anti-symmetric odd-mode pattern with a broadside pattern null, the symmetric even-mode pattern with a broadside pattern maximum, and an asymmetric pattern resulting from a superposition of the two patterns. The selection of a pattern in the wide-ranging characteristics may be performed in real time using a single control voltage.

6. Acknowledgements

This work was supported by the Air Force Research Laboratory under the contract number FA8718-09-C-0060.

7. References

[1] D. H. Lee, Y. J. Lee, J. Yeo, R. Mittra, and W. S. Park, "Design of novel thin frequency selective surface superstrates for dual-band directivity enhancement," *IET Antennas Mircrow. Propag.*, vol. 1, no. 1, pp. 248–254, 2007.

[2] A. Ourir, S. N. Burokur, R. Yahiaoui, A. de Lustrac, "Directive metamaterial-based subwavelength resonant cavity antennas – applications for beam steering," *C. R. Physique*, vol. 10, pp. 414–422, 2009.

[3] S. J. Franson and R. W. Ziolkowski, "Gigabit per second data transfer in high-gain metamaterial structures at 60 GHz," *IEEE Trans. Antennas Propag.*, vol. 57, no. 10, 2913–2925, Oct. 2009.

[4] J. Kim and A. Gopinath, "Simulations and experiments with metamaterial flat antenna lens using cubic high dielectric resonators," *Proc. 2009 IEEE Int. Workshop Antenna Technol. (iWAT 2009)*, Santa Monica, CA, Mar. 2009.

[5] A. Erentok and R. W. Ziolkowski, "Metamaterial-inspired efficient electrically small antennas," *IEEE Trans. Antennas Propag.*, vol. 56, no. 3, pp. 691–707, Mar. 2008.

[6] R. W. Ziolkowski, "An efficient, electrically small antenna designed for VHF and UHF applications," *IEEE Antennas Wirel. Propag. Lett.*, vol. 8, pp. 217–220, 2008.

[7] R. W. Ziolkowski, C.-C. Lin, J. A. Nielsen, M. H. Tanielian, and C. L. Holloway, "Design and experimental verification of a 3D magnetic EZ antenna at 300 MHz," *IEEE Antennas Wirel. Propag. Lett.*, vol. 8, pp. 989–993, 2009.

[8] P. Jin and R. W. Ziolkowski, "Low-Q, electrically small, efficient near-field resonant parasitic antennas," *IEEE Trans. Antennas Propag.*, vol. 57, no. 9, pp. 2548–2563, Sep. 2009.

[9] C. Caloz and T. Itoh, *Electromagnetic Metamaterials*, New York: Wiley, 2005.

[10] G. V. Eleftheriades and K. G. Balmain, Eds., *Negative-Refraction Metamaterials: Fundamental Principles and Applications*, Piscataway, NJ: Wiley-IEEE Press, 2005.

[11] A. Lai, T. Itoh, and C. Caloz, "Composite right/left-handed transmission line metamaterials," *IEEE Microw. Mag.,* vol. 5, no. 3, pp. 34–50, Sep. 2004.

[12] L. Liu, C.Caloz, and T. Itoh, "Dominant mode leaky-wave antenna with backfire-to-endfire scanning capability," *Electron. Lett.*, vol. 38, no. 23, pp. 1414–1416, Nov. 2002.

[13] A. Grbic and G. V. Eleftheriades, "Experimental verification of backward-wave radiation from a negative refractive index metamaterial," *J. Appl. Phys.*, vol. 92, no. 10, pp. 5930–5935, Nov. 2002.

[14] S. Lim, C. Caloz, and T. Itoh, "Metamaterial-based electronically controlled transmission-line structure as a novel leaky-wave antenna with tunable radiation angle and beamwidth," *IEEE Trans. Microw. Theory Tech.*, vol. 53, no. 1, pp. 161–173, Jan. 2005.

[15] S. Otto, C. Caloz, A. Sanada, and T. Itoh, "A dual-frequency composite right/left-handed half-wavelength resonator antenna," in *Proc. IEEE Asia-Pac. Microw. Conf.*, New Delhi, India, Dec. 2004.

[16] A. Rennings, T. Liebig, S. Abielmona, C. Caloz, and P. Waldow, "Tri-band and dual-polarized antenna based on composite right/left-handed transmission line," in *Proc. 37th Eur. Microw. Conf.*, Munich, Germany, Oct. 2007, pp. 720–723.

[17] A. Sanada, C. Caloz, and T. Itoh, "Zeroth order resonance in composite right/left-handed transmission line resonators," in *Proc. Asia-Pac. Microw. Conf.*, Seoul, Korea, Nov. 2003, pp. 1588–1592.

[18] J.-H. Park, Y.-H. Ryu, J.-G. Lee, and J.-H. Lee, "Epsilon negative zeroth-order resonator antenna," *IEEE Trans. Antennas Propag.*, vol. 55, no. 12, pp. 3710–3712, Dec. 2007.

[19] C. Caloz, A. Sanada, and T. Itoh, “A novel composite right-/left-handed coupled-line directional coupler with arbitrary coupling level and broad bandwidth,” *IEEE Trans. Microw. Theory Tech.*, vol. 52, no. 3, pp. 980–992, Mar. 2004.

[20] R. Islam and G. V. Eleftheriades, “Printed high-directivity metamaterial MS/NRI coupled-line coupler for signal monitoring applications,” *IEEE Microw. Wirel. Compon. Lett.*, vol. 16, no. 4, pp. 164–166, Apr. 2006.

[21] C. A. Balanis, *Antenna Theory Analysis and Design*, Hoboken, NJ: Wiley, 2005.

[22] D. K. Barton, *Radar System Analysis*, Dedham, MA: Artech House, 1976.

[23] D. M. Pozar, *Microwave Engineering*, 3rd ed., Hoboken, NJ: Wiley, 2005.

Time Domain Characterization of Equiangular and Archimedean Spiral Antennas

Mohamed A. Elmansouri* (1), and Dejan S. Filipovic (1)
(1) Department of Electrical, Computer, and Energy Engineering
University of Colorado, Boulder, CO 80309-0425
E-mail: mohamed.elmansouri@colorado.edu, dejan@colorado.edu

Abstract

In this paper, a detailed performance comparison between two-arm equiangular and Archimedean spiral antennas in a short pulse ultra-wideband (UWB) transmit-receive antenna system in frequency and time domains is discussed. Frequency domain characteristics of spiral antennas link are determined experimentally and numerically using method of moments (MoM). The time domain characterization is obtained by post processing frequency domain data using the Inverse Fast Fourier Transform (IFFT). Effects of transmit pulse shape on the antennas dispersion are also studied and it is shown that the proper pulse shaping can be used to mitigate the inherent spiral antenna dispersion.

1. Introduction

The ultra-wideband (UWB) systems transmit and receive extremely short pulses, permitting the corresponding antennas to distort the pulse shape. Thus the design of the antenna for a UWB system plays an important role for the quality of the communication and the complexity of the receiver and transmitter. A UWB antenna design transpires both the determination of conventional frequency domain parameters such as the return loss and radiation pattern, and the analysis of time domain response with minimal pulse distortion. Time domain characterization of a pulsed communication antenna system is critical since it provides enough details regarding the dispersion characteristics of the proposed antenna system. The frequency-domain analysis plus the time-domain diagnostics of a UWB antenna system fully describe the overall performance of the system. This paper demonstrates the aforementioned aspects by characterizing two classes of planar spiral antennas, equiangular and Archimedean, in time and frequency domains.

The equiangular and Archimedean spiral antennas [1] have frequency independent characteristics in terms of their input impedance and radiation pattern, thus making them viable candidates for UWB systems. However, due to their fundamental principles of operation, they are dispersive. Specifically, considering a spiral antenna and the bend theory of operation, the radiation occurs from the radiating ring which circumference directly corresponds to the excited mode of operation. Thus, the highest frequencies will radiate from the rings closer to the antenna center and lower frequencies will radiate from

the regions closer to the spiral perimeter. In view of a typical multi-octave bandwidth performance, this will introduce pulse spreading (distortion) in time domain. It has been shown that the spiral antennas are indeed dispersive and arguments were made that they are undesirable for pulsed communications [2,3]. In this paper, the dispersion properties of two classes of spiral antennas are investigated in frequency and time domain using measurements and full-wave modeling based on MoM. The performance of two-arm planar equiangular and Archimedean spirals with different number of turns in an UWB transmit-receive antenna system is studied in terms of the system's transfer function and its impulse response. The transfer function is determined in terms of the measureable S-parameter S_{21} where the antenna system is considered as a two-port network. The S_{21} in this case provides a complete description for the antenna system performance in frequency domain since all the transmit/receive antenna performance parameters such as impedance matching, gain, polarization matching, path loss, and phase delay are accounted [4]. The impulse response of the system is obtained by applying inverse fast Fourier transform (IFFT). Diagnosing the impulse response of the system gives an indication about the inherent dispersion of the antennas; however this is not enough to describe the performance of the antenna system in the time domain. The received pulses are calculated by convolving the input pulse and the impulse response of transmit-receive antenna system. Another way to calculate the received pulses is multiplying the input pulse spectrum by transfer function and transfer the result to time domain using the IFFT. Antenna fidelity factor (defined in (1)), which represents the maximum cross correlation between transmitted and received pulses [5], is also characterized. The fidelity factor is used to assess the quality of the received pulses, and it is one of the important factors that affects the signal to noise ratio (SNR) and bit error rate (BER) performance of the antenna system. Note that the maximum SNR of the overall system in a free-space channel is directly proportional to the square of fidelity factor as shown in (2) [6].

$$F = \max_{\tau}\left[\frac{\int_{-\infty}^{+\infty} s_t(t)s_r(t-\tau)dt}{\int_{-\infty}^{+\infty}|s_t(t)|^2dt\int_{-\infty}^{+\infty}|s_r(t)|^2dt}\right] \quad (1)$$

$$SNR = \frac{P_{inc}\eta_{sys}}{R_bN_o}(F(\,s_t(t),\,s_r(t))^2 \quad (2)$$

Where $s_t(t)$, and $s_r(t)$ are the transmitted and received pulses respectively, τ is the time shift, P_{inc} is incident wave power to the transmit antenna, η_{sys} is the antenna system transmission efficiency, R_b is data rate, and N_o is noise power spectral density (PSD).

Spiral antenna dispersion is evaluated for different pulse shapes and it is shown that a proper pulse shaping can mitigate the natural dispersion of the antenna. Obtained results demonstrate that these antennas with some restrictions can be used for pulsed communications, as suggested in [7] for conical spirals.

2. Studied Antennas and Experimental Setup

The two-arm Archimedean and equiangular spirals are fabricated on a 0.79mm thick Rogers RT5880 ($\varepsilon_r = 2.2, \tan\delta = 0.0009$) substrate. All fabricated antennas are self-complementary with outer radius of $r_{out} = 19mm$, inner radius of $r_{in} = 2mm$, and the same substrate size. They have different number of turns *(N)*,thus different expansion coefficients *(a)* utilized here to investigate their effect on antennas' dispersion. Geometrical parameters and the total length of unwrapped arms are given in Table 1. The photographs of several fabricated articles are shown in Fig.1(a). A wideband balun with impedance transformer is also designed and fabricated. The balun, shown in Fig.1(b), transforms a nonsymmetrical 50Ω (micorstrip line) at the input port to a symmetrical 65Ω (balanced strip line) which is transformed using impedance transformer based on a Klopfenstein taper to a symmetrical 150Ω (balanced strip line) at the feed point of the spiral antenna. The base substrate of the balun is Rogers RT5880 with dielectric thickness h=0.79mm.

Table 1: Parameters of the studied antennas

	Equiangular Spiral		Archimedean	
Number of Turns (N)	Expansion Coefficient (a) ($rad.^{-1}$)	Total Length of spiral (mm)	Expansion Coefficient(a) (mm/rad.)	Total Length of spiral (mm)
2	0.205	87.3	1.397	131.4
4	0.102	177.0	0.698	258.8
6	0.068	257.3	0.465	386.8
8	0.051	342.8	0.349	515.0

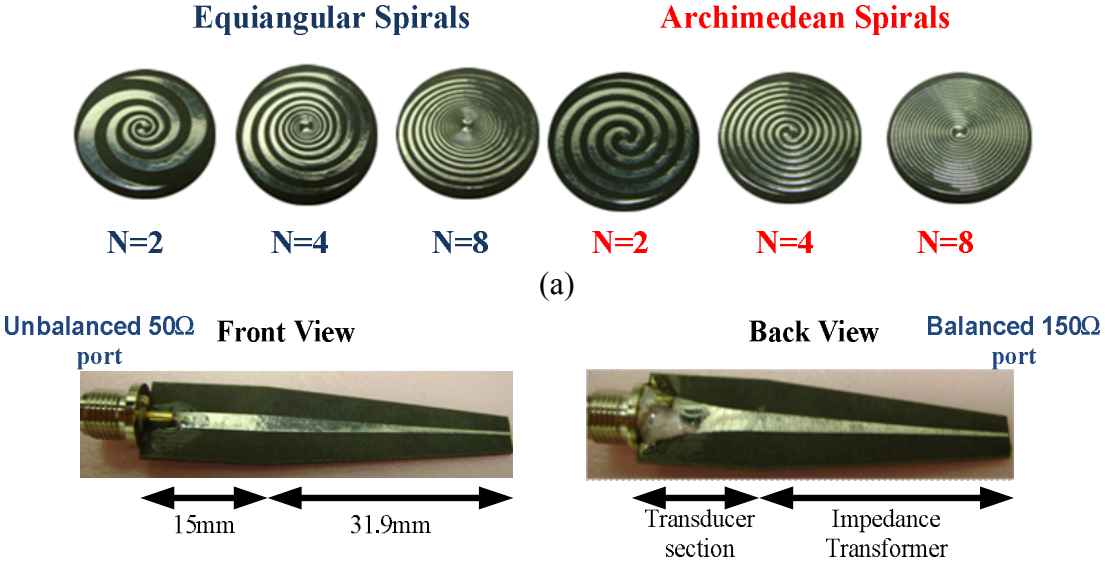

Fig.1: (a) Fabricated self-complementary spiral antennas (spirals with N=6 turns are not shown), (b) wide-band balun with impedance transformer

To guarantee that the balun does not affect the time-domain response of the studied antennas, the performance of the balun in time-domain has been evaluated numerically. The calculated fidelity factor between the input pulse at the port 1 and the received pulse at port 2 is 0.995. The obtained high fidelity factor is clearly observed in Fig.2.

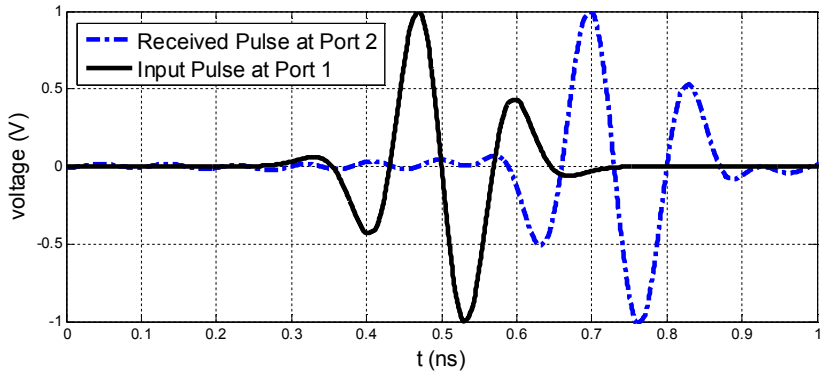

Fig.2: Time-domain response of the designed balun

The experimental setup with two polarization-matched antennas is shown in Fig.3. The transmit antenna is connected to port 1 of the network analyzer and the receiving antenna is connected to port 2. At the moment, the 2port {S}-parameters and group delay measurements are performed only for antennas' boresight direction. The simulation is conducted using frequency domain MoM code EMSS FEKO [8]. Time domain responses for measurements and simulation results are obtained using inverse Fourier transform. The monocycle first, second, and fifth derivative Gaussian pulses with pulse width designed to comply with Federal Communications Commission indoor mask [9] are used as excitation.

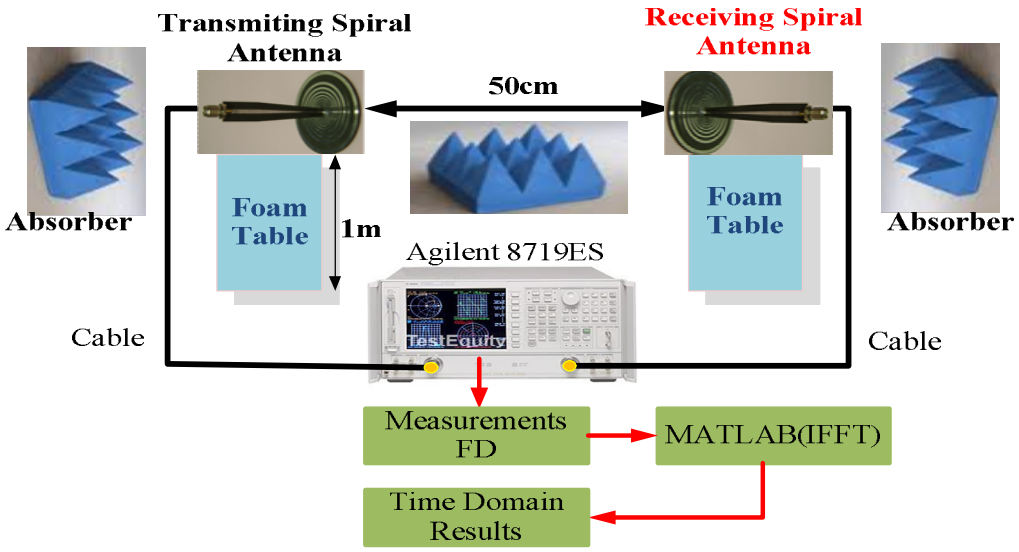

Fig.3: Experimental setup for time domain characterization

3. Results and Discussion

The measured reflection coefficients of the fabricated equiangular and Archimedean spiral antennas, plotted in Fig.4(a) and Fig.4(b) respectively, show a good impedance match throughout the designed bandwidth.

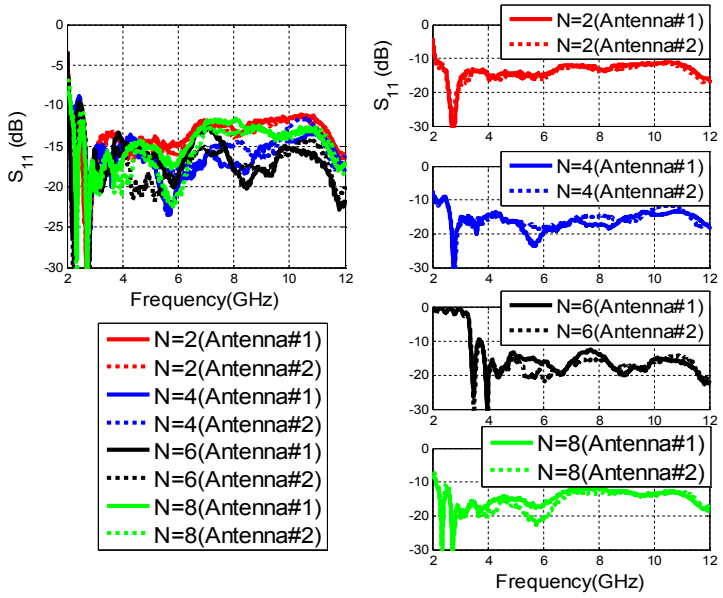

(a)

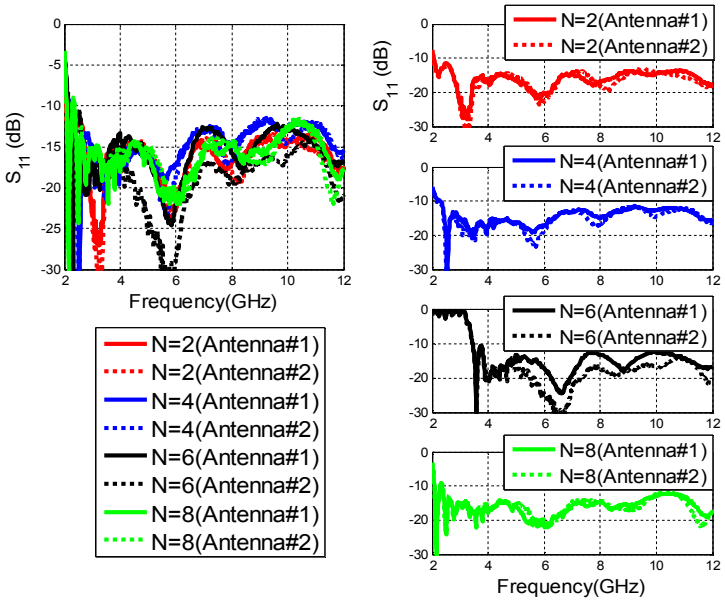

(b)

Fig.4: Return loss of studied spiral antennas: (a) Equiangular (b) Archimedean

The magnitude of the transfer function and its unwrapped phase of the equiangular and Archimedean spirals transmit-receive links are shown in Figures 5(a), 5(b), 6(a), and 6(b), respectively. As seen, the magnitudes are similar for different number of turns while the phase is heavily affected by the number of turns. This is expected as the two antenna types have similar gains while the phase cycling increases with tighter warp.

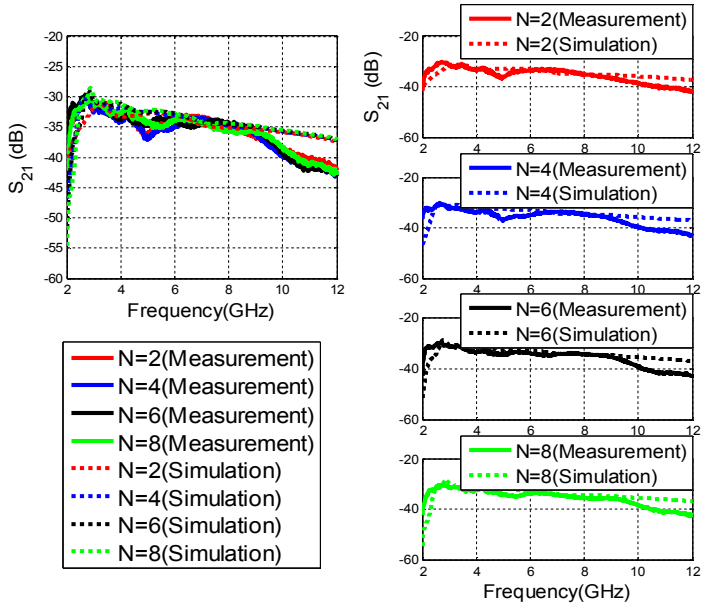

(a)

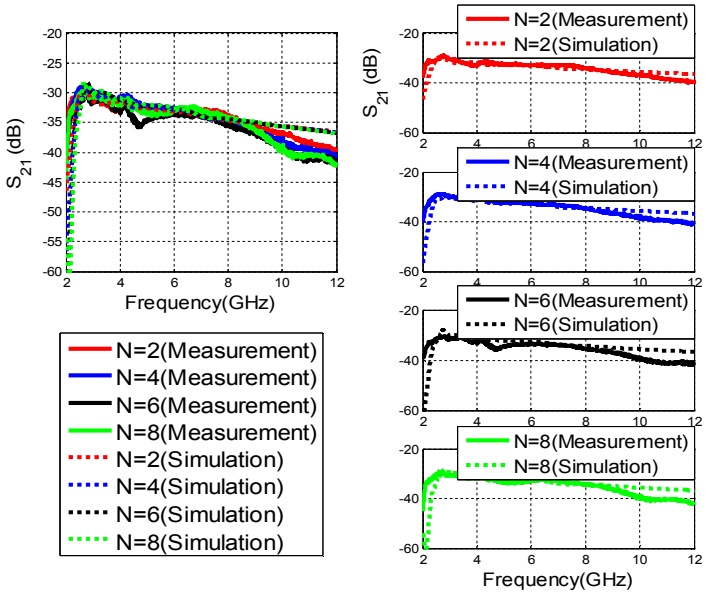

(b)

Fig.5: Magnitude of the transfer function of the planar spiral antenna links for different number of turns (N): (a) Equiangular (b) Archimedean

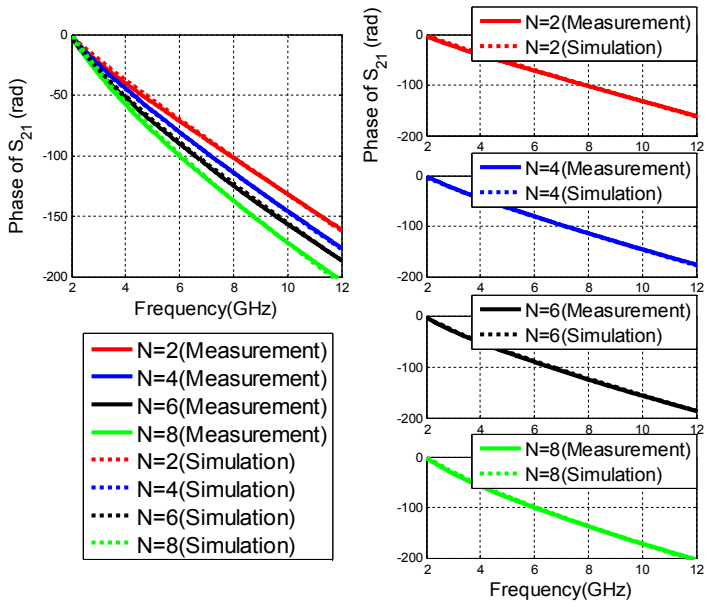

(a)

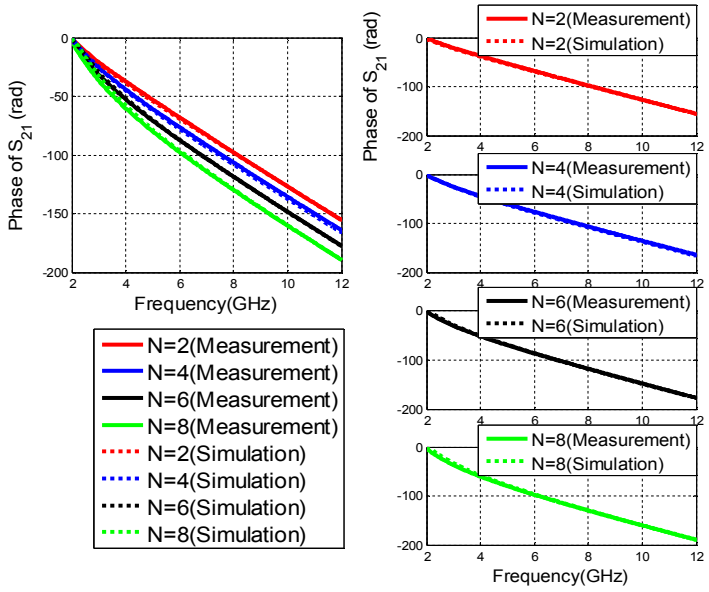

(b)

Fig.6: Phase of the transfer function of the planar spiral antenna links: (a) Equiangular (b) Archimedean.

The group delay curves, shown in Fig.7(a) for equiangular spiral and Fig.7(b) for Archimedean spiral are not constant which is expected because of the dispersive nature of the antennas. The group delay is used since the non-linearity of the transfer function phase cannot be clearly observed from the frequency swept phase response. The group

delay curves of equiangular spirals show more variation comparing to the Archimedean spirals curves indicating more pronounced dispersion.

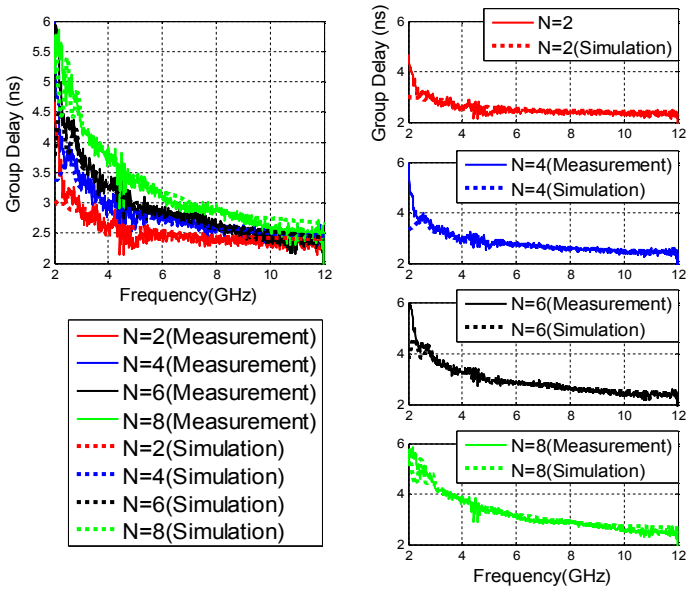

(a)

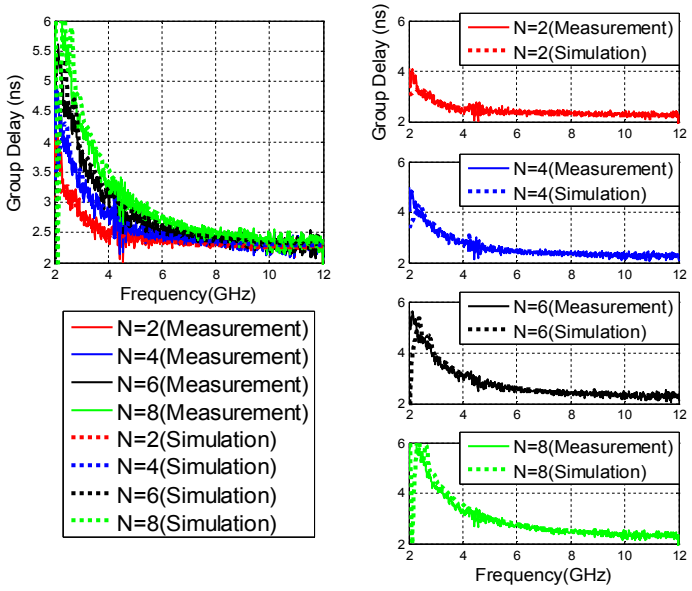

(b)

Fig.7: Group delay of the planar spiral antenna links: (a) Equiangular (b) Archimedean

The impulse response of the antennas exhibits a chirp with longer pulse duration with increased number of turns (see Figures 7(a) and 7(b)). The impulse responses of the

equiangular and Archimedean spirals are quite similar in terms of the amplitude and duration.

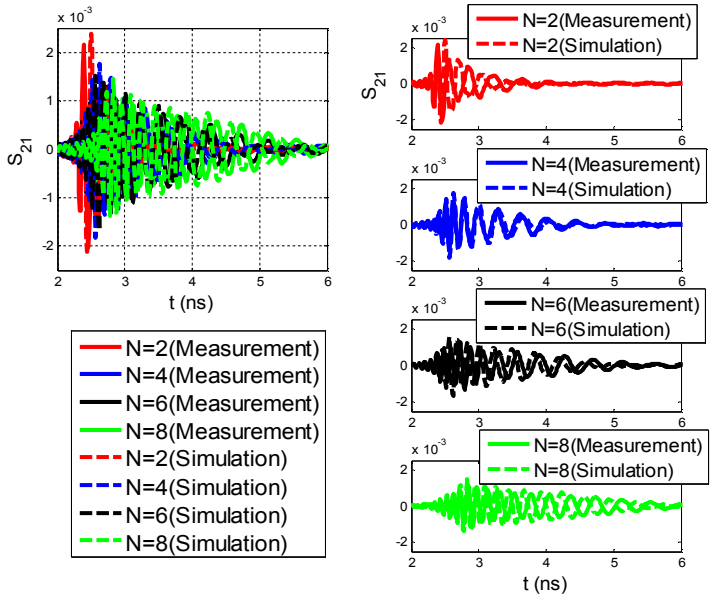

(a)

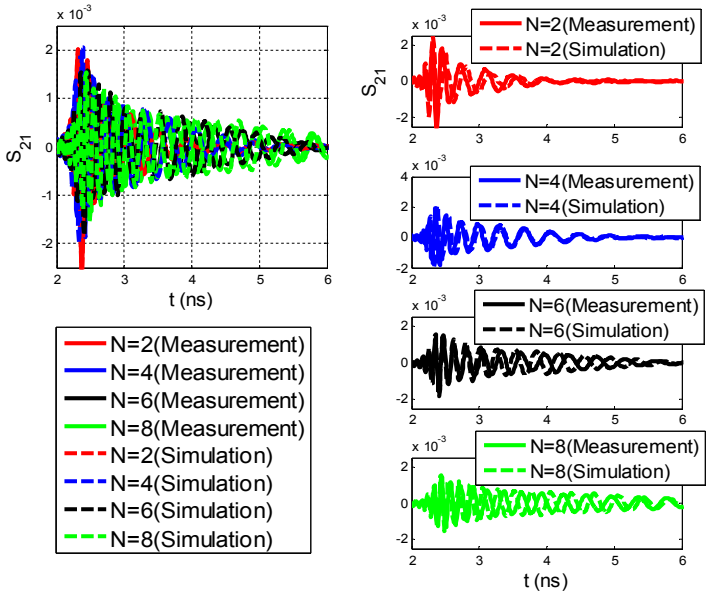

(b)

Fig.8: Impulse response of the link (a) Equiangular (b) Archimedean

Transmitted fifth derivative Gaussian pulse and received pulses obtained from measurement and simulation results are shown in Fig.8(a) and Fig.8(b). As seen, the received pulses duration increases with increased number of turns. Also, the results show

that the Archimedean spirals show less dispersive behavior comparing to the equiangular spiral antennas.

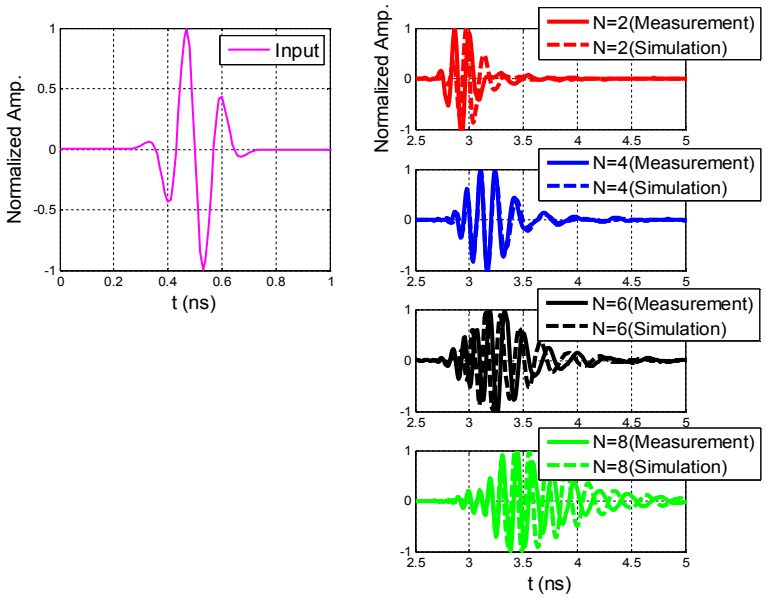

(a)

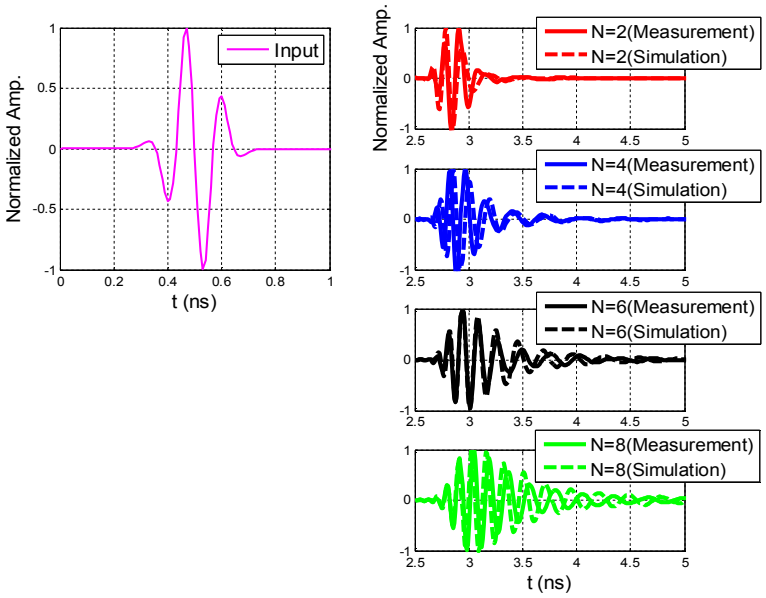

(b)

Fig.9: Normalized transmitted and received pulses (a) Equiangular (b) Archimedean

The fidelity factors between the input Gaussian pulses and the received pulses are also calculated and results are shown in Table 2. As seen, the excitation with a fifth derivative Gaussian pulse with $\sigma = 51ps$ mitigates the dispersive properties of the two types of

spiral antennas. The fidelity factor in the case of the fifth derivative Gaussian pulse is improved up to 50% comparing to the case of the first derivative. Thus the dispersion of equiangular and Archimedean spiral antennas can be mitigated by modifying the incident voltage. Notice that a satisfactory agreement between the measurements and MoM results is obtained.

Table 2: Fidelity factors of the studied antennas for different input pulses

a-First Derivative(σ=33ps)

	Measurement (Simulation)	
Number of Turns (N)	**Equiangular**	**Archimedean**
2	0.656(0.670)	0.662(0.645)
4	0.501(0.513)	0.501(0.465)
6	0.408(0.419)	0.423(0.381)
8	0.335(0.360)	0.350(0.337)

b-Second Derivative(σ=39ps)

	Measurement (Simulation)	
Number of Turns (N)	**Equiangular**	**Archimedean**
2	0.796(0.794)	0.818(0.759)
4	0.614(0.627)	0.662(0.594)
6	0.556(0.497)	0.564(0.487)
8	0.437(0.436)	0.466(0.435)

c-Fifth Derivative(σ=51ps)

	Measurement (Simulation)	
Number of Turns (N)	**Equiangular**	**Archimedean**
2	0.916(0.909)	0.949(0.931)
4	0.782(0.825)	0.859(0.821)
6	0.740(0.713)	0.785(0.728)
8	0.697(0.623)	0.721(0.659)

4. Conclusion

This paper discusses the time- and frequency domain performances of equiangular and Archimedean spiral antennas in a free space channel UWB transmit-receive system. It is demonstrated that the studied antennas have similar performance in the frequency domain; however, the Archimedean spiral is less dispersive for the same number of turns. Furthermore, the study shows that the natural dispersion of spiral antennas can be mitigated by pulse shaping. Specifically, it is shown that the fifth derivative Gaussian

pulse with $\sigma = 51ps$ designed for indoor UWB systems can be used to compensate the dispersive properties of the examined spirals with two turns and mitigate the dispersive behavior of studied spirals with more than two turns. A good agreement between the measured and MoM results verifies presented conclusions.

5. References

[1] J.D. Dyson, R. Bawer, P. E. Mayes, and J. I. Wolfe. "A Note on the Difference Between Equiangular and Archimedes Spiral Antennas,". *IRE Transactions on Microwave Theory and Techniques*, Vol. 9, pp. 203–205, March 1961.

[2] S. Licul, J.A.N. Noronha, W.A. Davis, D.G. Sweeney, C.R. Anderson, and T.M Bielawa, "A parametric study of time-domain characteristics of possible UWB antenna architectures," *Proc. of IEEE Vehicular Technology Conference (VTC 2003),* Vol. 5, pp. 3110–3114, October 2003.

[3] H.G. Schantz, "Dispersion and UWB antennas," *2004 International Workshop on Ultra Wideband System. Joint with Conference on Ultra Wideband System and Technologies*, pp. 161–165, May 2004.

[4] Z. N. Chen, X. H. Wu, H. F. Li, N. Yang, and M. Y. W. Chia, "Considerations for source pulses and antennas in UWB radio systems," *IEEE Transaction on Antennas and Propagation*, Vol. 52, No. 7, pp. 1739–1748, July 2004.

[5] D. Lamensdorf and L. Susman, "Baseband-pulse-antenna techniques," *IEEE Antennas and Propagation Magazine*, Vol. 36, No. 1, pp. 20–30, February 1994.

[6] T. Wang, Z. N. Chen, and K. S. Chen, "Effect of selecting antennas and templates on BER performance in pulsed UWB wireless communication systems," *Proceedings of IEEE International Workshop on Antenna Technology*, Singapore, pp. 446–449, March 2005.

[7] T.W. Hertel and G.S. Smith, "On the dispersive properties of the conical spiral antenna and its use for pulsed radiation," *IEEE Transaction on Antennas and Propagation*, Vol. 51, No. 7, pp. 1426-1433, July 2003.

[8] FEKO, EM Software & Systems, http://www.feko.info.

[9] H. Sheng, P. Orlik, A. M. Haimovich, L. J. Cimini, and J. Zhang ,"On the spectral and power requirements for ultra-wideband transmission," *Proc. of IEEE Int. Conf. on Communications*, Vol. 1, pp. 738–742, May 2003.

Asymmetrical Low Frequency Conformal Antennas for Small Unmanned Aerial Vehicles: Dipole and Monopole Tradeoffs

Brandan T. Strojny and Roberto G. Rojas
ElectroScience Laboratory
Department of Electrical and Computer Engineering
The Ohio State University, Columbus, OH
strojnyb@ece.osu.edu, rojas-teran.1@osu.edu

***Abstract*— Asymmetrical conformal antennas for small unmanned aerial vehicles (UAVs) are analyzed in this research. Specifically, the low frequency performance tradeoffs of a dipole and monopole antenna conformal to the vertical tail and fuselage plate of a Dakota UAV are investigated. Limited area combined with few vertical surfaces has performance implications on low frequency VHF/UHF antennas. Monopole antennas operate at lower frequencies compared to a dipole antenna with the same element length. However, due to limited fuselage width on small UAVs, the ground plane of the monopole becomes electrically small degrading the radiation performance. For this study, the fuselage is modeled by a rectangular planar plate. The effects on radiation pattern, bandwidth, input impedance and quality factor (Q) will be investigated while changing the size of the fuselage plate and feed location for both asymmetrical conformal dipole and monopole antennas. The tradeoffs in performance will be discussed.**

1. INTRODUCTION

Unmanned aerial vehicles (UAVs) have become increasingly popular for scientific research, remote sensing, transportation of goods, search and rescue as well as military applications. UAVs have several key advantages over piloted aircrafts including low cost and the ability to penetrate unattainable areas that would be classified as unsafe. Technological advances and miniaturization allow communication devices to be placed on small UAVs. An unmanned aircraft system (UAS) is a complex system that includes the ground station, communication links and the UAV. To integrate the UAV into the UAS, it must have at a minimum GPS and VHF/UHF communication antennas. The GPS antenna is used to control the UAV over its programmed flight, while the VHF/UHF communication antenna provides a two-way link with personnel on the ground to relay information. VHF/UHF antennas can also be used for various sensing and tracking applications.

One of the challenges for communication, sensing, tracking and other applications is the limited area available on the fuselage, wings and tail section of the UAV for the installation of antennas, especially at VHF frequencies. At VHF frequencies the UAV may become electrically small implying electrically small antennas (ESAs). ESAs have many design challenges including large impedance mismatch losses and narrowband operation (high stored energy). Moreover the vertical height of the UAV is generally limited to the tail section. UAV communication as well as some sensing and tracking antennas require vertically polarized, omnidirectional radiation pattern, and large bandwidth covering VHF/UHF frequency bands.

With limited vertical height and fuselage width it is necessary to understand the design tradeoffs and limitations of conformal low frequency UAV antennas. Derivatives of dipole and monopole antennas are commonly used for VHF/UHF communication. Typically monopole antennas are preferred over dipoles due to their lower operation frequency for a fixed height; however, a monopole antenna requires a ground plane. The fuselage of the UAV is used for this

purpose but is limited by the width typically resulting in a rectangular ground plane. Further, the monopole element is often not in the center of the ground plane. It is desirable for the ground plane radius to be larger than λ/4 at operation frequency. Small UAVs have very limited area to create a ground plane so the question becomes whether it is better to create a monopole with an electrically small ground plane or use the available height to create a dipole.

This research focuses on an asymmetrical conformal dipole and monopole antenna of the same vertical height and occupied volume. Both antennas will be designed using the tail section and fuselage plate of a Dakota UAV. To simplify the model, while maintaining the relevant physics, the fuselage will be modeled by a planar rectangular plate. At 50 MHz the length of a Dakota UAV is approximately λ/3 and vertical height of the tail is approximately λ/13. The effects on radiation pattern, bandwidth, feed location, quality factor (Q) and input impedance will be studied while changing the dimensions of the fuselage plate. Also the -20 dBi realized vertical gain point will be illustrated. Realized gain above -20 dBi is often the most challenging performance metric to meet because at VHF frequencies because the UAV becomes electrically small. To achieve the best low frequency performance, monopole antennas are generally used because they can operate at frequencies twice as low as corresponding dipole antennas.

2. UAV DESCRIPTION

The Dakota UAV shown in Fig. 1(a) is under investigation in this research for the analysis of low frequency antenna performance. This geometry is a simplified version of a more accurate model but is sufficient for the present purposes. The UAV is divided into three regions. Region I represents the tail section to which the antenna element is conformal to. This region is commonly utilized for the design of conformal VHF/UHF antennas, because it is one of the few vertical locations on the UAV yielding a vertically polarized antenna. Region II represents the fuselage plate which is the main parameter under investigation. This region can be used to create a ground plane for monopole type antennas. Region III is the fuselage of the UAV which, in this paper, will be removed. The fuselage skin is made of a fiberglass/epoxy composite and will not be considered for simplicity. The Dakota UAV is simplified further to only include the tail section and fuselage plate (i.e. Region I and II), shown in Fig. 1(b-d).

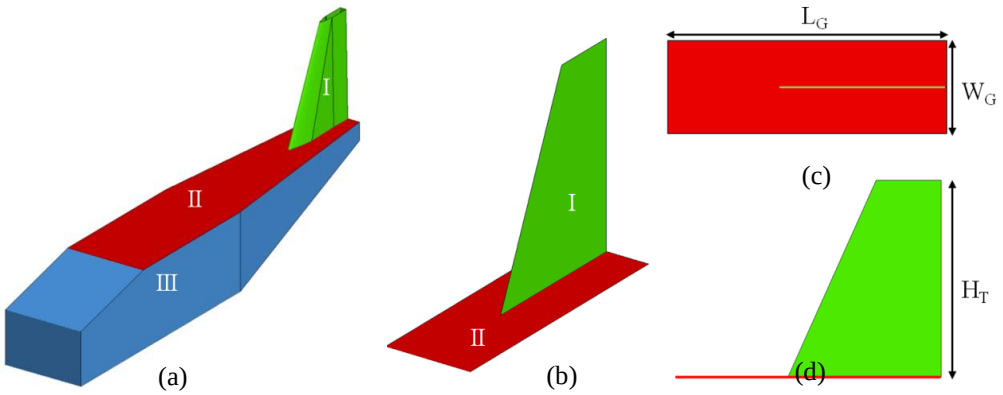

Fig. 1: Simplified Dakota UAV Model (a) UAV Sections: Tail (Region I), Fuselage Plate (Region II), Fuselage (Region III), (b) Simplified Model, (c) Top View, (d) Side View

The parameters under investigation are the width (W_G) and length (L_G) of the fuselage plate, Region II. The vertical height of the Dakota UAV tail (H_T) is fixed at 0.454 m. The vertical height and occupied volume are the physical properties establishing the low frequency antenna performance [1]. Mainly the vertical height establishes the radiation resistance, while the

occupied volume determines the antenna's bandwidth. At 50 MHz the electrical height of the Dakota UAV tail is approximately λ/13, thus the antenna is electrically small.

Two approaches to design an asymmetrical conformal UAV antenna will be taken. The first is to excite the tail as a dipole antenna. This involves creating a slot in the tail section to separate the arms as depicted in Fig. 2(a). The second approach is to excite the tail as a monopole. This involves creating a gap between the tail section and fuselage plate as shown in Fig. 2(b). In both cases the tail is modeled as a flat copper plate. For each antenna configuration, four fuselage plate cases will be investigated (also simulated as copper). The cases are listed in Table 1.

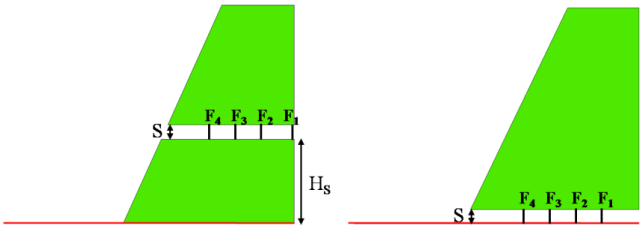

Fig. 2: Antenna Comparison with Four Feed Locations: (a) Dipole, (b) Monopole

Table 1
Fuselage Plate Dimensions

	W_G (m)	L_G (m)
Case 1	.1	.4
Case 2	.1	.6
Case 3	.2	.4
Case 4	.2	.6

3. REFERENCE ANTENNAS

To start the analysis, reference dipole and monopole antennas will be used. The reference antennas give a baseline performance metric and illustrate the advantage of using the monopole for low frequency operation. Each antenna is modeled using four different cases. The antenna element is initially modeled as a wire. The element is then modeled as a flat plate while varying the plate width (P_W) using widths of 5, 10 and 15 cm shown in Fig. 3. A P_W of 15 cm is representative of the maximum available tail width before the tapered region of the tail begins. The height (H) of the element is fixed at 0.454 m. A finite square ground plane for the monopole antenna was created. The width of the ground plane (W_G) is λ/2 at the λ/4 monopole operation frequency of 165.2 MHz.

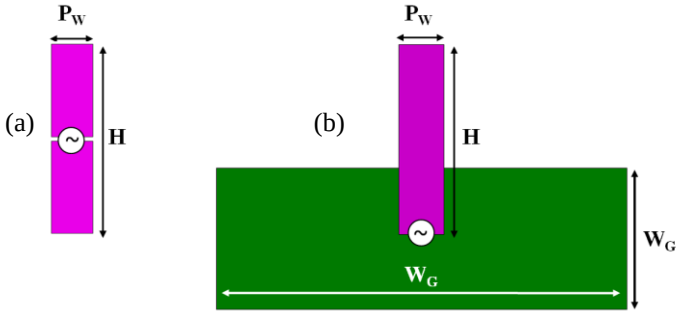

Fig. 3: Reference Antennas: (a) Dipole, (b) Monopole

The realized vertical gain in dBi vs. frequency for the reference antenna is shown in Fig. 4. For the wire case the gain peaks near the expected λ/2 and λ/4 (i.e. 330.4 and 165.2 MHz) operation frequencies for the dipole and monopole antennas, respectively. Both antennas are narrowband due to the limited volume they occupy. The elements are then simulated as a flat plate while varying the width P_W. As the width increases the realized gain increases and the low frequency performance is improved. The -20 dBi realized gain frequencies are shown in Table 2 and it is very clear the monopole has the low frequency performance advantage. For completeness, the $|S_{11}|$ in dB is shown in Fig. 5. As expected, the impedance match is greatly improved when the width of the plate is increased.

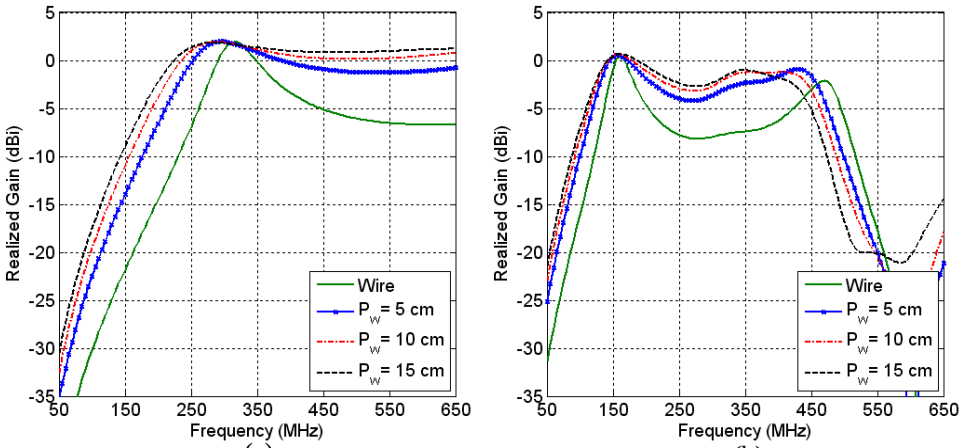

(a) (b)

Fig. 4: Reference Antenna's Realized Vertical Gain in dBi: (a) Dipole, (b) Monopole

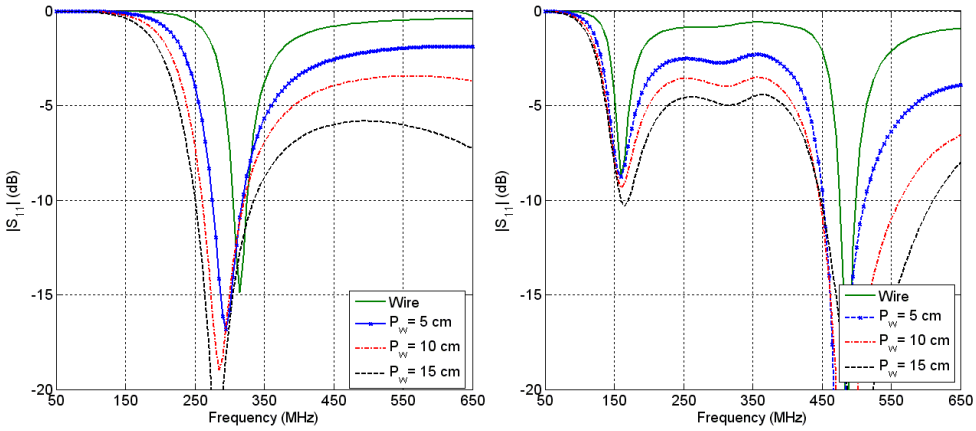

(a) (b)

Fig. 5: Reference Antenna's $|S_{11}|$ in dB: (a) Dipole, (b) Monopole

Table 2
Reference Antennas': Lowest -20 dBi Realized Vertical Gain and –3 dB $|S_{11}|$ Frequencies (MHz)

	-20 dBi		-3 dB $\|S_{11}\|$	
Antenna Element	Dipole	Monopole	Dipole	Monopole
Wire	162.00	85.79	284.3	146.1
5 cm	113.20	64.81	242.2	134.1
10 cm	97.83	58.24	223.2	129.9
15 cm	88.15	53.92	210.0	127.5

4. ASYMMETRICAL CONFORMAL DIPOLE ANTENNA

The asymmetrical conformal dipole is created by making a slot in the tail section at a height H_S from the fuselage plate as shown in Fig. 2(a). Arm 1 is formed by the top part of the tail while arm 2 is formed by the lower part of the tail and the fuselage plate. The arm separation S is 3 mm. The H_S was chosen to be 0.175 m determined from a Characteristic Mode analysis. This analysis showed a dominant mode similar to the fundamental dipole mode and was omitted for brevity. Four feeding locations (F_1 - F_4) are considered for each case (see Fig. 2(a)). The $|S_{11}|$ in dB of each case is shown in

Fig. 6 referenced to 50 Ω. As expected, the feed location has a significant effect on input impedance. Feed location F_1 (green curve) has the largest mismatch loss for all cases. It is also important to note that changing the width of the fuselage plate has minimal effects on input impedance whereas changing the length has a significant impact. The -3 dB frequencies are listed in Table 3.

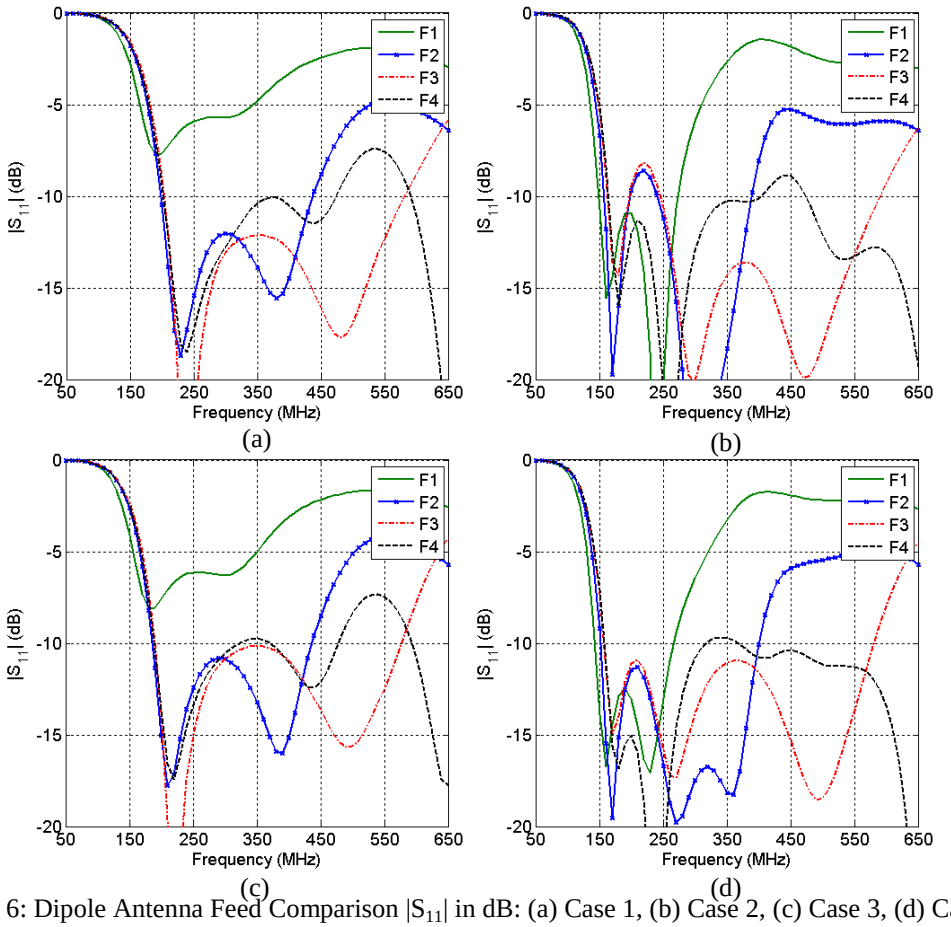

Fig. 6: Dipole Antenna Feed Comparison $|S_{11}|$ in dB: (a) Case 1, (b) Case 2, (c) Case 3, (d) Case 4

Table 3
Dipole Antenna: Lowest -3 dB $|S_{11}|$ Frequency (MHz)

	Case 1	Case 2	Case 3	Case 4
F1	151.2	127.9	142.5	122.3
F2	162.9	135.4	152.8	130.1
F3	166.8	139.1	156.0	132.4
F4	164.5	139.7	154.1	132.7

The realized vertical broadside gain (i.e. θ=90°) in dBi vs. frequency for each feed location is considered for all cases (Fig. 7 - Fig. 10). Similar to the impact on input impedance, changing the width of the fuselage plate has negligible effects on radiation pattern. However, changing the length has noticeable effects. It is important to note that for all cases F_1 has the largest null in radiation pattern starting at 300 MHz while F_3, has the most uniform radiation pattern over a large frequency range. The performance is attributed to having the feed near the center of the dipole arms. Table 4 list the frequency points in which the realized vertical gain reaches -20 dBi. The results show that increasing the size of the plate effectively loads the antenna, improving low frequency performance.

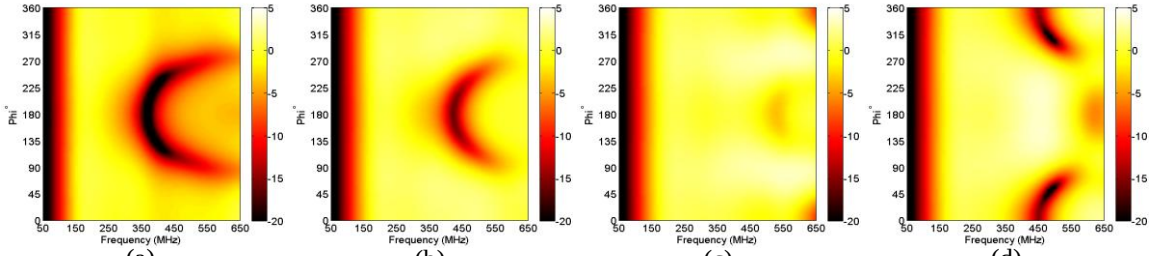

(a) (b) (c) (d)

Fig. 7: Dipole Realized Vertical Gain in dBi Case 1: (a) F_1, (b) F_2, (c) F_3, (d) F_4

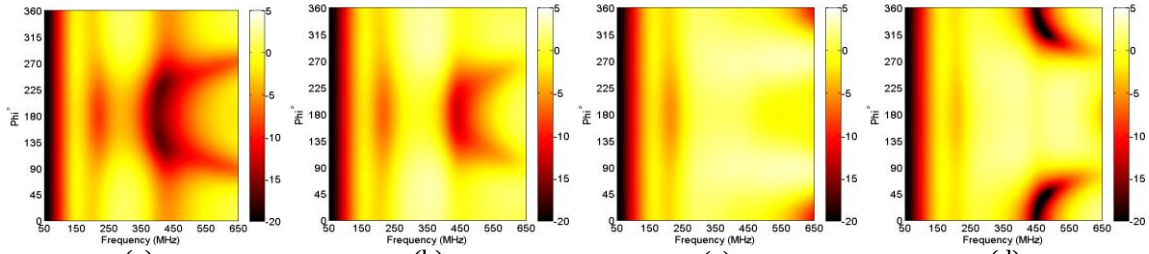

(a) (b) (c) (d)

Fig. 8: Dipole Realized Vertical Gain in dBi Case 2: (a) F_1, (b) F_2, (c) F_3, (d) F_4

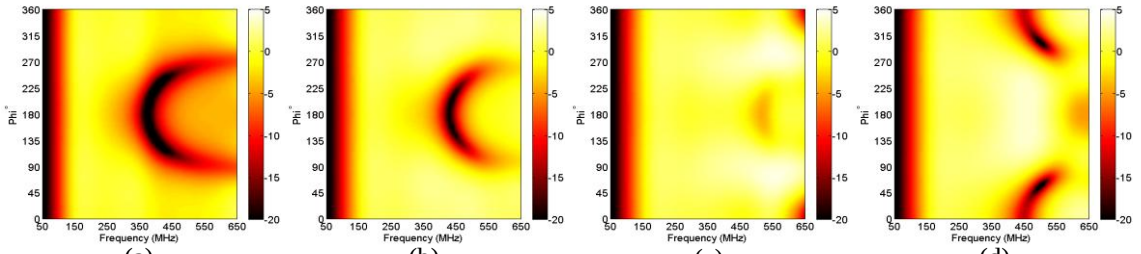

(a) (b) (c) (d)

Fig. 9: Dipole Realized Vertical Gain in dBi Case 3: (a) F_1, (b) F_2, (c) F_3, (d) F_4

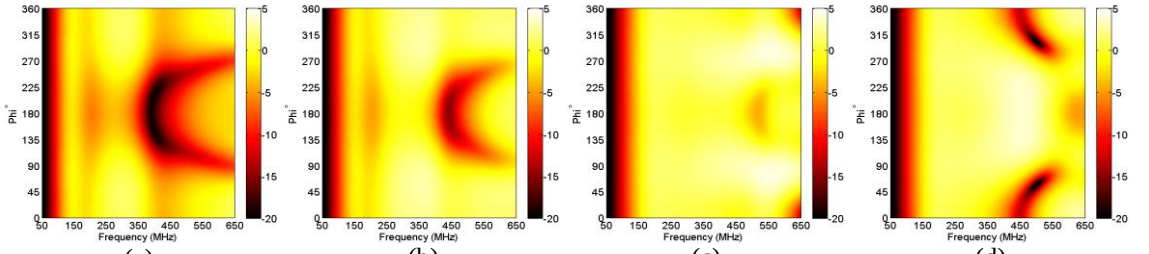

(a) (b) (c) (d)

Fig. 10: Dipole Realized Vertical Gain in dBi Case 4: (a) F_1, (b) F_2, (c) F_3, (d) F_4

Table 4
Dipole Antenna's: Lowest -20 dBi Realized Vertical Gain Frequencies (MHz)

	Case 1	Case 2	Case 3	Case 4
F1	67.38	63.34	63.56	60.11
F2	68.70	64.52	64.71	61.21
F3	69.00	64.82	64.97	61.48
F4	68.70	64.62	64.69	61.26

5. CONFORMAL MONOPOLE ANTENNA

The conformal monopole antenna is formed by removing the slot in the tail section and creating a gap S of 3 mm between the fuselage plate and tail section as shown in Fig. 2(b). In this case, the fuselage plate is used as a ground plane. The $|S_{11}|$ in dB vs. frequency and -3 dB frequencies are shown in Fig. 11 and Table 5, respectively, referenced to 50 Ω. The -3 dB $|S_{11}|$ frequency has increased by at least 42.6 MHz in cases 1 and 3 compared to the 15 cm reference monopole. The electrical dimensions of the fuselage plate at the monopole operation frequency of 165.2 MHz are λ/18.16 × λ/4.54 and λ/9.08 × λ/4.54 for case 1 and 3 respectively. Cases 2 and 4 frequencies are also increased but not as drastically.

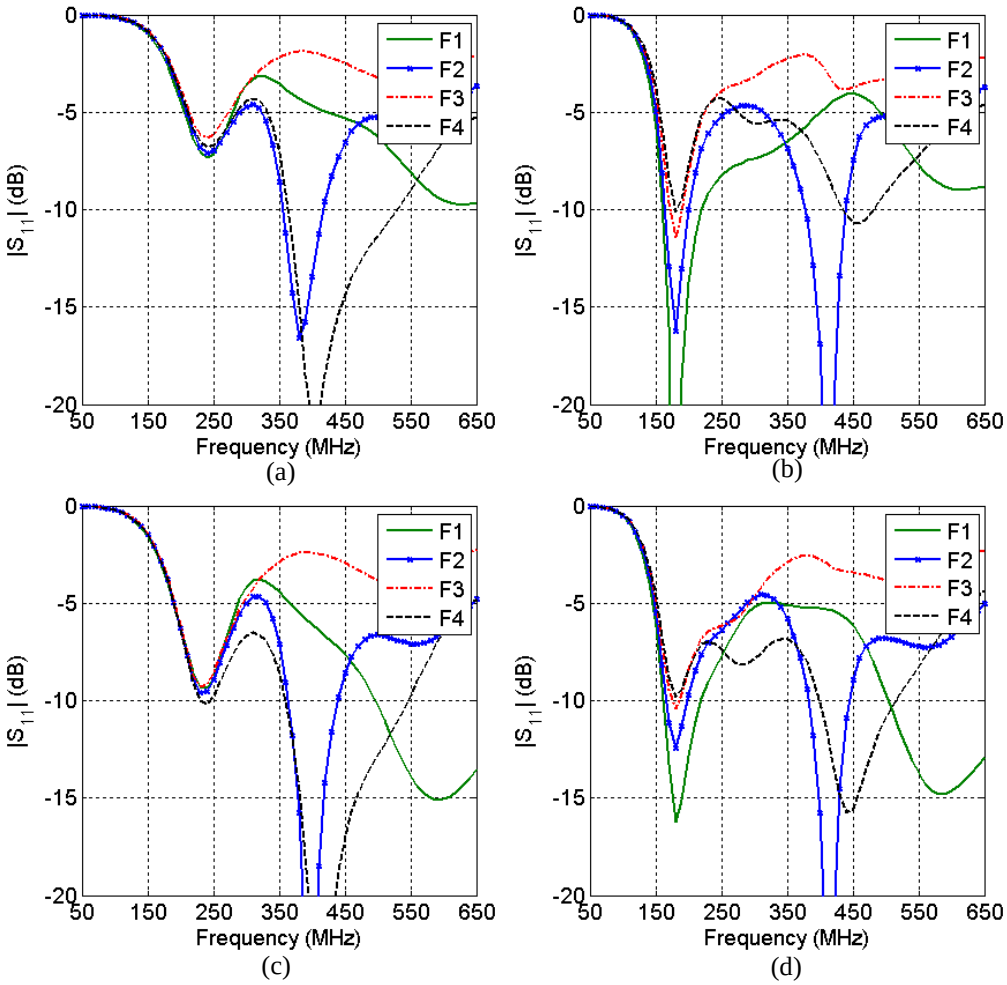

Fig. 11: Monopole Antenna Feed Comparison $|S_{11}|$ in dB: (a) Case 1, (b) Case 2, (c) Case 3, (d) Case 4

Table 5
Monopole Antenna: Lowest -3 dB $|S_{11}|$ Frequency (MHz)

	Case 1	Case 2	Case 3	Case 4
F1	184.4	136.5	170.1	133.5
F2	188.4	140.2	172.0	136.2
F3	191.0	143.1	172.8	138.5
F4	189.1	144.6	171.3	139.2

The realized vertical broadside gain in dBi vs. frequency for each feed location is considered for all cases (Fig. 12 - Fig. 15). Similar to the impact on input impedance, changing the width of the fuselage plate has negligible effects on radiation pattern, however changing the length has noticeable effects.

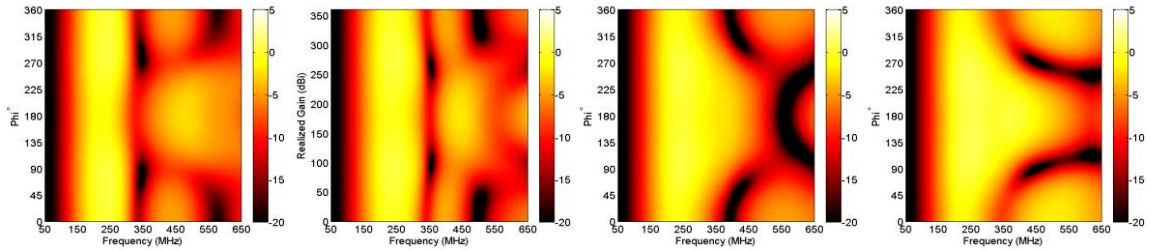

(a) (b) (c) (d)

Fig. 12: Monopole Realized Vertical Gain in dBi Case 1: (a) F_1, (b) F_2, (c) F_3, (d) F_4

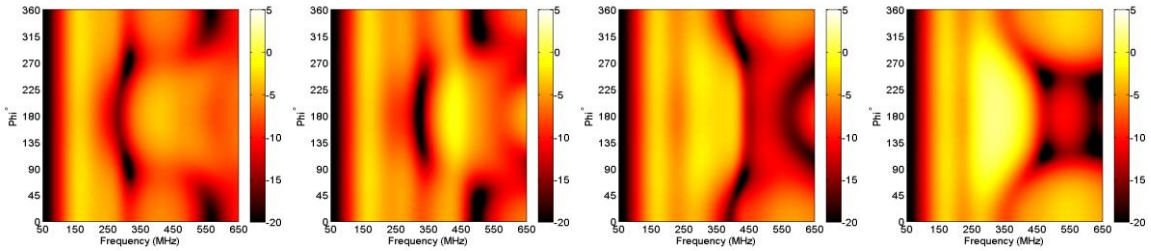

(a) (b) (c) (d)

Fig. 13: Monopole Realized Vertical Gain in dBi Case 2: (a) F_1, (b) F_2, (c) F_3, (d) F_4

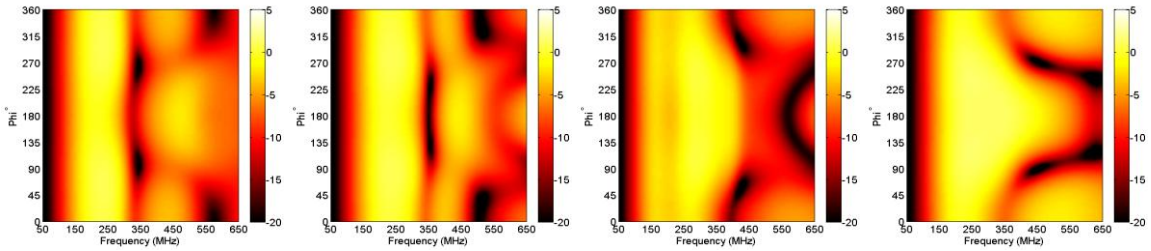

(a) (b) (c) (d)

Fig. 14: Monopole Realized Vertical Gain in dBi Case 3: (a) F_1, (b) F_2, (c) F_3, (d) F_4

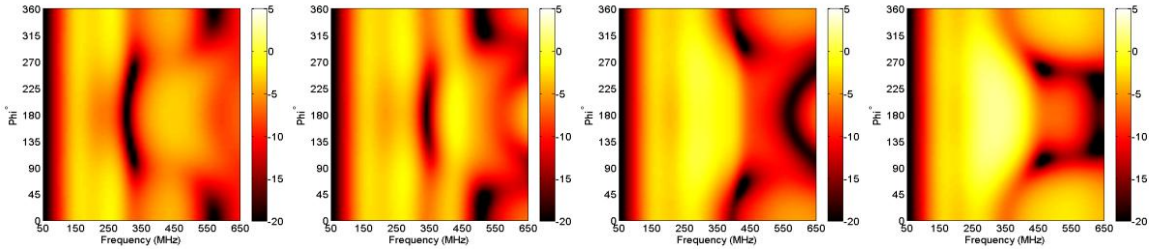

(a) (b) (c) (d)

Fig. 15: Monopole Realized Vertical Gain in dBi Case 4: (a) F_1, (b) F_2, (c) F_3, (d) F_4

Table 6
Monopole Antenna's: Lowest -20 dBi Realized Vertical Gain Frequencies (MHz)

	Case 1	Case 2	Case 3	Case 4
F1	74.59	66.32	65.29	60.19
F2	75.22	66.87	65.72	60.66
F3	75.53	67.30	65.92	60.86
F4	75.24	67.17	65.67	60.67

6. QUALITY FACTOR COMPARISON

The Q is another important performance metric for antennas. The quality factor is inversely related to the bandwidth of the antenna. Similarly, the Q gives insight into the bandwidth of a matching network. When the antenna becomes electrically small the Q becomes very large and the radiation resistance becomes very small. A matching network can be used to improve the realized gain, but if the Q is very high the bandwidth of the matching network may be very limited. The Q for the reference antennas vs. frequency is shown in Fig. 16 and frequencies in which the Q is equal to 50 are shown in Table 7. It is desirable to have a Q around 50 or less when creating a matching network. For Q>50, a matching network can still be used, however, the bandwidth will be limited.

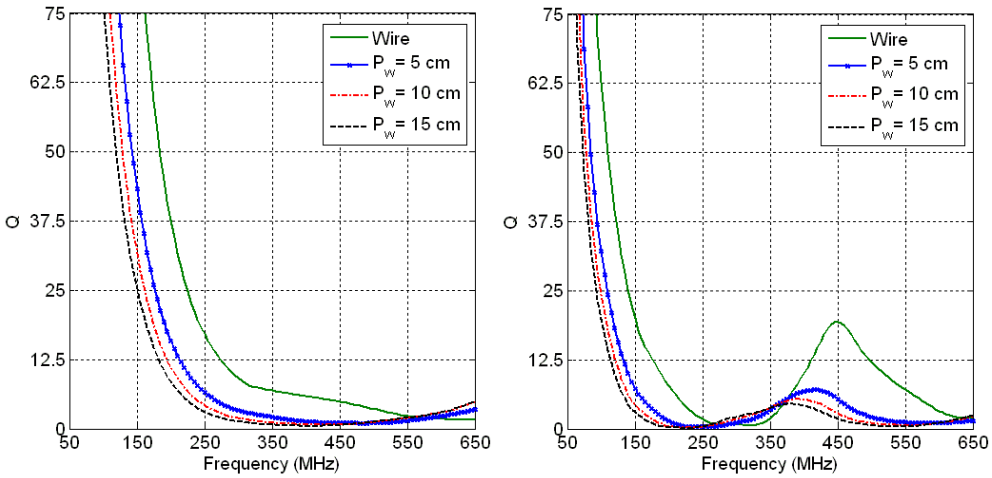

Fig. 16: Quality Factor Comparison for Reference Antennas: (a) Dipole, (b) Monopole

Table 7
Frequencies (MHz) in which the Reference Antennas' Quality Factor is Equal to 50

Antenna Element	Dipole	Monopole
Wire	184.1	109.7
5 cm	143	84.86
10 cm	128.8	77.81
15 cm	119.1	73.28

The Qs for asymmetrical dipole and monopole antennas are calculated for the optimum feed location and shown in Fig. 17. The optimum feed location for both antennas was F3. This location provides the best tradeoff between $|S_{11}|$ and uniform pattern vs. frequency. The Q=50

frequencies are shown in Table 8. As expected as the size of the fuselage plate increases the Q decreases.

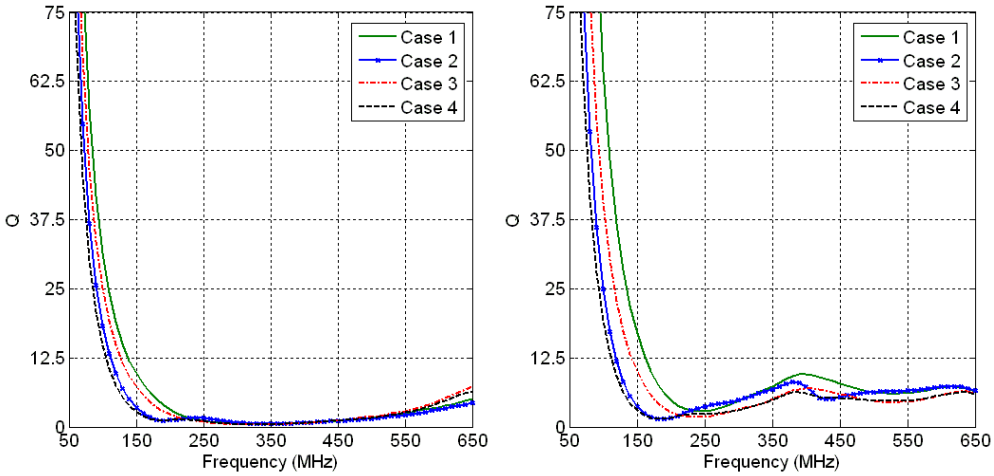

(a) (b)

Fig. 17: Quality Factor Comparison for Asymmetrical Antennas: (a) Dipole, (b) Monopole

Table 8
Frequencies (MHz) in which the Asymmetrical Antennas' Quality Factor is Equal to 50

	Dipole	Monopole
Case 1	84.81	109.0
Case 2	72.68	93.65
Case 3	78.30	81.98
Case 4	68.16	75.99

7. COMPARISON OF DIPOLE AND MONOPOLE ANTENNAS

For both antennas the most noticeable effect on input impedance and radiation pattern occurs when the length of the fuselage plate was changed. Changing the width of the fuselage plate has negligible effects. Increasing the length of the fuselage plate lowered the operating frequency for both antennas. The monopole resonant frequency decreases to 165 MHz when the fuselage plate was increased to 0.6 m (i.e. case 2 and case 4). This results in the monopole operating near the expected $\lambda/4$ resonant frequency.

The feed location effect on pattern can be explained by the changes between the distance of the primary radiation point and secondary radiation points. The primary radiation point is directly related to feed location, however secondary radiation points exist at the junction between Region I and II. Secondary radiation points also exist at the ground plane ends. Depending on the electrical distance, the radiation from the secondary radiation points can either constructively or destructively interfere with the primary radiation point causing a non-uniform radiation pattern. For the asymmetrical dipole the electrical distance from F1 to the front intersection between Region I and II is near 180° at 380 MHz. This secondary radiation point will destructively interfere causing a null in the pattern as seen in Fig. 7-10(a). Similarly, the physical distance between F2 and the front intersection between Region I and II shrinks causing the destructive interference to occur at a higher frequency point with respect to F1.

The deterioration of the monopole performance can be attributed to the electrically small ground plane. Typically monopole ground planes are greater than $\lambda/2$ in diameter (circular ground

plane), however due to the restrained width of the UAV fuselage plate the ground plane is electrically small degrading the performance. The bandwidth of the asymmetrical monopole antenna is acceptable, however with a rectangular electrically small ground plane the realized gain level decreases and the pattern is no longer uniform vs. azimuth. The reference monopole antennas realized vertical gain for ground plane widths of λ/2, λ/4 and λ/8 is shown in Fig. 18. When the ground plane shrinks with a fixed element size the operation frequency increases. The shift in operation frequency is shown in Fig. 19 and Table 9.

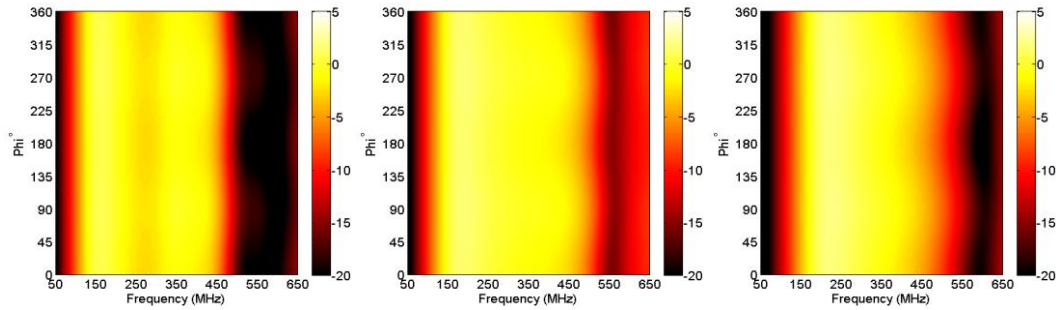

Fig. 18: Reference Monopole Square Ground Plane Comparison Realized Vertical Gain in dBi: (a) λ/2, (b) λ/4, (c) λ/8

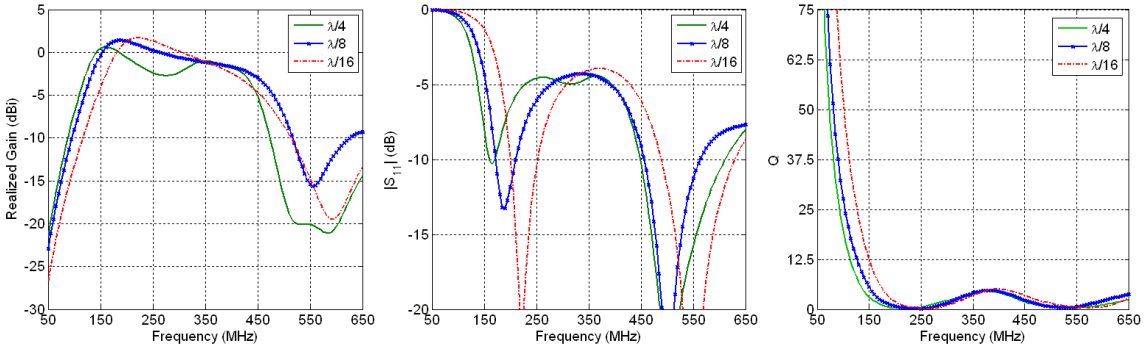

Fig. 19: Reference Monopole Square Ground Plane Comparison: (a) Realized Vertical Gain in dBi, (b) $|S_{11}|$ dB, (c) Q

Table 9
Reference Monopole's -20 dBi Realized Vertical Gain, –3 dB $|S_{11}|$ and Q=50 Frequencies (MHz)

W_G	-20 dBi	-3 dB $\|S_{11}\|$	Q
λ/2	53.97	127.5	73.28
λ/4	58.49	141.5	81.04
λ/18	71.51	169.9	101.8

The quality factor for the asymmetric dipole was reduced when increasing the fuselage plate length. When adding the fuselage plate to the dipole arm, the occupied volume of the antenna is increased reducing the stored energy lowering the Q. For the monopole, since the ground plane size is reduced from the reference case the occupied volume is reduced increasing the stored energy and thus resulting in an increased Q. For VHF communication design applications, it is very important to choose the antenna with a lower Q to try to cover the 30-80 MHz frequency band since a matching network will be required to achieve an acceptable gain level.

8. CONCLUSION

An asymmetrical conformal dipole and monopole VHF/UHF UAV antenna were investigated in this research. The fuselage plate parameters and feed location were varied and the effects on input impedance, radiation pattern and Q were compared. Results show that changing the width of the fuselage plate has minimal effects on input impedance and radiation pattern. For both antennas, F3 (near center fed) provides the best low frequency performance combine with uniform radiation pattern among all cases. It was shown that the asymmetrical dipole has superior performance compared to the monopole antenna. Monopole antennas typically have better low frequency performance over dipole antennas, which was illustrated by the reference antennas performance, however due to the electrically small ground plane the monopole's performance was severely degraded. Results show that for the Dakota UAV, a conformal dipole antenna will provide better antenna performance for VHF/UHF applications. At low frequencies, the quality factor for the asymmetrical dipole was lower than the monopole, thus making it easier to design a matching network. Having a lower Q will increase the bandwidth of a matching network. These findings are believed to be general. If the UAV has an electrically small ground plane, the antenna performance will be better in terms of radiation pattern and input impedance if fed like a dipole.

REFERENCES

[1] S. R. Best, "The Significance of Ground-Plane Size and Antenna Location in Establishing the Performance of Ground-Plane-Dependent Antennas," *IEEE Antennas and Propagation Magazine*, vol. 51, no. 6, pp. 29-43, 2009.

[2] S. R. Best, "A Discussion on Small Antennas Operating with Small Finite Ground Planes," *Proc. IEEE Int Antenna Technology Small Antennas and Novel Metamaterials Workshop*, pp. 152-155, 2006.

[3] M.-C. Huynh and W. Stutzman, "Ground plane effects on planar inverted-F antenna (PIFA) performance," *IEE Proc.-Microw., Antennas and Propag.*, vol. 150, no. 4, pp. 209-213, 2003.

IMPACT OF VARACTOR PLACEMENT ON RADIATION EFFICIENCY OF ELECTRICALLY SMALL FREQUENCY RECONFIGURABLE ANTENNAS

Siwen Yong and Jennifer Bernhard
Electromagnetics Laboratory
Department of Electrical and Computer Engineering
University of Illinois, Urbana, IL 61801

Abstract: The rapid decrease in sizes of electronic devices operating at multiple frequencies necessitates the use of electrically small frequency reconfigurable antennas. However, due to their small size, these antennas often radiate poorly, and any losses introduced by the inclusion of switching or tuning elements can adversely impact radiation efficiency. In this work, investigations indicate that an improvement in reconfigurable antenna radiation efficiency results when the tuning element creates asymmetric current flow in the structure. Measurements of antenna impedance and gain verify simulated results.

1. Introduction

Similar to conventional frequency reconfigurable antennas, incorporation of RF MEMs switches [1], PIN diodes [2], or varactors [3] enables frequency reconfiguration in electrically small antennas. Unfortunately, guidelines pertaining to the optimal placement of these tuning elements for highest radiation efficiency do not exist. To address this need, we performed studies on the electrically small inductively loaded dual sector antenna [4] modified for frequency reconfiguration. Section 2 introduces the antenna, and details the alterations performed to enable reconfiguration. Section 3 presents results relevant to the effects of varactor placement on radiation efficiency and impedance match. For proof of concept, commercially available chip capacitors with 1 pF and 2.4 pF capacitances and a series resistance of 0.2 Ω [5] replace varactors in both simulation and measurement. Section 4 concludes with a summary and a discussion of future work.

2. Electrically-Small Inductively Loaded Antenna

2.1 Single sector antenna

Unlike the dual sector antenna previously designed to achieve wide bandwidth [4], [6] the modified frequency reconfigurable single sector antenna utilizes a single brass sector to prevent dual frequency behavior. Figure 1 presents the antenna geometry with $ka = 0.838$ at 2.5 GHz.

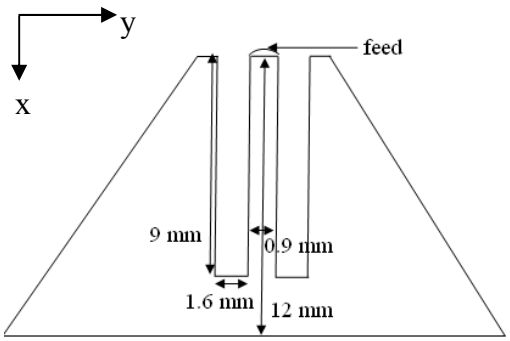

Figure 1(a). Top view of modified single sector antenna.

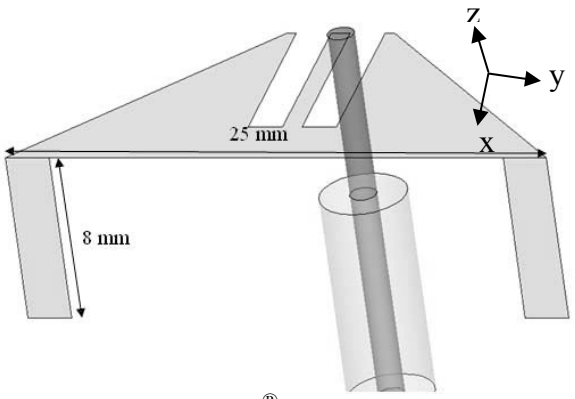

Figure 1(b). HFSS® simulation geometry of single sector antenna.

To model the fabricated antenna, simulations performed with Ansoft HFSS® utilized a circular copper ground plane of radius 30 cm in addition to the selection of brass as the material for the antenna sector and vertical inductive loads. Finally, placement of a constraint ensuring convergence when the calculated radiation efficiency changes by less than 1 % between successive passes results in improved accuracy of efficiency calculations. Figure 2 presents a Smith chart from 1 to 2.5 GHz for the single sector antenna.

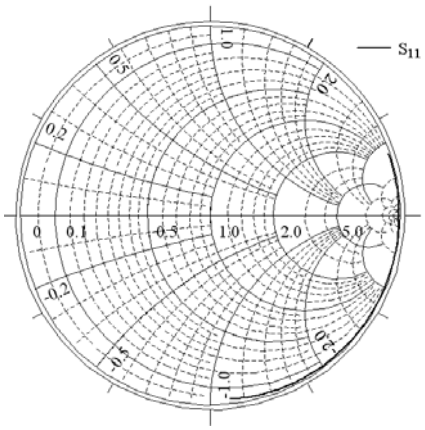

Figure 2. Smith chart plot from 1 to 2.5 GHz for single sector antenna

Figure 2 indicates that the reactance of the antenna is largely capacitive at the simulated frequencies. In addition, the large radius of the Smith chart circle results in a poor impedance match at these frequencies.

Since antenna modification for reconfiguration over a wide frequency range necessitates inclusion of a tuning varactor, incorporation of a capacitor in an inductive load provides proof of concept. In addition, two "Lumped RLC" boundaries of dimension 0.5 by 0.5 mm in series, one with a 1 pF capacitance and the other with loss resistance of 0.2 Ω, models the capacitor used in fabrication [5]. Figure 3(a) depicts the antenna geometry and Figure 3(b) presents the Smith chart from 1 to 2.5 GHz.

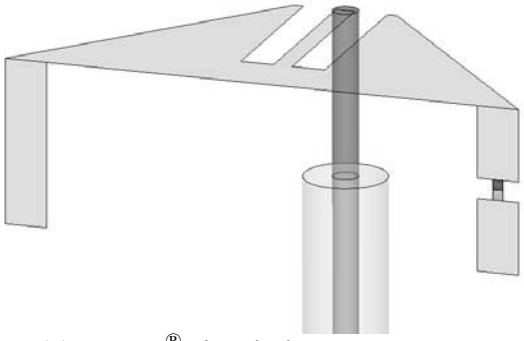

Figure 3(a). HFSS® simulation geometry indicating capacitor in inductive load.

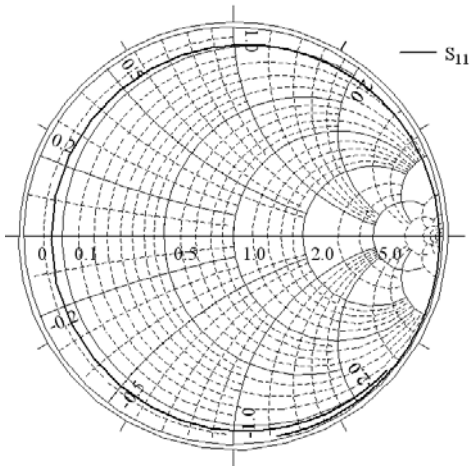

Figure 3(b). Smith chart plot from 1 to 2.5 GHz.

Comparison of Figures 2 and 3(b) indicates that with the addition of the tuning capacitor, the antenna reactance takes on both capacitive and inductive values over the frequency range. However, the large radius of the impedance circle results in minimal improvement in impedance matching. Consequently, the addition of three inductive loads in parallel ameliorates the problem by decreasing the overall inductance of the antenna, thereby tightening the impedance circle and improving the impedance match. Figure 4(a) and 4(b) present the antenna geometry and Smith chart plot respectively.

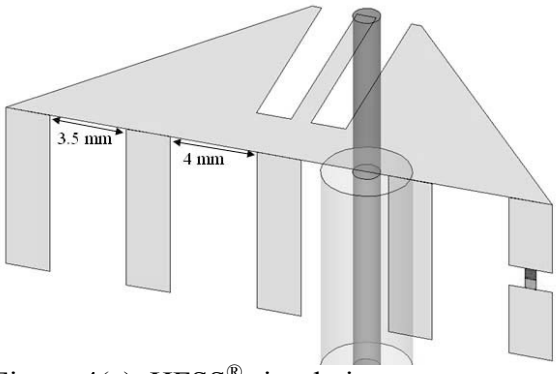

Figure 4(a). HFSS® simulation geometry of antenna with additional inductive loads

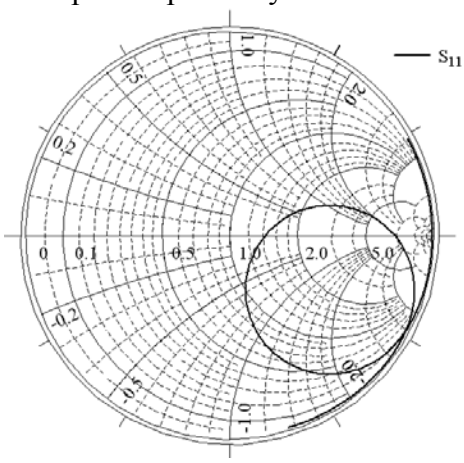

Figure 4(b). Smith chart plot from 1 to 2.5 GHz.

Examination of Figure 4(b) indicates that the addition of inductive loads results in the antenna being well matched at 1.82 GHz. However, with five inductive loads, additional locations for varactor placement exist and Section 3 presents the effects of varactor placement on impedance match and radiation efficiency.

3. Effect of Varactor Placement on Impedance Match and Radiation Efficiency

3.1 Simulations performed with 1 pF chip capacitor

Incorporation of a 1 pF chip capacitor [5] in the structure in two configurations enables the determination of the effects of varactor placement on impedance match for the electrically small antenna. Figures 5(a) and 5(b) present the antenna in both configurations, the first with the capacitor placed in the center inductive load and the second with the antenna at the corner inductive load. Figures 6 and 7 present the simulated results pertaining to the impedance match of the antenna in both configurations.

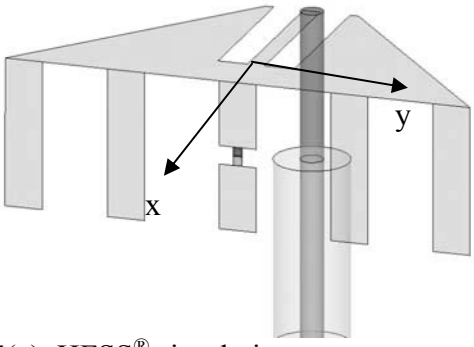

Figure 5(a). HFSS® simulation geometry indicating capacitor in configuration 1.

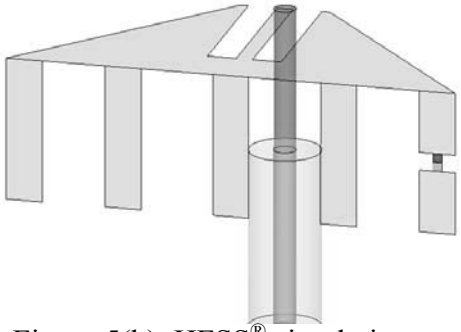

Figure 5(b). HFSS® simulation geometry indicating capacitor in configuration 2.

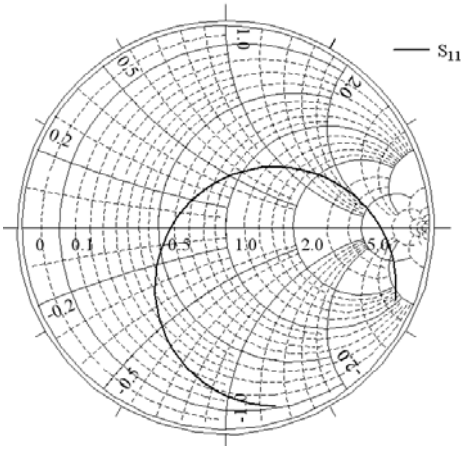

Figure 6(a). Smith chart plot from 2 to 2.1 GHz for antenna in configuration 1.

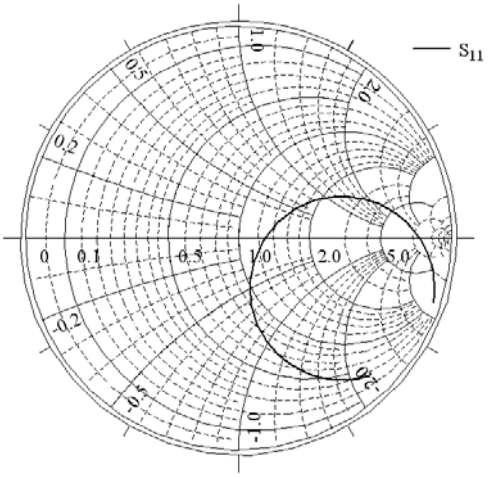

Figure 6(b). Smith chart plot from 1.6 to 1.75 GHz for antenna in configuration 2.

Examination of Figures 6 and 7 indicates that a good impedance match exists in both configurations. In addition, the antenna in configuration 2 exhibits a better impedance match at a lower frequency. However, a better impedance match does not guarantee higher radiated efficiency, and the total efficiency of the antenna can be poor

[6]. Section 3.2 presents both simulated and measured data pertaining to the radiation efficiency of the electrically small antenna with 1 pF tuning capacitors.

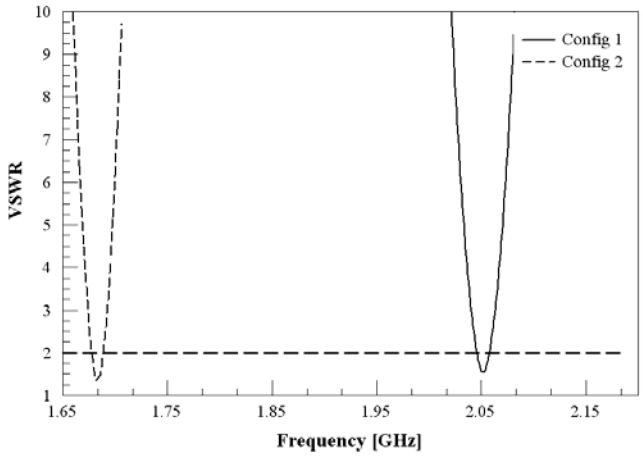

Figure 7. Plot of simulated VSWR vs frequency for antennas with 1 pF capacitance in configurations 1 and 2.

3.2 Simulations and measured results of antenna with 1 pF chip capacitors

3.2.1 Antenna fabrication

Using a precision milling machine, both the top sector and vertical inductive loads were first milled out from the same sheet of brass. Subsequently, incorporating CF series chip capacitors from Dielectric Laboratories [5] with series resistance identical to those used in simulation enables meaningful comparison of both simulated and measured data. Finally, mounting the antenna on a circular ground plane of radius one wavelength (30 cm) at 1 GHz completes the fabrication process. Figure 8 depicts the top view of the antenna whereas Figures 9(a) and 9(b) present pictures of the fabricated antenna in configurations 1 and 2, respectively.

Figure 8. Top view of fabricated antenna.

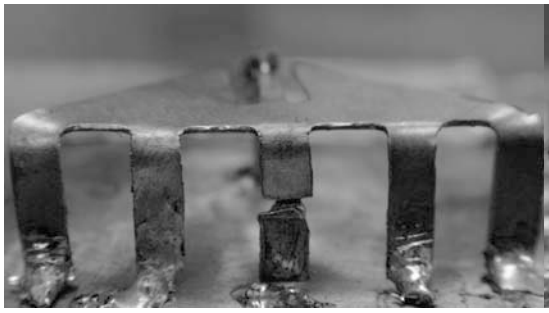

Figure 9(a). Rear view of fabricated antenna in configuration 1.

Figure 9(b). Rear view of fabricated antenna in configuration 2.

3.2.2 Comparison of simulated and measured efficiencies with 1 pF capacitors

Figure 10 presents impedance results from both simulation and measurements. In addition, Table 1 summarizes simulated radiation efficiencies calculated using the antenna parameters calculation tool in HFSS® and measured radiation efficiency utilizing the Wheeler cap method [7]. For accurate measurements, the resonant frequencies of the cap do not coincide with the measurement frequencies.

As indicated in Figure 10 and Table 1, comparison of match frequencies between simulation and measurement indicates higher measured match frequencies in both configurations. Possible reasons for the discrepancy include not accounting for the thickness of the copper and brass sheets in simulation, modeling the capacitor with "Lumped RLC" sheets instead of a 3D device, presence of curvature when bending the inductive loads and rounded connections at the junction of the antenna top sector and inductive loads, as indicated in Figure 11.

Intuitively, operating the antenna at a higher frequency enables more efficient radiation due to its larger electrical size [7]. However, examination of both measured and simulated data in Table 1 indicates that placing the capacitor at the center of the structure results in higher match frequency and lower radiation efficiency. Careful consideration of antenna geometry and its associated current flow provides an explanation for this phenomenon. For reference, Figure 12 provides a reproduction of the antenna geometries in both configurations.

Table 1. VSWR and radiated efficiency for antennas with 1 pF capacitance

	Simulated			Measured		
	Match frequency [GHz]	VSWR	Radiation efficiency	Match frequency [GHz]	VSWR	Radiation efficiency
Configuration 1	2.05	1.54	10.5%	2.29	1.75	11.2 %
Configuration 2	1.684	1.26	36.9%	1.82	1.31	41.5 %

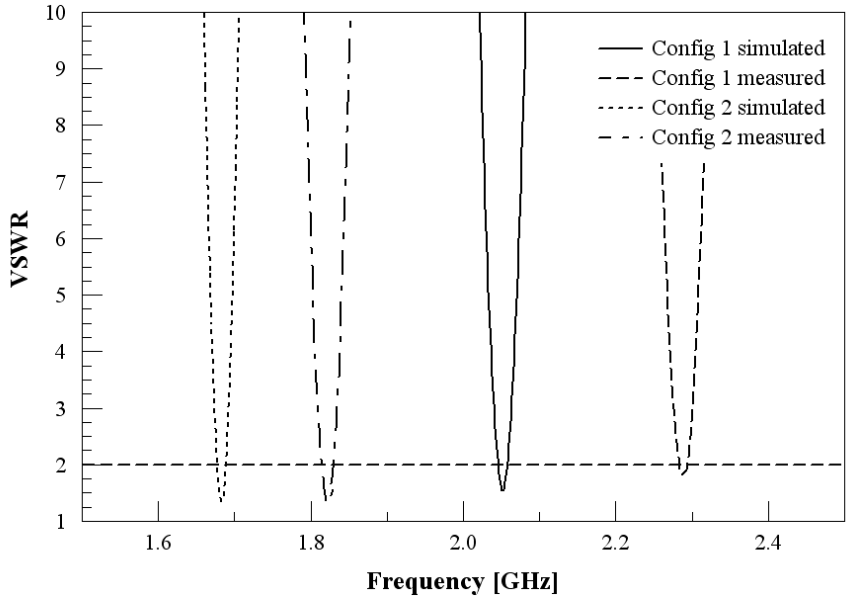

Figure 10. Simulated and measured VSWR for antenna in configurations 1 and 2.

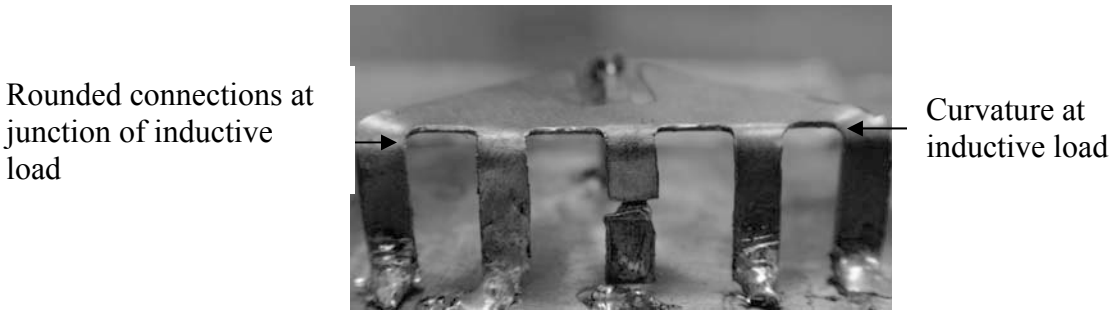

Figure 11. Picture of fabricated antenna indicating rounded connections and curvature at junction between antenna top sector and inductive loads.

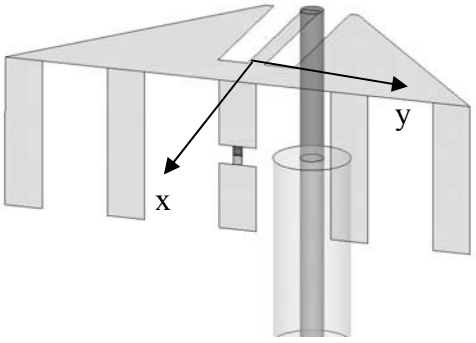

Figure 12(a). HFSS simulation file indicating capacitor in configuration 1.

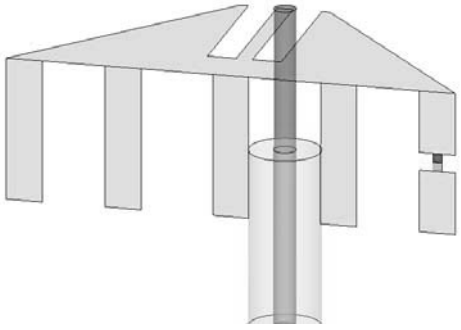

Figure 12(b). HFSS simulation file indicating capacitor in configuration 2.

As portrayed in the circuit models presented in Figure 13, placement of the capacitor in the center of an inductive load lowers the effective reactance of the arm, thus increasing current flow. Accordingly, capacitor placement in the center inductive load indicated in Figure 12(a) enables increased current flow through the center inductive load. Consequently, antenna geometry dictates that radiation from currents of equal magnitude parallel to the y-axis flowing in opposite directions towards the center inductive load cancel [8], thus reducing radiation efficiency. However, asymmetric capacitor placement in configuration 2 as indicated in Figure 12(b) yields no cancellation of radiation from these currents, thus increasing horizontally polarized radiation and improving radiation efficiency.

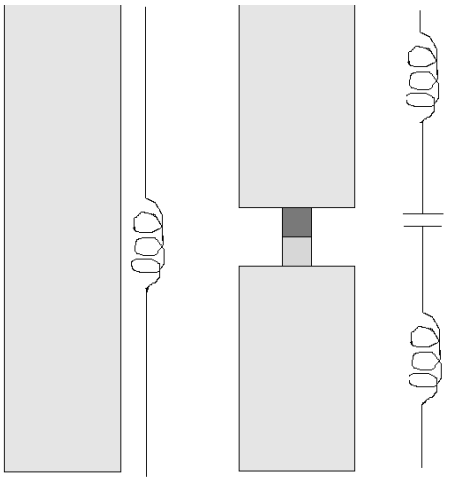

Figure 13. Circuit model of inductive loads with and without tuning capacitor.

Examination of simulated and measured gain plots at the match frequencies support this explanation. Figures 14(a) and 14(b) present the simulated elevation patterns in the $\phi = 0^0$ and $\phi = 90^0$ planes, respectively, for the antenna in configuration 1 and Figure 15(a) and 15(b) depict the simulated elevation plots in the $\phi = 0^0$ and $\phi = 90^0$ planes, respectively, of the antenna in configuration 2, all normalized to the maximum of their respective configurations. Similarly, the normalized measured elevation patterns in the $\phi = 0^0$ and $\phi = 90^0$ planes of the antenna in configuration 1 are portrayed in Figures 16(a) and 16(b), respectively, and Figure 17(a) and 17(b) report the normalized measured elevation patterns in the $\phi = 0^0$ and $\phi = 90^0$ planes, respectively, for the antenna in configuration 2.

Examination of Figures 14 and 16 indicate that the radiation pattern of the antenna in configuration 1 resembles that of a monopole in the $\phi = 90^0$ plane. In addition, simulated data in Figures 14(a) and 14(b) show that in the $\phi = 0^0$ plane, antenna radiation in configuration 2 possesses a significantly stronger horizontal component since G_φ is the dominant polarization in configuration 2 and G_θ is the dominant polarization in configuration 1. Consistent with Figures 14(a) and 15(a), Figures 14(b) and 15(b) reveal

G_θ as being stronger configuration 2, indicating a significantly higher horizontal radiation component. Measured results presented in Figures 15 and 16 exhibit similar trends, supporting the explanation that the asymmetry in capacitor placement in configuration 2 increases horizontally polarized radiation, thus improving radiation efficiency.

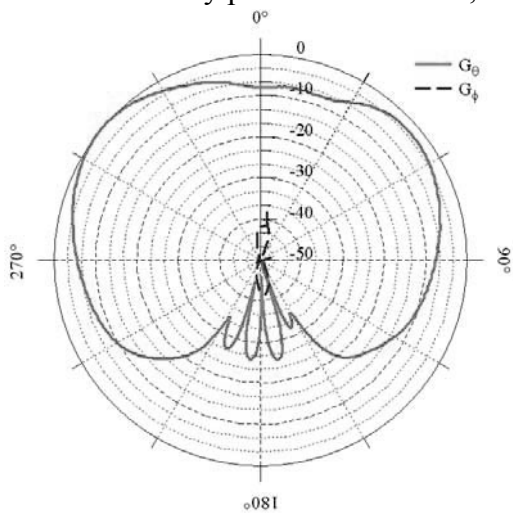

Figure 14(a). Simulated normalized gain plot in the $\phi = 0^0$ plane for the antenna in configuration 1.

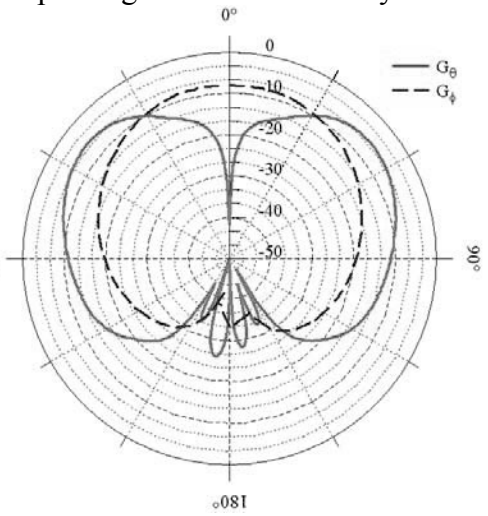

Figure 14(b). Simulated normalized gain plot in the $\phi = 90^0$ plane for the antenna in configuration 1.

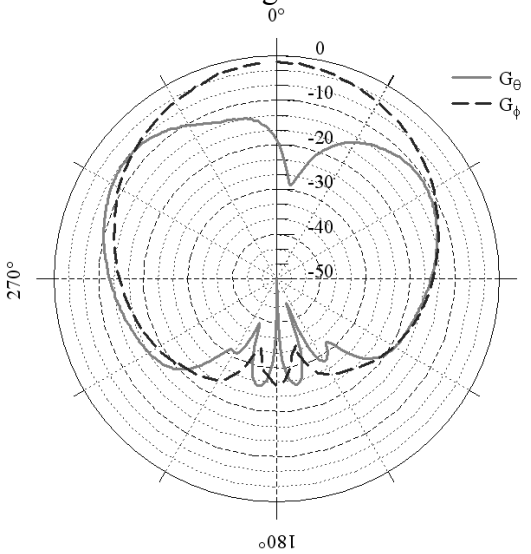

Figure 15(a). Simulated normalized gain plot in the $\phi = 0^0$ plane for the antenna in configuration 2.

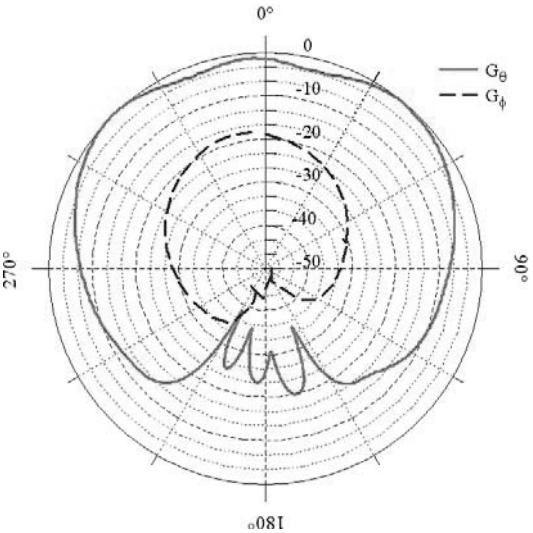

Figure 15(b). Simulated normalized gain plot in the $\phi = 90^0$ plane for the antenna in configuration 2.

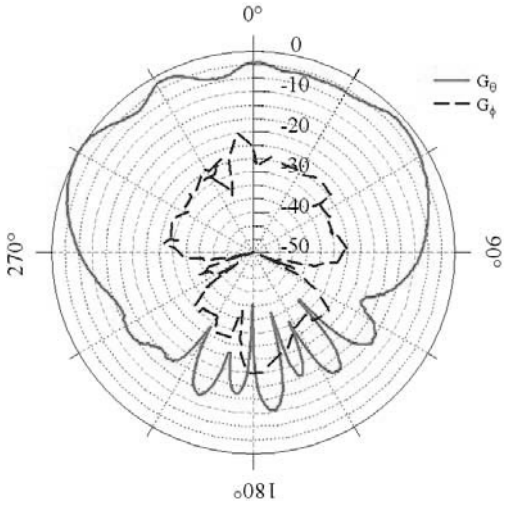

Figure 16(a). Measured normalized gain plot in the $\phi = 0^0$ plane for the antenna in configuration 1.

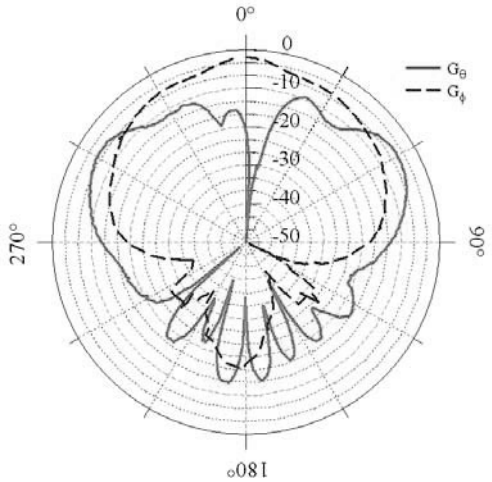

Figure 16(b). Measured normalized gain plot in the $\phi = 90^0$ plane for the antenna in configuration 1.

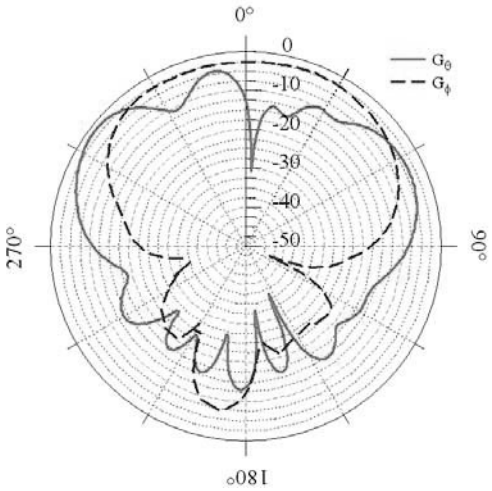

Figure 17(a). Measured normalized gain plot in the $\phi = 0^0$ plane for the antenna in configuration 2.

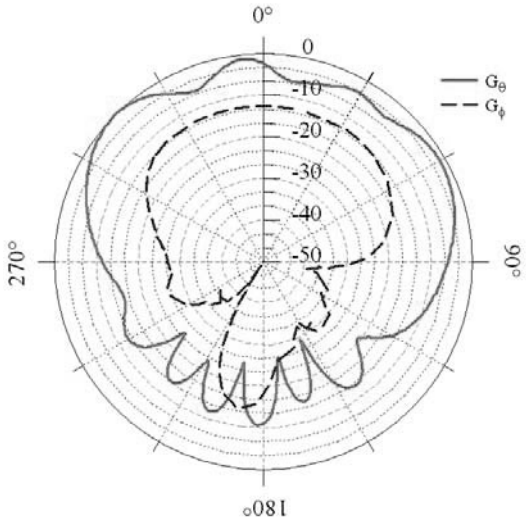

Figure 17(b). Measured normalized gain plot in the $\phi = 90^0$ plane for the antenna in configuration 2.

3.2.2 Comparison of simulation and measurements with 2.4 pF capacitors

Simulations and measurements performed with 2.4 pF capacitors examine the possibility of higher efficiency for antenna geometry in configuration 2 at lower frequencies and smaller electrical size. Figure 18 presents simulated and measured VSWR of the antenna in both configurations and Table 2 summarizes the data pertaining to both impedance match and radiated efficiency.

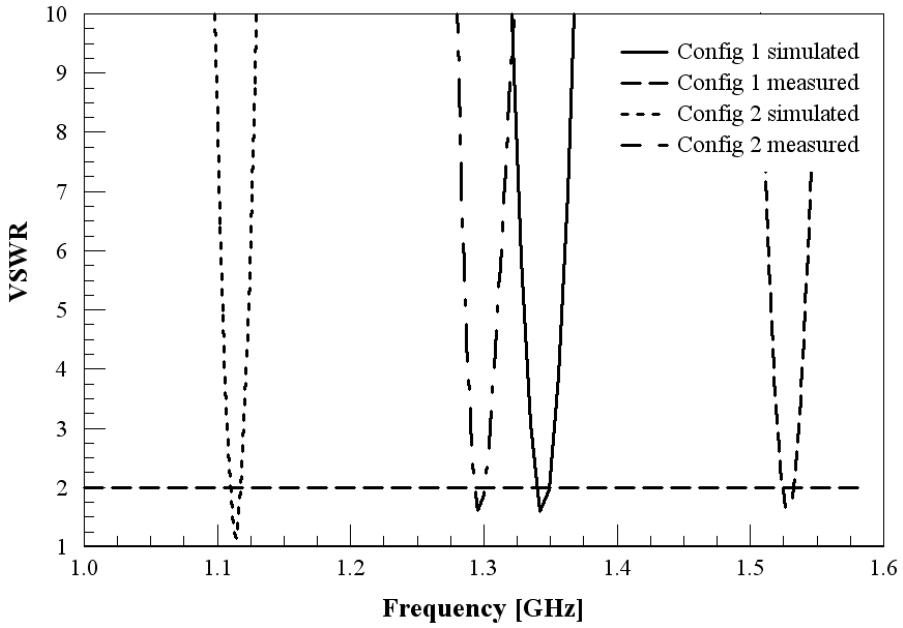

Figure 18. Plot of VSWR vs frequency for antennas with 2.4 pF capacitance in configurations 1 and 2.

Table 2. VSWR and radiated efficiency for antennas with 2.4 pF capacitance

	Simulated			Measured		
	Match frequency [GHz]	VSWR	Radiation efficiency	Match frequency [GHz]	VSWR	Radiation efficiency
Configuration 1	1.34	1.594	1.17 %	1.53	1.52	2.76 %
Configuration 2	1.11	1.1	9.67 %	1.3	1.53	27.4 %

Examination of simulated and measured data presented in Figures 18 and Table 4 indicates that, consistent with experiments performed with 1 pF tuning capacitors, higher match frequency and poorer radiation efficiency exist for the antenna in configuration 1. In addition, both simulated and measured gain plots exhibit trends identical to those portrayed in Figures 14 and 15, and are omitted here for brevity. Finally, comparisons of Tables 1 and 2 indicate that placing the tuning capacitor at the corner of the structure results in a tenfold increase in radiation efficiency at lower frequencies compared to a three fold increase in radiation efficiency at higher frequencies. Therefore, better improvements in radiated efficiency results with an introduction of an asymmetry in current flow at smaller antenna electrical sizes.

4. Conclusions and Future Work

Results from this study indicate that the radiation efficiency of an electrically small antenna can be appreciably improved by introducing an asymmetry in varactor

placement. In addition, both simulated and measured data suggest that the smaller the electrical size of the antenna, the larger the improvement in radiation efficiency when these asymmetries are introduced. Consequently, these results can guide the placement of tuning elements to increase the radiation efficiency of an electrically small frequency reconfigurable antenna. Future work involves fabrication and testing of the antenna utilizing surface mount varactors in place of chip capacitors.

5. Acknowledgments

The authors thank Steven Dawson for assistance in antenna fabrication.

REFERENCES

[1] L. M. Feldner, C. T. Rodenbeck, C. G. Christodoulou and N. Kinzie, "Electrically small frequency-agile PIFA-as-a-package for portable wireless devices," *IEEE. Trans. Antennas Propagat*., vol 55, no. 11, pp. 3310-3319, Nov. 2007.

[2] S. Nikolau, R. Bairavasubramanian, C. Lugo, Jr., I. Carrasquillo, D. C. Thompson, G. E. Ponchak, J. Papapolymerou, M. M. Tentzeris, "Pattern and frequency reconfigurable annular slot antenna using PIN diodes," *IEEE. Trans. Antennas Propagat*., vol. 54, no. 2, pp. 439-448, Feb. 2006.

[3] H. Jiang, M. Patterson, C. Zhang and G. Subramanyam, "Frequency agile microstrip patch antenna using ferroelectric thin film varactor technology," in *Proc. 2009 IEEE International Symposium on Antennas and Propa*gation *and USNC/URSI Nat. Radio Science Meeting,* pp. 1-4, Jun. 2009.

[4] N. C. Soldner, "Design and analysis of electrically-small inductively loaded dual sector antennas for surface sensing applications," Master's thesis, University of Illinois at Urbana-Champaign, Urbana, Illinois, 2006.

[5] "Dielectric Laboratories product catalogue," Dielectric Laboratories. [Online]. Available: http://www.dilabs.com/products/products.aspx?catid=8.

[6] C. A. Balanis, *Antenna Theory Analysis and Design*, Second ed. New York: Wiley, 2005.

[7] H. A. Wheeler, "The radiansphere around a small antenna," *Proc. IRE.*, pp. 1325-1331, Aug. 1959.

[8] S. R. Best "A discussion on the properties of electrically small self-resonant wire antennas," *IEEE. Antennas Propag. Mag.*, vol. 46, no. 6, pp. 9-22, Dec. 2004.

A Fully Planar Ultrawideband Array

S. S. Holland and M. N. Vouvakis
Center for Advanced Sensor and Communication Antennas
Department of Electrical and Computer Engineering
University of Massachusetts, Amherst, MA 01003
{sholland, vouvakis}@ecs.umass.edu

A fully planar ultrawideband (UWB) array is presented, where both the radiating aperture and feed lines are fabricated using low-cost PCB technology. The array is based on unbalanced-fed, tightly-coupled printed dipoles above a ground plane. This type of dipole feeding is known to develop a catastrophic common-mode at mid-band that has rendered the topology useless. This work proposes the use of a set of shorting posts that connect the dipole arms to the ground at appropriate locations, effectively tuning that common-mode out-of-band. This modified unbalanced feeding approach does not use feed organizers (to shield the feed lines) or external baluns, thus it can be realized using low-cost printed microwave fabrication techniques. When used in dual-offset dual-polarized arrays, this novel feeding method leads to modular designs that can be fabricated in tiles and then assembled to form an aperture. A proof of concept 7-21GHz (3:1 bandwidth) array has been designed, fabricated, and measured. First, infinite single- and dual-polarized versions with VSWR < 2.8 and low (-15dB for dual-pol) diagonal plane cross-polarization out to $\theta = 45°$ are presented. The measured results of a 16×16×2 dual-polarized prototype show very good agreement with simulations.

1. Introduction

Ultrawideband arrays are in high demand for a wide range of applications, including pulsed radars [1], satellite communications [2], radio telescopes [3], and multifunctional systems [4]. In many of these applications, Vivaldi arrays [5] have become standard because of their excellent impedance performance over wide scan ranges and their ability to directly connect to standard RF interfaces. Nonetheless, Vivaldi elements are not low-profile, leading to high cross-polarization levels in the diagonal plane, require vertical integration that complicates fabrication, and are difficult to assemble modularly due to gap-induced resonances [6].

In an attempt to reduce fabrication costs, enable manufacturability at higher frequencies, and reduce cross-polarization levels at wide angles in the diagonal plane, a number of planar wideband arrays have been developed. Two of the most popular planar wideband arrays are Ben Munk's Current Sheet Antenna (CSA) array [7], which uses tightly coupled dipole elements periodically arranged over a ground plane, and the Fragmented Aperture Array (FAA) [8], which uses connected elements whose shape is determined through genetic optimization algorithms and radiate in free-space or in a half space in the presence of Jaumann screens or R-cards. Despite the printed and planar radiating

aperture, both the CSA and FAA require non-planar, machined metallic feed organizers and external wideband baluns/hybrids [9] as shown in Figure 1(a). These feed organizers are placed between the ground plane and the array to shield the balanced feed lines, and play a crucial role in preventing a common-mode from developing when scanning in the E-plane [10], [11]. The presence of these feed organizers precludes truly planar fabrication of these arrays, and complicates aperture modularity. Additionally, balanced fed arrays such as the CSA and FAA are fed through external wideband baluns that tend to be large (passive baluns), or unidirectional and low-power (active baluns) [12].

This paper presents a fully planer/printed wideband array that does not require feed organizers or external baluns. The new array is called the Planar Ultrawideband Modular Antenna (PUMA) array, [13], and its fabrication is as simple as that of a typical narrowband microstrip patch array. What sets this array apart from other "quasi-planar" wideband array technologies is the unique approach to feeding the tightly coupled dipole elements. Instead of balanced feed lines, the PUMA uses an unbalanced feed line and strategically placed shorting posts (vias) to suppress a problematic common mode that arises when dipole arrays are fed with unbalanced feed lines, as shown in Figure 1(b). This novel concept grew out of the Banyan Tree Antenna array development presented at the 2009 Antenna Applications Symposium [14]. This feed arrangement eliminates the need for a feed organizer and external balun/hybrid, as shown in Figure 1(b). The shorting posts and unbalanced feed lines are implemented as plated vias, thus both the radiating aperture and feed lines of the PUMA array are fully planar, and can be printed as a single multilayer microwave PCB. The absence of feed organizers and electrical

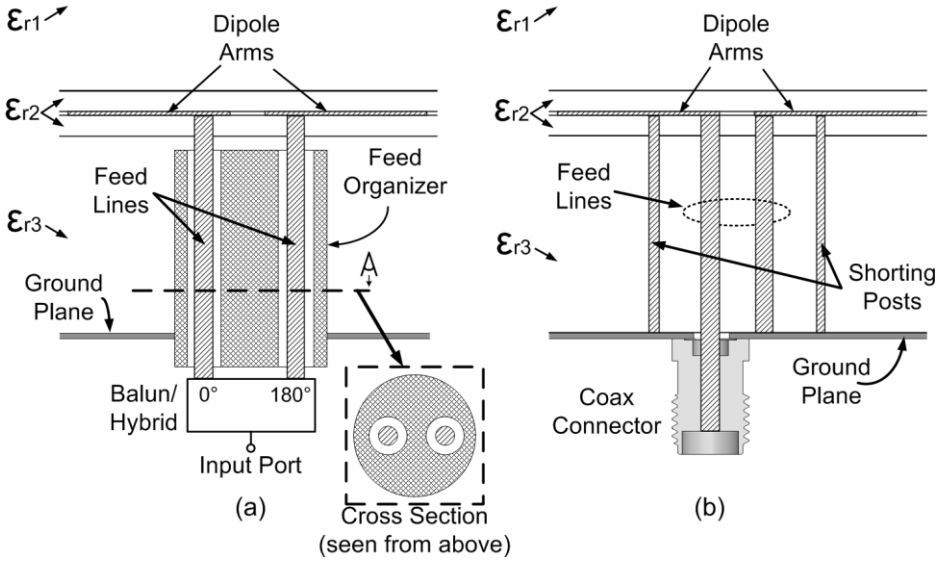

Figure 1 – Cross-sectional view of two wideband dipole arrays, showing the different feeding methods. (a)The CSA or FAA balanced feeding method requires a feed organizer to shield the balanced lines and an external balun. (b) The proposed PUMA feeding method uses unbalanced feed lines and shorting posts implemented with plated vias.

connection between dipole arms allows for the array substrate to be split in the region between the feed lines, thus enabling the modular construction. The overall depth of the PUMA array, including the thick superstrate cover, is approximately $\lambda/3$ at the highest frequency, and the depth is independent of the array bandwidth.

As a proof of concept, this paper presents a 7-21GHz (3:1 bandwidth) PUMA design in both single- and dual-polarized arrangements. A 16×16×2 dual-polarized finite array prototype was built and measured. Simulations and measurements are in good agreement and show good impedance behavior over the entire band, with VSWR < 2 at broadside, and VSWR < 3 out to θ=45° in E-, D-, and H-planes. The cross-polarization level of both predictions and measurements is approximately -15dB at θ = 45° in the D-plane.

2. The PUMA Topology

This section describes the PUMA array. A 16×16×2 dual-polarized PUMA array is shown in Figure 2, composed of four PCB modules arranged to form a square aperture. The simple, multilayer PCB fabrication reduces cost, allows for high volume production, and leads to a mechanically robust arrays even at high frequencies.

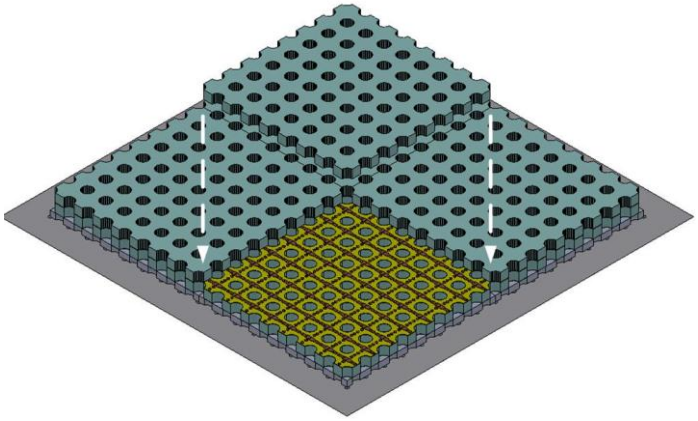

Figure 2 –Sketch of a 16×16×2 dual-pol PUMA array composed of four 8×8×2 modules. The top dielectric layer is removed from one module to reveal the radiating elements.

The top view and cross section of a single-polarized PUMA unit cell are depicted in Figure 3(a) and (b). The array consists of tightly packed tapered dipoles with strong capacitive coupling at their ends. The dipoles are printed onto each side of layer 2, Figure 3(b), comprised of Rogers 5880 (ε_r = 2.2). Layers 1 and 3 are comprised of Rogers 5880LZ (ε_r = 1.96), a PTFE dielectric that can support plated vias, chosen for its low permittivity and low thermal expansion (in thickness), and are approximately a quarter guided-wavelength thick at midband ($\lambda_{g,mid}/4$). Layer 3 spaces the dipoles appropriately from the ground plane, while layer 1 helps control impedance matching and serves as a wide angle matching (WAIM) layer that improves the scan performance. The dipole arms are connected at their feed point to a pair of vias, which form the unbalanced feed line. One feed line is connected to ground, and the other is fed by a coaxial

connection in the ground plane with $Z_o = 50\Omega$. The important aspect in this geometry is the presence of two additional shorting vias that connect each arm of the dipole to the ground at appropriately chosen locations. As it will be explained later, these vias allow a common-mode resonance to be shifted out of the operational band. Except for the feeding method, this structure is similar to Munk's CSA array, and the principle of operation is based on the inductive compensation of the capacitive coupled dipoles by the ground plane [15]. Several nuances in the operation arise due to the new feeding method, and those will be outlined in later sections.

When arranged for dual-pol operation, the PUMA uses a dual-offset dual-polarization lattice, as shown in Figure 3(c), which is different from the CSA or FAA arrays that are arranged in coincident phase center lattices. The dual-offset design, along with the absence of the feed-organizer, allows for split planes between feed lines as shown with

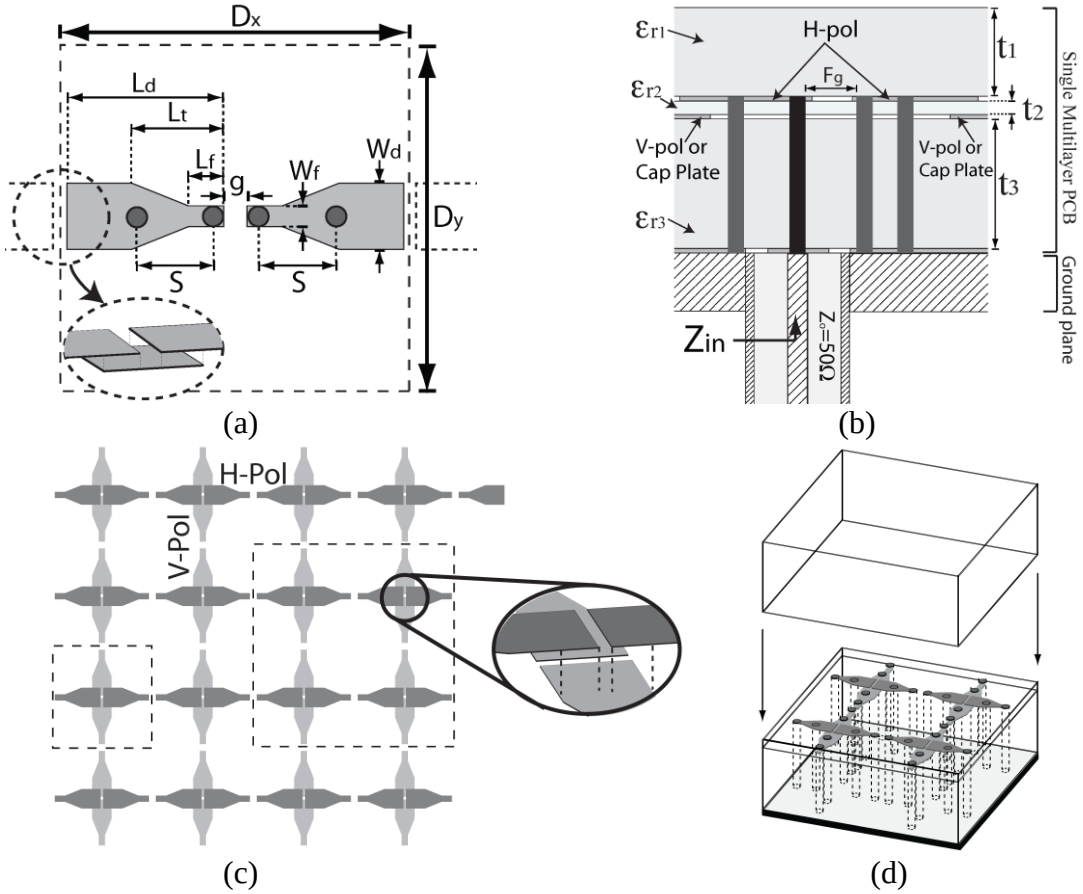

Figure 3 - Details of the PUMA array geometry. (a) Top view of single-pol PUMA unit cell. The insert shows the mechanism for increasing the capacitance between neighboring dipole arms. (b) Cross-sectional view of single-pol PUMA unit cell. (c) Top view of dual-pol PUMA, showing the locations where the module splits could occur. The inset shows the parallel plate capacitor formed between orthogonally polarized dipole arms, because they are printed on different layers and they partially overlap. (d) Isometric view of 2×2×2 dual-pol PUMA module.

dashed lines in Figure 3(c). The dipoles are arranged to overlap where four neighboring dipole arms meet (one pol on each layer, see inset for details), enhancing capacitive coupling through parallel plate capacitors formed between cross-polarized arms. Figure 3(d) shows an isometric view of a dual-pol PUMA, explicitly showing the arrangement of the vias and dipoles in the dielectric stack up. Having discussed the geometry of the array, the electrical performance of the showing posts is discussed in the next section.

3. Unbalanced Feed Arrangement with Shorting Posts

In [15], tightly-coupled, closely spaced dipoles above a ground are shown to exhibit wideband operation due to the reactive compensation from the ground plane. However, this theory is based on dipoles fed by perfectly balanced delta-gap sources placed between dipole arms as depicted in Figure 4(a). The frequency response of this delta-gap fed dipole arrangement operates well over 3-18GHz as shown in the solid line of Figure 4(f). In practice, this performance is difficult to achieve since ideal delta-gap sources do not exist, thus the CSA attempts to approximate the ideal delta-gap source using external baluns and shielded vertical feed lines. Alternatively, unbalanced fed tightly coupled dipoles, as shown in Figure 4(b), produce a similar frequency response except have a severe mid-band (f=15GHz) resonance shown with a dashed line in Figure 4(f). This resonance is due to a common-mode developed on the vertical feed lines, producing a monopole-like field. The resonant frequency f_{cm} of this common-mode is dictated by a resonant length L, the diagonal length of a unit cell, Figure 4(d), and is given by

$$f_{cm} = \frac{c_o}{2\sqrt{\varepsilon_{r3}}\sqrt{D_x^2 + D_y^2}}. \tag{1}$$

This common mode is excited at broadside only and becomes less severe with scan. Further details and physical explanations about the development of this common mode can be found in [16].

A simple way to avoid this resonance is to tune it out of band by reducing the resonance length L. In this work, this is accomplished by following a popular technique used by the signal integrity community that places shorting vias between ground/power planes in PCBs. Similarly, in the PUMA, this is achieved by placing shorting posts or vias that connect the dipole arms to the ground plane, effectively shortening L. The sketch in Figure 4(e) shows how L is shortened by forcing a field null at the shorting post locations (ground symbols). This modified common mode resonant frequency is now expressed as

$$f_{cm} = \frac{c_o}{2\sqrt{\varepsilon_{r3}}\sqrt{(D_x - 2s)^2 + D_y^2}}, \tag{2}$$

where s is the distance of the shorting via from the center of the unit cell. To validate the suppression of the common mode, the dashed-dotted line in Figure 4(f) shows the VSWR vs frequency of the unbalanced fed structure with shorting posts. The VSWR spike, which is due to the common-mode resonance, has been moved up above the operating band, though at the expense of a higher low-frequency limit, and a modest

increase in the mismatch around 16GHz. This array now operates over approximately 4-19GHz, a resonance-free 4.75:1 bandwidth.

To gain better insight into the tuning of the common-mode using shorting posts, the VSWR vs frequency of a series of single-pol PUMA arrays with progressively larger shorting post spacing *s* are shown in Figure 5. Without shorting posts, a severe VSWR spike is seen at midband, bisecting the operational bandwidth. Adding a pair of shorting post as close to the feed lines as possible, *s = 1.2mm*, significantly shifts the resonance to 19.5GHz. As *s* is increased further, the resonance moves higher and higher in frequency, until it is completely out of the operating band. The final *s=2.1mm* is the optimized design presented next. In this design the grading lobe frequency is at 22.7 GHz.

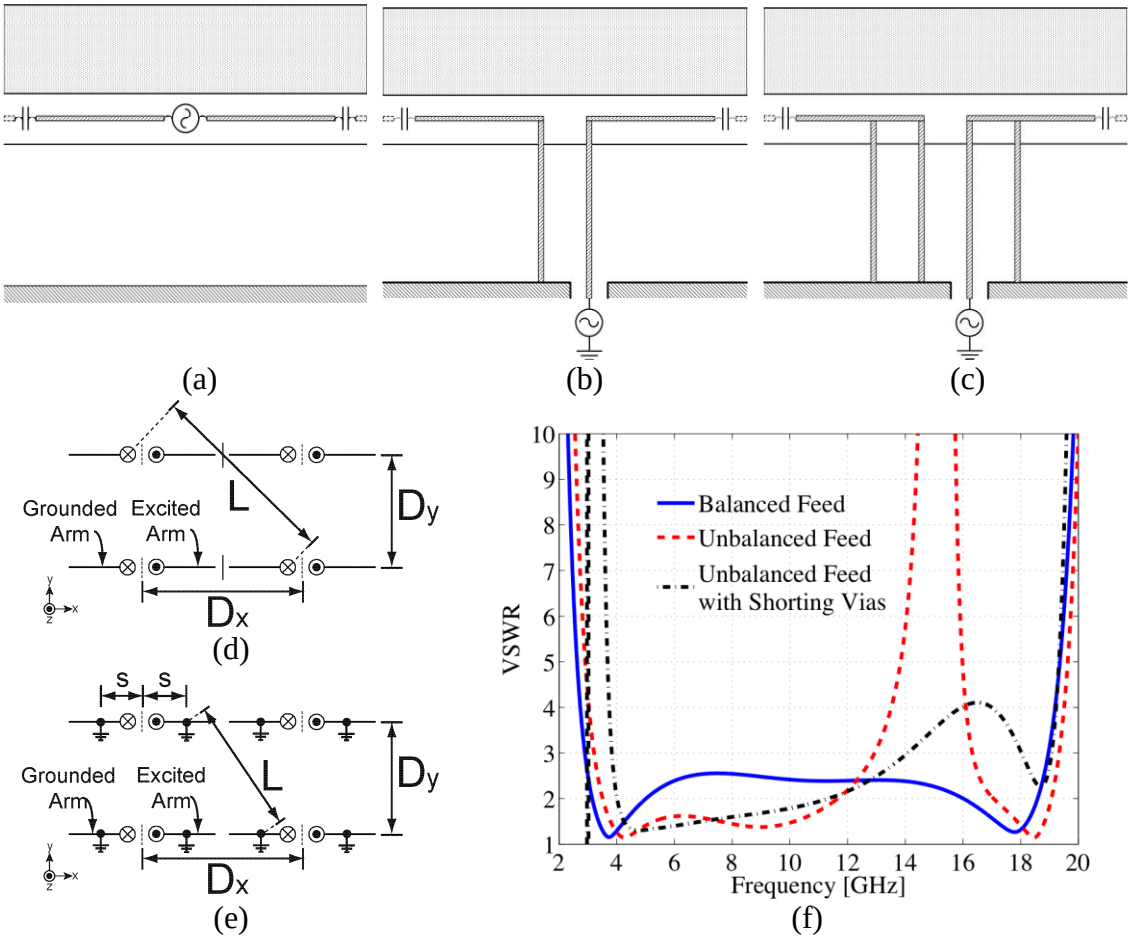

Figure 4 –Feeding methods for 2D single-polarized dipole arrays. (a) Balanced delta feed. (b) Unbalanced feed. (c) Unbalanced feed with shorting vias. (d) Top view of a unit cell, indicating resonant length *L* of the common-mode. (e) Top view of a unit cell, indicating the modified resonant length *L* of the common-mode due to the shorting vias. (f) Comparison of single-polarized infinite array VSWR performance for each method. Results are referenced to $Z_o = 100\Omega$, and no design optimization was attempted.

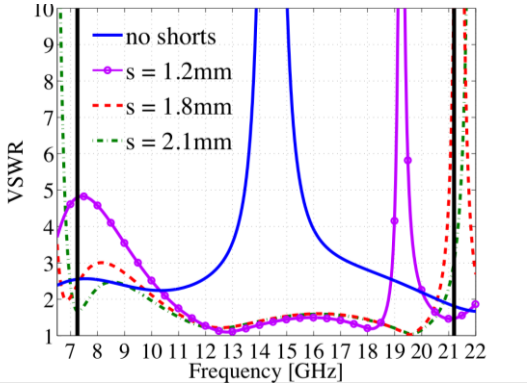

Figure 5 – . VSWR vs. frequency of single-pol PUMA arrays with various shorting via spacings *s*. The common-mode resonance can be tuned out-of-band using large shorting post spacings *s* for single-pol arrays. Note: *s = 2.1mm* is optimized single-pol design.

4. Single Polarized PUMA

The first optimized array is a single-pol PUMA, using the topology described in Figure 3(a-b), with geometrical and material parameters reported in Table I. The array is simulated using Ansoft/Ansys HFSS [17] infinite array analysis using realistic 50Ω port models, PML and periodic boundary conditions. The resulting VSWR vs. frequency (referenced to 50Ω) for broadside and E- and H-plane scans out to θ = 45° are shown in Figure 6(a) and (b), respectively. The E-plane scan shows little variation with scan in the 7-21GHz band, while the H-plane scan shows an increase in VSWR with θ, which is typical in phased arrays. The D-plane scan is not shown since it is an approximate average of the E- and H-planes. These results indicate a solid 3:1 bandwidth with low VSWR. Next, the co- and cross-polarization was calculated using Ludwig's third definition [18], shown in Figure 7. In the E-plane, the cross-pol is shown to be very low, < -40dB over the band , and in the D-plane it increases with θ until at θ = 45° the cross-pol is just under -10dB. Single-pol arrays, in general, have worse (higher) cross-pol in the D-plane compared to dual-pol implementations, as will be seen in Section 5.

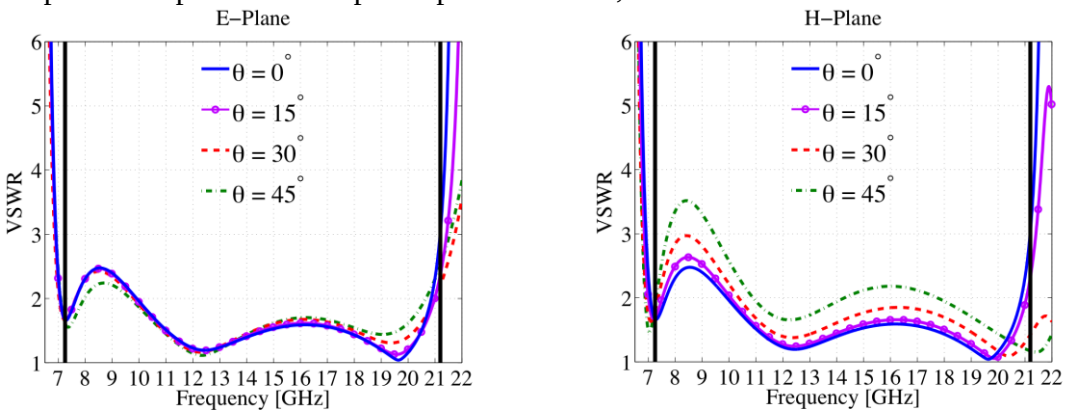

Figure 6 - Simulated infinite single-pol PUMA array VSWR vs. frequency for various scan angles along: (a) E-plane, and (b) H-plane. All results referenced to Z_o = 50Ω.

Table I – Single-pol PUMA design parameters. All values are in [mm].

D_x	D_y	W_f	W_d	L_d	L_t	L_f	g	s	t_1	t_2	t_3	ε_{r1}	ε_{r2}	ε_{r3}
6.60	6.60	0.79	1.78	3.0	2.11	1.60	0.61	1.47	3.00	0.13	3.00	1.96	2.2	1.96

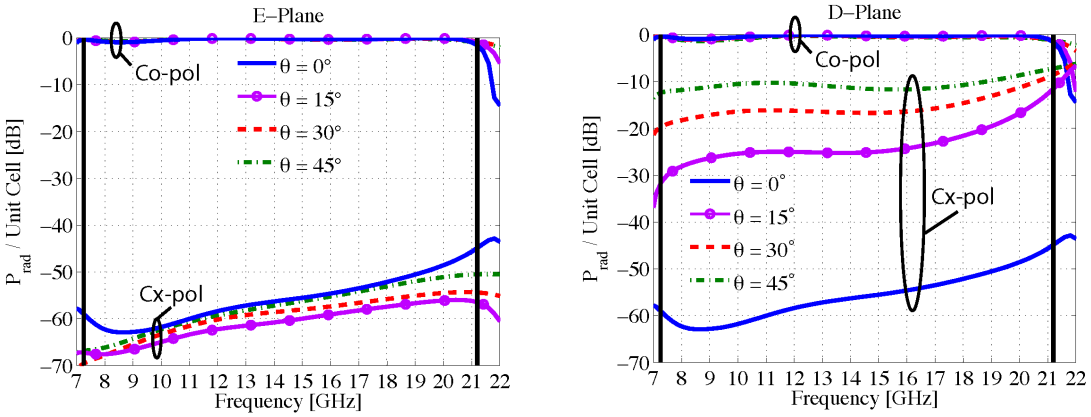

(a) (b)

Figure 7 – Infinite single-pol PUMA cross-polarization levels vs. frequency, calculated using Ludwig's third definition, for scanning along: (a) E-plane. (b) D-plane.

5. Dual-polarized 16×16×2 PUMA Array

The dual-pol PUMA array geometry is described in Section 2. Design parameters are very similar to the single-pol design of Section 4, see Table II. The element spacing is $D_x = D_y = 6.6$mm, such that $f_g = 22.7$GHz, and the overall PCB thickness is $< \lambda_{high}/2$. The 16×16×2 prototype array is shown in Figure 8 mounted on a ground plane; Figure 8(a) shows one 8×8×2 isolated module, and Figure 8(b) shows the fully assembled array. The ground plane beneath the array contains coaxial cables that are aligned with fuzz-button filled coaxial cable sections inserted into the thick ground on the back of each array module. This type of array/coax press contact interconnect simplifies the array's modular attachment and eliminates the need for expensive connectors and loads (e.g. GPPO or G3PO) since an SMA cable expander is used underneath the ground plane. The infinite

(a) (b)

Figure 8 – Modular assembly of a 16×16×2 (dual-pol) PUMA array. (a) One 8×8×2 module placed at on the top of a ground plane with coaxial feeds. (b) Four 8×8×2 modules forming the entire 16×16×2 aperture.

Table II – Dual-pol PUMA design parameters. All values are in [mm].

D_x	D_y	W_f	W_d	L_d	L_t	L_f	g	s	t_1	t_2	t_3	ε_{r1}	ε_{r2}	ε_{r3}
6.60	6.60	0.79	1.30	3.00	2.11	1.60	0.61	1.30	3.00	0.13	3.00	1.96	2.2	1.96

array VSWR results, calculated using Ansoft/Ansys HFSS [17], are shown in Figure 9(a-b), exciting one polarization and terminating the other, for scanning in the E- and H-planes of the array (with respect to the excited polarization) out to θ = 45°. The D-plane VSWR is omitted since it is essentially an average of the E-and H-plane VSWR curves. In the E-plane, the VSWR is less than 2.1 from 7-21.5GHz (the full band) at broadside, with very little variation with scan. In the H-plane, the VSWR is seen to increase with θ, until at θ = 45° the VSWR reaches 2.9 near f = 8.5Hz.

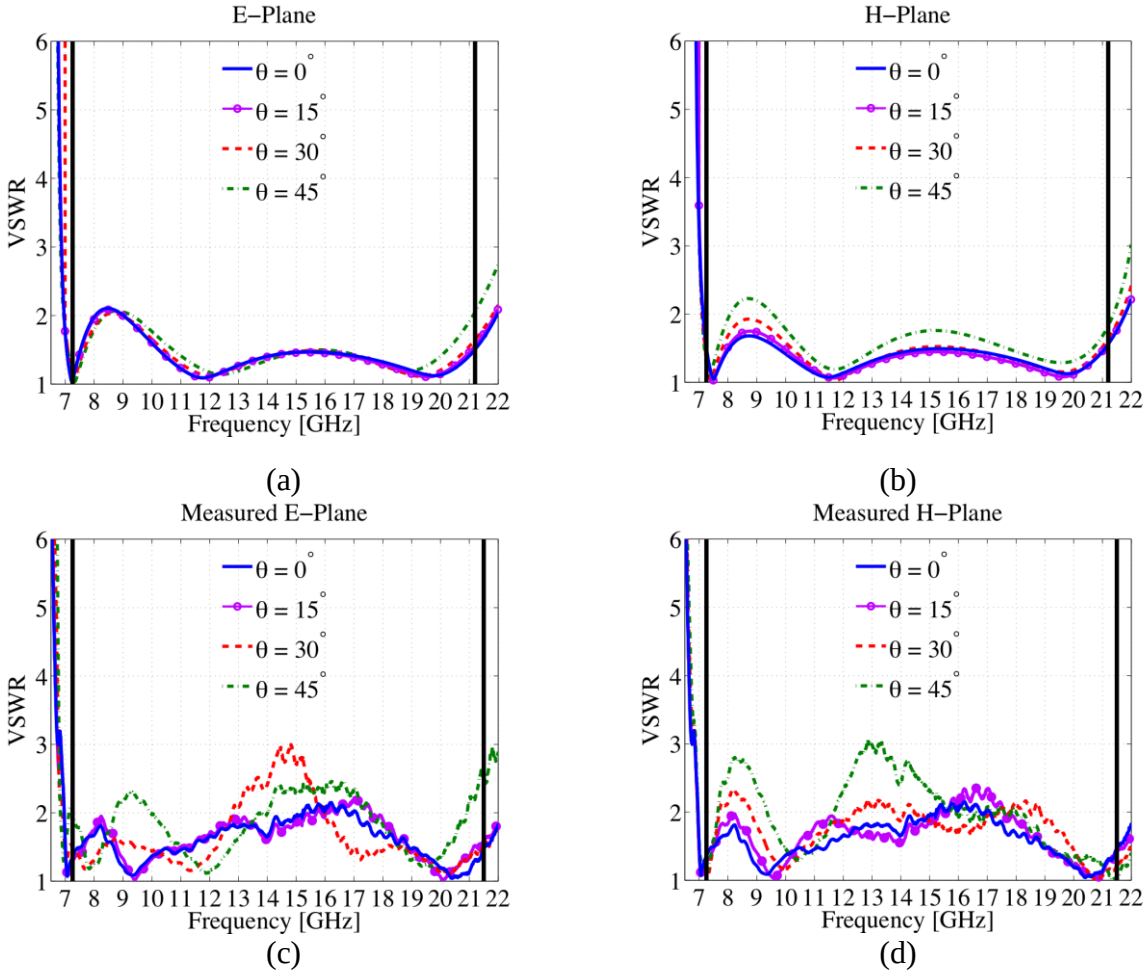

Figure 9 – Comparison of simulated and measured VSWR vs. frequency and scan angle of the 7-21GHz dual-pol PUMA array. (a) Simulated infinite array E-plane scan. (b) Simulated infinite array H-plane scan. (c) Measured 9×9 subarray E-plane scan. (d) Measured 9×9 subarray H-plane scan. In all cases, one polarization is excited and the other polarization is terminated to 50Ω. All results referenced to Z_o = 50Ω.

The coupling between polarizations, though not included here, is below -20dB, which implies good efficiency and low cross-polarization levels, as will be seen later in this section.

A 9×9 central section of the array was measured in a similar manner, exiting one polarization and terminating the other. The active reflection coefficient of a center element is calculated from the measured S_{11} and the S_{1j}'s; the VSWR is then calculated using this reflection coefficient and is shown in Figure 9(c-d) for scanning in the E- and H-planes. Compared to the infinite array analysis, the measured results bear the same overall shape and trends in the VSWR, though the measured VSWR is higher in the midband region, from 13-19GHz. In particular, the large humps at 14.5GHz at $\theta = 30°$ in the E-plane, and at 13.25GHz at $\theta = 45°$ in the H-plane may be due to truncation effects, and will be investigated further as the measurements progress (the authors are also eager to see how the VSWR changes when the full 16×16 array is measured). The low and high frequencies indicate good agreement on key trends. In the E-plane, Figure 9(c), the first hump near 8.5GHz remains at a VSWR of 2 out to $\theta = 45°$, while at 21.5GHz the measured VSWR shows the same increase with θ as in the infinite array prediction. In the H-plane, Figure 9(d), the first hump near 8.5GHz shows the same characteristic increase in VSWR with θ as observed in the infinite array case. Overall, these results indicate good agreement between the predicted and measured performance. Finally, the predicted cross-polarization vs. frequency is shown in Figure 10, calculated using Ludwig's third definition [18]. In the E-plane, cross-polarization is below -20dB over most of the band, approaching -17dB at wide scan angles at high frequency. In the D-plane, shown in Figure 10(b), the cross polarization is below -20dB over the band out to $\theta = 30°$, and is approximately -15dB over the band at $\theta = 45°$. Measured element patterns for a central element are shown in Figure 11. Notably, the D-plane pattern, shown in Figure 11(b), indicates a cross-pol level of -15dB at $\theta = 45°$, which is in good agreement with the predicted cross-pol levels.

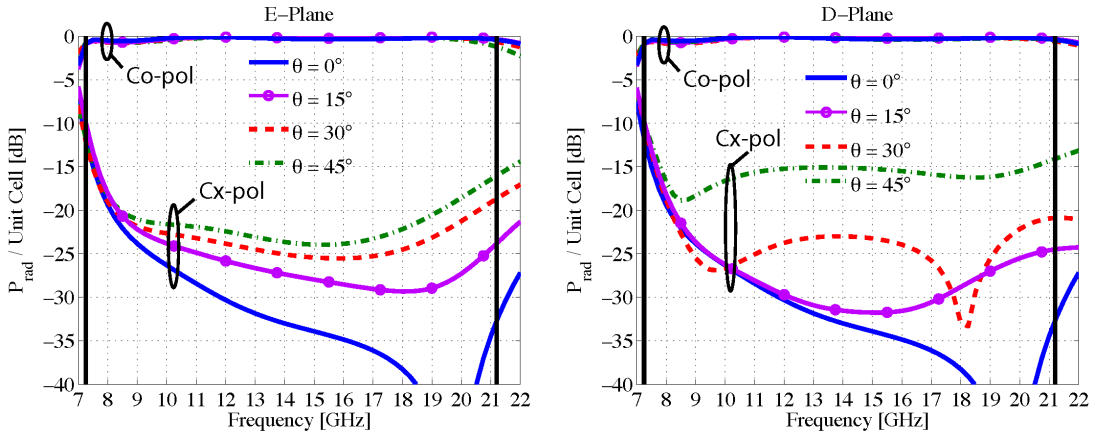

(a) (b)

Figure 10 – Infinite dual-pol PUMA cross-polarization levels vs. frequency, calculated using Ludwig's third definition, for scanning along: (a) E-plane. (b) D-plane.

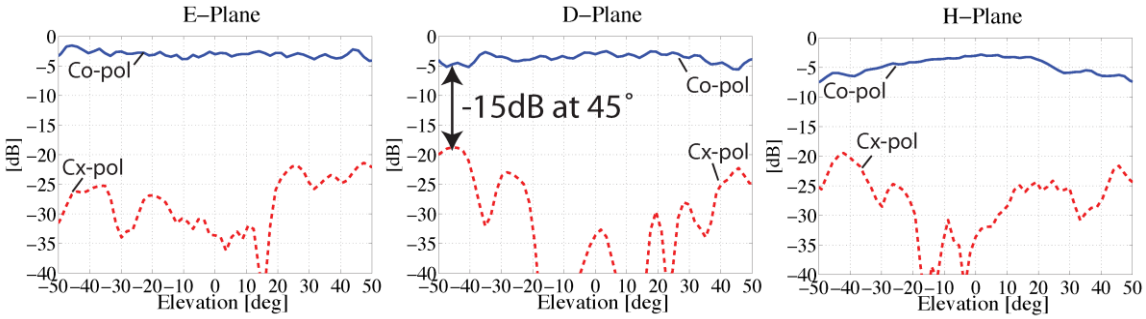

Figure 11 - Measured embedded element patterns of the dual pol 16×16×2 PUMA array, showing co- and cross-polarization levels. (a) E-plane. (b) D-plane. (c) H-plane.

5. Conclusion

The novel concept of the planar ultrawideband modular antenna (PUMA) array has been introduced. A 3:1 bandwidth dual-polarized PUMA array, operating over 7-21GHz, was designed, fabricated and measured. The array is fully planar (requiring only printed layers and plated vias), low-cost (≈$1/element at the prototype stage), low-profile (λ/3 at the highest frequency), modular, and directly connects to standard RF interfaces. Measurements and simulations show good agreement and indicate that the PUMA array maintains a broadside VSWR < 2 over the full operating band. The VSWR progressively increases to 3 at θ=45° in the E- and H-planes. More importantly, the cross-polarization level was predicted and measured to be below -15dB out to θ=45° in all planes, including the D-plane.

6. Acknowledgements

This work was funded by the US Naval Research Laboratory under contract N00173-08-1-G033.

7. References

[1] K. Trott, B. Cummings, R. Cavener, M. Deluca, J. Biondi, and T. Sikina, "Wideband phased array radiator," *Proc. IEEE Int. Symp. on Phased Array Systems and Technology*, pp. 383–386, 2003.

[2] V. Kumar Singh, M. Singh, A. Kumar, and A.K. Shukla, "Design of K-Band printed array antenna for SATCOM applications," *International Conference on Recent Advances in Microwave Theory and Applications*, pp.702-704, Nov. 2008.

[3] P. J. Hall, R. T. Schilizzi, P. E. F. Dewdney, and T. J. W. Lazio, "The square kilometer array (SKA) radio telescope: progress and technical directions," *URSI Radio Science Bulletin*, no. 326, pp. 4–19, Sep 2008.

[4] C. Hemmi, R. T. Dover, F. German, and A. Vespa, "Multifunction Wide-Band Array Design," *IEEE Trans. Antennas Propag.*, vol. 47, no. 3, pp. 425-431, March 1999.

[5] W. Croswell, T. Durham, M. Jones, D. Schaubert, P. Friederich and J. Maloney, "Wideband Antenna Arrays," Chapter 12 in *Modern Antenna Handbook*, edited by C.A. Balanis, John Wiley and Sons, 2008.

[6] D. H. Schaubert, "A gap-induced element resonance in single-polarized arrays of notch antennas," in *1994 IEEE . Intern. Symposium Antennas and Prop. Soc*, vol. 2, pp. 1264-1267, Jul. 1994.

[7] B. Munk, R. Taylor, T. Durham, W. Croswell, B. Pigon, R. Boozer, S. Brown, M. Jones, J. Pryor, S. Ortiz, J. Rawnick, K. Krebs, M. Vanstrum, G. Gothard, D. Wiebelt, "A Low-Profile Broadband Phased Array Antenna," *IEEE . Intern. Symposium Antennas and Prop. Soc*, vol.2, pp. 448 451, 22-27 June 2003.

[8] P. Friederich, L. Pringle, L. Fountain, and P. Harms, "A new class of broadband planar apertures," *Antenna Applications Symposium*, Allerton Park, Monticello, IL, September 2001.

[9] M. Jones and J. Rawnick, "A new approach to broadband array design using tightly coupled elements," *IEEE Military Communications Conference 2007*, pp. 1–7, Oct 2007.

[10] J. R. Bayard, D. H. Schaubert, and M. E. Cooley, "E-plane scan performance of infinite arrays of dipoles printed on protruding dielectric substrates: coplanar feed line and e-plane metallic wall effects," *IEEE Trans. Antennas Propag.*, vol. 41, no. 6, pp. 837–841, Jun 1993.

[11] E. de Lera Acedo, E. Garcia, V. Gonzalez-Posadas, J. L. Vazquez-Roy, R. Maaskant, and D. Segovia, "Study and design of a differentially fed tapered slot antenna array," *IEEE Trans. Antennas Propag*., vol. 58,

[12] K. Jung, W. R. Eisenstadt, R. Fox, A. Ogden, and J. Yoon, "Broadband active balun using combined cascode-cascade configuration," *IEEE Trans. Microw. Theory Tech.*, vol. 56, no. 8, pp. 1790–1796, Aug 2008.

[13] S. S. Holland and M. N. Vouvakis, "Planar ultrawideband modular antenna (PUMA) array," U. S. Patent Appplication 61/230,271, July 31, 2009.

[14] S. S. Holland, M. N. Vouvakis, and D. H. Schaubert, "A new modular wideband array topology," *Antenna Applications Symposium*, Allerton Park, Monticello, IL, September, 2009.

[15] B. Munk, Finite Antenna Arrays and FSS. Wiley, 2003.

[16] S. S. Holland and M. N. Vouvakis, "The banyan tree antenna array," Submitted to *IEEE Trans. Antennas Propag*.

[17] Ansoft HFSS, version 11.2, www.ansoft.com.

[18] A. Ludwig, "The definition of cross polarization," *IEEE Trans. Antennas Propag*., vol. 21, pp. 116–119, Jan 1973.

A PHASE-RECONFIGURABLE REFLECTARRAY ELEMENT USING FLUIDIC NETWORKS

Stephen A. Long and Gregory H. Huff
Electromagnetics and Microwave Laboratory
Texas A&M University, College Station, TX
E-mail: ghuff@tamu.edu

Abstract: This paper presents a phase-reconfigurable reflectarray element for beamforming applications. This topology relies upon fluidic networks to perform localized permittivity manipulation to achieve continuous, low-loss phase control of a reflected signal. This work addresses different aspects of design, modeling, and measurement for two different unit cell designs and includes a proof-of-concept for a 2nd iteration prototype. Initial measurements demonstrate up to 200° of phase shift and a return loss of less than 1.2 dB at the operating frequency of 3 GHz.

1. Introduction

Reflectarray (RA) antennas offer both the feeding efficiency of conventional shaped reflector antennas along with the planar form and beam-pointing capabilities of microstrip phased arrays [1]. Recent phase-shifting technologies for the latter have been adapted in RA elements to provide dynamic beam-steering. The resulting topologies are typically switch-based [2]-[5] or material-based [6]-[7] and rely on bias lines or other control circuitry integrated onto or within the antenna. In some cases this can lead to design challenges, fabrication difficulties, and potentially significant losses in the reflected signal. This work proposes the use of a microfluidic reactive impedance loading mechanism [8] to achieve low-loss and continuous phase control over the signal reflected from a RA microstrip patch element. Conceptually, this mechanism blends the phase line technique from [9] with the permittivity manipulation performed in [7] but removes the need for bias and control lines in the vicinity of the RA element.

The phase reconfigurable RA element and reactive loading mechanism are presented first. A prototype design without a dynamic fluid delivery system follows this to illustrate the impact of particle geometry and other design parameters. Measured results for the dispersions and the fabricated prototype are then provided. A second prototype is then presented along with results (measured and simulated) for a design with a dynamic fluidic delivery system. A brief discussion concludes the work.

2. Reflectarray Element and Reactive Loading Mechanism

Fig. 1 shows the RA element and the fluidic-based reactive loading mechanism. The RA element is a microstrip patch of length L and width W atop a substrate of height h and

permittivity ε_{rs}. The reactive loading mechanism is a Coaxial Stub Microfluidic Impedance Transformer (COSMIX); it has a coaxial length d and capacitive gap g along with an inner and outer coaxial radii a_2 and b_2 (a_1 and b_1 are not utilized in this application since the device connects directly to the patch). The COSMIX is centered about the patch width at $W/2$ and inset at a distance s from a radiating edge. This is structurally similar to a traditional integration of a probe-feed. The COSMIX uses the pressure-driven flow of a remotely manipulated fluidic colloidal dispersion with an effective permittivity $\varepsilon_{rd}(\vartheta)$ that is synthesized by homogeneously mixing a volume fraction ϑ of nanoparticle inclusions with ε_{r2} into a fluidic medium with ε_{r1}. Electrically dense nanoparticles (e.g., $\varepsilon_{r2} \gg \varepsilon_{r1}$) and non-ionic low viscosity fluids medium are ideal for this work and are used when possible to maximize the impact of mixing on the overall reconfigurability of the design.

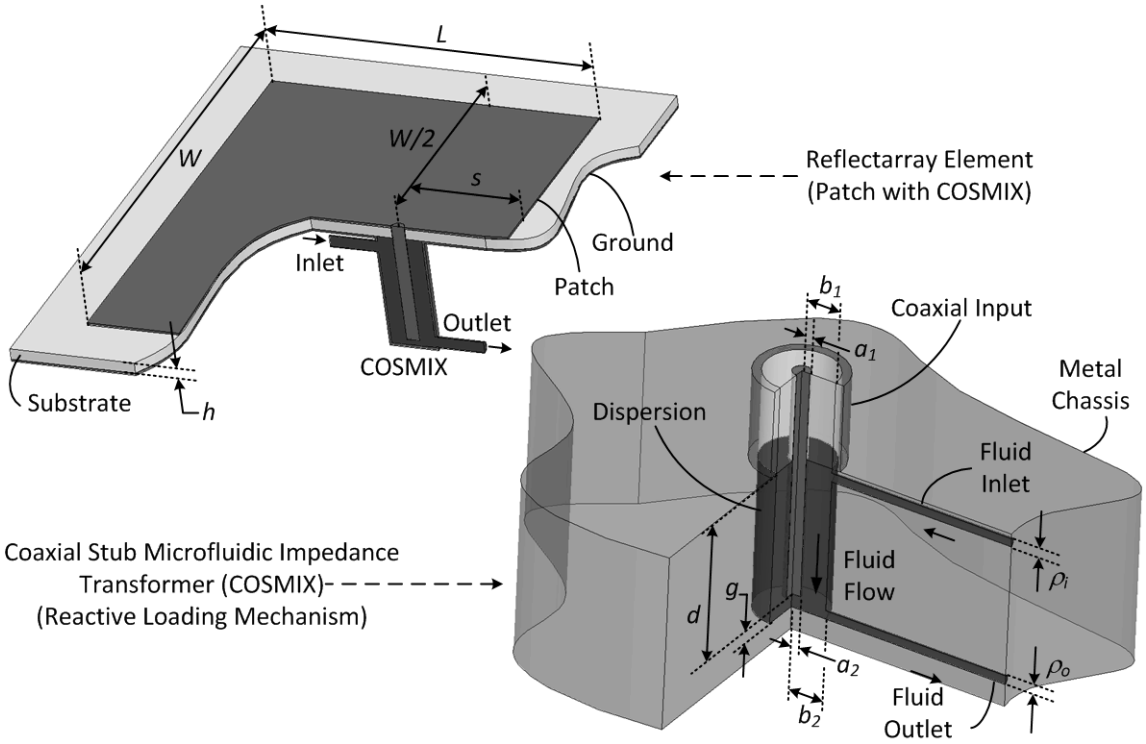

Fig. 1 - Diagrams of the COSMIX (right) and RA element (left).

This RA element operates in a conceptually similarly way to [10] and other designs that facilitate a true time delay phase shift through a two-terminal device connecting the patch and ground plane (variable length stubs, etc.). This work differs by utilizing the impedance mismatch between the patch and the COSMIX (also a two-port device), whose reactive impedance and resulting reflection coefficient seen by the patch at its terminals is altered by changing the materials in the dispersion. This reflection is transformed through the patch to facilitate a phase shift in the re-radiated signal.

2. Prototype I - Materials and Design Parameters

There are several material parameters and critical design dimensions that impact the reconfigurable performance of the RA element. The particle geometry, its permittivity ε_{r2}, and their orientation (or alignment) [11] in the dispersion all play a key role through their impact on $\varepsilon_{rd}(\vartheta)$. The left side of Fig. 2 shows the Maxwell-Garnet mixing formula [11] to illustrate how particle aspect ratio (e.g., colloids, flakes, and whiskers) impacts $\varepsilon_{rd}(\vartheta)$. This points to how higher aspect ratio particles achieve greater changes in the dispersion, especially at lower inclusion volume fractions. Colloidal Barium Strontium Titanate (BSTO) [12] (estimated as ε_{r2} ~500, *tan* δ_2 ~.05) with 800 nm maximum particle diameters and silicone heat transfer oil (ε_{r1} ~ 3 and *tan* δ_1 ~10^{-4}) were commercially obtainable and available in bulk quantities for experiments, so these material properties were used in simulations. The dimensions and position of the COSMIX are also important since it translates the aforementioned materials properties into the reflection and phase shift of the patch. The right side of Fig. 2 shows the CAD [13] model of the waveguide test fixture and a prototype of the RA element designed to operate at 3 GHz. (placed at the bottom of an expanded section of rectangular waveguide ($A_2 = B_2 = 80$ mm or 0.8 λ_0). This structure bolts to a WR-284 circular flange ($A_1 = 2.84$ in, $B_1 = 1.34$ in).

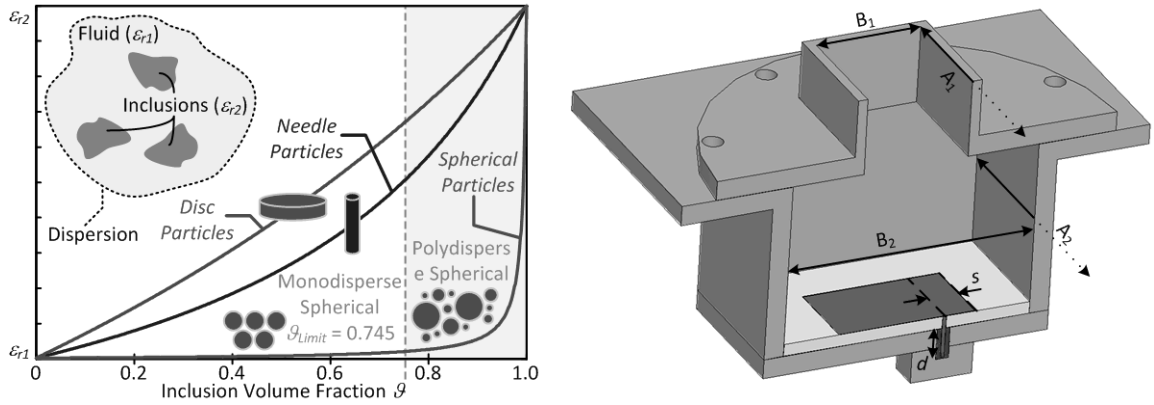

Fig. 2 - Maxwell Garnett mixing rule for particles of varying shape (left) and prototype design to examine the performance of the RA element (right).

The 3 GHz patch dimensions W = 50 mm and L = 44.45 mm were calculated from basic design equations for a Rochelle foam (ε_{rs} ~ 1, tan δ ~ 0) substrate of height h = 3.75 mm. The radii a_2 = 2.05 mm and b_2 = 0.615 mm of the COSMIX are similar to [8] (which matches an SMA probe) with its gap g = 0.5 mm [14]. It is desirable to keep the COSMIX as compact as possible so a series of studies examined the impact of design parameters s and d on the performance of the RA element. Fig. 3 (left) shows the simulated reflect-phase resulting from changing d (the COSMIX length) between 10 mm and 25 mm while sweeping the volume fraction ϑ of lossless (δ ~ 0) colloidal material in the dispersion to change its effective medium properties. The inset was fixed at s =10 mm. These results indicate that a COSMIX longer than 10 mm is not necessarily better for this patch design and inset.

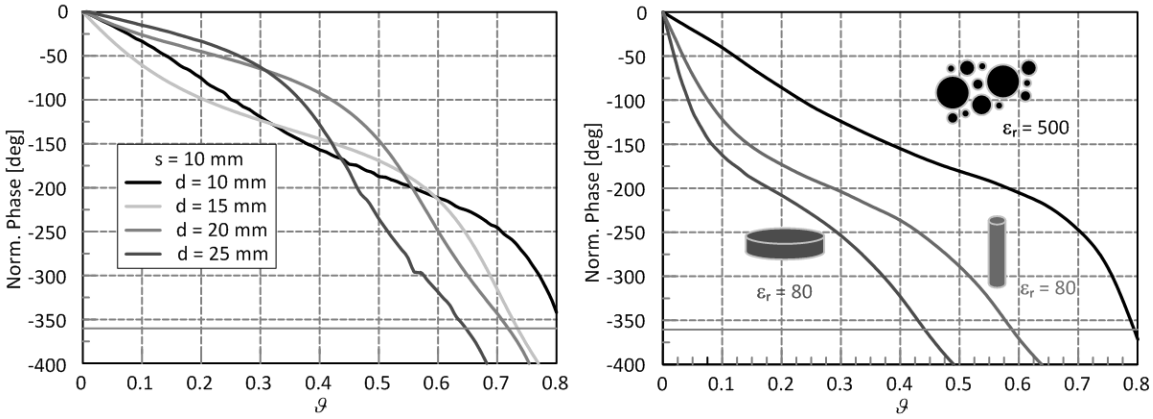

Fig. 3 - Simulated reflect-phase from varying COSMIX length (left) and reflect-phase from dispersions with different particle aspect ratios and material properties (right).

Fig. 3 (right) shows the reflect-phase for different lossy particle aspect ratios in the dispersion to highlight the impact of particle geometry (with $s = d = 10$ mm); note the slight difference in spherical particles when compared to identical but lossless dispersions in the left plot. The colloidal dispersion required a volume fraction of 78% while the requirement for needles and discs (both with $\varepsilon_{r2} = 80$) was 58% and 45%, respectively. These results indicate that particle shape can play a large role in reducing the volume fraction of solid materials necessary for 360° phase shift and manageable viscosities – even when compensating for a much lower particle permittivity. The results from both plots in Fig. 3 represent an off-broadside angle of incidence due to the placement of the RA element in the metallic waveguide, but the general trends are expected to be preserved for angles of incidence closer to broadside.

3. Prototype I - Experiment

The waveguide, patch antenna, and COSMIX were fabricated according to the CAD model in Fig. 2 and dimension obtained in the previous section ($s = d = 10$ mm). The process for experiments with this test fixture is shown in Fig. 4. The BSTO was first weighed out and mixed with the silicone oil to produce volume fractions up to 50% in 10% increments (Fig. 4a). An Agilent dielectric probe kit measured the dielectric constants of the dispersions prior to their injection into the COSMIX (Fig. 4b). A patch made from copper sheet with the center probe conductor attached was then placed inside (Fig. 4c). A thin Teflon toothed-ring around the probe's center conductor secured its symmetric axial orientation within the COSMIX and allowed materials to flow around it (this showed no significant impact on the performance). The WR-284 coax-to-waveguide adapter closed off the expanded waveguide and an Agilent PNA was used to measure the reflected phase and loss (Fig. 4d). The entire test fixture was disassembled for cleaning and insertion of new dispersion materials for each volume fraction.

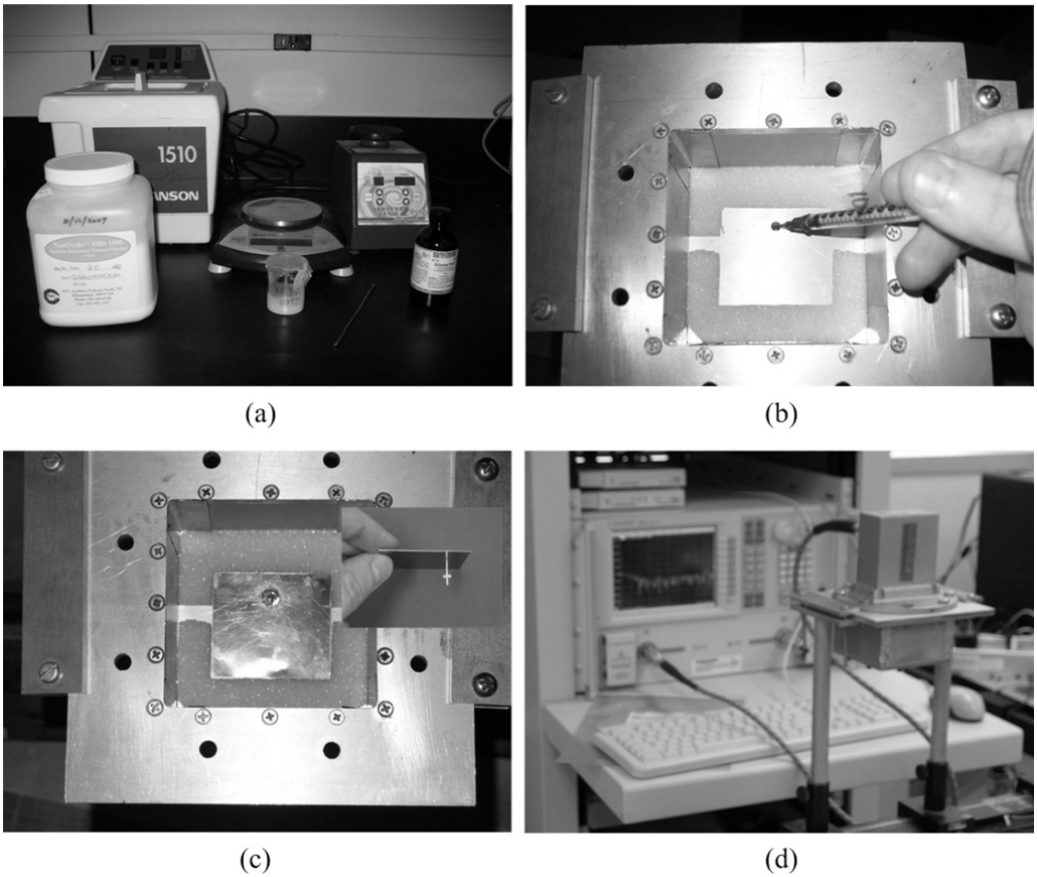

Fig. 4 - Proof-of-concept experiment for COSMIX loaded RA element.

Fig. 5 shows the results for the six experiments using different volume fractions. The measurements from the dielectric probe (Fig. 5a) shows excellent agreement with the mixing rule's predictions. At 3 GHz the fabricated element achieved up to 200° of phase shift with only 1.2 dB of loss. There are deviations between the simulated and measured results but the general trends are in agreement. The 0.4 dB baseline loss shown in Fig. 5d is a measurement of the waveguide with no patch or other materials present. The actual dielectric properties – specifically losses and tan δ - of the materials may contribute additional phase and loss error. Although the simulations suggested little or no contribution from the Teflon spacer, a "plunging" effect was observed that accelerated particle settling within the capacitive gap of the COSMIX – this introduces a small but additional mechanism for error. Particle settling may also have been accelerated due to the conic recession at the bottom of the COSMIX resulting from the use of a drill bit to bore out the COSMIX. Disassembly and cleaning between each measurement also impacted the experiment's repeatability, but the measured phase shift followed its expected behavior from simulations.

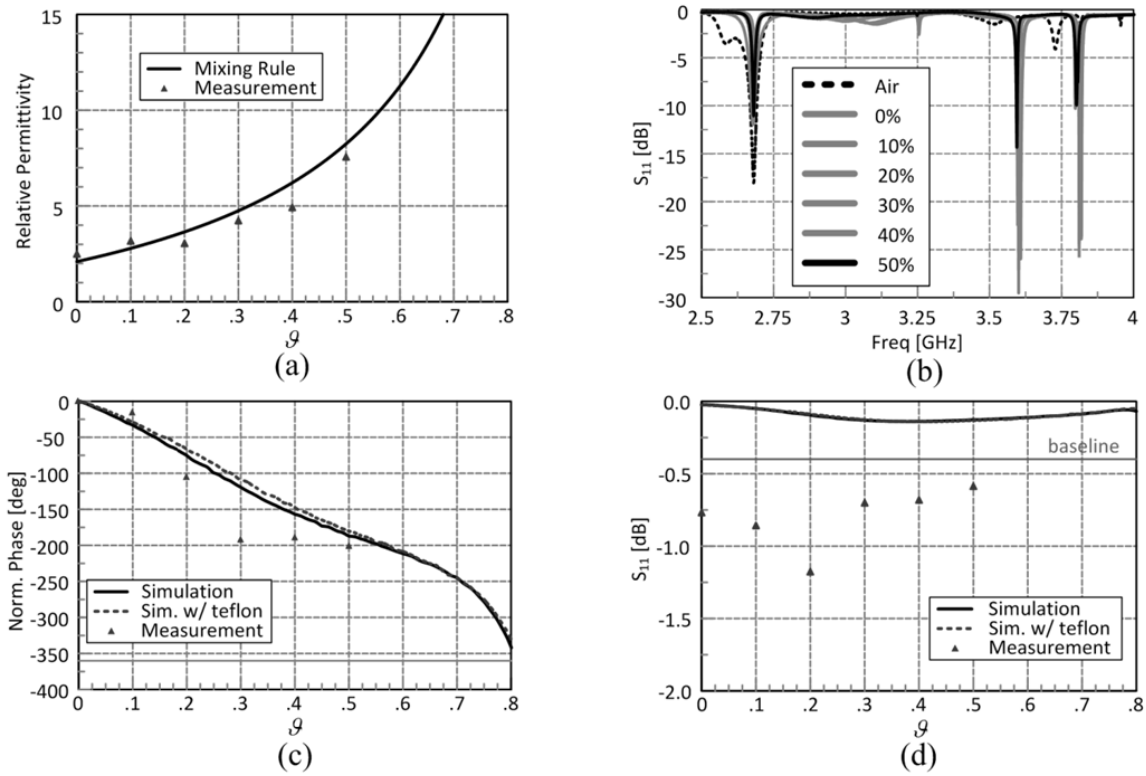

Fig. 5 - Experimental results for the proof-of concept design.

4. Prototype II – Design Process for Ideal Materials

The proof-of-concept experiment provided promising results but highlighted several considerations for fabrication and operation of future designs. This experiment was redesigned for a more thoroughly designed RA element and test fixture. The waveguide in Fig. 6 now represents a smaller unit cell (50 mm x 80 mm or .5 λ_0 x .8 λ_0) and a reduced discontinuity with the WR-284 flange. A mechanically milled patch on a 125 mil Duroid 5870 (ε_{rs} = 2.33, tan δ =.0012) substrate replaces the Rochelle foam and hand-cut copper sheet of the first experiment. The substrate introduces more loss from reflection at the dielectric-air boundary, but this fabrication method provides greater precision in the patch's dimensions, the probe placement, and the orientation of the patch in the waveguide. The COSMIX inner conductor's placement through a thicker and more rigid substrate replaces the need for the Teflon spacer in securing the probe's axial orientation.

The introduction of a dielectric substrate reduces the physical size of the patch from the previous experiment to L = 30.4 mm and W = 39.8 mm, allowing it to fit in the smaller unit cell. Nylon screws tighten the substrate against the ground plane to eliminate leakage from the COSMIX but do not interfere with the RA element's performance. Two circular fluidic channels with 1 mm diameters are milled into the aluminum base plate where the COSMIX resides. This eliminates the static material injection method of the first experiment and enables dynamic measurements with a closed-loop fluidic system. A

milling bit replaces a drilling bit in the fabrication in order to ensure a flat bottom when boring out the COSMIX. The outer radii of the COSMIX has been increased to b_2 = 3/16" representing the smallest milling bit available in a typical machine shop. The dispersion properties in the design remain virtually unchanged ($\varepsilon_{r1} \sim 3$, $tan\ \delta_1 \sim 10^{-4}$, $\varepsilon_{r2} \sim 500$, $tan\ \delta_2 \sim .05$) aside a smaller particle geometry of less than 100 nm.

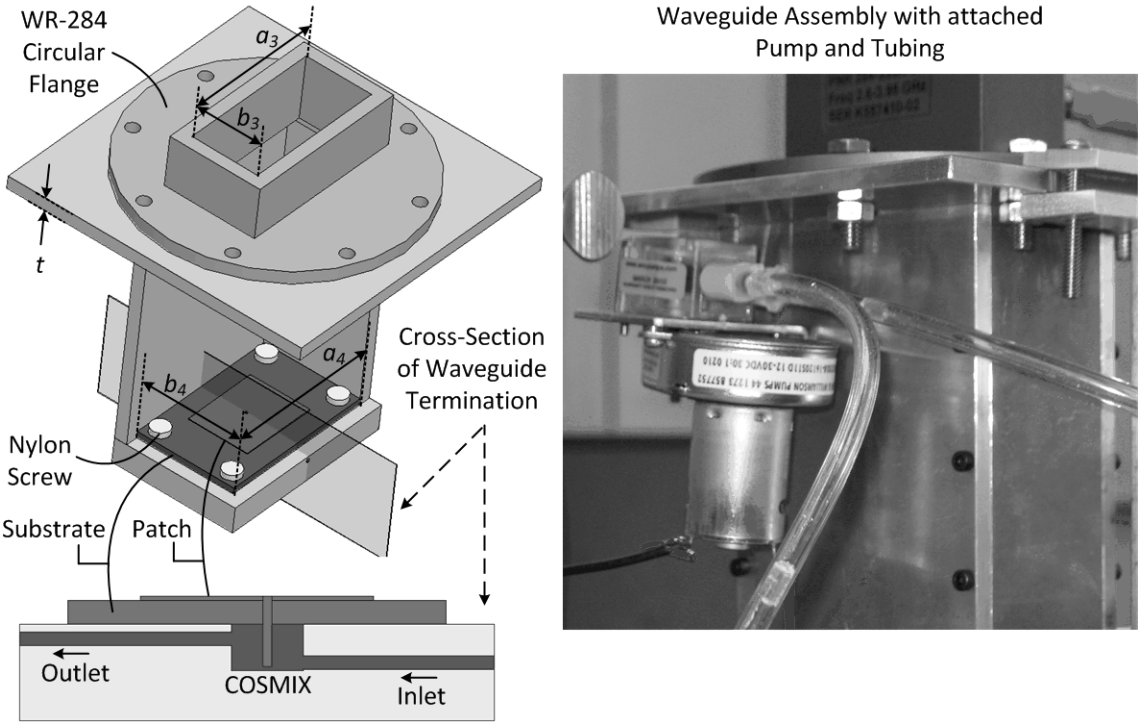

Fig. 6 - CAD model of redesigned RA element (left) and experimental test fixture (right).

The COSMIX inset (s = 14 mm) and length (d = 6 mm) come from an effort to maximize the reflect-phase response for volume fractions below 25%; this ensures that the dispersion can be less viscous and easily pumped through the system. This process began by replacing the COSMIX in the simulated model with a coaxial impedance port. The impedance was swept from -j300 to +j300 to representing the equivalent input reactance provided by the COSMIX as the inset was moved along the length of the patch. The phase curves of Fig. 7 (left) illustrate that as the probe is moved closer and closer to the middle of the patch, the reflected phase becomes more and more sensitive to impedance changes at the reference plane of the COSMIX. Placing the probe in the middle of the patch (L/2) results in no phase change, as expected, due to the quasi-zero field point of the patch's operating mode; from a transmission line perspective the COSMIX is in shunt with a virtual short in this position.

By observing the results an impedance window can be determined for reactive loading that generates the desired phase shift. With the inset of 14 mm, the reactance range necessary to reconfigure the current design of the RA element is approximately -j45 to -

j30 (shown in gray shading). From simulated COSMIX results (Fig. 7, right), a length of d = 6 mm provides this impedance range at lower volume fractions. The new length and position of the COSMIX yield the simulated results of Fig. 8. More than 350° of phase change and approximately 2 dB of insertion loss occur with a volume fraction less than 15%. As a reference, simulations of the first prototype (Fig. 3) required a volume fraction close to 80% to achieve a similar goal. This study illustrates an important process for designing the RA element and maintaining manageable dispersion viscosities.

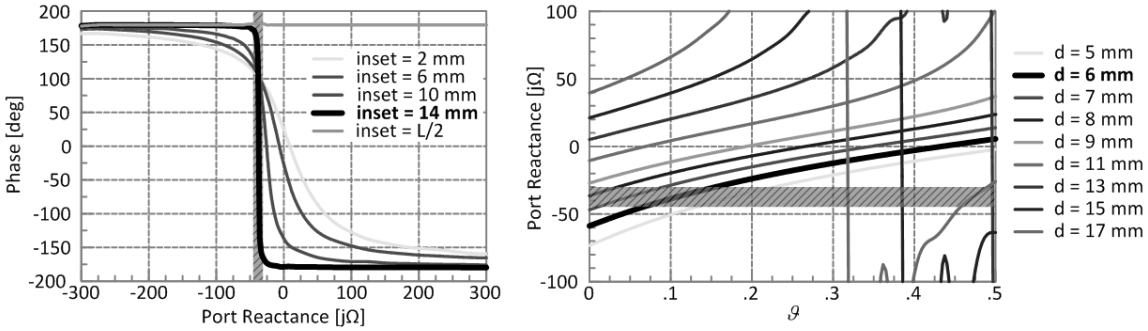

Fig. 7 - Impedance port modeling (left) and COSMIX length tuning (right) at 3 GHz.

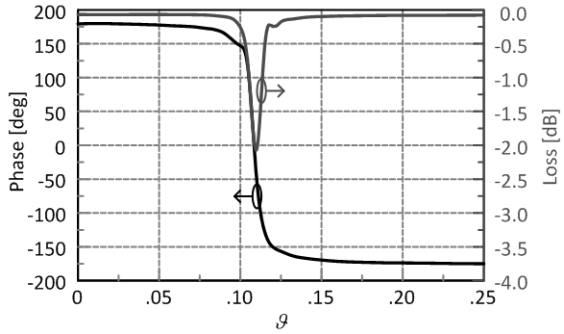

Fig. 8 - Phase response and loss of the redesigned RA element at 3 GHz.

5. Prototype II – Experiment

The measurement setup in Fig. 6 (right) allows for simultaneous operation of the circulating fluidic network, the Agilent dielectric probe, and the network analyzer for measuring the phase and loss of the RA element as the fluid is manipulated. An Agilent DC supply powers a peristaltic pump to continually circulate the dispersions between the COSMIX and a reservoir. A magnetic stirrer keeps the dispersion in a glass beaker reservoir agitated and homogeneously mixed. The experiment begins with a high volume fraction ϑ = 20%; after several minutes of circulation and repeated phase and loss measurements to confirm operational stability the dispersion's dielectric constant is measured and an injection of oil into the reservoir dilutes the dispersion by 2%. This was repeated until the volume fraction reached 8%. In the first run of the experiment no phase shift or resonances were observed. Fig. 9 shows the resulting phase measurements that have been normalized to the initial state when ϑ = 20%.

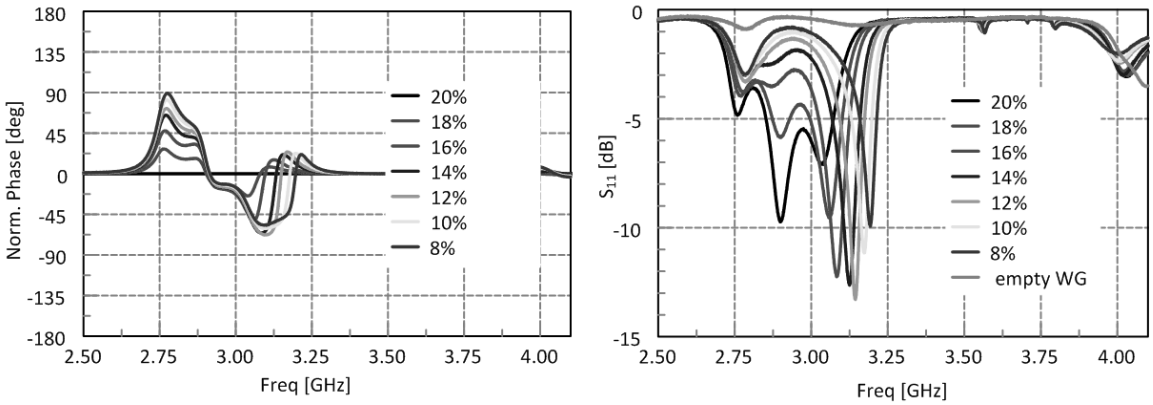

Fig. 9 - Phase (left) and loss (right) measurements of the 2nd iteration prototype.

Although phase shifting does occur, the operating frequency (3 GHz) experiences little or no phase shift. Furthermore the losses are much greater than in the initial experiment. In each measurement three resonances were observed; one is fixed at roughly at 2.75 GHz and another close to 2.88 GHz. The third resonance was observed shifting to a higher frequency as ϑ was lowered; as it passed through a given frequency, that frequency experienced a phase-shift. Differences in material properties account for these deviation from the expected results; the colloidal BSTO used in this experiment came from a different batch than in the initial experiment. A rigorous study of these materials in a SIW tunable filter [15] revealed the actual properties of the BSTO may be closer to $\varepsilon_{r2} \sim 100$, $tan\ \delta_2 \sim 0.5$. Furthermore, the fluid used was polydimethylsiloxane (PDMS) in place of the silicone heat transfer oil. The work in [16] characterized its (cured) properties at RF as $\varepsilon_{r1} \sim 2.68$, $tan\ \delta_1 \sim .04$ but the uncured material is considerably more lossy. This likely represents the heaviest contributor to the experiment's losses since in a colloidal dispersion the properties of the fluid dominate (Fig. 2) at low volume fractions. Fig. 10 shows the simulated results using these material properties. Similar trends in these results help confirm suspicions regarding the materials used.

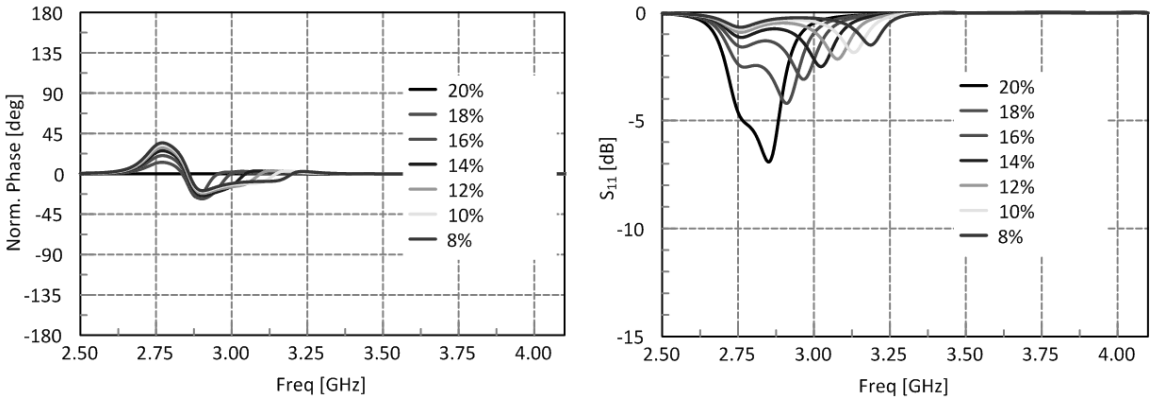

Fig. 10 - Simulated phase (left) and loss (right) using alternate material properties.

The new batch of commercially obtained colloidal BSTO with particle sizes smaller than 100 nm was also examined using X-ray diffraction (XDR) to determine its actual crystal system and better characterize the major difference between observations and expectations. Fig. 11 shows the results from three sets off available materials with different ratios of Barium and Strontium; the peaks in this plot correspond to the diffraction from major crystallographic lattice planes given by the Miller indices (*h k l*) [17]. The key result of this experiment occurs in the neighborhood of $2\theta \sim 46^{o}$ where the (002) and (200) lattice planes of BSTO can be detected (this area is highlighted in the figure for all three sets of available materials). Both cubic and tetragonal crystal systems of BSTO will result in a diffraction within this neighborhood (the response is similar and shifted slightly based on the Ba:Sr ratio) but the cubic and tetragonal systems have diffraction characteristic individual to each particular crystal system. The cubic (non-ferroic) phase will show a single broad peak in this neighborhood since the (002) and (200) lattice planes are nearly indistinguishable; however, the tetragonal phase (the electrically dense and ferroelectric Perovskite structure) will show two closely spaced but very distinct peaks for each of these lattice planes due to its tetragonal crystal structure.

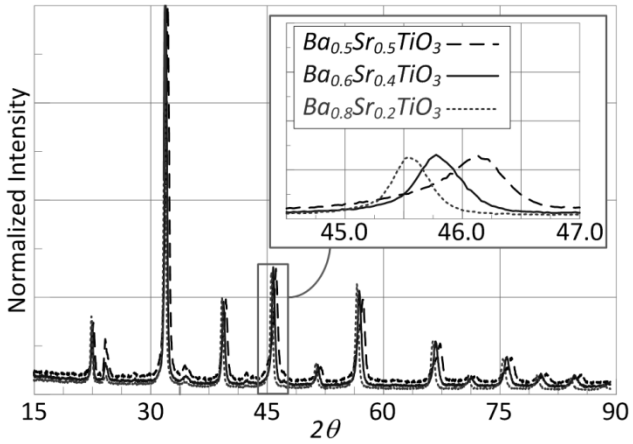

Fig. 11 - X-ray diffraction (XDR) used to determine the crystal system of three different sets off colloidal BSTO with particle sizes less than 100 nm.

The single-peak structures are observed in all curves shown in Fig. 11, and the well-defined XDR data indicates that there are very few contaminants, so this behavior (e.g., a lower permittivity and higher losses) is attributed primarily a size-dependent effect that has been reported previously [18] for BTO colloids less than 100 nm (also the size used in this work). This also supports earlier assumptions that the particle permittivity is closer to 100. This value for ε_{r2} is very close to Rutile (TiO_2), which has a simple tetragonal structure (near-cubic) and a permittivity similar to observations and more rigorous characterizations [19]. XDR measurements were not available for the larger 800 nm particle sizes but these experienced less variation between observations and expectations.

6. Conclusion

The design and experiment of a phase reconfigurable RA unit cell enabled by a COSMIX has been presented. A phase shift of 200° was demonstrated at 3 GHz with only 1.2 dB of loss in a proof-of-concept experiment. Discrepancies in the phase behavior are attributed to fabrication challenges as well as the more dominant and observed effect of particle settling within the capacitive gap of the COSMIX. A redesigned RA element and test fixture has also been presented and preliminary measurements highlight the need for more advanced material systems. Ongoing work includes the automation of a fluid delivery system, mixing mechanisms for control of colloidal material in the dispersion, and further stabilization of the dispersion to prevent aggregation within the COSMIX.

7. Acknowledgements

Funding for this work was provided in part by the United States Air Force Office of Scientific Research (grant #FA9550-08-1-0329) and the United States National Science Foundation (grant #ECCS-0846865). The authors also thank Zoubeida Ounaies and her research group for providing the XDR measurements.

8. References

[1] J. Huang and J. A. Encinar, *Reflectarray Antennas*. Hoboken, NJ: John Wiley & Sons, 2008.

[2] S. V. Hum, M. Okoniewski, and R. J. Davies, "Realizing an electronically tunable reflectarray using varactor diode-tuned elements," *IEEE Microwave and Wireless Comp. Letters*, vol. 15, pp. 422-424, June 2005.

[3] C. Chih-Chieh and A. Abbaspour-Tamijani, "Design and experimental verification of steerable reflect-arrays based on two-bit antenna-filter-antenna elements," in *Microwave Symposium Digest*, 2009, pp. 1181-1184.

[4] H. Rajagopalan, Y. Rahmat-Samii, and W. A. Imbriale, "RF MEMS Actuated Reconfigurable Reflectarray Patch-Slot Element," *IEEE Trans. Antennas Propag.,*vol. 56, pp. 3689-3699, Dec. 2008.

[5] O. Bayraktar, K. Topali, M. Unlu, and O.A. Civi, "Beam Switching Reflectarray using RF MEMS Technology," in *Proc. EuCAP*, 2007, pp. 1-6.

[6] R. Marin, A. Mossinger, J. Freese, S. Muller, and R. Jakoby, "Basic investigations of 35 GHz reflectarrays and tunable unit-cells for beamsteering applications," in *Proc. EURAD*, 2005, pp. 291-294.

[7] R. R. Romanofsky, "Advances in Scanning Reflectarray Antennas Based on Ferroelectric Thin-Film Phase Shifters for Deep-Space Communications," *IEEE Proc.*, vol. 95, pp. 1968-1975, Oct. 2007.

[8] G. H. Huff and S. Goldberger, "A Coaxial Stub Microfluidic Impedance Transformer," *IEEE Microwave and Wireless Comp. Letters*, vol. 20, pp. 154-156, March 2010.

[9] R. D. Javor, X. Wu, and K. Chang, "Beam steering of a microstrip flat reflectarray antenna," in *Proc. APS International Symposium*, 1994, pp. 956-959

[10] F. Venneri, S. Costanzo, and G. Di Massa, "Transmission line analysis of aperture-coupled reflectarrays," *Progress In Electromagnetics Research*, vol. 4, pp. 1-12, 2008.

[11] Sihvola, *Electromagnetic mixing formulas and applications,* vol. 47. London: IEE, 1999.

[12] TPL, Inc., NanOxideTM and NanosperseTM, Albuquerque, NM.

[13] Ansoft, HFSS v12.0, Pittsburgh, PA, 2009.

[14] N. Marcuvitz, *Waveguide Handbook*. London: Peter Peregrinus Ltd., 1986.

[15] J. D. Barrera and G. H. Huff, "An adaptive SIW filter and dual-linearly polarized patch antenna using vertically-oriented fluidic material perturbations," in *Proc. NASA/ESA Conf. Adaptive Hardware Systems,* Anaheim, CA, June 2010, pp. 205-208.

[16] N. Tiercelin, P. Coquet, R. Sauleau, V. Senez, and H. Fujita, "Polydimethylsiloxane membranes for millimeter-wave planar ultra flexible antennas," Journal of Micromechanics and Microengineering, vol. 16, pp. 2389-2395, 2006.

[17] J. F. Nye, *Physical Properties of Crystals: Their Representation by Tensors and Matrices*. London: Oxford University Press, 1985.

[18] M. E. Tobar, J. Krupka, E. N. Ivanov, and R. A. Woode, "Anisotropic complex permittivity measurements of mono-crystalline rutile between 10 and 300 k," *J. Appl. Physics,* vol. 83, pp. 1604-1609, 1998.

[19] B. Li, X. Wang, L. Li, H. Zhou, X. Liu, X. Han, Y. Zhang, X. Qi, and X. Deng, "Dielectric properties of fine-grained BaTiO3 prepared by spark-plasma-sintering," *J. Materials Chemistry Physics*, vol. 83, pp. 23-28, 2004.

Miniaturized Patch Antennas with Multiple Bands of Operation for Microwave Breast Imaging

Mudar Al-Joumayly, Suzette Aguilar, Nader Behdad, and Susan C. Hagness
Department of Electrical and Computer Engineering
University of Wisconsin, Madison, WI, 53706
aljoumayly@wisc.edu, smaguilar@wisc.edu,
behdad@wisc.edu, and hagness@engr.wisc.edu

***Abstract* – We propose new designs for dual- and tri-band miniaturized patch antennas. The proposed antennas are to be used as array elements in a three dimensional (3D) microwave tomography system for breast imaging. Multi-band operation is obtained by reducing the resonant frequencies of the third and the fifth longitudinal higher-order modes of the patch antenna as well as that of its fundamental mode. This is achieved by loading the antenna with non-resonant slots at specific locations across the patch. This loading technique is also used to design patch antennas with enhanced bandwidth of operation. By judicious choice of the locations and dimensions of slot loadings, the bandwidth can be increased by a factor of 300% while reducing the center frequency of operation by a factor of 15.5%. Prototypes of the proposed antennas are fabricated, tested, and their performance and radiation characteristics are verified experimentally in a biocompatible immersion medium.**

1. INTRODUCTION

Microwave tomography has been investigated over the last few years as a low-cost, non-ionizing, three-dimensional (3-D) breast imaging tool [1]-[2]. In microwave tomography systems, low-power microwave signals are transmitted into the breast tissue by an array of antennas surrounding the breast, the scattered signals are then measured, and the spatial distribution of the dielectric properties throughout the breast volume is estimated by solving an electromagnetic nonlinear inverse scattering problem. For the inverse problem, it has been shown that its degree of ill-posedness is reduced when the density of observation points and the number of frequencies used are increased [3]. The antenna array and its elements, as essential components of the microwave tomography system, have a direct impact on these factors and, thus, on the accuracy of microwave imaging.

The 3-D antenna array that surrounds the breast of a prone patient is ideally composed of a large number of elements to permit dense 3-D spatial sampling of scattered fields. Thus, each antenna element should occupy a very small footprint relative to the total surface area of the breast. In addition, it is advantageous for the miniaturized antennas to operate

efficiently at multiple frequencies. Solving the inverse scattering problem at a single frequency poses inherent challenges because the stability and resolution of the imaging algorithm represent competing demands in choosing the frequency [4]. In contrast, the advantages of both lower and higher frequencies are retained with a multi-frequency approach [5]. The use of a parametric model to reconstruct the frequency-dependent dielectric properties reduces the ill-posed nature of the inverse problem [6] and computational burden of the multi-frequency algorithm [7]. In particular, antenna elements that operate within the frequency range of 0.5–3.0 GHz are desired. Frequencies below and above this range are non optimal in terms of spatial resolution and penetration depth, respectively. In addition, the antenna needs to operate in an immersion medium that improves coupling efficiency of the low-power microwave signals into and out of the breast. Finally, the antenna design should not be so complex as to render it impractical to model in the reconstruction algorithm.

In this paper, multi-band miniaturized patch antennas are proposed to populate an array for use in a 3-D microwave tomography system. Our proposed antenna, which has been specifically designed to meet the specifications described above, offers several advantages over what are arguably the most widely used radiating elements in microwave tomography, namely monopole and dipole antennas [8], [9], [10], [11]. Monopoles and dipoles, as well as simple patches and slots, offer simplicity in terms of forward-problem modeling and may be impedance-matched across a wide bandwidth when immersed in a lossy medium. However, this broadening of the bandwidth is done through the addition of loss into the system and at the expense of reducing the radiation efficiency of the antenna over a large bandwidth [12]. Our rationale for using a multiband antenna stems in part from the expectation that the higher gain exhibited at the design frequencies will provide a higher signal-to-noise ratio and imaging sensitivity when immersed in a low-loss coupling medium. The planar design of our proposed antenna elements also offers several added benefits. The ground plane backing prevents undesired illumination of scatterers outside of the breast and thereby avoids environmental interference that can occur with omni-directional radiators. Furthermore, the antenna characteristics are independent of the coaxial feed cables. This isolation increases the accuracy of the antenna modeling required in the forward simulations of the inverse scattering algorithm, which we conduct using the finite-difference time-domain (FDTD) method (e.g., [2]). The planar design and relatively large feature sizes of the proposed antenna contribute to its ease of modeling using FDTD.

2. ANTENNA DESIGN

The proposed multi-band antennas are designed and optimized for operation in a biocompatible immersion medium comprised of safflower oil. The immersion medium is used to improve the coupling efficiency of the microwave signals into and out of the breast. Al-Joumayly, et al. [13] reported the following Debye parameters for safflower oil: ε_∞=2.24, ε_s=2.97, σ_s=0, and τ=5 ps.

In this section, the design procedure of the dual-band miniaturized patch antenna reported in [13] is first discussed. This procedure is, then, further developed and utilized to design tri-band miniaturized patch antenna. The developed design procedure can also be used to enhance the operational bandwidth of the patch antenna by merging operating two bands together. The topology of the dual-band miniaturized patch antenna is shown in Fig. 1. The antenna consists of a rectangular patch with a length of 29 mm and width of 28 mm loaded with two slots that are parallel to and near the radiating edges of the patch, and a third slot located at the center of the patch. The antenna is also loaded with meandering slots at the non-radiating edges of the patch. To better understand the principle of operation of the proposed antenna, we consider a simpler structure which consists of only two slots near the radiating edges of the patch, as shown in Fig. 2. Maci, et al. [14] have shown that a dual-band response can be obtained from this structure. The lower frequency of operation of this antenna is determined by the resonant frequency of the dominant mode, TM_{100}, of a rectangular patch antenna, while the upper operating frequency is determined by the resonant frequency of a perturbed third order, TM_{300}, longitudinal mode. For the dominant mode, the effect of adding these two slots near the radiating edges of the patch is not significant as its resonant frequency is only slightly reduced. This is due to the fact that the two slots are located close to the current minima of that mode. The effect of adding these two slots, however, is more significant on the TM_{300} mode (and, as will be shown later, on the fifth order mode, TM_{500}) because they are positioned in regions where the current for that higher-order mode is significant. These two slots increase the current path of the TM_{300} mode at the edges of the patch, and hence reduce its resonant frequency. Another advantage of adding these slots is that the radiation characteristics of the TM_{300} mode can be made similar to that of the dominant mode by judicious choice of the dimensions and location of the slots.

The operating frequencies of the two bands are further reduced by adding a third slot located at the center of the patch, where both TM_{100} and TM_{300} modes have current maxima. The addition of this slot increases the current path for both modes and, thus, their electrical lengths increase and thereby their operating frequencies are reduced. The addition of this slot, however, does not have any effect on the second mode, TM_{200}, since the slot is located at the current minimum of this mode. It can be shown that as the length of the center slot increases, the operating frequencies of both first and third modes decrease without any significant change on the operating frequency of the second mode. However, a further increase in the length of the center slot causes the operating frequency of the third mode to merge with that of the second mode. This is not desirable since the radiation pattern of the second mode has a null in the broadside direction.

To further miniaturize the antenna, meandering slots are added symmetrically at the non-radiating edges of the patch [15]. These slots cause the current paths of all longitudinal modes to be increased, thereby permitting a further reduction in the operating frequencies of these modes. It can be shown that as the length of the meandering slots increases, the operating frequencies of all longitudinal modes of the miniaturized patch antenna are reduced. Even though the location of the meandering slots does not affect the radiation

pattern of the first mode, they have a significant effect on the current distribution, and thus radiation patterns, of the third mode. Therefore, in order to increase the current path without disturbing the current distribution of the third mode, the meandering slots are added around the current minima of that mode. A major advantage of our proposed design is that a symmetrical radiation characteristics and low cross polarized radiation can be obtained. This is not possible in the case of the antenna presented in [15], where the asymmetric nature of the structure results in high cross polarized and tilted radiation patterns when the antenna is immersed in oil.

As mentioned earlier, loading the antenna with two slots parallel to and near the radiating edges of the patch affects not only the operating frequency of TM_{300} mode, but also that of TM_{500}. The length of these two slots and their loading effect on the operating frequencies of the higher-order modes, however, is limited by the width of the patch. To overcome this limitation, two symmetric spirals are added at each end of the slot as shown in Fig. 3. This permits a greater reduction in the operating frequencies of both TM_{300} and TM_{500} modes, which are now determined by the effective length of the slot that is from one end of one spiral to the corresponding end of the other spiral. The longer the effective length of these spiral-loaded slots, the lower the operating frequencies of TM_{300} and TM_{500} modes. By increasing the effective length of the spirals, the operating frequency of TM_{500} can be reduced significantly such it operates within the frequency range of interest. Consequently, a patch antenna with tri-band response within 0.5-3 GHz frequency range can be obtained.

An added benefit of using the spiral slot is that, in conjunction with the center slot, it offers greater flexibility not only in reducing the operating frequencies of TM_{300} and TM_{500}, but also in determining the separation between the operating frequencies of TM_{100} and TM_{300}. Using the structure presented in [14] the ratio between the two frequencies of operation (f_{300}/f_{100}) can only be changed in a limited range of 1.6-2.0, where f_{300} and f_{100} refer to the operating frequency of TM_{300} and TM_{100} modes, respectively. However, using the proposed antenna, this ratio can be designed to be as small as 1.0 and as large as 2.0. This means that the resonant frequencies of both modes can be merged together to achieve a wider band of operation than that of either mode, if desired, and a corresponding larger fractional bandwidth. The topology of the proposed bandwidth-enhanced patch antenna is shown in Fig. 4.

3. RESULTS AND DISCUSSION

The proposed designs of the miniaturized patch antenna discussed in the previous section are simulated using CST Microwave Studio. The dimensions of these antennas immersed in safflower oil are optimized to operate within the 0.5–3.0 GHz frequency range of interest. Prototypes of the miniaturized antennas are patterned on 32-mil-thick RO4003 substrate (from Rogers Corp.) and are probe-fed using the center conductor of an SMA

connector. In what follows the calculated and measured results of the fabricated prototypes are discussed in details.

3.1 Dual-band antenna

Fig. 5 shows the calculated reflection coefficient of the miniaturized dual-band patch antenna whose topology is shown in Fig. 1 and whose physical dimensions are reported in the caption of that figure. The antenna exhibits a multiband response with resonances at 1.37, 1.95, and 2.90 GHz. However, only the first and the third frequency are of interest, since the radiation pattern of the second mode, TM_{200}, has a null in the broadside direction. The frequencies of the two desirable modes of interest represent a reduction of 37% and 23%, respectively, relative to the slot-loaded patch antenna reported in [14]. Fig. 5 also shows the measured reflection coefficient of the fabricated prototype immersed in a 32×15×11 cm tank filled with safflower oil. Excellent agreement between the simulated and measured reflection coefficients is observed. The slight discrepancy between the simulation and measurement results is attributed to the inherent uncertainty in the electrical properties of the safflower oil. Fig. 6 shows the measured transmission coefficient for a system of two miniaturized patch antennas separated by a distance of 10 cm in the oil. As expected, the system has transmission peaks at 1.37 and 2.9 GHz. The transmission peak at 1.95 GHz is very low which confirms that the radiation pattern has a broadside null at this frequency.

The radiation patterns of the miniaturized patch antenna, while immersed in oil, are also characterized. The radiation pattern measurements were taken at a distance of 15 cm from the patch. The co- and cross-pol radiation patterns in the E- and H-plane of the fabricated prototype at the two frequencies of interest are measured and depicted in Fig. 7. The measured cross-pol level is 20 dB lower than co-pol at broadside for both frequencies. As is observed, there is a better agreement between measurement and simulation in the co-pol radiation patterns than those of the cross-pol. This discrepancy in the cross-pol is attributed to the fact that the very low cross-pol levels are more susceptible to measurement imperfections.

3.2 Tri-band antenna

Fig. 8 shows the calculated reflection coefficient of the proposed miniaturized tri-band antenna shown in Fig. 3. The physical dimensions are reported in the caption of that figure. The antenna exhibits a multiband response in the 0.5-3 GHz range with resonances corresponding to those of the first five higher-order longitudinal modes. However, only three of these frequencies are of interest, since they have maximum radiation in the broadside direction. These frequencies are 1.35, 1.72 and 2.98 GHz and they correspond to resonant frequencies of the TM_{100}, TM_{300}, and TM_{500} modes, respectively. Fig. 9 shows the calculated transmission coefficient for a system of two

miniaturized patch antennas separated by a distance of 10 cm in the oil. As expected, three transmission peaks are observed at these frequencies.

The radiation patterns of the miniaturized antenna are also calculated. Fig. 10 shows the co- and cross-pol radiation patterns in the E- and H-plane. The measured reflection and transmission coefficients of the fabricated prototype as well as its radiation characteristics will be presented in the symposium.

3.3 Bandwidth-enhanced antenna

By loading the antenna with spiral slots parallel to and near the radiating edges, a greater flexibility in determining the separation between the operating frequencies of TM_{100} and TM_{300} is achieved. Furthermore, the ratio between the two frequencies can be designed to be as small as 1.0. In the section, this type of loading along with center slot loading is used to improve the operational bandwidth of the patch antenna. Fig. 4 shows the topology of the proposed antenna and its physical dimensions are reported in the caption of that figure. By judicious choice of the length of the center slot and the effective length of the spiral slot, the frequency of TM_{300} is merged to that of TM_{100}. Fig. 11(a) shows the calculated reflection of the coefficient of the proposed antenna shown in Fig. 4. The center frequency of operation is optimized to be at 1.81 GHz with a fractional bandwidth of 3.3%. This represents a bandwidth improvement of more than 300% and a 15.5% reduction in the frequency of operation when compared to the slot loaded patch antenna reported in [14]. The radiation patterns within the bandwidth of operation are also calculated and shown in Fig. 11(b)-(d). As depicted, a consistent radiation patterns are maintained across the band. The complete measurements of the frequency response and the radiation characteristics of the fabricated prototype of the bandwidth-enhanced miniaturized patch antennas will also be presented in the symposium.

4. CONCLUSION

In this paper, designs of dual- and tri-band miniaturized patch antennas for microwave breast imaging were presented and validated experimentally by fabricating prototypes and measuring their performances in a biocompatible immersion medium. The multi-band response is obtained by manipulating the dominant mode, TM_{100}, and two of the higher order modes of the patch antenna, namely the TM_{300} and TM_{500} modes. The multi-band response and miniaturization of the patch antenna is achieved by loading the patch antenna with a series of slots located near the radiating edges, in the center of the patch, and along its non-radiating edges. This technique, using spiral slots near to and parallel to the radiating edges of the patch antenna, can also be used to enhance the operation bandwidth by a factor of 300% while reducing the operating frequency by a factor of 15.5%. This is achieved by merging the resonance of the TM_{300} mode with that of the TM_{100}.

References

[1] P. M. Meany, M. W. Fanning, T. Raynolds, C. J. Fox, Q. Q. Fang, C. A. Kogel, S. P. Poplack, and K. D. Paulsen, "Initial clinical experience with microwave breast imaging in women with normal mammography," Academic radiology, vol. 14, no. 2, pp. 207-218, Feb 2007.

[2] J. D. Shea, P. Kosmas, B. D. Van Veen, and S. C. Hagness, "Contrast enhanced microwave imaging of breast tumors: A computational study using 3-D realistic numerical phantoms," Inverse Problems, 2010, vol. 26, no. 7, Sp. Iss. SI Article Number: 074009, Jul 2010.

[3] Q. Fang, P. M. Meaney, and K. D. Paulsen, "Singular value analysis of the Jacobian matrix in microwave image reconstruction," IEEE Trans. Antennas Propag., vol. 54, no. 8, pp. 2371–2380, Aug. 2006.

[4] W. Chew, Waves and Fields in Inhomogeneous Media. Piscataway, NJ: IEEE Press, 1995.

[5] Q. Fang, P. M. Meaney, and K. D. Paulsen, "Microwave image reconstruction of tissue property dispersion characteristics utilizing multiple-frequency information," IEEE Trans. Microw. Theory Tech., vol. 52, no. 8, pp. 1866–1875, Aug. 2004.

[6] B. Brandstatter, K. Hollaus, H. Hutten, M. Mayer, R. Merwa, and H. Scharfetter, "Direct estimation of Cole parameters in multifrequency EIT using a regularized Gauss-Newton method," Physiol. Meas., vol. 24, no. 2, pp. 437–448, May 2003.

[7] C. Yu, M. Yuan, J. Stang, E. Bresslour, R. T. George, G. A. Ybarra, W. T. Joines, and Q. H. Liu, "Active microwave imaging II: 3-D system prototype and image reconstruction from experimental data," IEEE Trans. Microwave Theory Techn., vol. 56, no. 4, pp. 991-1000, 2008.

[8] D. W. Winters, J. D. Shea, P. Kosmas, B. D. Van Veen, and S. C. Hagness, "Three-dimensional microwave breast imaging: Dispersive dielectric properties estimation using patient-specific basis functions," IEEE Trans. Med. Imaging, vol. 28, no. 7, pp. 969-981, July 2009.

[9] T. Rubaek, O. S. Kim, and P. Meincke, "Computational validation of a 3-D microwave imaging system for breast cancer screening," IEEE Trans. Antennas Propag., vol. 57, no. 7, pp. 2105–2115, Jul. 2009.

[10] P. M. Meaney, K. D. Paulsen, A. Hartov, and R. K. Crane, "An active microwave imaging system for reconstruction of 2-D electrical property distributions," IEEE Trans. Biomed. Eng., vol. 42, no. 10, pp. 1017–1027, Oct. 1995.

[11] D. Li, P. Meaney, T. Raynolds, S. A. Pendergrass, M. W. Fanning, and K. D. Paulsen, "Parallel-detection microwave spectroscopy system for breast imaging," Rev. Sci. Inst., vol. 75, no. 7, pp. 2305–2313, 2004.

[12] N. Behdad, D. Shi, W. Hong, K. Sarabandi, and M. P. Flynn, "A 0.3 mm^2 miniaturized X-band on-chip slot antenna in 0.13 μm CMOS," in Proc. IEEE RFIC Symp., Jun. 2007, vol. 1, pp. 441–444.

[13] M. A. Al-Joumayly, S. M. Aguilar, N. Behdad, and S. C. Hagness, "Dual-band miniaturized patch antennas for microwave breast imaging," IEEE Antennas and Wireless Propag. Lett., vol. 9, no. 1, pp. 268-271, April 2010.

[14] S. Maci., G. Biffi Gentili, P. Piazzesi, and C. Salvador, "Dual-band slot-loaded patch antenna," IEE Proc. Microwave, Antennas and Propagation, vol. 142, no. 3, pp. 225-232, June 1995.

[15] S. Dey and R. Mittra, "Compact microstrip patch antenna," Microwave Opt. Techn. Lett., vol. 13, no. 1, pp. 12-14, Dec. 1998.

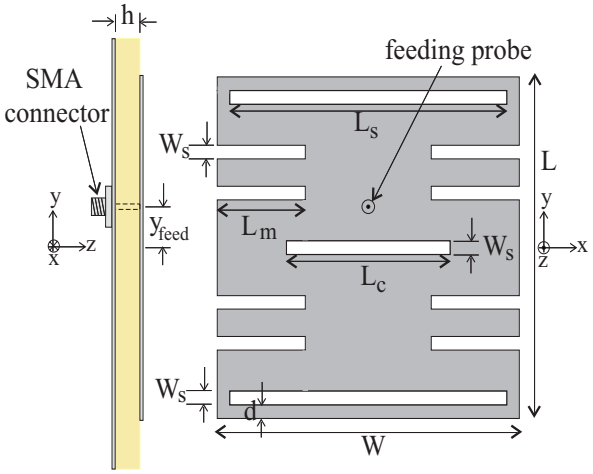

Fig. 1. Side view and top view of the proposed miniaturized dual-band patch antenna. W=28 mm, L=29 mm, W_s=1 mm, L_s=24 mm, L_c=12 mm, d=2 mm, L_m=10 mm, h=0.81 mm, and y_{feed}=4.5 mm.

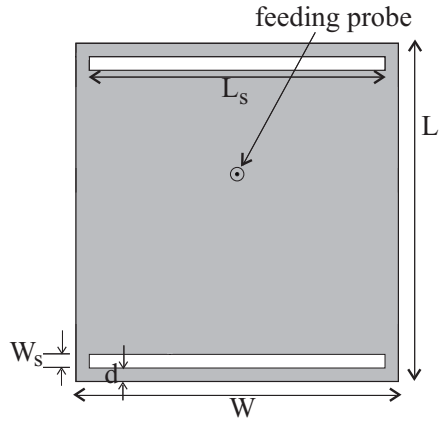

Fig. 2. Top view of the slot-loaded dual-band patch antenna reported in [15]. W=28 mm, L=29 mm, W_s=1 mm, L_s=24 mm, d=2 mm, and y_{feed}=9.5 mm.

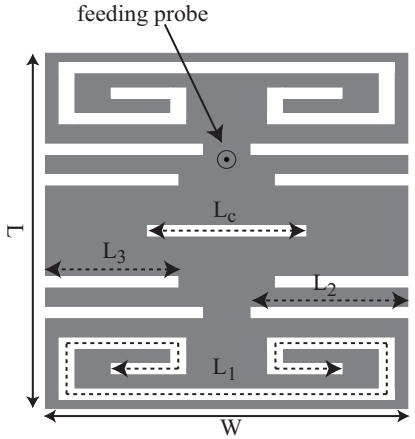

Fig. 3. Top view of the proposed miniaturized tri-band patch antenna. W=31 mm, L=31 mm, L_c=16 mm, L_1=39 mm, L_2=8 mm, L_3=7 mm, h=0.81 mm, and y_{feed}=2.5 mm.

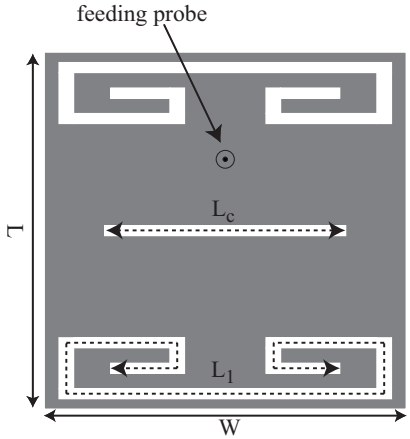

Fig. 4. Top view of the proposed bandwidth-enhanced patch antenna. W=32 mm, L=31 mm, L_c=16 mm, L_1=41 mm, h=0.81 mm, and y_{feed}=9 mm.

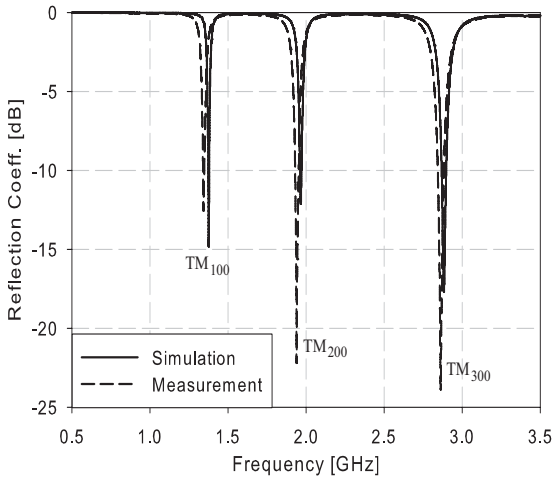

Fig. 5. Simulated and measured reflection coefficients of the miniaturized dual-band patch antenna of Fig. 1 immersed in safflower oil.

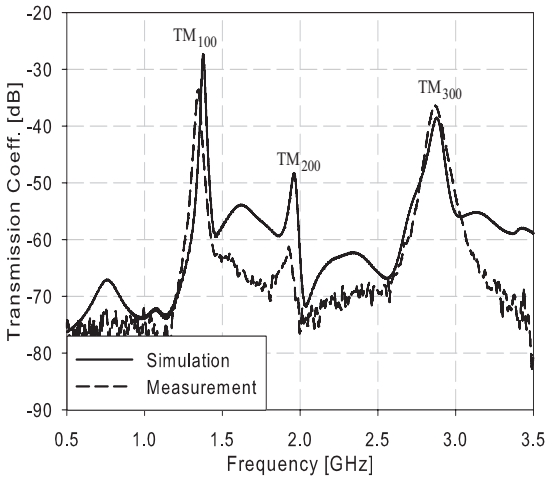

Fig. 6. Simulated and measured transmission coefficients of a two dual-band antenna system separated by a distance of 10 cm and immersed in safflower oil.

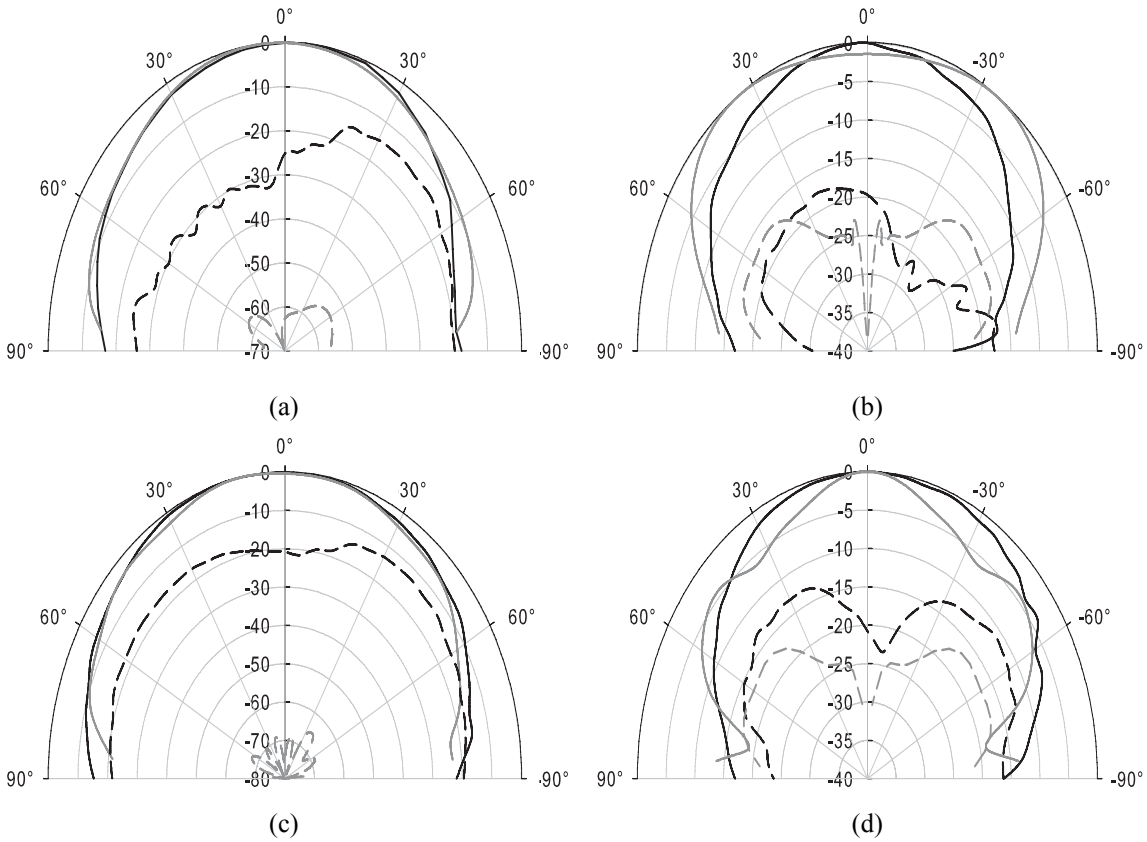

Fig. 7. Measured and calculated radiation patterns of the dual-band miniaturized patch antenna in oil: (a) E-plane at 1.37 GHz, (b) H-plane at 1.37 GHz, (c) E-plane at 2.9 GHz, and (d) H-plane at 2.9 GHz. Co-pol (solid lines) and X-pol (dashed lines). Simulation (gray) and measurement (black).

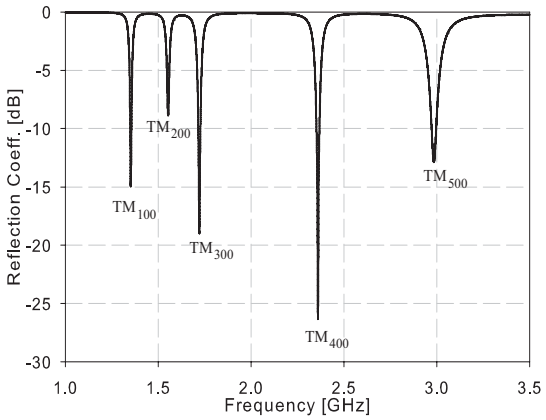

Fig. 8. Simulated reflection coefficient of the miniaturized tri-band patch antenna of Fig. 3 immersed in safflower oil.

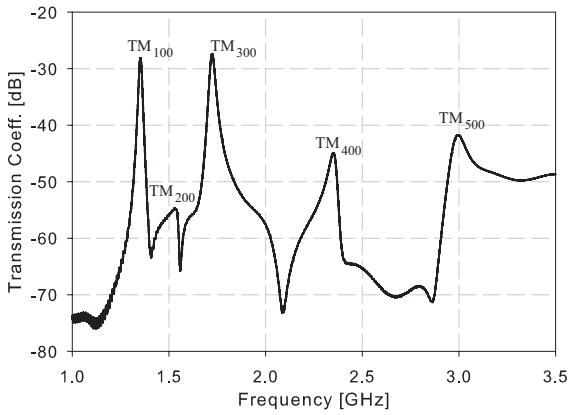

Fig. 9. Simulated transmission coefficient of a two tri-band antenna system separated by a distance of 10 cm and immersed in safflower oil.

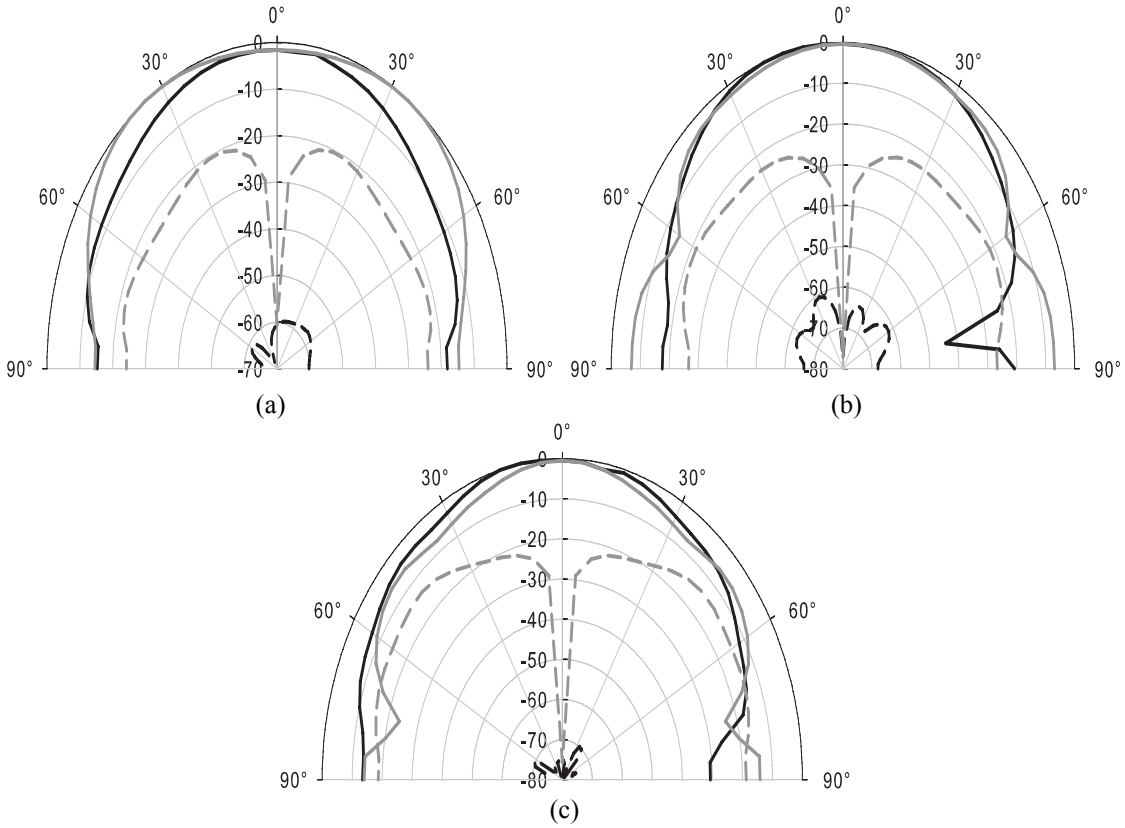

Fig. 10. Calculated radiation patterns of the tri-band miniaturized patch antenna in oil (a) at 1.35 GHz, (b) at 1.72 GHz, and (c) at 2.98 GHz. Co-pol (solid lines) and X-pol (dashed lines). E-plane (black) and H-plane (gray).

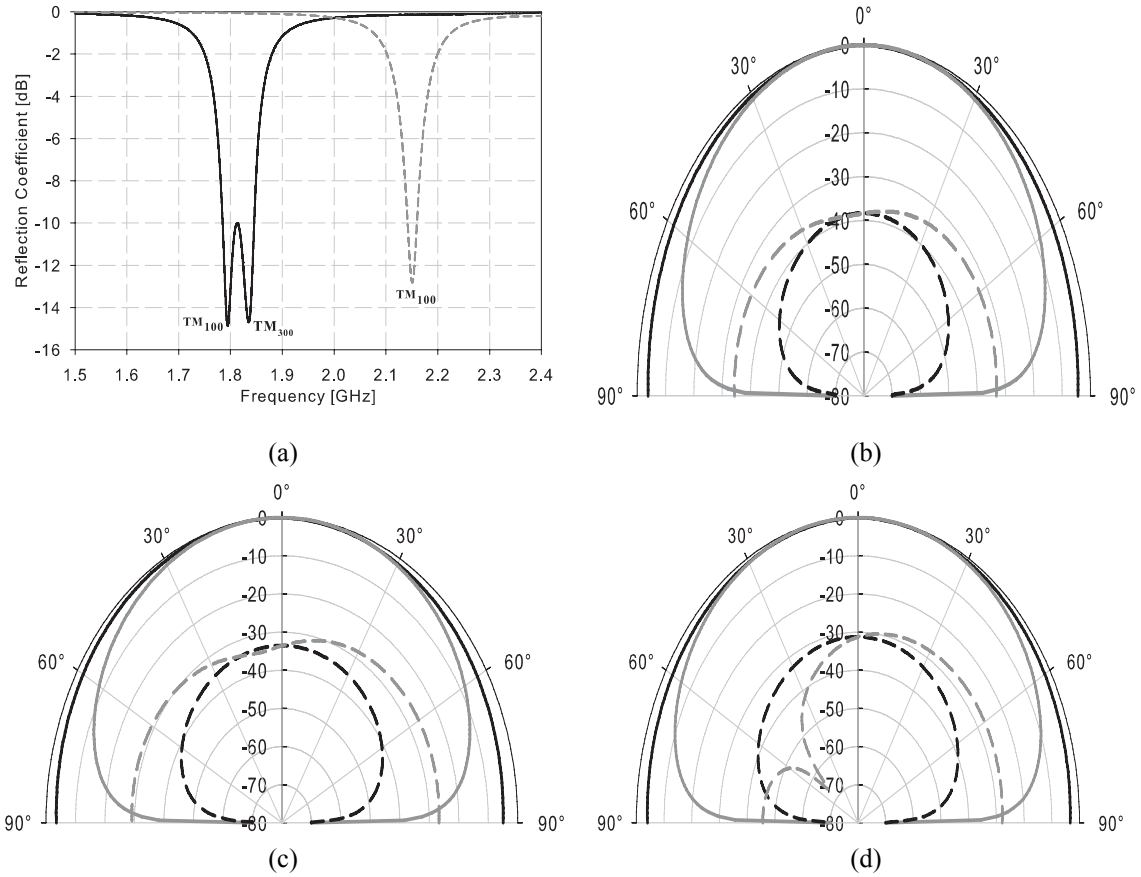

Fig. 11. Bandwidth-enhanced miniaturized patch antenna immersed in oil. (a) Calculated reflection coefficients of the bandwidth-enhanced miniaturized patch antenna and the slotted-patch antenna of the same size. Calculated radiation patterns (b) at 1.79 GHz, (c) at 1.81 GHz, and (d) at 1.83 GHz. Co-pol (solid lines) and X-pol (dashed lines). E-plane (black) and H-plane (gray)